2D and 3D numerical modelling of multilayer detachment folding and salt tectonics

Dissertation
zur Erlangung des akademischen Grades
„Doktor der Naturwissenschaften"

im Promotionsfach Geologie/Paläontologie

am Fachbereich Chemie, Pharmazie und Geowissenschaften
der Johannes Gutenberg-Universität Mainz

von
Naiara Fernández Terrones
geb. in Donostia-San Sebastián (Spanien)

Mainz, Juli 2014

D77

Dekan:

1. Berichterstatter:
2. Berichterstatter:

Datum der mündlichen Prüfung: 31.10.2014

Versicherung

für das Gesuch um Zulassung zur Promotion in dem Fachbereich 09

Hiermit versichere ich gemäß
§ 10 Abs. 3d der Promotionsordnung vom 24.07.2007

a) Ich habe die jetzt als Dissertation vorgelegte Arbeit selbst angefertigt und alle benutzten Hilfsmittel in der Arbeit angegeben.

b) Ich habe oder hatte die jetzt als Dissertation vorgelegte Arbeit nicht als Prüfungsarbeit für eine staatliche oder andere wissenschaftliche Prüfung eingereicht.

c) Ich hatte weder die jetzt als Dissertation vorgelegte Arbeit noch Teile davon bei einer anderen Fakultät bzw. einem anderen Fachbereich als Dissertation eigereicht.

Abstract

Numerical modelling was used to study the dynamics of multilayer detachment folding and salt tectonics.

Multilayer detachment folding phase diagrams that show the existence of several folding modes were derived with analytical solutions. The analytically predicted fold wavelength is well preserved in 3D numerical simulations. However, the 3D simulations exhibit a wide variety of fold shapes due to the interactions between growing fold segments. The influence of pre-existing salt diapirs on the 3D folding instability was also studied. Although the fold wavelength is not strongly influenced in most cases, the folding patterns are affected as pre-existing diapirs localize the initial deformation by accommodating folding. If diapir spacing is much smaller than the dominant folding wavelength, diapirs appear in different structural positions such as fold synclines or flanks.

Next, the patterns of down-building diapirism in 3D numerical models were studied. Sedimentation rate is shown to have a strong influence on whether diapirs will form or not but it also controls the initial diapir shape and can further influence final patterns. The relationship between salt extrusion and observed sediment geometries around diapirs is established in the 3D simulations.

The same numerical codes used in the forward modelling of salt diapirs were used to retrodeform modelled salt diapirs formed by two different processes. Reverse modelling is able to retrieve the initial geometries of a 2D Rayleigh-Taylor instability with non-linear rheologies. Yet, in the case of 3D down-built diapirs, even though intermediate geometries are correctly retrieved, both forward and reverse modelling solutions deviate at the final stage.

Finally, the dynamics of fold-and-thrusts belts formed over a tilted viscous detachment is studied. The mechanical stratigraphy has an impact on the deformation style, switching the deformation to be either thrust- or fold-dominated. The basal angle of the detachment, on the other hand, controls the deformation sequence within the fold-and-thrust belt. The results are discussed within the critical wedge theory.

CONTENTS

Chapter 1

Introduction

1.1 Introduction

Salt tectonics is defined as the deformation in which there is salt flow, and as such it can involve both regional extension and compression as well as deformation purely driven by gravity (halokinesis) (Hudec and Jackson, 2007). Salt, when understood in the broadened term that encompasses all evaporitic deposits (Archer et al., 2012), displays an almost unique behaviour if compared to other rocks due to its high mobility. As it was already noticed by Nettleton (1934) salt behaves as a viscous fluid. The reason for such behaviour is that salt has very low yield stress and therefore deforms very easily. Other important physical characteristic of salt is that it is relatively incompressible and that it is usually less dense than most of the rocks.

When salt is present in compressional settings and a fold and thrust belt develops, the fold and thrust belt is wider and has lower taper angles (Davis and Engelder, 1985) than when salt is absent. The deformation in such cases can propagate faster, structures are more symmetric and there might not be a forelandwards propagation of the deformation (Costa and Vendeville, 2002). These differences rise, from the fact that salt has different properties than those of other frictional materials that result in different dynamics in the fold-and-thrust belts (Ruh et al., 2012). But the different mechanical properties are important not only when salt is at the base of a sedimentary cover, but also if intermediate salt levels or other weaker materials are present within the cover. In this case, the deformation style is also affected, and it be can switch from thrusting dominated, to folding dominated (Yamato et al., 2011).

One of the main driving forces in salt tectonics is differential loading. Because salt is incompressible, its density does not change when buried under other compacting materials. As a result, a density inversion develops that can cause salt to be buoyant and rise. Although in most cases more processes and not only buoyancy need to be invoked (e.g. extension or compression), gravitational instability is the main cause that salt diapirs can form.

Salt has had an important role in petroleum exploration since the beginning of the twentieth century. Much of the interest in salt tectonics is still derived from the oil industry today due to the fact that many of world's oil reserves are located in salt provinces, such as the Gulf of Mexico, North Sea, Santos Basin and the Zagros (Archer et al., 2012). According to Hudec and Jackson (2007) around 120 of the worldwide salt basins have been affected by salt tectonics (see Figure 1.1).

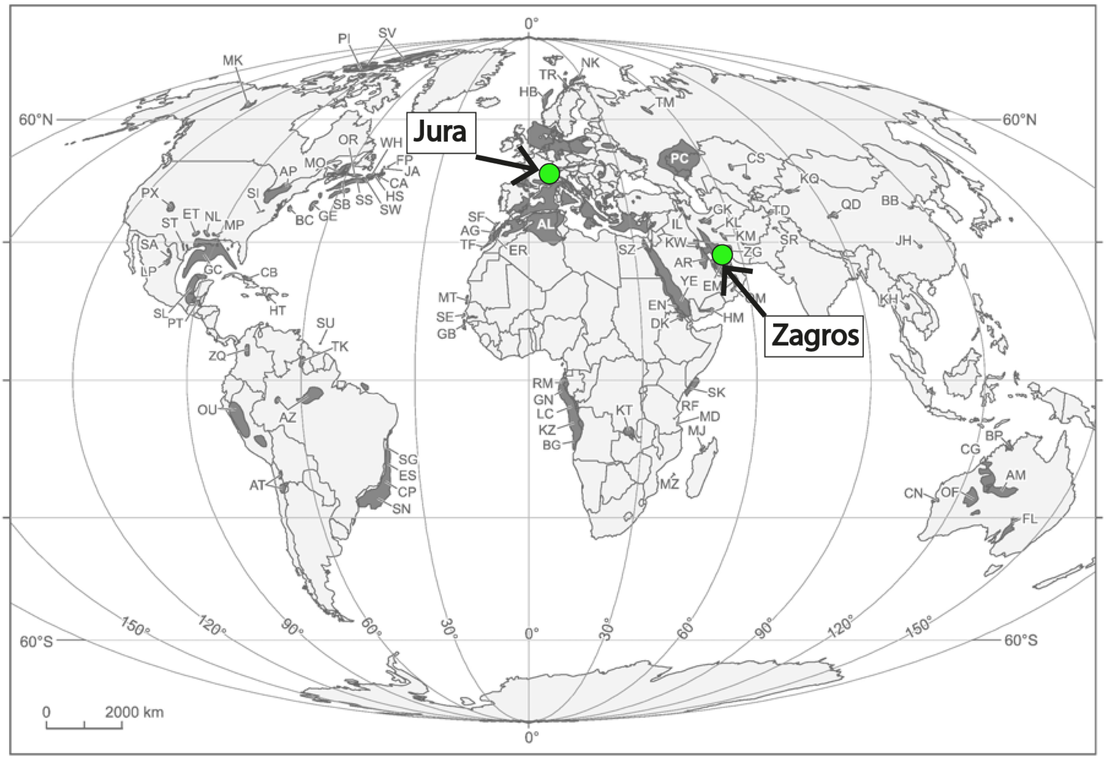

Figure 1.1. Map of the global distribution of basins affected by salt tectonics (grey areas). Basins with undeformed salt are omitted. The green dots indicate the location of the Jura and Zagros Mountains. Modified from Hudec and Jackson (2007). See the original source for the meaning of the abbreviations.

Within the previously mentioned examples, the Zagros Mountains might be one of the best well-known example where the role of salt in compressional settings can be studied (see Figure 1.1). In the Zagros Simply Folded Belt, folding is one of the main processes by which the sedimentary cover has accommodated shortening (Colman-Sadd, 1978). The folds in the Zagros, although quite regularly spaced around a dominant wavelength value, exhibit also very diverse aspect ratios and shapes. Despite the 2D folding instability has been extensively studied since several decades (e.g. Biot, 1961), there have not been studies that take into account a three dimensional multilayer system, which is more appropriate for the Zagros (Yamato et al., 2011). One of the questions this study addresses is whether a folding instability in 3D multilayer detachment models can explain the many folding related features observed in the Zagros.

However, the south-eastern area of the Zagros is also well known for the hundreds of salt plugs/diapirs formed of Precambrian salt that “pierce” the sedimentary cover and whose relation with folding in the area has for long been noticed (Kent, 1979). Initial phases of salt movement in the area are proposed to predate folding on the basis of reworked Precambrian salt and unconformities close to the diapirs (e.g. Jahani et al., 2007). Furthermore, it has been recently proposed that the diapirs of south-eastern Zagros were formed by syn-depositional passive diapirism or down-building and that therefore they were either exposed at the surface or very shallowly buried when folding developed (Callot et al., 2007). One of the questions that arise is to which extent the existing salt diapirs might have controlled the later folding, and how the characteristics spacing of diapirism (Biot, 1966) and characteristic wavelength of folding interact together.

The regular spacing of the salt diapirs in south-eastern Zagros has been postulated to be related to trends in the basement that controlled initial salt thickness deposition (Kent, 1979). However, regular spacing and polygonal patterns of diapirs are recognized in many other salt basins such as the Gulf of Mexico and the Santos Basin in Brazil. These polygonal patterns are usually formed by salt ridges with the diapirs located at the junctions and minibasins formed within the areas delimited by the ridges. Sedimentation rate is known to influence the shape of diapirs formed by down-building syn-depositional processes and to control whether diapirs will form or not (Fuchs et al., 2011). Yet, the effect of sedimentation rate on the final three-dimensional patterns had not been addressed so far. This question is also addressed in this study.

Retrodeformation techniques have since long been used to validate cross sections or seismic interpretations in salt tectonics areas. However, many of the widely used techniques, such as kinematic or mechanical-elastic retrodeformation techniques, do not account for the high mobility of salt. The numerical codes that are normally used for geodynamic forward modelling can also be applied for retrodeforming structures by reversing the processes that drove the deformation forwards in a dynamically consistent manner (e.g. Lechmann et al., 2010). It has however, not been investigated whether the reverse modelling is a valid approach to retrodeform salt diapirs formed in 3D by down-building or in 2D by up-building with non-linear rheologies.

Another different example of a salt basin affected by compression is found on the Jura Mountains (Figure 1.1). The Jura is also a widely studied example of a fold-and-thrust belt over a weak detachment in middle and upper Triassic evaporites (e.g. Laubscher, 1977). As such, it exhibits most of the corresponding characteristics, including low taper angle and an arcuate shape that correspond to the thickest area of the salt basin below (Sommaruga, 1999). Although it is recognized that the presence of basal evaporitic level played an important role in its formation, the current position of the Jura fold-and-thrust belt several kilometres far away from the Alpine front, is still not fully understood.

During the work presented in this thesis, several of the processes (folding, diapirism) involved in the mentioned areas have been studied by using numerical modelling tools in order to address some of the questions outlined before. The aim of this work has been to understand the dynamics behind those processes and to discuss its implications for the studied areas.

1.2 Method

In this work, a continuum mechanics approximation is used. The use of a continuum medium assumption implies that at macroscopic scale the material that is being considered does not contain mass-free voids or gaps (Gerya, 2009). For such a medium, a continuous description of the physical properties is required, where each physical property can vary through the medium. The equations used to describe the displacement of a continuous medium are given by the set of balance equations for mass and momentum together with their constitutive relationships. In most of the part of this work the materials involved in the studied processes are described as slowly creeping incompressible viscous materials, which is appropriate to study the long term behaviour of rocks.

The conservation equations can be solved analytically in certain cases. However, when these equations become too complicated to get an exact solution or cannot be solved analytically, they can be transformed into discrete equations to be solved numerically (Ismail-Zadeh and Tackley, 2010). Following the numerical grid, numerical modelling requires that a finite approximation is chosen in the discretisation process. Finite differences and finite element approximations are two of the most widely used approximations in geodynamics.

The basis of the finite differences method is to reduce the ordinary partial differential equations to discrete equations that are approximate and that can be implemented for computation (Ismail-Zadeh and Tackley, 2010). For this purpose, the continuous derivative is replaced with finite difference approximations.

In the case of finite element methods, instead of using approximations of the partial differential equations, the integration of the differential equation over the modelling domain is required. The modelled domain is divided into subdomains (elements) and solution of the differential equation approximated by a polynomial function on each element (Ismail-Zadeh and Tackley, 2010).

Two different codes have been used during the work presented in this thesis. The 2D visco-elasto-plastic finite element code MILAMIN_VEP and the 3D parallel code LaMEM (Lithosphere and Mantle Evolution Model). When possible, analytical solutions have been used to compare the results. The particular aspects of the methods used for the individual studied problems are explained in each of the chapters. However, the used numerical codes will be also described very briefly next.

For the 2D simulations, equations are solved within the 2D Lagrangian finite element code MILAMIN_VEP (Kaus, 2010) that solves the equations of conservation of momentum and of mass for incompressible materials with visco-elasto-plastic rheologies. MILAMIN_VEP is based on the Matlab solvers MILAMIN (Dabrowski et al., 2008).

For the 3D simulations, equations are solved within LaMEM, which has a framework that allows both Finite Element and Finite Differences methods in the same code. In both cases, properties of the materials are also tracked with particles (also known as markers) and advected in a Lagrangian manner. In the case of the finite element method, the high order element Q_2P_{-1} was used, whereas in the finite differences method a fully staggered scheme is used. LaMEM is based on the C written PETSc libraries, which provide parallel solvers that have contributed to the massively parallel configuration of the code. In fact, recent advances in computer power and software have opened new possibilities for high-resolution numerical modelling that takes advantage of the use of high performance clusters. 3D simulations shown in this work were performed on the Cray XT5 "Monte Rosa" supercomputer of the Swiss National Supercomputing Centre, on the IBM Blue Gene/Q JUQUEEN supercomputer of the Forschungszentrum Jülich, Germany and on MOGON supercomputer of Johannes Gutenberg University of Mainz, Germany.

1.3 Outline of the thesis

This thesis is divided into five different research chapters, each one addressing a different aspect outlined in the introduction and a final concluding chapter. All five research chapters are conceived as independent chapters and therefore have their own abstract, introduction, method/setup section, results, discussion, conclusion and references.

Chapter 2. Fold interaction and wavelength selection in 3D models of multilayer detachment folding. This chapter focuses on the folding instability on 3D multilayer detachment models. Initially, a 2D semi-analytical solution is used to construct folding phase diagrams. The scaling laws and boundary equations for the various folding modes that exist in multilayer systems under the influence of gravity were derived. These scaling laws are compared with numerical simulations in 2D and 3D to confirm that the results hold for high amplitude folding. Several 3D high resolution simulations are used to study the interaction between the different growing fold segments in 3D. The results are discussed with regards to the Fars area of the Zagros Simply Folded Belt. *This chapter is in press in Tectonophysics as: Fernandez, N. and Kaus, B.J.P. (2014) "Fold interaction and wavelength selection in 3D models of multilayer detachment folding". DOI: 10.1016/j.tecto.2014.06.013*

Chapter 3. Influence of pre-existing salt diapirs on 3D folding patterns. The existence of initial heterogeneities or weak zones, such as pre-existing salt plugs within the sedimentary cover, might affect fold development as well. Therefore, in this chapter we also investigated how the fold pattern is affected by pre-existing salt structures. Synthetic diapir distributions are initially considered to compare the effect of pre-defined diapir spacing on folding wavelength and lateral growth. Finally, a south-eastern Zagros-like diapir distribution is considered. The results are discussed with regards to the Fars area of the Zagros Simply Folded Belt. *This chapter is submitted as: Fernandez, N. and Kaus, B.J.P. (2014) "Influence of pre-existing salt diapirs on 3D folding patterns".*

Chapter 4. 3D patterns of down-built diapirs. In this chapter the formation and evolution of salt diapirs formed by down-building syn-depositional processes is studied. The focus of the chapter is to investigate how the final patterns of down-built diapirs develop and how they relate to the initial polygonal patterns that are the result of the buoyancy instability. The role of the sedimentation rate is studied at the initial stages of the simulations as well as during the more evolved stages of diapirs. The salt extrusion in the model domains is also studied and related to the sediment geometries that are observed close to the diapirs.

Chapter 5. Reverse modelling of 2D and 3D salt structures. In this chapter, the same numerical codes that are used for forward modelling are used to retrodeform salt structures by using the reverse time step approach. The validity of a reversed time step approach is checked for two specific cases: 2D Rayleigh-Taylor instability (up-built diapirs) using non-linear viscous rheologies and on down-built diapirs in 3D. Although the approach has been applied successfully in previous studies of up-built diapirs with simple rheologies, the retrodeformation of down-built diapirs the way they are implemented in this work poses some challenges that need to be addressed in future work.

Chapter 6. Dynamics of thin-skinned fold and thrust belts with a tilted detachment. A 2D mechanical code is used to study the dynamics of a fold-and-thrust belt forming over a viscous detachment with a tilted topography. Two different boundary conditions, both applicable to convergent areas, are tested and compared. Then, the influence of the basal angle of a uniformly dipping detachment or of a detachment with a slope change is studied. The effect of the mechanical stratigraphy in the overall dynamics of the system is also investigated. Finally, the impact of the flexed shape of the basal detachment on the surface slope is studied by using an analytical solutions. The results are discussed with regards to the Jura fold-and-thrust belt.

Chapter 7. Conclusions. This final chapter summarizes briefly the conclusions of the previous chapters.

1.4 References

Archer, S.G., Alsop, G.I., Hartley, A.J., Grant, N.T., and Hodgkinson, R., 2012, Salt tectonics, sediments and prospectivity: an introduction: Geological Society, London, Special Publications, v. 363, p. 1-6.

Biot, M.A., 1961, Theory of Folding of Stratified Viscoelastic Media and Its Implications in Tectonics and Orogenesis: Geological Society of America Bulletin, v. 72, p. 1595-1620.

Biot, M.A., 1966, Three-dimensional gravity instability derived from two-dimensional solutions: Geophysics, v. 31, p. 153-166.

Callot, J.P., Jahani, S., and Letouzey, J., 2007, The Role of Pre-Existing Diapirs in Fold and Thrust Belt Development, *in* Lacombe, O., Roure, F., Lavé, J., and Vergés, J., eds., Thrust Belts and Foreland Basins: Frontiers in Earth Sciences, Springer Berlin Heidelberg, p. 309-325.

Colman-Sadd, S.P., 1978, Fold development in Zagros simply folded belt, Southwest Iran: AAPG Bulletin, v. 62, p. 984-1003.

Costa, E., and Vendeville, B.C., 2002, Experimental insights on the geometry and kinematics of fold-and-thrust belts above weak, viscous evaporitic décollement: Journal of Structural Geology, v. 24, p. 1729-1739.

Dabrowski, M., Krotkiewski, M., and Schmid, D.W., 2008, MILAMIN: MATLAB-based finite element method solver for large problems: Geochemistry, Geophysics, Geosystems, v. 9, p. Q04030.

Davis, D.M., and Engelder, T., 1985, The role of salt in fold-and-thrust belts: Tectonophysics, v. 119, p. 67-88.

Fuchs, L., Schmeling, H., and Koyi, H., 2011, Numerical models of salt diapir formation by down-building: the role of sedimentation rate, viscosity contrast, initial amplitude and wavelength: Geophysical Journal International, v. 186, p. 390-400.

Gerya, T., 2009, Introduction to numerical geodynamic modelling, Cambridge University Press.

Hudec, M.R., and Jackson, M.P.A., 2007, Terra infirma: Understanding salt tectonics: Earth-Science Reviews, v. 82, p. 1-28.

Ismail-Zadeh, A., and Tackley, P., 2010, Computational methods for geodynamics, Cambridge University Press.

Jahani, S., Callot, J.-P., Lamotte, D., Letouzey, J., and Leturmy, P., 2007, The Salt Diapirs of the Eastern Fars Province (Zagros, Iran): A Brief Outline of their Past and Present, *in* Lacombe, O., Roure, F., Lavé, J., and Vergés, J., eds., Thrust Belts and Foreland Basins: Frontiers in Earth Sciences, Springer Berlin Heidelberg, p. 289-308.

Kaus, B.J.P., 2010, Factors that control the angle of shear bands in geodynamic numerical models of brittle deformation: Tectonophysics, v. 484, p. 36-47.

Kent, P.E., 1979, The emergent Hormuz salt plugs of southern Iran: Journal of Petroleum Geology, v. 2, p. 117-144.

Laubscher, H.P., 1977, Fold development in the Jura: Tectonophysics, v. 37, p. 337-362.

Lechmann, S.M., Schmalholz, S.M., Burg, J.P., and Marques, F.O., 2010, Dynamic unfolding of multilayers: 2D numerical approach and application to turbidites in SW Portugal: Tectonophysics, v. 494, p. 64-74.

Nettleton, L.L., 1934, Fluid mechanics of salt domes: AAPG Bulletin, v. 18, p. 1175-1204.

Ruh, J.B., Kaus, B.J.P., and Burg, J.-P., 2012, Numerical investigation of deformation mechanics in fold-and-thrust belts: Influence of rheology of single and multiple décollements: Tectonics, v. 31, p. TC3005.

Sommaruga, A., 1999, Décollement tectonics in the Jura forelandfold-and-thrust belt: Marine and Petroleum Geology, v. 16, p. 111-134.

Yamato, P., Kaus, B.J.P., Mouthereau, F., and Castelltort, S., 2011, Dynamic constraints on the crustal-scale rheology of the Zagros fold belt, Iran: Geology, v. 39, p. 815-818.

Chapter 2

Fold interaction and wavelength selection in 3D models of multilayer detachment folding[1]

Abstract

Many fold-and-thrust belts are dominated by folding and exhibit a fairly regular fold-spacing. Yet, in map-view, the aspect ratio of doubly-plunging anticlines varies considerably from very elongated, and sometimes slightly curved, cylindrical folds to nearly circular, dome-like structures. In addition, the fold spacing often varies significantly around an average value. So far, it remains unclear whether these features are consistent with a folding instability.

Therefore, we here study the dynamics of multilayer detachment folding, process by which shortening can be accommodated in thin-skinned fold-and-thrust belts. We start by analysing the physics of this process by using both a semi-analytical thick plate theory and numerical simulations. Results show that several different folding modes occur, about half of which are affected by gravity and have a wavelength that depends on the background deformation rate. Non-dimensional expressions are derived that predict the dominant wavelength and growth rate of each of these folding modes and mechanical phase diagrams are presented that illustrate the applicability of each of the modes.

Next, we perform 3D simulations and compare the results with those of 2D models and analytical theory. Both 2D and 3D numerical simulations have wavelengths that are in good agreement with the analytical predictions. In the high-resolution 3D simulations the lateral growth of folds is studied, in particular with respect to fold segments interactions and evolution of fold width-length aspect ratio.

The numerical simulations show a number of similarities with the Fars region of the Zagros fold-and-thrust belt including a large range of fold aspect ratio and a normally distributed fold wavelength around a dominant one.

Keywords: multilayer detachment folding; folding modes; fold interactions; 3D folding; numerical modelling

---

[1] This chapter is in press in Tectonophysics as: Fernandez, N. and Kaus, B.J.P. (2014) *Fold interaction and wavelength selection in 3D models of multilayer detachment folding.* DOI: 10.1016/j.tecto.2014.06.013

2.1 Introduction

Buckling or folding is one of the processes by which a mechanically layered system that undergoes layer parallel compression can accommodate shortening. Folds that occur as a result of this mechanical instability have been reported at all scales in nature, from millimetre to lithosphere scale, the most spectacular examples of which can be found in folding-dominated fold-and-thrust belts. Some fold and thrust belts, such as the Makran, appear to be dominated by thrusting, whereas others such as the Simply Folded Belt at Zagros Mountains are dominated by folding and yet others, such as the Jura Mountains, appear to be in an intermediate stage (Simpson, 2009). In order to explain these observations, Yamato et al. (2011) performed systematic numerical and analytical simulations. They showed that brittle crustal rocks would develop faults and thrust-sheets unless a crustal-scale folding instability is active which amplifies sufficiently fast. In the Zagros Simply Folded Belt, they argued that weak intermediate crustal layers act as a ‘lubricant’ and drastically increase the growth rate of the folding instability that therefore results in regularly spaced crustal-scale folds. If such weak layers are not present or if these intermediate layers are insufficiently weak, crustal-scale folds develop too slowly and the crust reacts to compression by forming thrust sheets (Ruh et al., 2012; Simpson, 2009; Yamato et al., 2011). A similar transition from folding to viscous over-thrusting might also occur for discontinuous single layers that are embedded in a matrix with a power-law viscous rheology (Jaquet et al., 2014).

If a folding instability occurs, we can use the observed fold spacing to constrain parameters that control the physics or the material parameters of the deformed crust on a geological timescale. Better understanding the physics of large-scale detachment folding is thus potentially important.

The folding instability has been studied for different rheologies: e.g. elastic, viscous (Biot, 1961; Fletcher, 1977; Smith, 1977), visco-elastic (Biot, 1961; Schmalholz and Podladchikov, 1999), power-law viscous (Fletcher, 1974; Smith, 1977) and more recently also for visco-elasto-plastic (Gerbault et al., 1999; Yamato et al., 2011). Some of the existing studies consider the problem of a competent layer embedded in a matrix (Biot, 1961) or the case of a multilayer embedded in the matrix (Biot, 1961; Ramberg, 1964; Schmalholz and Schmid, 2012; Schmid and Podladchikov, 2006). However, in order to have better insights into the dynamics of crustal scale fold belts in which due to the scale of the structures gravity effects might have played an important role, we must consider a different setup: a layer or multilayer overlying a matrix (Ramberg, 1964; Schmalholz et al., 2002; Schmalholz and Schmid, 2012).

All of the mentioned studies show that during the first incremental stages of the folding instability (when the amplitudes are infinitesimal or very small), certain values of the horizontal wavelength show faster growthrates than others and therefore a dominant wavelength can be defined. Despite the fact that the theory only considers infinitesimal amplitudes, the obtained dominant wavelength is the one expected to develop in nature by selection and locking during strain and consequent amplification of folds, which is confirmed by numerical simulations (Schmalholz and Podladchikov, 2000) and laboratory experiments (Hudleston, 1973; Mancktelow and Abbassi, 1992). It is also known that folds cannot amplify infinitely and that amplification velocity due to this mechanical instability decelerates when the passive or kinematic stage of growing is reached (Cobbold, 1976). Recently, the folding instability theory was extended beyond the initial stages of folding with a theoretical finite amplitude theory analysis (Adamuszek et al., 2013; Schmalholz and Podladchikov, 2000). The finite amplitude folding theory is essentially a correction to a linear folding theory and can predict the amplification of folds after the linear theory breaks down and amplification deviates from the exponential amplification curve predicted by instability analysis (Adamuszek et al., 2013; Schmalholz and Podladchikov, 2000), and was extended to 3D by Kaus and Schmalholz (2006).

As it was previously suggested that multilayer detachment folding is the dominant mode of deformation that accommodates most of the shortening of the sedimentary cover in the Simply Folded Belt of the Zagros (Yamato et al., 2011), we here focus on this folding mode. Of particular interest is how this folding mode develops in 3D as observations in the Fars province of the Zagros Mountains show that the area exhibits both elongated and sinusoidal curved long fold trains as well as nearly circular folds. There is only a limited amount of work published on 3D folding modelling, which either focussed on the general instability for small amplitudes (Fletcher, 1991, 1995), on the single layer folding instability (Kaus and Schmalholz, 2006; Schmalholz, 2008) or on detachment folding but with only a single viscous layer above the detachment layer (Grasemann and Schmalholz, 2012; Schmid et al., 2008).

On the other hand, multilayer folding has been previously studied for a set of layers embedded in a matrix using both Newtonian and non-Newtonian materials (Schmalholz and Schmid, 2012; Schmid and Podladchikov, 2006). The viscosity ratio between the competent layers causes a switch in behaviour of the multilayer stack from an effective single layer (low viscosity contrast) to a real multilayer behaviour when the viscosity contrast is sufficiently high. However, the real multilayer behaviour is limited to a particular range of the thickness ratios between the strong and the intermediate weak layers (matrix) equivalent to the contact strain theory of Ramberg (1962).

Our goal here is to study the physics of 3D multilayer detachment folding for both small and large viscosity contrasts under the influence of gravity. In order to understand the interaction and linkage of folds with time, we need to perform high-resolution three-dimensional simulations, which require the use of parallel high-performance computers. For computational reasons we restrict ourselves to Newtonian viscous layers. In order to understand the numerical simulations, we also derive expressions for the growth rate and dominant wavelength of the multilayer detachment folding setup as a function of material parameters and model setup and compare the predictions with 2D and 3D numerical simulations.

2.2 Methodology

2.2.1 Governing Equations

We use a continuum mechanics approximation where the equations used to describe geological processes consists of a set of balance equations for mass and momentum together with their constitutive relationships.

Conservation of mass and momentum for a highly viscous incompressible fluid are given by

$$\frac{\partial v_i}{\partial x_i} = 0 \qquad [2.1]$$

$$-\frac{\partial P}{\partial x_i} + \frac{\partial \tau_{ij}}{\partial x_j} = -\rho g_i \qquad [2.2]$$

where *i,j* represent spatial directions and repeated indices are summed, v_i are the velocities, x_i are the coordinates, P = $-\sigma_{ii}/3$ is pressure, σ_{ij} are the components of the total stress tensor, τ the deviatoric stress tensor, ρ the density (assumed to be constant per layer) and g, the gravitational acceleration.

We employ a linear viscous (Newtonian) constitutive relationship given by

$$\tau_{ij} = 2\eta\, \dot{\varepsilon}_{ij} \qquad [2.3]$$

where η is the Newtonian viscosity which is constant for each of the material phases (or rock type), and $\dot{\varepsilon}_{ij}$, the deviatoric strain rate tensor is given by

$$\dot{\varepsilon}_{ij} = \frac{1}{2}\left(\frac{\partial v_i}{\partial x_j} + \frac{\partial v_j}{\partial x_i}\right) \qquad [2.4]$$

These equations are solved analytically and numerically as described below.

2.2.2 2D Semi-analytical approach

The analytical solution we use is a thick plate stability analysis (Johnson and Fletcher, 1994). While thin plate is a valid approximation for one layer problem in which the shear stresses between the competent layer and matrix can be omitted in certain cases, the thick plate is a more suitable approach for the multilayer case where the shear stresses occurring at different interfaces cannot be ignored. The thick plate analysis for a multilayer system assumes that a sinusoidal shaped perturbation is present in one of the interfaces or in all of them. The description is based in the perturbation analysis explained in Burg et al. (2004), based on Johnson and Fletcher (1994).

Equation [2.1] is used to express v_x through v_z and the velocity is split in a sinusoidal perturbed part and a background part, due to pure shear shortening.

$$v_x = \bar{v}_x(z)\exp(I\omega x) - \dot{\varepsilon}_{bg}x \qquad [2.5]$$

$$v_z = \bar{v}_z(z)\exp(I\omega x) + \dot{\varepsilon}_{bg}z \qquad [2.6]$$

where $I = \sqrt{-1}$ and $\dot{\varepsilon}_{bg}$ is the background pure-shear strain rate assumed to be constant over the model. Substituting equations [2.5] and [2.6] in the set of balance equations for incompressible Stokes flow [2.1] and [2.2] and dividing by $\mu I exp(I\omega x)/\omega$ gives a fourth order ODE for $\bar{v}_z(z)$

$$\frac{\partial^4 \bar{v}_z(z)}{\partial z^4} - 2\omega^2 \frac{\partial^2 \bar{v}_z(z)}{\partial z^2} + \omega^2 \bar{v}_z(z) = 0 \qquad [2.7]$$

a general solution for equation [2.7] is the following,

$$\bar{v}_z(z) = \mathrm{A}e^{(\omega z)} + \mathrm{B}ze^{(\omega z)} + \mathrm{C}e^{(-\omega z)} + \mathrm{D}ze^{(-\omega z)} \qquad [2.8]$$

For each of the layers considered in the system, equation [2.8] applies and this means that there will be 4 unknown coefficients (A-D) per layer. In order to solve for the given number of unknowns, boundary conditions need to be defined at the interfaces between the different layers as well as at the top and bottom of the domain.

At the interface between the layers continuity of horizontal and vertical velocity is defined. Also stresses should be continuous across the interfaces. The four equations that apply on each layer are:

$$\bar{v}_x{}^{ab} - \bar{v}_x{}^{be} = 0 \qquad [2.9]$$

$$\bar{v}_z{}^{ab} - \bar{v}_z{}^{be} = 0$$

$$\bar{\sigma}_{xz}{}^{ab} - \bar{\sigma}_{xz}{}^{be} = 4\dot{\varepsilon}_{bg}(\eta^{ab} - \eta^{be})\frac{\partial h}{\partial x}$$

$$\bar{\sigma}_{zz}{}^{ab} - \bar{\sigma}_{zz}{}^{be} = (\rho^{ab} - \rho^{be})gh$$

where $h=A(t)\cos(\omega x)$ is the sinusoidally perturbed interface and A(t) is the perturbation amplitude which grows exponentially with time. ^{ab} and ^{be} indicate values above and below the interface.

The bottom boundary condition is a free slip boundary whereas the surface boundary (top boundary) is stress free or free deformable surface, and is either initially flat or initially perturbed with a sinusoidal perturbation that has the same amplitude as the initial amplitude at the lowermost interface.

$$\bar{\sigma}_{xz}{}^{lo} = 0 \qquad [2.10]$$

$$\bar{v}_z{}^{lo} = 0$$

$$\bar{\sigma}_{xz}{}^{up} = 0$$

$$\bar{\sigma}_{zz}{}^{up} = -\rho g A_{surf}$$

where A is the amplitude of the perturbation and ^{up} and ^{lo} indicate the upper and lower boundaries respectively.

For simple setups, such as for a single layer folding setup without gravity, it is possible to analytically solve these equations and obtain a closed form expression of wavelength and amplification rate as a function of layer thickness and viscosity contrast. This, in turn can be used to compute a dominant growthrate and dominant wavelength (see e.g. Fletcher, 1974).

For the more general multilayer setup discussed here, the resulting expressions would become excessively long. We therefore solve the governing equations with time using a Matlab ODE solver, which tracks the amplitude of each of the interfaces for a given initial wavelength. By doing this for various wavelengths, we can numerically find the dominant growthrate and corresponding wavelength. This can be used to derive approximate expressions of dominant growthrate and wavelength as a function of model parameters (see Kaus (2005) for a description including MAPLE scripts and Burg et al. (2004) and Kaus and Becker (2007) for a more detailed explanation).

2.2.3 Finite Element Code

The analytical theory is derived only for the first incremental stages of folding or for very low dipping fold limbs. For this reason we need a different method that works beyond initial stages of folding so that we can see how the predicted wavelength is selected during strain.

2.2.3.1 LaMEM

LaMEM (Lithosphere and Mantle Evolution Model) is a 3D finite difference and finite element code that solves the mass and momentum conservation equations [2.1] and [2.2] using a marker in cell Lagrangian method using an implicit formulation.

In this work we use the finite element solvers of LaMEM, in combination with a higher order discretization scheme that uses Q_2P_{-1} elements (Lechmann et al., 2011). Even though this is computationally expensive, it has shown to give highly accurate results as long as the element boundaries coincide with jumps in viscosity (Deubelbeiss and Kaus, 2008). We employ the code in a Lagrangian manner and no remeshing had to be applied for the results shown here. Material properties are tracked using tracers.

LaMEM uses the PETSc library (www.mcs.anl.gov/petsc) that provides several parallel solvers. LaMEM has been successfully tested on high performing clusters on over 16’000 cores. The results that we present here are based on runs performed in 1024 processors in Rosa Cray XT5 machine (currently updated to Cray XE6) of the Swiss Super Computing Centre (www.cscs.ch) in Manno (Switzerland) and on the Blue Gene/Q JUQUEEN Supercomputer of the Forschungszentrum Jülich, Germany. Good scalability is crucial in order to perform the high-resolution runs required in a reasonable CPU time, and high-resolution runs are required for the multilayer folding setup to provide a statistically meaningful number of folds.

For our study we have used high order Q_2P_{-1} elements, which have quadratic shape functions for velocity and linear, discontinuous shape functions for pressure. The high-resolution 3D runs use 256x256x13 elements (512x512x27 nodes) for a model domain of 200x320x6.5 km, and a fully coupled solution scheme in combination with a Galerkin geometric multigrid method pre-conditioner was used so solve the resulting saddle point problem. The computational requirements of the 3D simulations presented here are significant, and a typical simulation with ~250 timesteps takes about 3-4 days on 1024 cores, and the required time increases with increasing viscosity contrast. Yet, we are able to resolve up to 10^4 contrasts in viscosity in the 3D simulations reported here. Quasi-2D runs were performed by using 1 element in the third dimension and by using direct solvers.

Several boundary conditions are implemented in LaMEM, including a deformable free surface on top. One of the many advantages that can be attributed to the Finite Element Method over the Finite Differences Method is that a free surface can be implemented straightforward. For most of the runs, free slip boundary conditions are used everywhere except on the top boundary where a deformable free surface is used to allow topography to develop. Compression is achieved by imposing a positive constant normal velocity on one side of the model, parallel to X direction of the domain, in such a manner that the background strain rate remains constant throughout the simulation.

In the case of the analytical solution, the folding instability arises due to the presence of a sinusoidal shaped perturbation in one or all layer interfaces. In the case of the numerical simulation we can reproduce the same perturbation in the mesh to benchmark the code and compare the growthrate (see Section 2.3.1). However, in order to study which wavelength is selected during strain, we have added some random noise in the numerical mesh corresponding exactly to the interface between the lower detachment/salt layer and the overburden layers. The random noise was generated with the parallel random number generator of PETSc. The same random noise has been used for all the 3D high-resolution runs that are shown in here, enabling direct comparison between the runs with different parameters.

2.2.4 Topography Analysis Methods

We use two different methods to analyze the evolution of topography through time in the high-resolution 3D numerical runs, namely spectral and curvature analysis.

2.2.4.1 Curvature Analysis

In order to quantitatively analyze the aspect ratio of folds, they must be first identified in an automated manner such that they can be isolated and measured. Curvature analysis was recently proposed as an effective tool that allows classification of folded surfaces (Lisle and Toimil, 2007; Mynatt et al., 2007). By considering both Mean and Gaussian curvatures, the surface can be classified into different folding geometries. Usually, both curvatures can be calculated as the average or the product of maximum and minimum principal curvature. A shortcut is offered by the differential geometry as explained by (Mynatt et al., 2007). Here, we apply the curvature values obtained from differential geometry to distinguish between the 3D folding geometries proposed by Mynatt et al. (2007). The Matlab script provided in (Pollard and Fletcher, 2005) has been used for this purpose requiring an initial processing of the 3D topography to convert it to a regular grid. Schmid et al. (2008) used an eroded Gaussian curvature binary image to isolate domes and basins. By performing binary image erosion the features within images, domes and basin in this case, shrink by stripping away a layer of pixels, deleting details and therefore enhancing the gaps in between them. Here, we focus only on the evolution of dome features through time that are identified as areas of positive Gaussian and Mean curvatures, that are apart from one another and as a result there is no need for applying the binary image erosion. These dome features have been isolated and their aspect ratio and orientation calculated as in Schmid et al. (2008).

2.2.4.2 Spectral Analysis

In order to compute folding wavelength versus time, we used a 1D Fourier analysis both parallel and orthogonal to the compression orientation. For this purpose, we use the in-built *fft* function of Matlab that provides the discrete Fourier transform of a given vector, and apply it to a topography that was interpolated on a regularized mesh. Results of the *fft* function for each orientation are averaged, and the maximum, minimum and mean amplitude and corresponding wavelength are extracted.

2.3 Multilayer Detachment Folding

2.3.1 Comparison of 2D semi – analytical and quasi-2D numerical runs

In order to check the accuracy of the numerical results, we first compared the numerical quasi-2D runs (having 1 element in the y-direction) with the 2D semi-analytical solution, in which a sinusoidal perturbation of varying initial wavelength is applied only to the salt/overburden interface. The active vertical velocity (the total velocity minus that caused by pure shear deformation) was normalized over the amplitude of the sinusoidal perturbation to give a growthrate q. A comparison of the numerical results with the analytical solution shows an excellent fit (Figure 2.1), demonstrating that the employed numerical resolutions are sufficient. We have performed the same test with both direct and iterative solvers, and found the results to be nearly identical which suggests that the parameters used in the iterative multigrid solvers are appropriate to correctly resolve the folding instability.

The dominant growthrate and wavelength strongly depend on the type of setup: if only the salt-overburden interface is perturbed and all other layers (in particular the free surface) are initially flat, the dominant wavelength is around 40 km whereas the dominant growthrate is around 105 using the parameters of Simulation 1 listed in Table 2.1. If, on the other hand, all layers including the free surface are perturbed in a sinusoidal manner, the dominant growth rate and wavelength is significantly smaller using the same parameters, in agreement with semi-analytical predictions (Figure 2.1). An analysis shows that this is mainly caused by the presence of topography at the free surface; this topography acts as a load that works against gravity, which explains why the folds amplify slower.

In the numerical simulations described in the remaining part of this paper, we only perturbed the lowermost interface with random noise, and used an initially flat free surface. In those simulations, the initial fastest growing wavelength corresponds to the dashed line in Figure 2.1. Yet, as soon as some topography develops, a much smaller wavelength becomes the fastest amplifying wavelength (solid line in Figure 2.1). The finite amplitude folds that develop in the numerical simulations have a wavelength that is close to this wavelength.

This change in wavelength selection only occurs for gravity-dominated folding mode. If one wishes to derive semi-analytical expressions for the dominant wavelength that develops in such folding modes, it is thus crucial to perturb all layers in the analytical setup, which is what we did in the following sections.

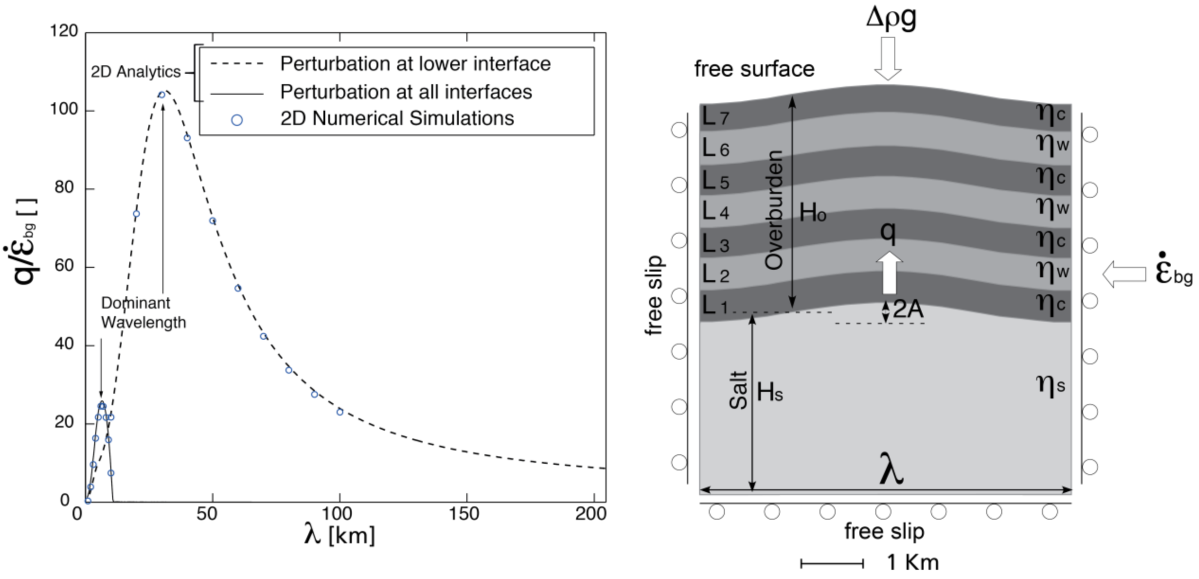

Figure 2.1. Analytical and numerical growth rate versus wavelength for two different setups (perturbation at all interfaces or perturbation at lower interface). Parameter values used to calculate these curves are the same as in Simulation 1 of Table 2.1. Inset on the right shows the setup with perturbation at all interfaces. Amplitude is exaggerated 100 times in the figure (as compared to the employed 1 m amplitude). L_1 to L_7 indicate the overburden layers of equal thickness. For explanation of the other parameters see text.

Table 2.1. Parameters used in the setups described in the text, in the 2D simulations A to F and in the six different high-resolution simulations 1 to 6 that are showed in this work

	Name	Perturbation		Number of layers	Thickness overburden layer	H_o	H_s	g	η_s,	η_c	η_w	R_1	R_2	ρ_s	ρ_o	$\dot{\varepsilon}_{bg}$	Shortening
		Type	Position	[]	[m]	[m]	[m]	[m/s^2]	[Pa s]	[Pa s]	[Pa s]	[]	[]	[Kg/m^3]	[Kg/m^3]	[s^{-1}]	[]
2D	Analytical	Sinusoidal	Base L_1 (all interfaces)	7	500	3500	3000	range (10)	range(10^{16} and 10^{19})	range	range	range	range	ρ_o	range (2700)	range (10^{-15})	0
quasi-2D	Simulation a	Random noise	Base L_1	7	500	3500	3000	10	10^{19}	10^{21}	10^{20}	10^{2}	10	2700	2700	10^{-15}	31%
quasi-2D	Simulation b	Random noise	Base L_1	7	500	3500	3000	10	10^{19}	10^{23}	10^{22}	10^{4}	10	2700	2700	10^{-15}	31%
quasi-2D	Simulation c	Random noise	Base L_1	7	500	3500	3000	10	10^{19}	10^{23}	10^{20}	10^{4}	10^{3}	2700	2700	10^{-15}	11%
quasi-2D	Simulation a*	Random noise	Base L_1	7	500	3500	3000	0	10^{19}	10^{21}	10^{20}	10^{2}	10	2700	2700	10^{-15}	31%
quasi-2D	Simulation b*	Random noise	Base L_1	7	500	3500	3000	0	10^{19}	10^{23}	10^{22}	10^{4}	10	2700	2700	10^{-15}	31%
quasi-2D	Simulation c*	Random noise	Base L_1	7	500	3500	3000	0	10^{19}	10^{23}	10^{20}	10^{4}	10^{3}	2700	2700	10^{-15}	11%
quasi-2D	Simulation d	Random noise	Base L_1	7	500	3500	3000	0	10^{19}	10^{25}	10^{24}	10^{6}	10	2700	2700	10^{-15}	2.5%
quasi-2D	Simulation e	Random noise	Base L_1	7	500	3500	3000	10	10^{19}	10^{25}	10^{22}	10^{6}	10^{3}	2700	2700	10^{-15}	2.5%
quasi-2D	Simulation f	Random noise	Base L_1	7	500	3500	3000	10	10^{19}	10^{25}	10^{20}	10^{6}	10^{5}	2700	2700	10^{-15}	3.8%
high-res 3D	Simulation 1	Random noise	Base L_1	7	500	3500	3000	10	10^{19}	10^{22*}	10^{20}	10^{3}	10	2200	2700	10^{-15}	28%
high-res 3D	Simulation 2	Random noise	Base L_1	7	500	3500	3000	10	10^{19}	10^{22*}	10^{20}	10^{3}	10	2200	2700	10^{-13}	28%
high-res 3D	Simulation 3	Random noise	Base L_1	7	500	3500	3000	0	10^{19}	10^{22*}	10^{20}	10^{3}	10	2200	2700	10^{-15}	28%
high-res 3D	Simulation 4	Random noise	Base L_1	7	500	3500	3000	10	10^{19}	10^{22}	10^{20}	10^{3}	10	2200	2700	10^{-15}	28%
high-res 3D	Simulation 5	Random noise	Base L_1	7	500	3500	3000	10	10^{19}	10^{23}	10^{22}	10^{4}	10	2200	2700	10^{-15}	40%
high-res 3D	Simulation 6	Random noise	Base L_1	7	500	3500	3000	10	10^{19}	10^{23}	10^{20}	10^{4}	10^{3}	2200	2700	10^{-15}	14%

2.3.2 Mechanical phase diagrams and dominant wavelength expressions

As we confirmed that the numerical simulations and amplification velocities obtained for the initial time step are in good agreement with semi-analytical predictions, we next want to use the semi-analytical method in a systematic manner to understand the folding modes that are to be expected as a function of material and model parameters. From previous work, it is known that different folding modes exist, some of which are affected by gravity whereas others do not depend on it (Schmalholz et al., 2002). Schmalholz et al. (2002) relied on using thin-plate expressions which allowed them to derive closed form analytical expressions that distinguish different folding modes. Yet, in cases when such closed form expressions do not exist or are too lengthy to give much insights, it is still possible to obtain insights in the physics by plotting the dominant wavelength as a function of model parameters, as done by Burg et al. (2004) for detachment folding versus diapirism for a case with fast erosion, or in Kaus and Podladchikov (2006) for shear localization. In such analyses, it is nearly always found that different mechanical modes of deformation are characterized by different dependencies of the dominant wavelength on the model parameters. The boundaries between different mechanical deformation modes are typically sharp and we can thus use the semi-analytical method to derive approximate expressions for each of the folding modes.

To make the problem tractable we have to make a number of simplifying assumptions and we here limit ourselves to 7 overburden layers, and apply a constant density for the whole domain (tests revealed that changing density has a minor effect). We consider three different viscosities: the viscosity of the salt or basal detachment layer (η_s), the viscosity of competent layers (η_c) in the overburden and viscosity of weak layers (η_w) in the overburden. The thickness of the basal layer is H_s, and the total thickness of the overburden (layers above the salt layers) is H_o, The thickness of the competent and that of the incompetent layer is assumed to be identical such that we are in a true multilayer-folding domain (according to previous work by Schmid et al., 2008). The total model thickness is kept constant throughout most of this work (see Figure 2.1 for setup), however, the dominant wavelength and maximum growth rate depend on the following parameters $f(\eta_s, \eta_c, \eta_w, \dot{\varepsilon}_{bg}, \Delta\rho, g, H_s, H_o)$. Being η_s, η_c, η_w, the viscosities of the lower detachment level or salt layer and the competent and weak layers in the overburden. $\dot{\varepsilon}_{bg}$ is the applied background strain rate, $\Delta\rho$ the density difference between the competent layers and air (zero density), and H_s and H_o, the thickness of the salt layer and of the overlying overburden composed of different layers.

Scaling analysis and previous results suggest that we can combine these parameters into four non-dimensional parameters. The first two parameters that are considered will be called R_1 and R_2, and they correspond to the two different viscosity ratios:

$R_1 = \eta_c/\eta_s$

$R_2 = \eta_c/\eta_w$

The basal layer (lower detachment level) thickness is also used as a parameter and non-dimensionalized using the thickness of the overburden as:

H_s/H_o

Finally, the effect of gravity over background strain rate is expressed in the Argand number similar to Burg et al. (2004) which is defined in a different form than as in Schmalholz et al. (2002) and it is argued to be problem dependant:

$Ar = (\Delta\rho\ g\ H_o)/(2\eta_s\ \dot{\varepsilon}_{bg})$

Using those four parameters, the corresponding scaling laws can be derived for each of the folding domains and plotted as a function of R_1 and R_2. Examples of such plots are shown in Figure 2.2, in which different folding modes can be clearly distinguished as the isocontours of wavelength and growthrate are different in the various parts of the diagram. The coloured background in the diagrams of Figure 2.2 are the calculated values for both wavelength and growthrate in the R_1- R_2 parameter space for the following parameters (see also Table 2.1): $\dot{\varepsilon}_{bg}=10^{-15}s^{-1}$, $\Delta\rho=2700$ kg m^{-3}, g = 9.8 m s^{-2}, $H_s=3000$m and $H_o=3500$ m and η_s of 10^{19} Pa s (Figure 2.2a) and $\eta_s=10^{16}$ Pa s (Figure 2.2b), that results in two different Argand numbers. Diagram for Ar = 0 is also shown in Figure 2.2c. Within each one of the folding modes we have also investigated the influence of Ar and H_s/H_o by varying them and keeping R_1 and R_2 fixed.

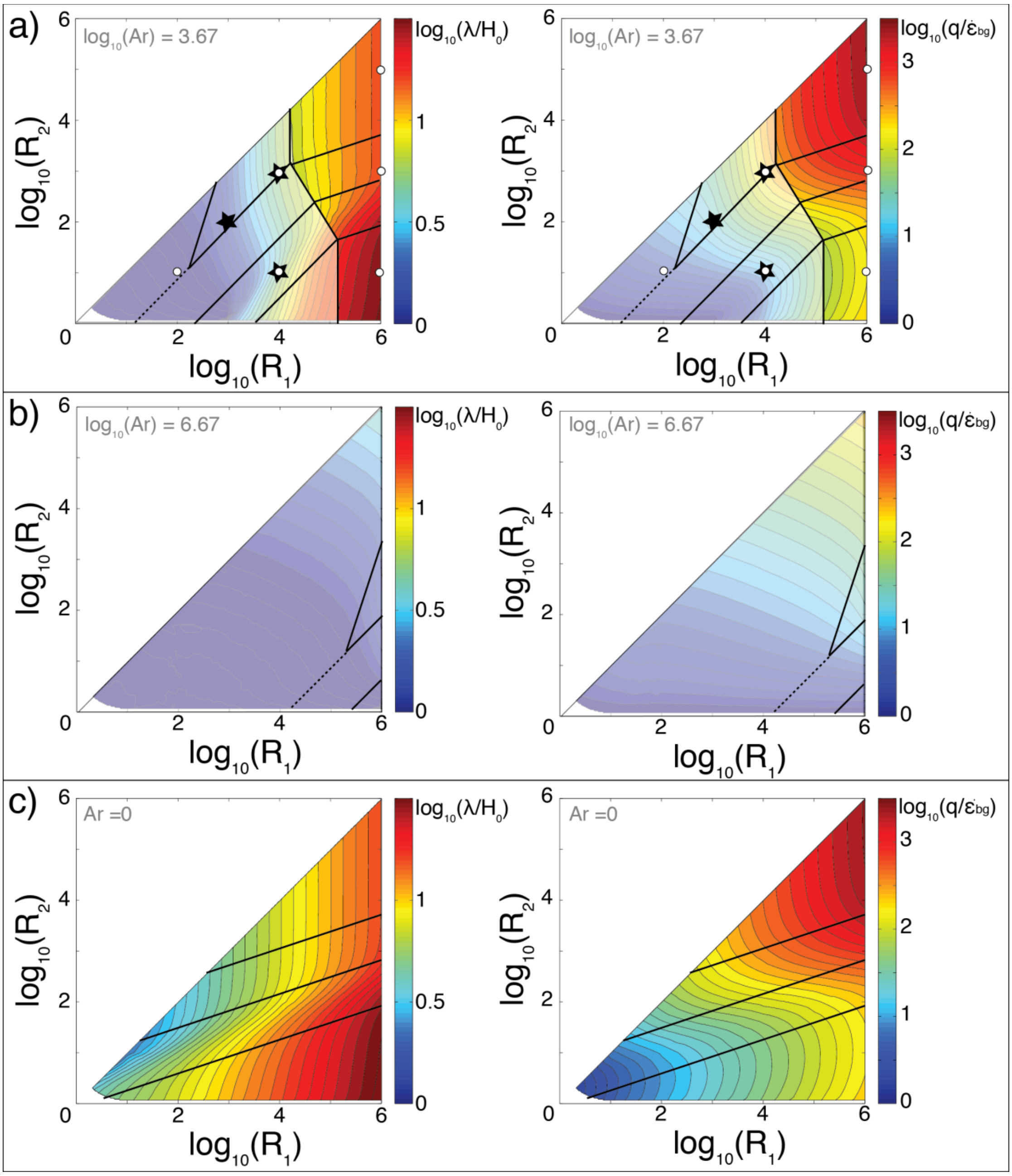

Figure 2.2. Phase diagrams, or normalized wavelength and growth rate in the R_1-R_2 space with coloured background values corresponding to calculations for three different Argand numbers corresponding to two different η_s of 10^{19} Pa s (a) and 10^{16} Pa s (b) and g=0 (c), for the rest of parameters see text. Each diagram is based on more than 6000 calculations of the analytical solution. In a) star symbols represent the approximate R_1-R_2 values of the high-resolution simulations and circles represent R_1-R_2 values of the 2D simulations.

It can be seen that the main controlling parameter in all folding modes in Figure 2.2 and Figure 2.3 is the R_1 parameter. Furthermore, we can overall distinguish four domains that are independent of the Ar number, but that depend on the H_s/H_o thickness ratio (see Figure 2.2 and Figure 2.3). If gravity is absent, those are the only folding modes. The two main folding domains, NGml and NGsl, correspond to the non-gravity influenced multilayer folding and the non-gravity influenced effective single layer folding (Figure 2.3). Within these two domains, dominant wavelength and growthrate have the same expressions except for the prefactor. In between, those two main non-gravity domains we have defined a transition zone. Because in this transition zone, one unique scaling law for the growthrate applies but two for the wavelength, we have divided it into two. Therefore, we have defined two transition-folding modes in the non-gravity influenced area of the diagram: NGt1 and NGt2. NGt1 have the same scaling law for the wavelength as NGml (Figure 2.3).

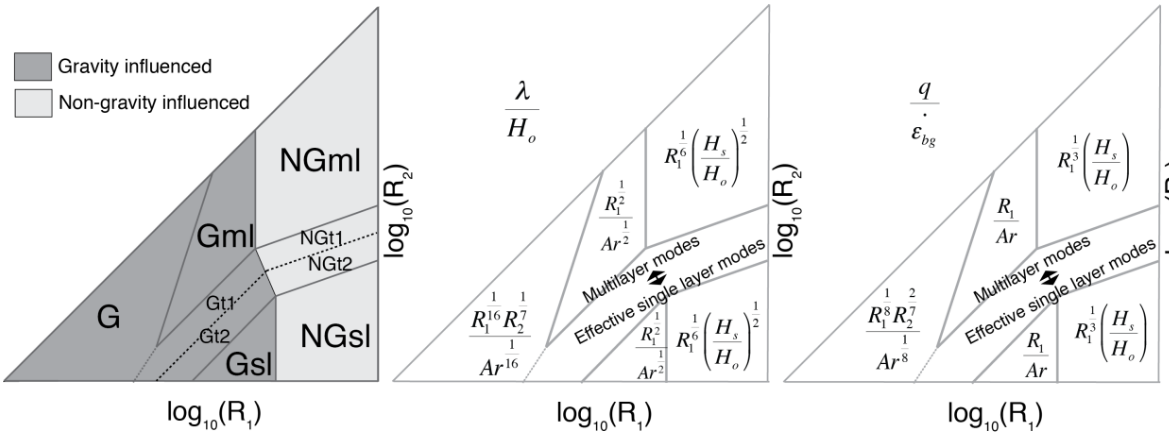

Folding modes		Gravity influenced	Non-gravity influenced
	(abbreviation)	(G)	(NG)
Multilayer	(ml)	Gml	NGml
Transition 1	(t1)	Gt1	NGt1
Transition 2	(t2)	Gt2	NGt2
Effective single layer	(sl)	Gsl	NGsl

Figure 2.3. Sketched domain boundaries in the R_1-R_2 space and the controlling non-dimensional parameters for normalized wavelength and growthrate. Domain names are shown in the table and are as follow: G, Gml, Gsl, Gt1 and Gt2 correspond to Gravity influenced domains, while NGml, NGsl and NGt1 and NGt2 correspond to non-gravity influenced domains. For complete scaling equations including multiplying prefactor see Table 2.2 and Table 2.3.

In the presence of gravity, additional folding modes occur that have *Ar* as controlling parameter. We can also distinguish five folding modes in the area of lower R_1 within the diagram, where gravity exerts an influence and both dominant growthrate and wavelength depend on the Argand number. As in the non-gravity influenced domains, here we can also distinguish a multilayer domain, Gml, and an effective single layer domain, Gsl, separated by two transitional domains, Gt1 and Gt2, plus a folding mode at the lower R_1 and R_2 combinations (Figure 2.3). As in the case of non-gravity influenced domains, Gsl and Gml show similar scaling laws that differ only in the prefactor.

Scaling parameters in the main folding domains are shown in Figure 2.3 and complete scaling laws that are applicable in the middle of the different domains of the folding phase diagrams are listed in Table 2.2 (the non-gravity influenced domains) and Table 2.3 (gravity influenced domains).

The diagrams show the R_1 and R_2 combination values under which transition from gravity-dependent to gravity independent domain occurs. Within the gravity-dependent domains, the salt thickness must be below a critical value for detachment folding (mainly H_s/H_o controlled folding mode) to occur, see Schmalholz et al. (2002).

The equations that describe the transition between the different domains have also been derived. The boundaries between two adjacent folding modes are typically continuous, which allows computing explicit expressions for those boundaries (Table 2.4), indicated as black lines in Figure 2.2 and Figure 2.3. The boundary expressions of Table 2.4, correspond in most of the cases to the ones calculated using the growthrate scaling laws. The exceptions are the boundaries between the transitional domains NGt1-NGt2 and Gt1 and Gt2 whose boundaries correspond to the wavelength scaling laws.

A comparison with the work of Schmalholz et al. (2002) in which the authors used a setup with a single layer overlying a matrix or detachment layer, shows that the existence of a true multilayer system increases the number of folding modes. They distinguished three folding modes: gravity-controlled, matrix-controlled and detachment folding. Our scaling laws within the gravity influenced domains, Gml and Gsl, are comparable to the scaling laws in the gravity-controlled modes of Schmalholz et al. (2002). In gravity-controlled domains, we have to decrease the thickness of the salt layer below a certain value in order to enter the detachment folding modes of Schmalholz et al. (2002). However, here, we have derived the scaling laws for values of much higher viscosity contrast than previously considered, which shows that above a critical R_1 ratio gravity no longer influences folding and the main controlling parameters are the thickness ratio and R_1. The scaling laws for NGml and NGsl, are comparable to the detachment folding modes of Schmalholz et al. (2002).

Table 2.2. Scaling laws for the non-gravity folding domains derived using the semi analytical solution and the calculated phase diagrams of Figure 2.2. Note that the scaling for the effective single layer and effective multilayer systems is the same, apart from a prefactor (which shows that growthrates of multilayer systems are significantly larger but wavelengths are slightly smaller for a multilayer system). Simplified expressions of Lambda have are added for R_1-R_2=100 as explained in the text.

Folding domains	Dominant wavelength	Dominant wavelength (R_1=R_2=100)	Growth Rate
NGml	$\frac{\lambda}{H_o} = 1.85 R_1^{\frac{1}{6}} \left(\frac{H_s}{H_o}\right)^{\frac{1}{2}} \approx \frac{1}{2}\frac{\lambda_{NGsl}}{H_o}$	$\frac{\lambda}{H_o} \propto 3.99 \left(\frac{H_s}{H_o}\right)^{\frac{1}{2}}$	$\frac{q}{\dot{\varepsilon}_{bg}} = 33.88 R_1^{\frac{1}{3}} \left(\frac{H_s}{H_o}\right) \approx 15 \frac{q_{NGsl}}{\dot{\varepsilon}_{bg}}$
NGt1	$\frac{\lambda}{H_o} = 1.85 R_1^{\frac{1}{6}} \left(\frac{H_s}{H_o}\right)^{\frac{1}{2}}$	$\frac{\lambda}{H_o} \propto 3.99 \left(\frac{H_s}{H_o}\right)^{\frac{1}{2}}$	$\frac{q}{\dot{\varepsilon}_{bg}} = 2.23 R_1^{\frac{1}{9}} R_2^{\frac{2}{3}} \left(\frac{H_s}{H_o}\right)^{\frac{2}{5}}$
NGt2	$\frac{\lambda}{H_o} = 3.66 R_1^{\frac{5}{18}} R_2^{-\frac{1}{3}} \left(\frac{H_s}{H_o}\right)^{\frac{4}{5}}$	$\frac{\lambda}{H_o} \propto 0.81 R_1^{\frac{5}{18}} \left(\frac{H_s}{H_o}\right)^{\frac{1}{2}}$	$\frac{q}{\dot{\varepsilon}_{bg}} = 2.23 R_1^{\frac{1}{9}} R_2^{\frac{2}{3}} \left(\frac{H_s}{H_o}\right)^{\frac{2}{5}}$
NGsl	$\frac{\lambda}{H_o} = 3.66 R_1^{\frac{1}{6}} \left(\frac{H_s}{H_o}\right)^{\frac{1}{2}}$	$\frac{\lambda}{H_o} \propto 7.87 \left(\frac{H_s}{H_o}\right)^{\frac{1}{2}}$	$\frac{q}{\dot{\varepsilon}_{bg}} = 2.23 R_1^{\frac{1}{3}} \left(\frac{H_s}{H_o}\right)$

Table 2.3. Scaling laws for the gravity influenced folding domains derived using the semi analytical solution and the calculated phase diagrams of Figure 2.2. Note that the scaling for the effective single layer and effective multilayer systems is the same, apart from a prefactor (which shows that growthrates of multilayer systems are significantly larger but wavelengths are almost equal to a multilayer system). Simplified expressions of Lambda have are added for R_1*-*R_2*=100 as explained in the text.*

Folding domains	Dominant wavelength	Dominant wavelength (R_1=R_2=100)	Growth Rate
G	$\frac{\lambda}{H_o} = 0.74\frac{R_1^{\frac{1}{16}}R_2^{\frac{1}{7}}}{Ar^{\frac{1}{16}}}$	$\frac{\lambda}{H_o} \propto \frac{1.90}{Ar^{\frac{1}{16}}}$	$\frac{q}{\dot{\varepsilon}_{bg}} = 5.43\frac{R_1^{\frac{1}{8}}R_2^{\frac{2}{7}}}{Ar^{\frac{1}{8}}}$
Gml	$\frac{\lambda}{H_o} = 4.12\frac{R_1^{\frac{1}{2}}}{Ar^{\frac{1}{2}}} \approx \frac{\lambda_{Gsl}}{H_o}$	$\frac{\lambda}{H_o} = 4.12\frac{R_1^{\frac{1}{2}}}{Ar^{\frac{1}{2}}}$	$\frac{q}{\dot{\varepsilon}_{bg}} = 167.86\frac{R_1}{Ar} \approx 61\frac{q_{Gsl}}{\dot{\varepsilon}_{bg}}$
Gt1	$\frac{\lambda}{H_o} = 2.01\frac{R_1^{\frac{3}{8}}R_2^{\frac{1}{8}}}{Ar^{\frac{3}{8}}}$	$\frac{\lambda}{H_o} \propto 3.57\frac{R_1^{\frac{3}{8}}}{Ar^{\frac{3}{8}}}$	$\frac{q}{\dot{\varepsilon}_{bg}} = 2.31\frac{R_1^{\frac{1}{4}}R_2^{\frac{3}{4}}}{Ar^{\frac{1}{4}}}$
Gt2	$\frac{\lambda}{H_o} = 4.15\frac{R_1^{\frac{5}{6}}R_2^{-\frac{1}{3}}}{Ar^{\frac{5}{6}}}$	$\frac{\lambda}{H_o} \propto 0.91\frac{R_1^{\frac{5}{6}}}{Ar^{\frac{5}{6}}}$	$\frac{q}{\dot{\varepsilon}_{bg}} = 2.31\frac{R_1^{\frac{1}{4}}R_2^{\frac{3}{4}}}{Ar^{\frac{1}{4}}}$
Gsl	$\frac{\lambda}{H_o} = 4.05\frac{R_1^{\frac{1}{2}}}{Ar^{\frac{1}{2}}}$	$\frac{\lambda}{H_o} = 4.05\frac{R_1^{\frac{1}{2}}}{Ar^{\frac{1}{2}}}$	$\frac{q}{\dot{\varepsilon}_{bg}} = 2.75\frac{R_1}{Ar}$

Table 2.4. Equations defining the boundaries between the different folding domains of Figure 2.2 and Figure 2.3.

Domain boundary	Boundary equation
NGml – NGt1	$R_2^{\frac{2}{3}} = 15.19 R_1^{\frac{2}{9}} \left(\frac{H_s}{H_o} \right)^{\frac{3}{5}}$
NGt1 – NGt2	$R_2^{\frac{1}{3}} = 1.98 R_1^{\frac{1}{9}} \left(\frac{H_s}{H_o} \right)^{\frac{3}{10}}$
NGt2 – Ngsl	$R_2^{\frac{2}{3}} = 1.00 R_1^{\frac{2}{9}} \left(\frac{H_s}{H_o} \right)^{\frac{3}{5}}$
NGml – Gml	$R_1^{\frac{2}{3}} = 0.20 Ar \left(\frac{H_s}{H_o} \right)$
NGsl – Gsl	$R_1^{\frac{2}{3}} = 0.81 Ar \left(\frac{H_s}{H_o} \right)$
G – Gml	$R_2^{\frac{2}{7}} = 30.91 \frac{R_1^{\frac{7}{8}}}{Ar^{\frac{7}{8}}}$
Gml – Gt1	$R_2^{\frac{3}{4}} = 72.67 \frac{R_1^{\frac{3}{4}}}{Ar^{\frac{3}{4}}}$
Gt1 – Gt2	$R_2^{\frac{1}{4}} = 2.07 \frac{R_1^{\frac{1}{4}}}{Ar^{\frac{1}{4}}}$
Gt2 - Gsl	$R_2^{\frac{3}{4}} = 1.19 \frac{R_1^{\frac{3}{4}}}{Ar^{\frac{3}{4}}}$
Gt1/Gt2 – NGt1/NGt2	$R_2^{\frac{1}{12}} = 0.97 R_2^{-\frac{5}{36}} Ar^{\frac{1}{4}} \left(\frac{H_s}{H_o} \right)^{\frac{2}{5}}$

One of the interesting results is that there is a viscosity ratio between the competent and weak layers of the overburden that causes an offset of the dominant wavelength and growth rate, while otherwise the values are mostly dependent on the viscosity ratio between the competent layer and the salt layer. A true multilayer system thus results in an increase in the dominant growthrate of the folding instability (Schmid and Podladchikov, 2006), which in our phase diagrams occurs once the intermediate weak layers are sufficiently weak (or R_2 has exceeded a critical value). They thus represent the true multilayer effect in the system and therefore the gravity influenced domains and non-gravity influenced domains are split into a multilayer and an effective single layer domain, with a transitional zone in between them, with the same scaling parameters but different prefactors. Although in both gravity and non-gravity influenced domains the growthrate in the multilayer domains is considerably higher than in the effective single layer domains, this is not the case for the wavelength. The wavelength in the multilayer cases is either slightly smaller in non-gravity influenced domains, or almost equal in the gravity-influenced domains. Therefore, the multilayer domain equations can be expressed as corrections of the effective single layer equations (Table 2.2 and Table 2.3).

The folding phase diagrams of Figure 2.2 consider viscosity ratios of up to 10^6; however, viscosity contrasts in nature vary mostly between 10 and 1000. Within the range of the viscosity contrasts that are found in nature, some of the scaling laws of Table 2.2 and Table 2.3 can be simplified to first order relations. We will illustrate the applicability of the scaling laws for a viscosity contrast of 100, in which case scaling of the viscosity ratio can become small enough (below 3) to be substituted by a numerical value. These simplified scaling laws are shown in second column of Table 2.2 and Table 2.3, where only the scaling laws for the dominant wavelength have been included. For low viscosity ratios (≤ 100) for which the simplified equations of the second column of Table 2.2 and Table 2.3 are applicable, we can see that none of the folding modes has a strong dependency on R_2 for the dominant wavelength. In other words: the true multilayer effect increases the growthrate of the folding instability significantly, but does not have a main effect on the dominant wavelength.

2.4 2D Numerical models

The thick plate perturbation method used in the previous section is theoretically only valid for the first incremental stages of folding when amplitudes are small, but finite amplitude folding studies have shown that the results are still accurate for limbs of up to 20 degrees dip (Chapple, 1968; Schmalholz, 2006). Because fold wavelength is selected during those very low dipping limb stages (Chapple, 1968), several studies confirmed that under certain conditions the predicted wavelength is the one that develops (Adamuszek et al., 2013; Schmalholz, 2006; Schmalholz and Podladchikov, 2000). Whereas these previous studies focussed on single-layer folds, or multilayer stacks embedded in a matrix, we next analyse whether this holds for multilayer systems overlying a detachment layer as well.

2.4.1 Evolution of individual folds from systems with sinusoidal perturbation and deviation of folding from the linear theory

Fold evolution is usually best described by means of amplification versus strain. Linear theory that is used to calculate the initial growth rate and dominant wavelength assumes a continuous amplification of the fold, but this is only applicable during the first incremental stages of fold instability. Furthermore, it has long been proposed that folds go through different stages such as birth or nucleation, dynamic amplification and kinematic or passive amplification (Cobbold, 1976). Finite amplitude folding theory (Schmalholz and Podladchikov, 2000) provides an estimate of the crossover amplitude and strain where the linear theory breaks down. Schmalholz (2006) employs an analytical solution based on a thin plate analysis in which the boundaries of those different stages could be determined using a non-dimensional parameter called scaled stretch. The author demonstrated that the amplification of the selected dominant wavelengths fits into these stages, which was previously only described qualitatively. The finite amplitude folding theory was then decomposed into a linear component (similar to the thick plate analysis we just described), and a correction to this component.

A numerical simulation in which an initially sinusoidal perturbation is added to each of the layers with a wavelength (length) that corresponds to the dominant wavelength of the used parameters shows that each of the layers exhibits a slightly different evolution.

In (Figure 2.4), we have plotted the normalized values of the amplitude (A), growth rate (q) and amplification velocity (V) versus the wavelength ($\boldsymbol{\lambda}$) of two interfaces: the ones of the salt-L_1 interface and of the topography. While the lowermost layer amplifies faster, the amplitude decreases towards the top of the overburden. The folding stages that are indicated in Figure 2.4 correspond to the values of the salt-L_1 interface.

Similar to the case of single-layer folds we can distinguish various folding stages. First, the nucleation stage during which the measured amplitude remains small and most of the shortening is accommodated by layer-parallel shortening. This stage is characterized by an increase in the amplitude velocity (V) towards a maximum (see Figure 2.4) and a very low amplitude evolution.

Following the nucleation stage, a dynamic amplification stage shows a sudden increase in the measured amplification although amplification velocity has started to decrease after its maximum was reached.

Finally, when the growth rate due to the mechanical instability vanishes and becomes zero, the amplitude keeps growing but only as a result of passive kinematic growth.

Despite the fact that the folding instability theory only considers infinitesimal amplitudes, the obtained dominant wavelength is the one expected to develop in nature by selection and locking during strain at the initial stages of fold evolution and by consequent amplification of the nucleated fold at later stages.

When a layer system with an initial perturbation that corresponds to the calculated dominant wavelength is compressed in the gravity influenced folding domains Gml and Gsl, the fold might amplify so fast that gravity starts to affect the centre of the fold, which collapses under the effect of gravity with the result that a box shaped fold forms. We have observed the formation of box folds, in Gsl folding domain. Furthermore, it can occur that the fold is split into two different folds. This effect we have observed in folding domain Gml, where the $> 25\frac{\lambda}{H_o}$. In that case, the wavelength predicted from the analytical theory would not be applicable as the observed one corresponds exactly to half of the dominant wavelength. When the system has only random noise, less periodic and regular shape of folds form, which in most of the cases do not result in the formation of folds with a wavelength that is half of the predicted one.

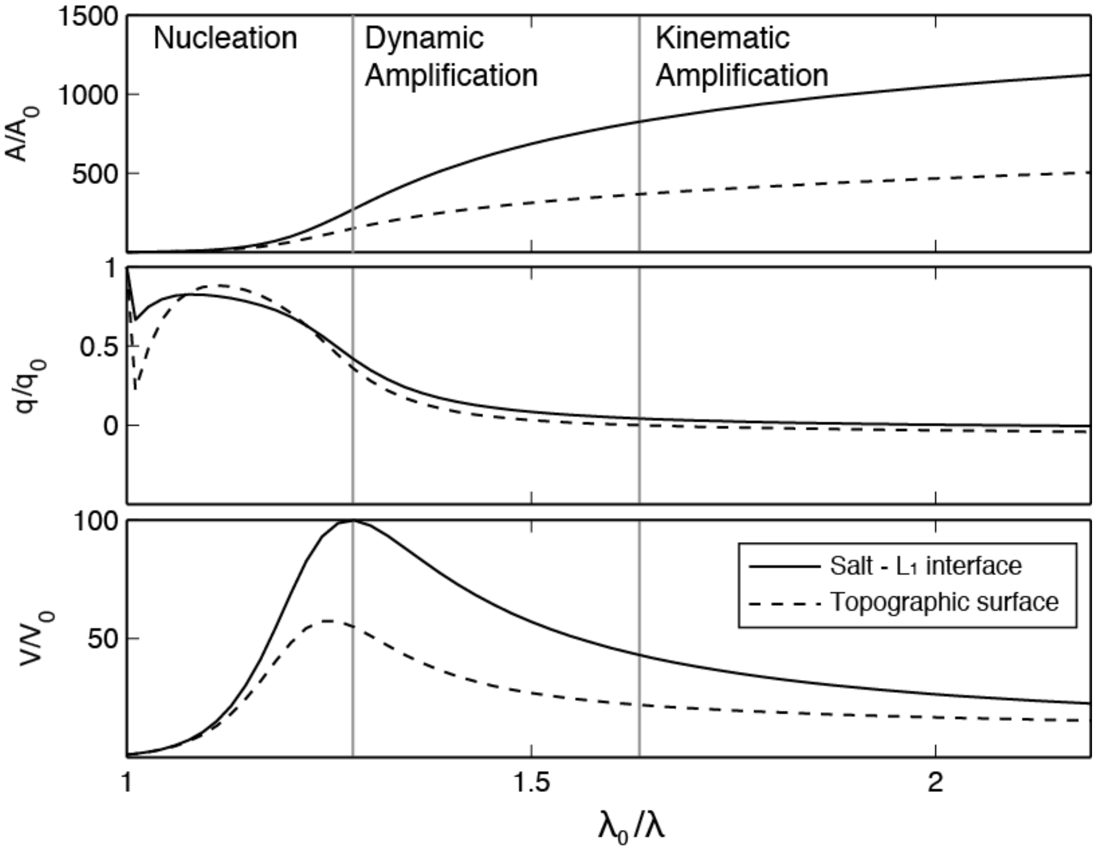

*Figure 2.4 Numerically computed curve of the amplitude (A), instantaneous growth rate (q) and amplification velocity (V) versus wavelength (**λ**) (stretch). Values are normalized over the initial value. The setup corresponds to an initial sinusoidal perturbation with length corresponding to dominant wavelength for parameters of simulation 1 of Table 2.1. The different stages of fold evolution are illustrated for the solid curve.*

2.4.2 Amplification and wavelength selection in multilayer folding from random noise

Next, we studied the wavelength and amplitude evolution in quasi-2D setups in which only random noise has been added to the lowermost interface. The quasi-2D runs use the same multilayer setup as shown in Figure 2.1, but reduced in the Y direction (only 1 element) and extended in the X direction. Since the free surface is initially perfectly horizontal, the first initial wavelength observed is on the order of magnitude of the dominant wavelength calculated for the one interface perturbed case (Figure 2.1). Yet, with increasing strain the wavelength decreases dramatically until it reaches the dominant wavelength computed for the analytical model in which all interfaces are perturbed. It takes a certain amount of layer parallel homogeneous shortening to select the wavelength as was already noticed by Sherwin and Chapple (1968) who introduced a modified wavelength selection theory to take that shortening into account. The layer parallel shortening required for fold wavelength to be selected is higher in the case of the gravity-influenced folding domains of Figure 2.2a where the lowest viscosity ratios are found.

Several simulations have been performed, with a wide range of values for R_1 and R_2. Here we show six quasi-2D simulations that will be referred as simulations A to F. The R_1 and R_2 values that correspond to these simulations are shown in the phase diagram of Figure 2.5 and in Table 2.1. The simulations A, B and C are within the gravity influenced domains (see Figure 2.2a), whereas simulations D, E and F are in the non-gravity influenced domains.

In order to show the influence of gravity in the Argand number, and therefore in the predicted wavelength and growth rate, we have repeated the simulations in the gravity influenced domain (A, B and C) under g=0 conditions. The results can be seen in Figure 2.5. When g=0, the domain boundaries are changed, and we only have the non-gravity influenced domains. In that case both dominant wavelength and growthrate contours correspond to the scaling laws shown in

Table 2.2, which give higher growthrate values. Gravity dominated folds have clearly smaller wavelengths, which are typically on the order or only slightly larger than the thickness of the modelled domain.

Simulations D, E and F differ only in the R_2 parameter and are therefore appropriate to observe the effect of a true multilayer system (Figure 2.5). If we consider simulation D, which is the one with the lowest R_2 of the three, the dominant wavelength is higher than in E and F, although the growthrate is lower. As we increase the R_2 value, we first go through the transition domain and above a given value we enter the true multilayer-folding mode, which has a smaller wavelength and larger growthrates.

A comparison of predicted and computed wavelengths shows a good agreement for these quasi-2D simulations (see insets in Figure 2.5). The measured spectral amplitude in the topography of simulations A to F shows a peak at the value that correspond to the dominant wavelength predicted with the analytical solution (see insets in Figure 2.5).

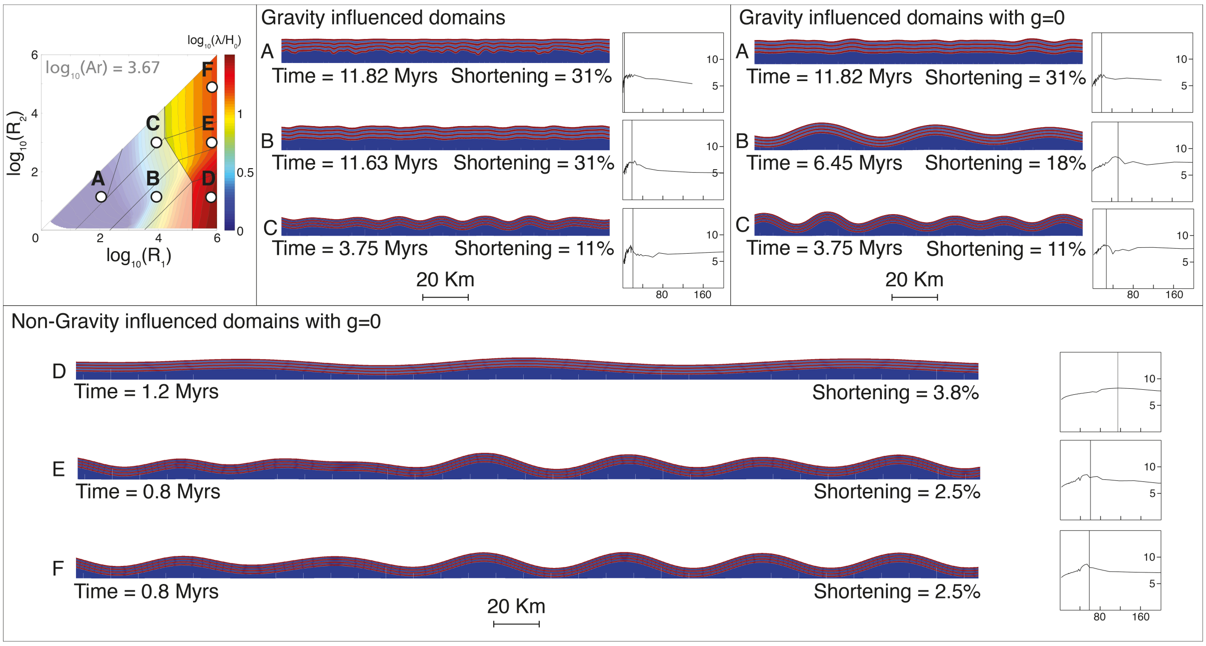

Figure 2.5. Several quasi-2D simulations A to F corresponding to the viscosity ratios indicated on the coloured phase diagram. Folds are shown after a strain value that is indicated for each simulation. Insets show the measured spectral amplitude of wavelength (in km) at the given strain in compression direction. Vertical lines in the insets indicate the wavelength predicted with the analytical solution.

2.5 3D evolution of multilayer folds

2.5.1 Wavelength selection and amplification

Next, we perform 3D simulations compressed in the x-direction. The multilayer setup that we have used is the same as in Figure 2.1, but in 3D: it is shown in Figure 2.6. Here, we show six high-resolution simulations that from now onwards will be referred to as simulations 1 to 6 (Figure 2.7, Figure 2.8 and Figure 2.9). In each run, different parameters have been changed, not only the viscosity structure of the multilayer stack (see Table 2.1 for parameters). Due to the fact that higher viscosity contrasts in the simulations result in a larger number of iterations needed to get a solution for the velocity every time step, we have limited the 3D high-resolution simulations to viscosity contrasts of four orders of magnitude between the competent layers in the overburden and the salt layer below. The approximate position of the values used in the 3D simulations in the R_1-R_2 parameter space can be seen in the Figure 2.2. All simulations are in the gravity affected folding domains (see Figure 2.2a), and therefore it is expected that the dominant wavelength and growthrate scale not only with R_1 and R_2 but also with the Argand number.

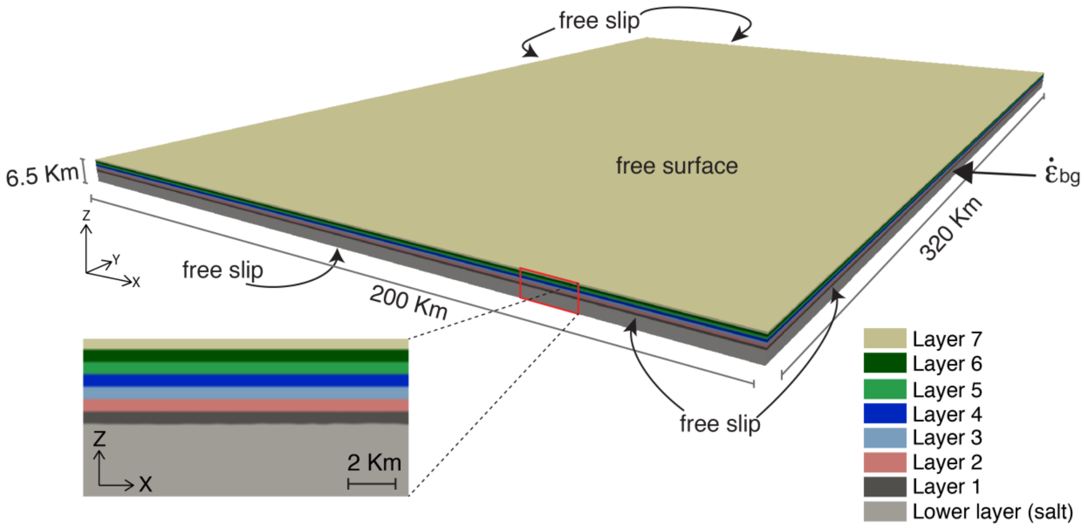

Figure 2.6. Setup of the 3D multilayer detachment folding, with seven layers above a lower salt detachment layer.

It is worth noting that the same initial random noise has been used in all simulations. Previous works (i.e. Schmid et al., 2008) have shown that the pattern of the initial random noise controls the location of folds and the final 3D pattern that develops. In order to see if this is the case in our simulations we must be able to compare the different runs, which we can only do if we apply the same initial random noise.

Simulations 1 to 3 have the same viscosity structure, but in simulation 2, a two orders of magnitude higher background strain rate was employed compared to simulation 1 (Table 2.1). Simulation 3 differs from simulation 1 in that it was performed with zero gravity. Simulations 1 to 3 therefore, show the influence of the Argand number on the selected wavelength and the final fold pattern (Table 2.1 and Figure 2.7). The $\log_{10}$(Argand) of Simulation 1 is 3.67 and of Simulation 2 is 1.67 Simulation 3 has an Argand number of zero.

In simulations 4 to 6, different viscosity structure and therefore different R_1 and R_2 values have been used (Table 2.1). In most of the cases the simulations have been performed until a shortening of 30%, which according to our initial work in 2D is enough to obtain finite amplitude folding. However, simulation 5 due to its low dominant growthrate and simulation 6 due to its high growthrate (Table 2.5) were performed until a shortening of 40% and 14% respectively was reached (Figure 2.8).

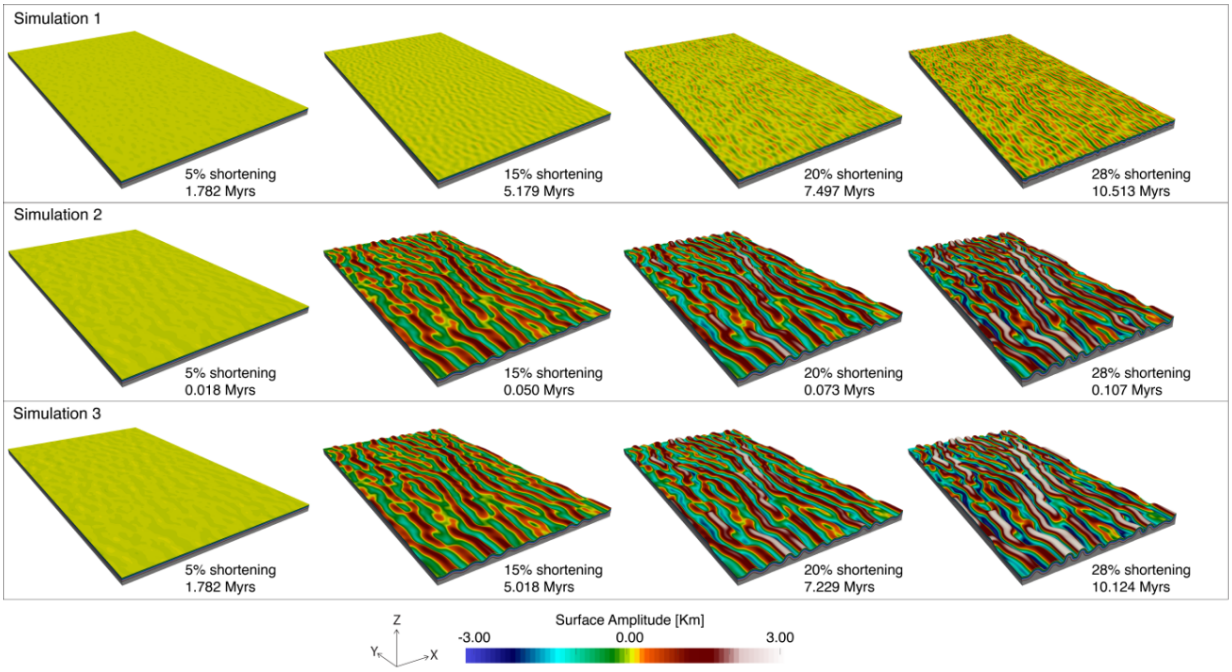

Figure 2.7. Time and strain evolution of simulations 1 to 3 (see Table 2.1 for parameters). Amplitude is coloured with the same scale for all the simulations for direct comparison.

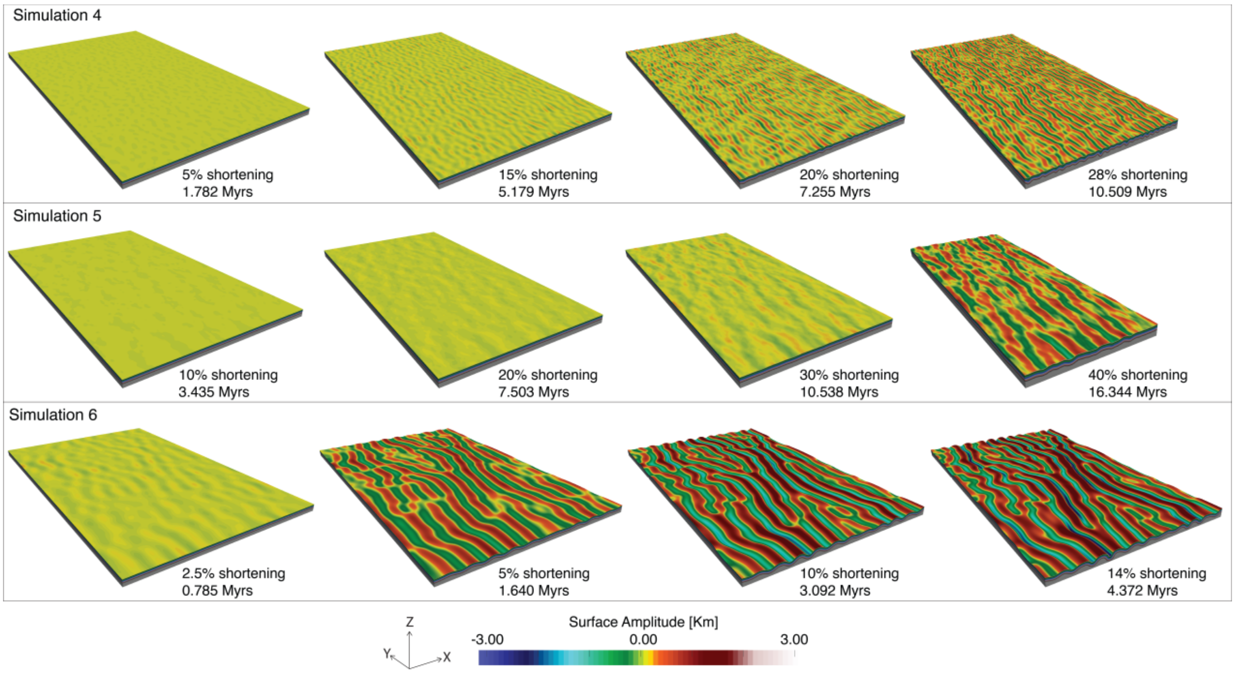

Figure 2.8. Time and strain evolution of simulations 4 to 6 (see Table 2.1 for parameters). Amplitude is coloured with the same scale for all the simulations for direct comparison.

Table 2.5. Dominant wavelength and growthrate for the parameters used in the 3D simulations. Calculated with the semi-analytical solution.

	Dominant wavelength [km]	Dominant growthrate [ ]
Simulation a	3.6	9
Simulation b	21.1	14
Simulation c	21.1	239
Simulation a*	19.2	14
Simulation b*	52.3	48
Simulation c*	27.0	398
Simulation d	115.4	184
Simulation e	60.1	920
Simulation f	59.5	2718
Simulation 1	6.2	26
Simulation 2	17.9	72
Simulation 3	17.2	70
Simulation 4	7.5	29
Simulation 5	21.1	14
Simulation 6	21.1	239

The analytical solution has been used to calculate the dominant wavelength and growthrate of the parameters that correspond to each one of these 3D simulations. The values can be seen in Table 2.5. The predicted values show already how the predicted dominant wavelength and growthrate change for the given parameters.

The main results from these high-resolution simulations (Figure 2.7, Figure 2.8 and Figure 2.9) are commented here.

In agreement with 2D results, amplification of the 3D folds from random noise through time shows an initial stage with slow amplification where most of shortening is accommodated by thickening of the layers and which is followed by a stage with significantly larger amplification rates. However, the duration of the stage with pure shear thickening of the layers depends on the growthrate, and therefore we find less initial thickening of the layers in the runs with higher dominant growthrates.

In order to compare the fold wavelength that develop from random noise in the 3D simulations we have used a spectral analysis method, which gives a proxy of the wavelength that is most prevalent in the topography, equivalent to a dominant wavelength. How the results compare to the predicted wavelength can be seen in Figure 2.10. The dominant wavelength of folds that form perpendicular to the main compression direction after a shortening of 30% for most of the cases, are in excellent agreement with our semi-analytical predictions. Spectral analysis of the topography for all the time steps reveals that the final wavelength is already present as a dominant during early folding stages.

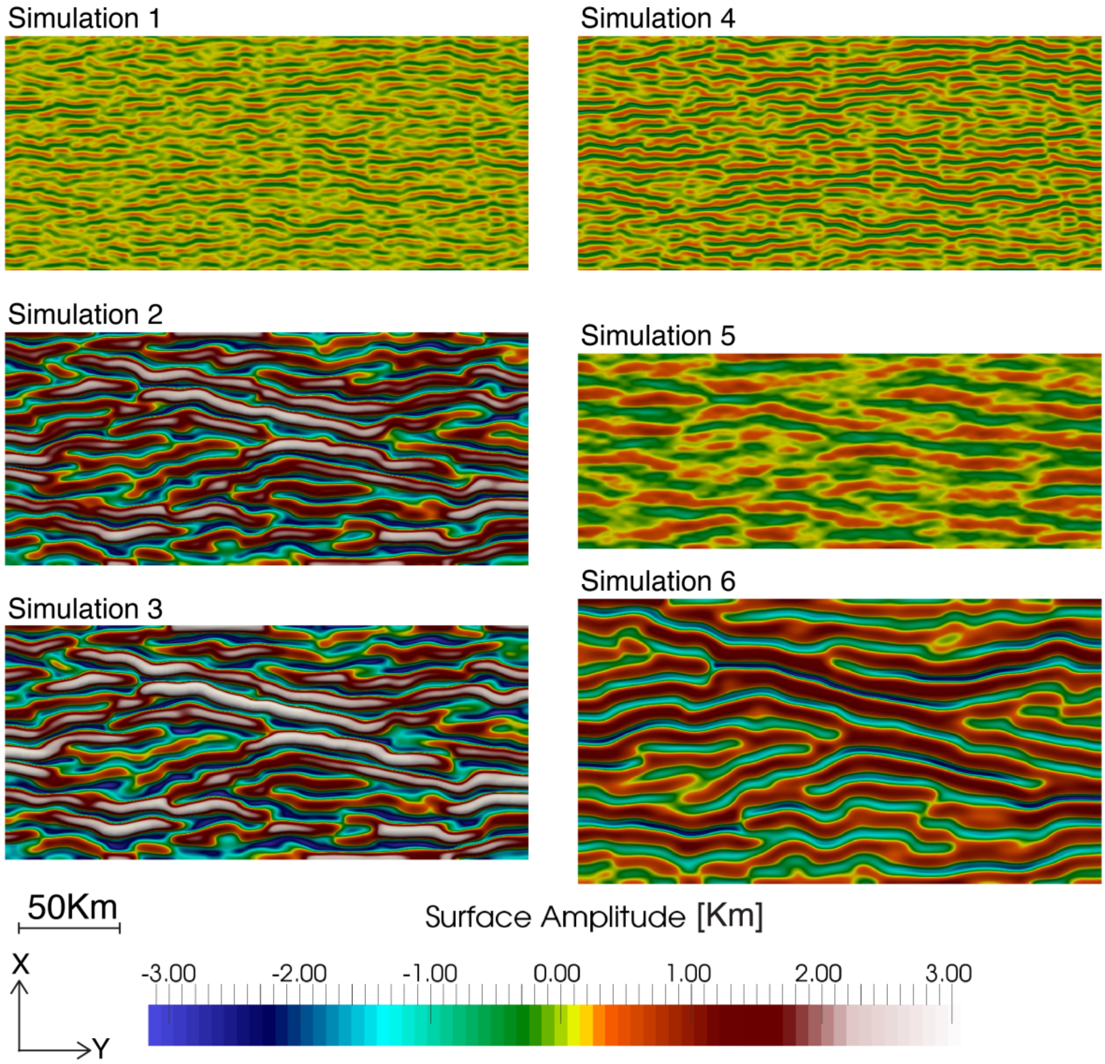

Figure 2.9. Map view of the final stage of the high-resolution simulations 1 to 6. Amplitude is coloured with the same scale for all the simulations for direct comparison. Shortening is 28% for simulations 1 to 4, 40% for simulation 5, and 14% for simulation 6.

Since the initial pure shear thickening stage varies from run to run, depending on the folding growthrate, we have calculated the normalized amplitude from the topography (Figure 2.7, Figure 2.8 and Figure 2.9). This amplitude has been obtained by extracting the mean surface to the absolute height in each time step.

Comparing simulations 1 to 3 (Figure 2.7), shows that changing either the background strain rate or switching off gravity, has an important effect on the dominant growthrate and wavelength, as we are changing the corresponding Argand number with which both growthrate and wavelength scale. In fact, switching off gravity or increasing the strain rate two orders of magnitude have exactly the same effect, as seen in the values of Table 2.5 and in the resulting fold patterns in Figure 2.7 and Figure 2.9.

On the other hand, if we consider simulations 4 to 6, they show a clear control of the R_1 on the developed wavelength. R_1 is the same in simulations 5 and 6, but is one order of magnitude smaller in simulation 4. The difference between simulations 5 and 6 is the R_2 number, which as we can see in the phase diagram, results in the same wavelength but in a very different growthrate (239 in simulation 6 compared to 14 in simulation 5). The effect of this difference in the growth rate in the 3D simulations can be observed in Figure 2.8 and Figure 2.9.

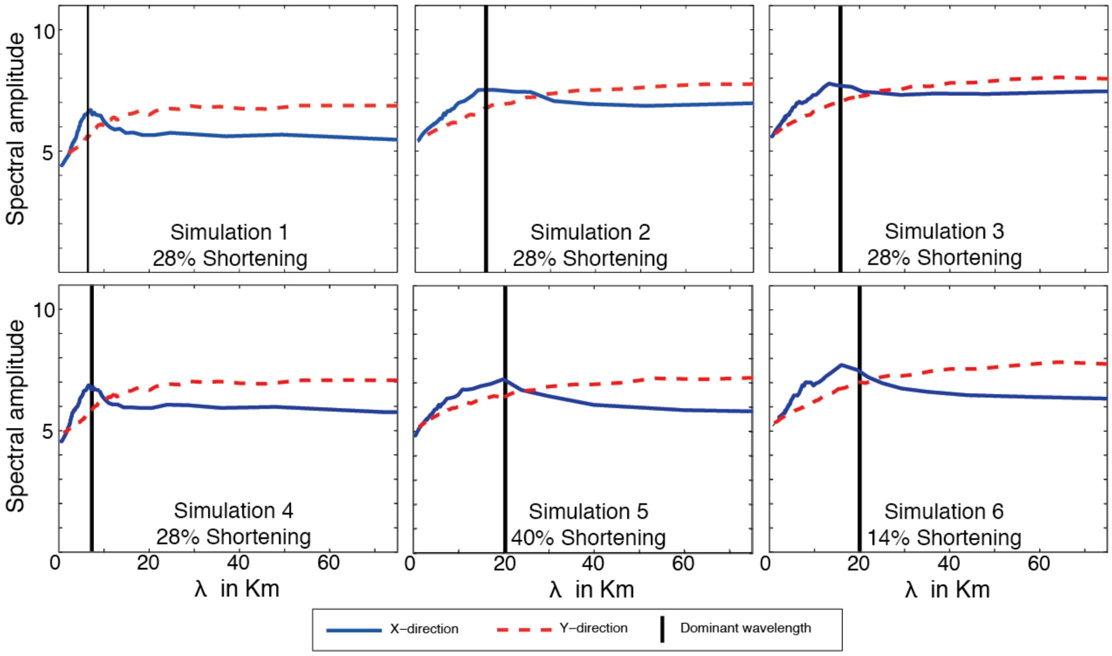

Figure 2.10. Spectral analysis of the topography of the 3D high-resolution simulations after the indicated shortening. Black continuous vertical line shows analytically predicted dominant wavelength.

Even if in both cases the predicted wavelength is the same, and it is the one that develops in the simulations, simulation 5 needs significantly more shortening before the folds start to amplify dynamically. As a result, simulation 5 accommodates much more pure shear thickening than simulation 6, the folds are less amplified. On the contrary, simulation 6, due to the high growthrate, needs much less shortening for folds that amplify dynamically and reach high amplitude. The slight offset between the predicted wavelength and the one measured with the spectral analysis (Figure 2.10) can also be explained with the high growth rate, and the fact that with only 14% of shortening we are already kinematically amplifying the folds and reducing the wavelength.

One noteworthy feature is that when the predicted wavelength and growthrate for a given set of parameters is equal or very similar, the resulting fold pattern is nearly identical. This is because the initial random noise controls where the folds form. The similarity between fold patterns in simulations 2 and 3 (Figure 2.7 and Figure 2.9), and in simulations 1 and 4 can also be observed in the Figure 2.9. Also, similar folding pattern can be seen in simulation 6, even though the growthrate is much higher, and the predicted wavelength is not the same as in simulation 2 and 3 (Figure 2.9). In these three simulations we can see that in the central part of the modelled domain very long folds exist, that show an oblique orientation with respect to the compression direction. While these folds are almost identical in simulations 2 and 3, there are some differences in simulation 6. However, for completely different predicted dominant wavelengths (e.g. simulation 1 and 2, or simulation 4 and 6) or even for similar predicted wavelength but very different growthrate (simulation 5 and 6), the fold pattern is different as can be observed in Figure 2.9.

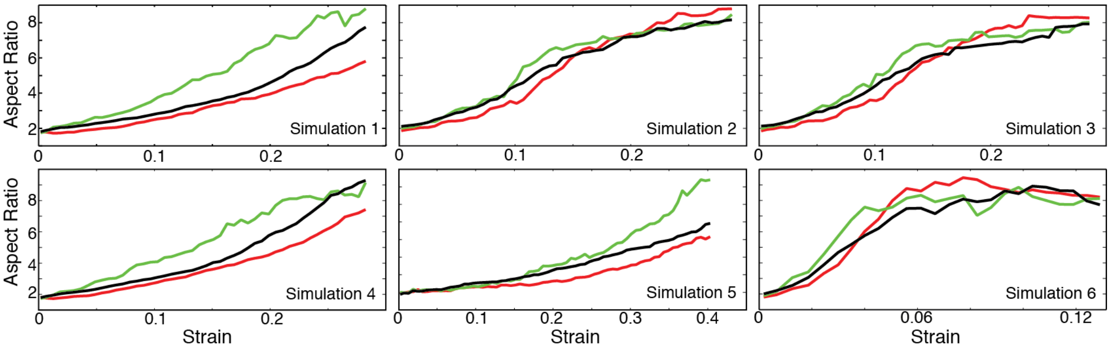

Figure 2.11. Evolution of aspect ratio obtained by fitting ellipse shapes to the isolated fold segments above given height levels. Colours indicate the height levels, using the mean amplitude (green), half the maximum amplitude (red), or a quarter of the maximum amplitude (black).

The resulting developed fold patterns in all six simulations show a wide variety of fold aspect ratios. In fact, spectral analysis performed in the direction orthogonal to the compression direction shows no clear wavelength selectivity (Figure 2.10), which is consistent with predictions by Fletcher (1995) and confirmed by Schmid et al. (2008) for the 3D evolution of a single layer folding. This confirms also the findings of Kaus and Schmalholz (2006), who looked at the dominant wavelength using a sinusoidal perturbed layer. The growth rate maps shown in Kaus and Schmalholz (2006), of combinations of λ_x and λ_y calculated for the multilayer case show that, for cases of dominant λ_x when $\lambda_y/\lambda_x > 1$, all the combinations show similar growth rates, and therefore there is no preferred aspect ratio. This is why there is not wavelength selectivity in y direction and most probably the reason there is such a wide variability in the aspect ratio of the structures.

So, the results of the six simulations show that a range of fold structures form, with both small aspect ratios (egg-type structures) as well as more elongated ones. The aspect ratio evolution of dome shaped features have been analysed in all simulations by using curvature analysis described in 2.2.4.1. This analysis of the folded surface is not shown here, although it has been used to analyse the aspect ratio as it is described here. We can say that the evolution of the dome shaped features in multilayer detachment folding is similar to that of the single layer case (Schmid et al., 2008): they are formed at very early stages with small amplitude but elongated shapes (aspect ratio > 1), and with no strong prevalent orientation at the time step zero. With time, their aspect ratio increases and they are oriented orthogonal to main compression.

Next, we studied the aspect ratio of the isolated folds segments that remain above different height levels. The evolution of the mean aspect ratio obtained in this way is shown in Figure 2.11, where the coloured lines correspond to the delimiting height (mean topography, half of the maximum amplitude and a quarter of the maximum amplitude). There is a limitation to the upper value of the aspect ratio in simulations 2, 3, and 6 due to the long folds that extend across the full domain and the calculated aspect ratio should be considered as a minimum value. The average aspect ratio of all folds as a function of strain for different numerical simulations can be seen in Figure 2.11. An overall trend can be observed in which the obtained aspect ratio after certain strain (>0.1) is different for the different runs, being higher in the run with a higher viscosity ratio ($R_1 = 4$) and for the run with higher strain rate. In both cases there is a clear increase in the dominant wavelength.

2.5.2 3D Fold interactions

As individual folds grow in 3D they also propagate laterally in the direction orthogonal to the main compression direction. This can result in different interactions between adjacent growing folds. Linkage of folds during their lateral propagation is sometimes invoked as the mechanism to explain abnormally high aspect ratios of folds, or sinusoidal shapes where different culminations and saddles along the axis are observed.

Analogue and numerical models have shown that depending on the influence area or contact strain around the structures, folds may link in a linear manner, obliquely, or if outside the influence area of each other they, can keep growing independently. Field evidence for lateral fold propagation has been provided from some examples in the Zagros Mountains by Bretis et al. (2011). They illustrated the proposed fold linkage mechanisms with the results of the 3D fold pattern evolution study of Schmid et al. (2008) and they concluded that the linkage mechanisms they inferred from field and geomorphological studies could be the result of lateral fold propagation as seen in numerical models. However, the main concern of Schmid et al. (2008) regarding fold linking processes was to illustrate that same linkage processes occur even if different compression conditions were applied in the numerical simulations.

A more recent study by Grasemann and Schmalholz (2012), studied the lateral linkage mode of initially isolated fold segments. Two initial folds were added to their model as line shaped perturbations, and the authors showed that a critical separation distance exists of about half the dominant wavelength above which folds do not link. Linking locations are characterised by a lower amplitude saddle points.

Our simulations start with random initial perturbations and the folds have larger growthrates than the single-layer detachment folding cases studied by Schmid et al. (2008). It is thus interesting to study fold linkage under these conditions.

Several examples of fold interactions are present in our numerical runs that occur even if loading conditions are maintained constant with time. A conceptualization of the different fold interactions is shown in Figure 2.12. Depending on the distance or position with respect to other folds, some of them grow independently resulting in almost dome shaped or low aspect ratio folds (Figure 2.13), whereas in other cases folds link from only one or from both sides. This linking can be linear or oblique; in the first case, the linkage area might be evident as a depressed area in-between two culminations whereas in the latter case, the linkage produces longer folds with a deflection of the hinge line. The observed long length antiforms, which in most cases show a deflected hinge line, are the result of several of the mentioned fold segments getting aligned and merged with time. Fold locking occurs when the distance between the individual folds is such that it is too high for folds to link, but sufficiently small for them to interact their respective grow. Our models thus confirm the previous findings of Grasemann and Schmalholz (2012).

However, here we describe some new fold interactions to which little attention has been paid previously. In earlier numerical 3D models by Schmid et al. (2008) triple linkage of folding have also been observed, that give rise to fork structures. In our numerical simulations, those triple linkage interactions occur frequently and can be grouped into synchronous and asynchronous triple linkage. In the latter, a new fold segment links to other already linked fold segments. This type of triple fold linkage can be observed in all our high-resolution simulations and examples can be seen in Figure 2.13.

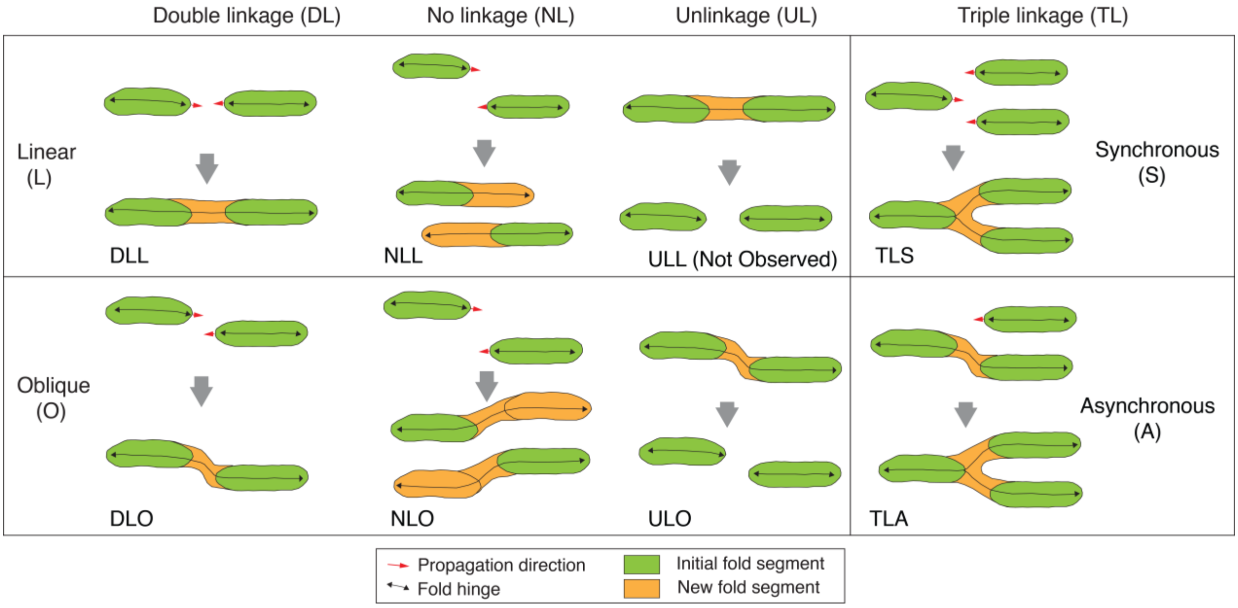

Figure 2.12. Conceptualized fold interactions observed in the 3D simulations (after Bretis et al., 2011). Examples of these fold interactions observed in the numerical simulations are shown in Figure 2.13.

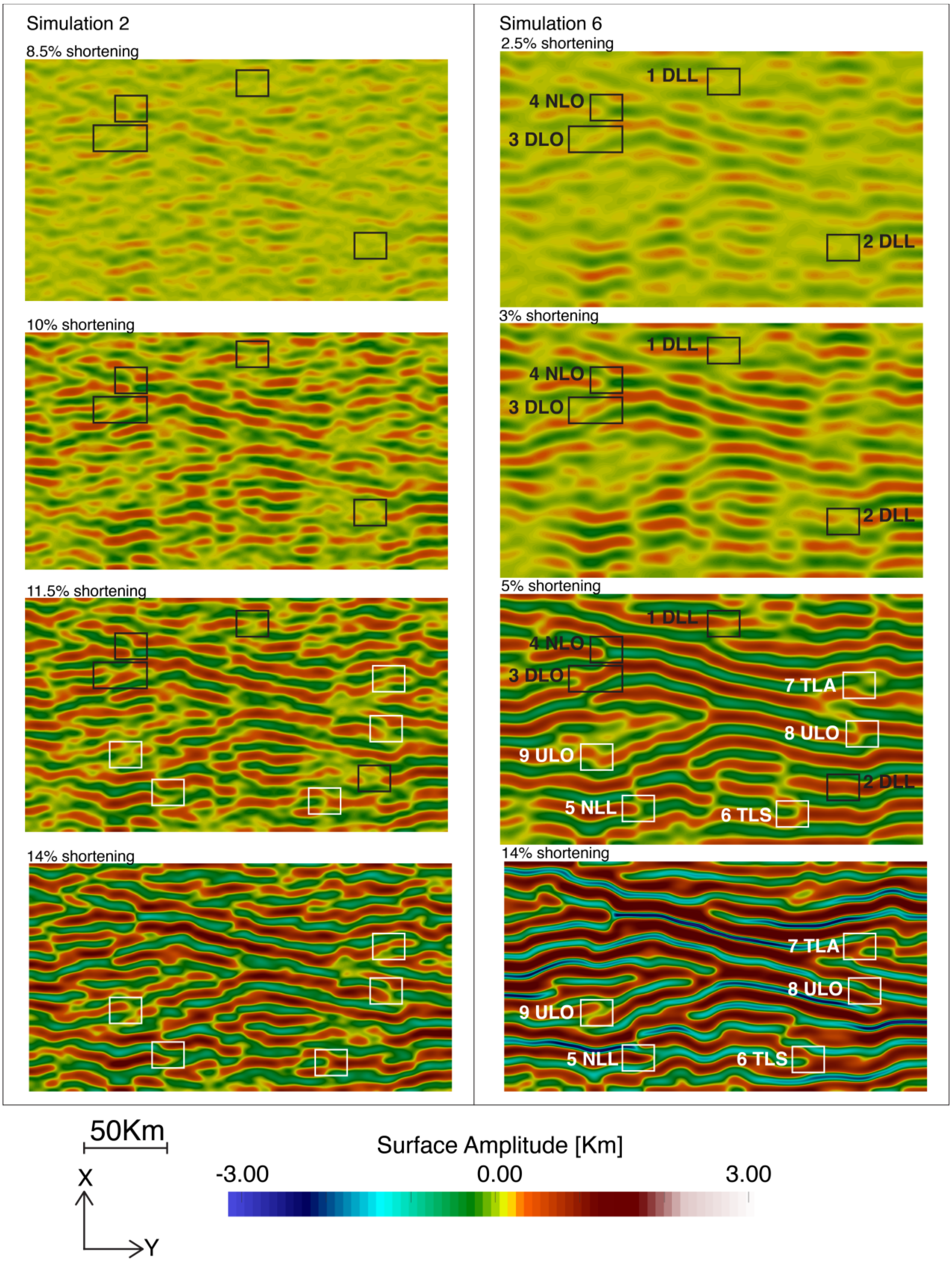

Figure 2.13. Map view of the topography of four different strain stages of simulations 2 and 6. Various examples of fold linkage mechanisms are indicated with the numbers 1 to 9, and the abbreviation for the observed fold interactions in Simulation 6 as sketched in Figure 2.12. Same areas are also indicated in Simulation 2 for comparison.

Another fold interaction that has not been described previously is the unlinkage of fold segments. Conceptually, both linear and oblique unlinking should happen, although in our simulations we have only observed oblique unlinkage of folds. Two examples of this unlinking process are shown in Figure 2.13.

Comparing simulations 2 with simulation 6 one can see that the fold interactions are different, even though the final fold pattern and wavelength are similar in both simulations. To better illustrate the differences, we have compared simulations 2 and 6 at certain shortening stages with similar fold amplitudes, and at the same shortening final stage of 14%. Differences can be seen in Figure 2.13, where folding interactions have been highlighted and labelled in simulation 6, and the same areas are indicated in simulation 2. While in both simulations most double and triple linkage happen during early shortening stages, the unlinking process and asynchronous triple linkage, is mainly observed in simulation 6 after significant amplification of folding has already taken place. In the cases where an unlinking process was observed in simulation 6, the same fold segments were never linked in simulation 2. Simulation 6 also shows some examples of folds splitting into two of smaller wavelength in compression direction as described in section 2.4.1.

As the 3D simulations demonstrate, folds developing from random noise result in a complex 3D pattern as a result of several fold interactions with increasing strain. Therefore, despite a unique compression direction being used in all our simulations, fold hinges are frequently oblique with respect to the compression direction. This deviation from the main compression direction has also been observed in early experimental models of buckle folding by Ghosh and Ramberg (1968) that employed a single compression direction. Such folding patterns can thus not be taken as evidence for several compressional events.

2.6 Comparison with a natural example

The Zagros Simply Folded Belt is a typical example of a folding-dominated fold and thrust belt. Originally interpreted as buckle folds (Colman-Sadd, 1978), the folds occurring there have been explained by a number of mechanisms, ranging from fault-bend folds to faulted detachment folds and detachment folds. Some authors argued that there are several facts that point towards buckling as a the main folding mechanism

(Lacombe et al., 2007; Mouthereau et al., 2007), namely the fact that the amplitude to wavelength ratio does not vary much across the belt, and that the differential peak stresses, inferred from calcite twins in synfolding veins, is rather homogeneous across the belt at 40 ± 15 MPa.

The Fars area of the Zagros is characterized by well-developed double plunging folds (periclines) that show a wide variability of aspect ratios: from almost dome-like features to several tens of kilometres long structures, yet with a fold wavelength that is remarkably similar throughout the region and around 14 km with a significant standard deviation (see Figure 2.14a). The longest anticlines are often sinusoidal rather than linear and have several saddles and culminations. A comparison of the results of the numerical simulations with this natural example shows some remarkable similarities (Figure 2.14) even though the scales might be different (caused by the fact that the numerical simulation had a dominant wavelength between 6 and 20 km, rather than one of 14 km as in the Zagros), and despite the fact that the numerical simulations used a significantly thicker basal salt layer than the one observed in the Zagros. An obvious difference is that the synclines are deeper in the numerical simulations, which is to be expected, as we did not take erosion and sedimentation into account in the simulations.

Although in the Fars area of the Zagros the folds show a prevalent spacing or wavelength of around 14 Km, it has a wide range of values of wavelength around this dominant value. In our simulations we have mainly compared the predicted dominant wavelength value of the analytical solution with the numerical runs by means of the spectral analysis of the topography. However, if we make a statistical analysis of the folds present in simulation 6 (by measuring the peak-to-peak distance of adjacent folds in a similar way as for the Zagros), we can also see that there is a wide range of wavelength values around the predicted dominant one (see histogram in Figure 2.14b).

From the six 3D high-resolution simulations that we show here, the ones that are closest to the wavelength of the Fars region are simulations 2, 3, 5 and 6. However, 2 and 3, even if they have a wavelength of 17 kilometres, cannot be compared to the natural example, because in simulation 2 the high strain rate, results in very high amplitude folds after less than one Myrs, whereas simulation 3 was performed without gravity. Simulation 5 shows a very low growth rate of the folds. Therefore, the most appropriate one to compare with folds from the Zagros Fars area is simulation 6. This simulation, although it has a predicted dominant wavelength of 21 kilometres, due to the high growth rate, has also a kinematically decreased wavelength of around 16.5 kilometres with a standard deviation of 2 kilometres, and it is therefore quite close to the observed wavelength in the Fars area.

Lateral growth of fault related folds has usually been related to the subjacent fault slip (Champel et al., 2002; Delcaillau, 2001; Ramsey et al., 2008). However, a study based on several geomorphological evidences by Bretis et al. (2011) has argued that certain long folds in the Simply Folded Belt in Iraq could have formed through linkage of laterally growing fold segments. Their study was based in the analysis of pinched rivers, asymmetric forked tributary river networks and curved wind gaps. Our simulations support this hypothesis, and show that long fold trains can indeed form as a result of linking smaller scale folds.

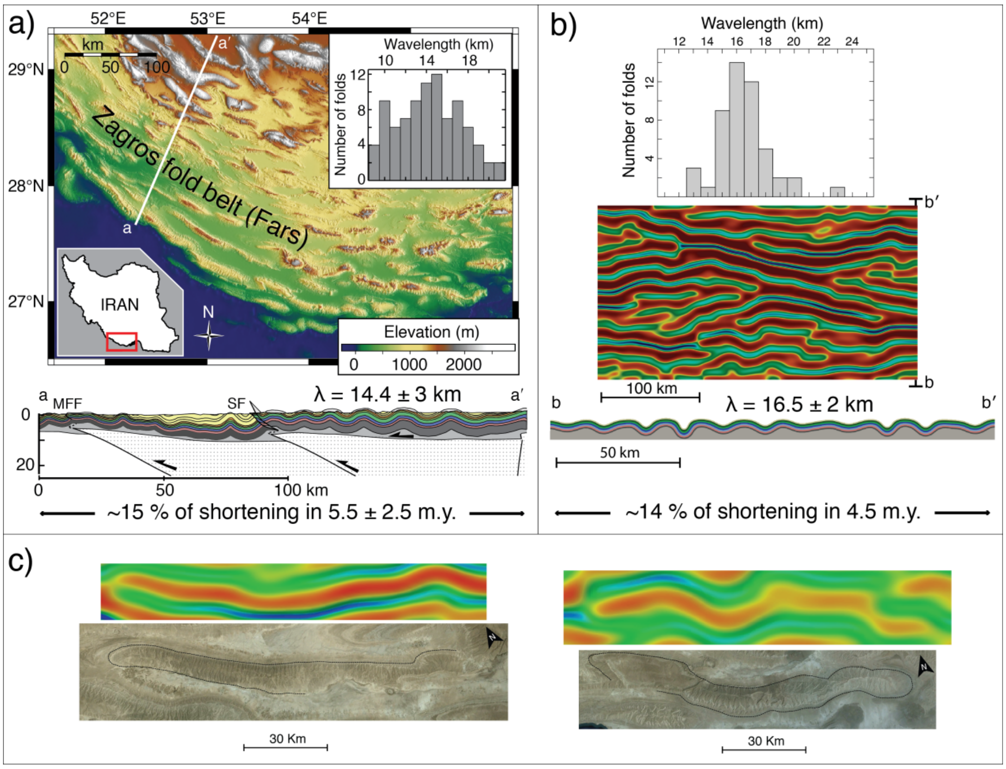

Figure 2.14. Comparison of some features observed in simulation 6 with the Fars province in the Zagros folded belt. A) Digital elevation model of the Fars province in Iran, with histogram inset showing measured wavelength of folds and cross section (from Yamato et al., 2011). B) Results of simulation 6, after 14% of shortening (same as Figure 2.9), with wavelength of folds measured and plotted in a histogram and a cross section. C) Detail of two 3D fold geometries of the simulation compared to two folds observed in the Fars region in the Zagros Mountains (Images from Google Earth).

2.7 Discussion

Our study is limited to linear viscous rheologies as we focus on the general aspects of multilayer detachment folding instability. For the Zagros Simply Folded Belt this seems appropriate as previous 2D results with a more complicated viscoelastoplastic rheologies demonstrated that the observations can be explained by a multilayer folding instability and relatively little thrusting and brittle deformation structures occur under such conditions (Yamato et al., 2011). Our conclusions with respect to the 3D interactions of folds are thus likely to hold even for more complicated brittle rheologies as long as the crust is in a folding-dominated deformation mode. The predictions on fold wavelength and growthrate and the mechanical folding phase diagrams are likely to be different if more complex rheologies are considered.

We have shown that phase diagrams of dominant wavelength and growthrate are very useful to better understand the physics of multilayer folding, and that the analytically predicted dominant wavelength is the one that is selected during 2D and 3D numerical simulations of multilayer folding. For the parameters that were not considered in our study it is potentially possible to construct such phase diagrams using thousands of solutions of the analytical solution and would still be computationally much cheaper than running 3D high-resolution simulations with high order elements.

For example, other parameters that could have been further investigated are the number of layers and the thickness ratio between the competent and the weak layers within the overburden. The effect of the number of layers in a multilayer stack embedded in a matrix was already considered in previous works (Biot, 1961; Schmid and Podladchikov, 2006) where the viscosity ratio in the dominant wavelength and growthrate expressions is changed accordingly to the number of layers of the stack. Schmid and Podladchikov (2006) showed that in true multilayer folding of isolated multilayer systems, with increasing number of layers, the growthrate increases more (in comparison to effective single layer domain) than the wavelength. For the non-gravity influenced domains of our work, where we have considered 7 layers, wavelength is smaller in the multilayer domain NGml than in effective single layer domain NGsl. However, it is important to note that our setup is different from the multilayer stack embedded in a matrix.

The thickness ratio between competent and weak layers was also addressed in 2D by Schmid and Podladchikov (2006), who showed that there is a certain thickness ratio of weak and competent layers which promotes the growth rate of the whole multilayer system and to which they refer as true multilayer system. If the weak layers are significantly thinner than the stronger layers, the whole overburden behaves as a single competent layer, whereas each of the layers folds independently if the separation distance between competent layers is significantly larger than thickness of the competent layers. In a true multilayer mode, growthrates are enhanced compared to single layer models (Biot, 1961; Ramberg, 1962; Schmid and Podladchikov, 2006). For a multilayer stack embedded in a matrix, it was shown that when the thickness ratio between the competent and weak layers is equal to one, the growthrate is maximum irrespective of the viscosity contrast between the layer and matrix and therefore a true multilayer system behaviour of the system occurs. In our phase diagrams (Figure 2.2), R_1=R_2 corresponds to the case where only two different viscosities are considered. However, our results show that there is a boundary between the effective single layer behaviour and multilayer behaviour that depends on the two viscosity ratios R_1 and R_2 despite the thickness ratio between competent and weak layers being equal to one.

The high-resolution simulations have been limited to the given parameters of Table 2.1, being the viscosity of salt 10^{19} Pa s and the H_s and H_o fixed with a ratio H_s/H_o close to one. The influence of those parameters have been illustrated with the folding phase diagrams of Figure 2.2 and Figure 2.3 and the corresponding scaling laws and boundary equations of Table 2.2, Table 2.3 and Table 2.4. The rheology of salt is vigorously debated and reported values of salt viscosity range several orders of magnitude for linear viscous rheologies (Mukherjee et al., 2010), being the most commonly used values between 10^{16} to 10^{21} Pa s, see Mukherjee et al. (2010) for a compilation of values. The detachment layer/salt layer viscosity has a first order influence on the wavelength and growthrate of detachment multilayer folding, and which can be illustrated by plotting the phase diagrams for two different salt viscosities (see Figure 2.2a and Figure 2.2b). Because the Argand number changes, the boundaries of the folding modes change. Within the folding modes that depend on R_1 influenced domains, changing salt viscosity results in different wavelengths and growthrates. For example, reducing the salt viscosity by three orders of magnitude while keeping overburden viscosities the same, increases both the dominant wavelength and growthrate. On the other hand, the H_s employed in most of our models is thicker than for example in the Zagros, where salt thickness has been reported to be around 1000 meters (Kent, 1979). Decreasing H_s/H_o decreases both the wavelength and growthrate within the non-gravity influenced domains, whereas in the low viscosity ratios used in the simulations, H_s needs to be below around 1000 meters to have a strong influence on the growthrate and wavelength.

It has been discussed by some authors that the selectivity of the wavelength decreases with strain, as the amplification velocity or growth rate decreases the higher the amplitude is. According to Schmalholz and Podladchikov (2000), this explains why folds in nature usually show aperiodic form and not a regular and sinusoidal shape as the instability analysis usually considers. For the Zagros, it has been argued that the maximum non-dimensional amplification rate was around 100. This value is sufficient for large amplitude folds to form, but is not extraordinary large. Numerical simulations show that fold-spacing for such growthrates is somewhat more irregular than for cases in which the dominant growthrate is 1000 or larger, in which fold trains are significantly more cylindrical (Figure 2.5). Our 3D numerical simulations confirm this and show that folds are more periodic for cases that have a larger growthrate. Yet, even in those cases folds have a wide range of aspect ratios (Figure 2.7, Figure 2.8 and Figure 2.9).

Our results can be applied to folding dominated fold and thrust belts, where we can use observable parameters such as H_s/H_o and λ/H_o to constrain the corresponding folding mode. Figure 2.15 has been constructed using the scaling laws and boundary equations of Table 2.2, Table 2.3 and Table 2.4 and it shows the transition between different folding domains at the H_s/H_o and λ/H_o space. For example, for the same Argand number of Figure 2.2a, Figure 2.15a shows the H_s/H_o ratio at which the transition from G or Gml domains to NGml domain occurs. We have plotted the approximate position that corresponds to folding of the Zagros Simply Folded Belt, which for the used Argand number is close to the transition between the three different folding domains. Different Argand numbers would result in shifted boundaries as shown in Figure 2.15b.

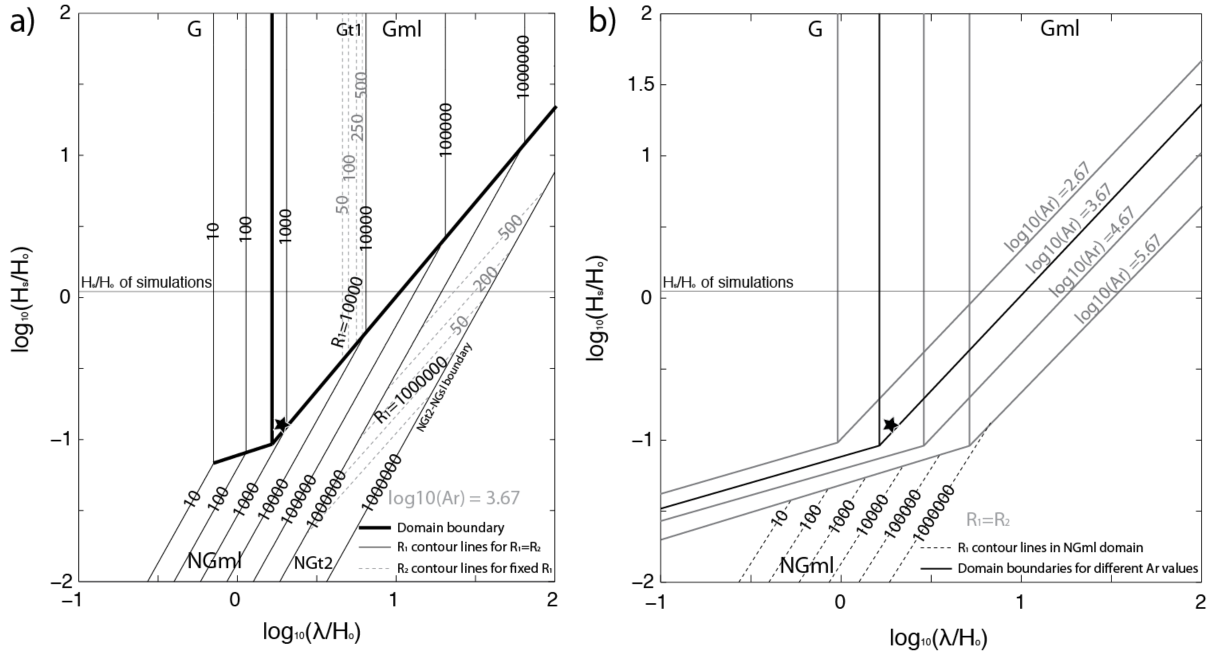

Figure 2.15. Diagrams showing the transition between folding domains at the λ/H_0 - H_S/H_0 parameter space, which are observable parameters in different folding dominated fold and thrust belts. Star symbol indicates approximate values of the Zagros Simply Folded Belt in southeast Iran. a) Diagram for a given Argand number. b) Diagram with folding domain boundaries for different Argand numbers.

We have compared the results of the 3D fold patterns in the simulations with those of the Fars region, in the Zagros Simply Folded Belt. For natural conditions such as those in that area of the Zagros Mountains, fold wavelengths are ~14 km, whereas the sedimentary pile has a thickness of around 8 km. Single layer detachment folding instabilities with wavelength over thickness ratios of less than 2 typically have very small growth rates, which implies that a folding instability would never develop. In order to obtain a multilayer folding instability, we therefore would need very large power law exponents of the overburden (larger than 23 in the case of the Zagros), or a true multilayer folding instability, both of which result in significantly larger growthrates. The previous work of Yamato et al. (2011) showed that in order for a folding instability to develop instead of thrusting in the sedimentary cover with known H_S/H_0, both weak intermediate layers and low friction angles were required. Here, we limited our study to linear viscous materials. In order to have fold growth rates that are sufficiently large for folding to develop within the given time constrains, we had to employ a different H_S/H_0 ratio to the one of the Zagros Simply Folded Belt. Despite folding instability predicts a dominant wavelength that is the one selected in the simulations, our setup shows that the final 3D patterns are complex due to fold segments interactions. However, the fold wavelength variation that exists along strike in the Simply Folded Belt cannot be ignored. In the Lurestan province for example, Casciello et al. (2009) differentiated three areas where the different wavelength of folds could be linked to the characteristics of the multilayer sedimentary cover in which the folds develop. They also reported decoupled folding in the areas where one decoupling level (weak layer) was thicker, allowing for disharmonic folding above. Our models consider a heterogeneous multilayer system with weaker layers in between. Although the transition from a multilayer to effective single layer behaviour has been depicted with our simulations and phase diagrams, the competent to weak layers ratio is chosen such that there is not disharmonic folding. Besides, our models do not have any initial variation of properties or thickness within the same layers, which would result in spatial variability of fold patterns, as seen in the Lurestan province (Casciello et al., 2009). Furthermore, the existence of weak zones in the sedimentary cover would also affect the final folding patters. For example, the fact that many of the exposed salt plugs in the Fars area might have been already formed when folding developed (e.g. Jahani et al. (2007) and references therein), can have influenced the localization and propagation of folds (e.g. Callot et al., 2007).

2.8 Conclusions

We have used two different approaches to study the multilayer detachment folding instability: a semi analytical 2D approach based on a thick plate analysis and 3D numerical simulations. Results from both methods are in good agreement and show that several multilayer-folding modes exist, some of which are affected by gravity.

The results from numerical simulations agree well with analytical predictions in 2D, and show that the final wavelength is in overall agreement with the calculated phase diagrams and the resulting wavelengths measured using spectral analysis of the topography are close to the analytically predicted values.

In order to confirm that this wavelength selection also occurs in 3D finite amplitude folding, we have performed several 3D simulations. The simulations show that folds with a wide range of aspect ratios form, which are however in general agreement with theoretical predictions, suggesting that a 2D folding analysis is in many cases sufficient to understand fold dynamics. Yet, compared to 2D cases a somewhat wider spread in folding wavelengths occurs around a dominant value. The numerical simulations show that folds can link to form longer fold trains, and that simultaneously, dome-like structures can form at other locations.

A comparison of natural observations of the Fars region in the Zagros show a number of similarities, reinforcing the idea large parts of the Zagros could have formed as a result of a crustal-scale folding instability.

2.9 Acknowledgements

We thank *** and *** for their reviews, which helped to improve this paper. Funding was provided by the European Research Council under the European Community's Seventh Framework program (FP7/2007-2013) ERC Grant agreement #258830. 3D simulations were performed on the Cray XT5 "Monte Rosa" supercomputer of the Swiss National Supercomputing Center, on the IBM Blue Gene/Q JUQUEEN supercomputer of the Forschungszentrum Jülich, Germany and on MOGON supercomputer of Johannes Gutenberg University Mainz.

2.10 References

Adamuszek, M., Schmid, D.W., and Dabrowski, M., 2013, Theoretical analysis of large amplitude folding of a single viscous layer: Journal of Structural Geology, v. 48, p. 137-152.

Biot, M.A., 1961, Theory of Folding of Stratified Viscoelastic Media and Its Implications in Tectonics and Orogenesis: Geological Society of America Bulletin, v. 72, p. 1595-1620.

Bretis, B., Bartl, N., and Grasemann, B., 2011, Lateral fold growth and linkage in the Zagros fold and thrust belt (Kurdistan, NE Iraq): Basin Research, v. 23, p. 615-630.

Burg, J.-P., Kaus, B.J.P., and Podladchikov, Y.Y., 2004, Dome structures in collision orogens: Mechanical investigation of the gravity/compression interplay: Geological Society of America Special Papers, v. 380, p. 47-66.

Callot, J.P., Jahani, S., and Letouzey, J., 2007, The Role of Pre-Existing Diapirs in Fold and Thrust Belt Development, *in* Lacombe, O., Roure, F., Lavé, J., and Vergés, J., eds., Thrust Belts and Foreland Basins: Frontiers in Earth Sciences, Springer Berlin Heidelberg, p. 309-325.

Casciello, E., Vergés, J., Saura, E., Casini, G., Fernández, N., Blanc, E., Homke, S., and Hunt, D.W., 2009, Fold patterns and multilayer rheology of the Lurestan Province, Zagros Simply Folded Belt (Iran): Journal of the Geological Society, v. 166, p. 947-959.

Champel, B., van der Beek, P., Mugnier, J.-L., and Leturmy, P., 2002, Growth and lateral propagation of fault-related folds in the Siwaliks of western Nepal: Rates, mechanisms, and geomorphic signature: Journal of Geophysical Research: Solid Earth, v. 107, p. ETG 2-1-ETG 2-18.

Chapple, W.M., 1968, A Mathematical Theory of Finite–Amplitude Rock–Folding: Geological Society of America Bulletin, v. 79, p. 47-68.

Cobbold, P.R., 1976, Fold Shapes as Functions of Progressive Strain: Philosophical Transactions of the Royal Society of London. Series A, Mathematical and Physical Sciences, v. 283, p. 129-138.

Colman-Sadd, S.P., 1978, Fold development in Zagros simply folded belt, Southwest Iran: AAPG Bulletin, v. 62, p. 984-1003.

Delcaillau, B., 2001, Geomorphic response to growing fault-related folds: example from the foothills of central Taiwan: Geodinamica Acta, v. 14, p. 265-287.

Deubelbeiss, Y., and Kaus, B.J.P., 2008, Comparison of Eulerian and Lagrangian numerical techniques for the Stokes equations in the presence of strongly varying viscosity: Physics of the Earth and Planetary Interiors, v. 171, p. 92-111.

Fletcher, R.C., 1974, Wavelength selection in the folding of a single layer with power-law rheology: American Journal of Science, v. 274, p. 1029-1043.

Fletcher, R.C., 1977, Folding of a single viscous layer: Exact infinitesimal-amplitude solution: Tectonophysics, v. 39, p. 593-606.

Fletcher, R.C., 1991, Three-dimensional folding of an embedded viscous layer in pure shear: Journal of Structural Geology, v. 13, p. 87-96.

Fletcher, R.C., 1995, Three-dimensional folding and necking of a power-law layer: are folds cylindrical, and, if so, do we understand why?: Tectonophysics, v. 247, p. 65-83.

Gerbault, M., Burov, E.B., Poliakov, A.N.B., and Daignières, M., 1999, Do faults trigger folding in the lithosphere?: Geophys. Res. Lett., v. 26, p. 271-274.

Ghosh, S.K., and Ramberg, H., 1968, Buckling experiments on intersecting fold patterns: Tectonophysics, v. 5, p. 89-105.

Grasemann, B., and Schmalholz, S.M., 2012, Lateral fold growth and fold linkage: Geology, v. 40, p. 1039-1042.

Hudleston, P.J., 1973, An analysis of “Single-layer” folds developed experimentally in viscous media: Tectonophysics, v. 16, p. 189-214.

Jahani, S., Callot, J.-P., Lamotte, D., Letouzey, J., and Leturmy, P., 2007, The Salt Diapirs of the Eastern Fars Province (Zagros, Iran): A Brief Outline of their Past and Present, *in* Lacombe, O., Roure, F., Lavé, J., and Vergés, J., eds., Thrust Belts and Foreland Basins: Frontiers in Earth Sciences, Springer Berlin Heidelberg, p. 289-308.

Jaquet, Y., Bauville, A., and Schmalholz, S.M., 2014, Viscous overthrusting versus folding: 2-D quantitative modeling and its application to the Helvetic and Jura fold and thrust belts: Journal of Structural Geology, v. 62, p. 25-37.

Johnson, A.M., and Fletcher, R.C., 1994, Folding of viscous layers: New York, Columbia University Press.

Kaus, B.J.P., 2005, Modelling approaches to geodynamic processes.

Kaus, B.J.P., and Becker, T.W., 2007, Effects of elasticity on the Rayleigh–Taylor instability: implications for large-scale geodynamics: Geophysical Journal International, v. 168, p. 843-862.

Kaus, B.J.P., and Podladchikov, Y.Y., 2006, Initiation of localized shear zones in viscoelastoplastic rocks: Journal of Geophysical Research: Solid Earth, v. 111, p. B04412.

Kaus, B.J.P., and Schmalholz, S.M., 2006, 3D finite amplitude folding: Implications for stress evolution during crustal and lithospheric deformation: Geophys. Res. Lett., v. 33, p. L14309.

Kent, P.E., 1979, The emergent Hormuz salt plugs of southern Iran: Journal of Petroleum Geology, v. 2, p. 117-144.

Lacombe, O., Amrouch, K., Mouthereau, F., and Dissez, L., 2007, Calcite twinning constraints on late Neogene stress patterns and deformation mechanisms in the active Zagros collision belt: Geology, v. 35, p. 263-266.

Lechmann, S.M., May, D.A., Kaus, B.J.P., and Schmalholz, S.M., 2011, Comparing thin-sheet models with 3-D multilayer models for continental collision: Geophysical Journal International, v. 187, p. 10-33.

Lisle, R.J., and Toimil, N.C., 2007, Defining folds on three-dimensional surfaces: Geology, v. 35, p. 519-522.

Mancktelow, N.S., and Abbassi, M.R., 1992, Single layer buckle folding in non-linear materials—II. Comparison between theory and experiment: Journal of Structural Geology, v. 14, p. 105-120.

Mouthereau, F., Lacombe, O., Tensi, J., Bellahsen, N., Kargar, S., and Amrouch, K., 2007, Mechanical Constraints on the Development of the Zagros Folded Belt (Fars), *in* Lacombe, O., Roure, F., Lavé, J., and Vergés, J., eds., Thrust Belts and Foreland Basins: Frontiers in Earth Sciences, Springer Berlin Heidelberg, p. 247-266.

Mukherjee, S., Talbot, C.J., and Koyi, H.A., 2010, Viscosity estimates of salt in the Hormuz and Namakdan salt diapirs, Persian Gulf: Geological Magazine, v. 147, p. 497-507.

Mynatt, I., Bergbauer, S., and Pollard, D.D., 2007, Using differential geometry to describe 3-D folds: Journal of Structural Geology, v. 29, p. 1256-1266.

Pollard, D.D., and Fletcher, R.C., 2005, Fundamentals of structural geology, Cambridge University Press.

Ramberg, H., 1962, Contact strain and folding instability of a multilayered body under compression: Geologische Rundschau, v. 51, p. 405-439.

Ramberg, H., 1964, Selective buckling of composite layers with contrasted rheological properties, a theory for simultaneous formation of several orders of folds: Tectonophysics, v. 1, p. 307-341.

Ramsey, L.A., Walker, R.T., and Jackson, J., 2008, Fold evolution and drainage development in the Zagros mountains of Fars province, SE Iran: Basin Research, v. 20, p. 23-48.

Ruh, J.B., Kaus, B.J.P., and Burg, J.-P., 2012, Numerical investigation of deformation mechanics in fold-and-thrust belts: Influence of rheology of single and multiple décollements: Tectonics, v. 31, p. TC3005.

Schmalholz, S.M., 2006, Finite amplitude folding of single layers: elastica, bifurcation and structural softening: Philosophical Magazine, v. 86, p. 3393-3407.

Schmalholz, S.M., 2008, 3D numerical modeling of forward folding and reverse unfolding of a viscous single-layer: Implications for the formation of folds and fold patterns: Tectonophysics, v. 446, p. 31-41.

Schmalholz, S.M., and Podladchikov, Y., 1999, Buckling versus folding: Importance of viscoelasticity: Geophys. Res. Lett., v. 26, p. 2641-2644.

Schmalholz, S.M., and Podladchikov, Y.Y., 2000, Finite amplitude folding: transition from exponential to layer length controlled growth: Earth and Planetary Science Letters, v. 179, p. 363-377.

Schmalholz, S.M., Podladchikov, Y.Y., and Burg, J.P., 2002, Control of folding by gravity and matrix thickness: Implications for large-scale folding: J. Geophys. Res., v. 107, p. 2005.

Schmalholz, S.M., and Schmid, D.W., 2012, Folding in power-law viscous multi-layers: Philosophical Transactions of the Royal Society A: Mathematical, Physical and Engineering Sciences, v. 370, p. 1798-1826.

Schmid, D.W., Dabrowski, M., and Krotkiewski, M., 2008, Evolution of large amplitude 3D fold patterns: A FEM study: Physics of the Earth and Planetary Interiors, v. 171, p. 400-408.

Schmid, D.W., and Podladchikov, Y.Y., 2006, Fold amplification rates and dominant wavelength selection in multilayer stacks: Philosophical Magazine, v. 86, p. 3409-3423.

Sherwin, J.-A., and Chapple, W.M., 1968, Wavelengths of single-layer folds; a comparison between theory and observation: American Journal of Science, v. 266, p. 167-179.

Simpson, G.D.H., 2009, Mechanical modelling of folding versus faulting in brittle–ductile wedges: Journal of Structural Geology, v. 31, p. 369-381.

Smith, R.B., 1977, Formation of folds, boudinage, and mullions in non-Newtonian materials: Geological Society of America Bulletin, v. 88, p. 312-320.

Yamato, P., Kaus, B.J.P., Mouthereau, F., and Castelltort, S., 2011, Dynamic constraints on the crustal-scale rheology of the Zagros fold belt, Iran: Geology, v. 39, p. 815-818.

Chapter 3

Influence of pre-existing salt diapirs on 3D folding patterns[2]

Abstract

The 3D detachment folding instability gives rise to a wide variety of fold shapes (e.g. from dome shape structures to long en-echelon or straight anticlines) as a result of interactions between growing fold segments. The 3D growth of these fold, as well as the wavelength and lateral propagation of folds, are controlled by the physical parameters of a detachment layer and its overburden. However, the existence of initial heterogeneities, such as pre-existing salt plugs within the sedimentary cover, might affect fold development as well.

Here, we use numerical modelling to investigate how the fold pattern is affected by pre-existing salt structures. High-resolution 3D folding simulations (with and without pre-existing salt structures) were performed, in which we varied the shape, height and spacing of pre-existing diapirs. In a first geometric setup, we employed a multilayer setup and synthetic diapir distributions in order to study the influence of diapir spacing on fold spacing and patterns. In a second geometric setup, we used a diapir distribution that fits the observed exposed diapir distribution in the south-eastern Zagros. Results show that the presence of diapirs does not considerably change the wavelength of the folds, which is in all cases close to the dominant folding wavelength that develops in the absence of diapirs.

Yet, the presence of pre-existing structures speeds up the folding instability in those locations and also affects folding patterns as the diapirs localize the initial deformation by accommodating folding above them, which results in the diapirs being located in the core of the folds. If diapir spacing is much smaller than the dominant folding wavelength, diapirs are located in different structural positions such as fold synclines or flanks.

Keywords: 3D folding, fold patterns, salt diapirs, numerical modelling

---

[2] This chapter is submitted as: Fernandez, N. and Kaus, B.J.P. (2014) *Influence of pre-existing salt diapirs on 3D folding patterns*

3.1 Introduction

The role of a weak basal detachment level composed of a viscous material (e.g. salt) on the style of deformation in fold-and-thrust belts has been studied since decades (e.g. Davis and Engelder, 1985). It has long been known that a viscous detachment results in lower taper angles than in the case of a frictional detachment, as well as in faster propagation of the deformation front (Davis and Engelder, 1985), which can also lead to simultaneous evolution of the structures at different positions (Costa and Vendeville, 2002). In most studies, the basal weak layer is considered to have a more or less regular geometry, although gradual spatial changes in thickness and/or different extent of the basal layer have also been addressed by analogue modelling (e.g. Bahroudi and Koyi, 2003). However, the topography of this basal layer can be far from regular at all, and could potentially include abrupt changes in thickness prior to the compressional stage. An example is when a halokinetic phase predates the formation of the fold and thrust belt, when the topography of the basal salt layer can include the many different salt structures described in Hudec and Jackson (2007), ranging from buried salt domes, to salt walls or salt plugs etc.

Contraction of salt diapirs has been recognized in different geological settings that range from passive margins and extensional basins (e.g. Rowan and Vendeville, 2006) to convergent settings (e.g. Letouzey et al., 1995). The Zagros is an example of the latter case (Bahroudi and Koyi, 2003; Letouzey and Sherkati, 2004), where the relation between folds and diapirs has drawn the attention of early works in the area (e.g. Colman-Sadd, 1978; Kent, 1979). Although much of those works already mentioned salt to have moved previous to the main folding events (e.g. Ala, 1974; Kent, 1958, 1979), the idea that most of the salt structures were exposed or shallowly buried at the time of the onset of the Zagros main folding event was recently reinforced by Jahani et al. (2007), who made an attempt to classify the salt plugs of south-eastern Zagros with respect to folding in the area. While Letouzey and Sherkati (2004) showed that in the central Zagros, the salt diapirs are associated with major strike slip and tear faults, and tend to localize the position of faults, the diapirs of the south-eastern Zagros are mainly related to anticlines.

There are some analogue modelling studies that address the shortening of salt diapirs subjected to compression (e.g. Callot et al., 2007; Dooley et al., 2009; Koyi, 1988; Roca et al., 2006; Rowan and Vendeville, 2006). Those models show that it is common that anticlines are first localized above pre-existing diapirs (Callot et al., 2007). However, the initial geometry of the diapir might also cause differences in the deformation style from one diapir to another. The width of the compressed diapir, for example, can affect the amount by which the roof rises above it (Vendeville and Nilsen, 1995). Differences in shapes and height of the diapirs with respect to the sedimentary cover may also favour welding, thrusting or folding (Callot et al., 2007). Yet, most analogue experiments employed a brittle overburden, whereas the Zagros is a folding-dominated fold-and-thrust belt. It was argued recently that these folding and thrusting dominated deformations are two end-member modes of deformation (Ruh et al., 2012; Yamato et al., 2011). Therefore, experiments with a purely brittle and thrusting-dominated deformation might not be representative of the mechanics of the Zagros on geological timescales.

Here, our aim is to study the effect of pre-existing salt diapirs on the overall folding pattern of an area, and for this reason we mainly focus on regular patterns of salt diapirs rather than on single diapirs. Regular map view patterns in salt diapirs have been long been recognized in many of the well-known halokinetic regions (e.g. Rowan and Vendeville, 2006), but also in the south-eastern Zagros (Kent, 1979). In several cases, the regular distribution of the salt structures has been associated with basement faults that may have controlled the salt deposition thickness (e.g. Kent, 1979). However, analogue and numerical models have shown (e.g. Kaus and Podladchikov, 2001; Talbot et al., 1991) that diapirs rising from a constant thickness buoyant underlying layer can also develop regular patterns.

On the other hand, the folding instability itself also results in a characteristic spacing (wavelength) as a function of physical and geometrical parameters. Such parameters include the effective viscosity ratio between the overburden and basal salt layer or the thickness ratio between the two layers, among others. It is therefore of interest to study whether the folding wavelength adjusts to the spacing of pre-existing salt diapirs, or whether it is unaffected.

For this purpose, we here analyse how different patterns of regularly spaced diapirs (six different distributions) and a south-eastern Zagros-like diapir distribution influence the folding patterns. The results of simulations with pre-existing diapirs are compared to reference models without diapirs, but which employ the same random noise distribution. In order to test how robust our findings are with respect to differences in the viscosity structures, we use two rheological setups (referred as setup 1 and 2). These two rheological setups have parameters that result in different fold wavelengths (but in both cases close to the 14-15 km observed in the area (Yamato et al., 2011) and growthrates. We also relate the effect of the diapirs to the folding growth rate for each of the setups.

3.2 Method

We use a continuum mechanics approximation where the equations used to describe geological processes consists of a set of balance equations for mass and momentum together with their constitutive relationships.

Conservation of mass and momentum for slowly moving incompressible fluids are given by

$$\frac{\partial v_i}{\partial x_i} = 0 \qquad [3.1]$$

$$-\frac{\partial P}{\partial x_i} + \frac{\partial \tau_{ij}}{\partial x_j} = -\rho g_i \qquad [3.2]$$

where *i,j* represent spatial directions and repeated indices are summed, where v_i indicates velocity, x_i coordinates, $P = -\sigma_{ii}/3$ is pressure, σ_{ij} are the components of the total stress tensor, $\tau_{ij} = \sigma_{ij} + P$ the deviatoric stress tensor, ρ the density and g, the gravitational acceleration (acting in the vertical direction).

We employ a linear viscous (Newtonian) constitutive relationship given by

$$\tau_{ij} = 2\,\eta\dot{\varepsilon}_{ij}$$

where η is the Newtonian viscosity which is constant for each of the material phases, and $\dot{\varepsilon}_{ij}$, the deviatoric strain rate tensor given by

$$\dot{\varepsilon}_{ij} = \frac{1}{2}\left(\frac{\partial v_i}{\partial x_j} + \frac{\partial v_j}{\partial x_i}\right) \qquad [3.3]$$

Equations [3.1] to [3.3] are discretized using a staggered grid finite differences scheme within the parallel code LaMEM (Lithosphere and Mantle Evolution Model, r. 5056). Material properties are tracked using markers, here referred to as particles. These particles are advected in a Lagrangian manner with the velocities obtained from solving the equations [3.1]-[3.3].

LaMEM uses PETSc and solvers that allow running massively parallel forward simulations. For this study, a fully coupled Stokes solver solution method has been used with GCR and an algebraic multigrid preconditioner (HYPRE) for the full velocity block and the inverse viscosity as a preconditioner for the pressure block.

The internal free surface that allows topography to form is approximated in LaMEM by the “sticky air” approach, in which a low viscosity, zero density layer overlies the free internal surface. Recent benchmark studies have shown that the sticky air is a good approximation of the free surface provided it is sufficiently weak and of sufficient thickness, both of which are guaranteed in our study (Crameri et al., 2012). A parallel implementation of the Voronoi cells for phases visualization as described in May (2012) is implemented in LaMEM, which simplifies the visualization of the runs.

A semi analytical solution based on thick-plate theory that solves the same equations [3.1] to [3.3] for the multilayer setup considered here but for small limb dips has been used to compute growthrate vs. wavelength diagrams. The growthrate vs. wavelength diagrams are used to obtain a dominant wavelength (the wavelength with the highest growthrate) for the given setup. A full description of the semi-analytical solution is provided in Kaus (2005) and Kaus and Becker (2007).

In order to analyse the obtained topography, we used a 1D Fourier analysis both parallel and orthogonal to the compression orientation. For this purpose, we use the built-in *fft* routine of Matlab that provides the discrete Fourier transform of a given vector, and apply it to a topography that was interpolated on a regularized mesh. Results of the *fft* function for each orientation are averaged, and the maximum, minimum and mean amplitude and corresponding wavelength are extracted. As in previous studies (Schmid et al., 2008) we have used the spectral amplitude as a proxy of the prevalent fold wavelength present in the topography.

3.3 Diapir distribution in the Zagros

Previous attempts to classify salt plugs have been made by Talbot and Alavi (1996) and Jahani et al. (2007) among others. They have classified the salt plugs along the south-eastern Zagros according to their morphology, which can be correlated to a stage in their evolution, ranging from buried domes to salt plugs.

Our analysis of the geometries of the salt plugs that are present in the south-eastern Zagros (Figure 3.1a) is derived from outcropping geology in geological maps of Iran, scale 1:250,000 and literature (Jahani et al., 2007; Jahani et al., 2009). The shape is quite variable from circular to elongate and includes salt glaciers. The size of them varies from 1 km to 15 km of the elongated axis (Talbot and Alavi, 1996). The size of the diapirs that lie within the rectangle of Figure 3.1a, has been calculated by assuming a quasi-circular shape of the diapirs and calculating the approximate radius of the circle that would fit to the outcropping salt area. According to this simplification the diapirs that lie within the study area (37 exposed diapirs) have a radius that ranges from 300 meters to 6 km, with an average of 2.2 km. Using results of Jahani et al. (2007), we have also classified the diapirs in the study area according to whether they were already exposed at the surface before the Zagros orogeny or not.

We consider all diapirs of Figure 3.1a (exposed and buried) to compute the spacing, which we calculate as the distance to the closest diapir (irrespective of the direction). The histogram of diapirs changes whether we consider only exposed diapirs or buried ones (Figure 3.1b). It ranges from 2 to 46 km, with an average distance of 17.8 km if we inly consider exposed diapirs and 20.8 km for buried diapirs. When we limit the analysis to the 37 diapirs in the study area (rectangle in Figure 3.1a, only exposed diapirs), the average spacing is slightly lower with around 12 km.

Almost half of the diapirs are located near the pericline termination of the anticlines (48%), or in the core of the anticlines (18%), which sums up to 66% of the diapirs being located in the anticlines. The proportion of salt diapirs that are located along faults is also considerable (29%), although still less important than in the central Zagros (Jahani et al., 2009). On the other hand, there are only a small proportion of diapirs that are located within synclines (5%) (Jahani et al., 2009).

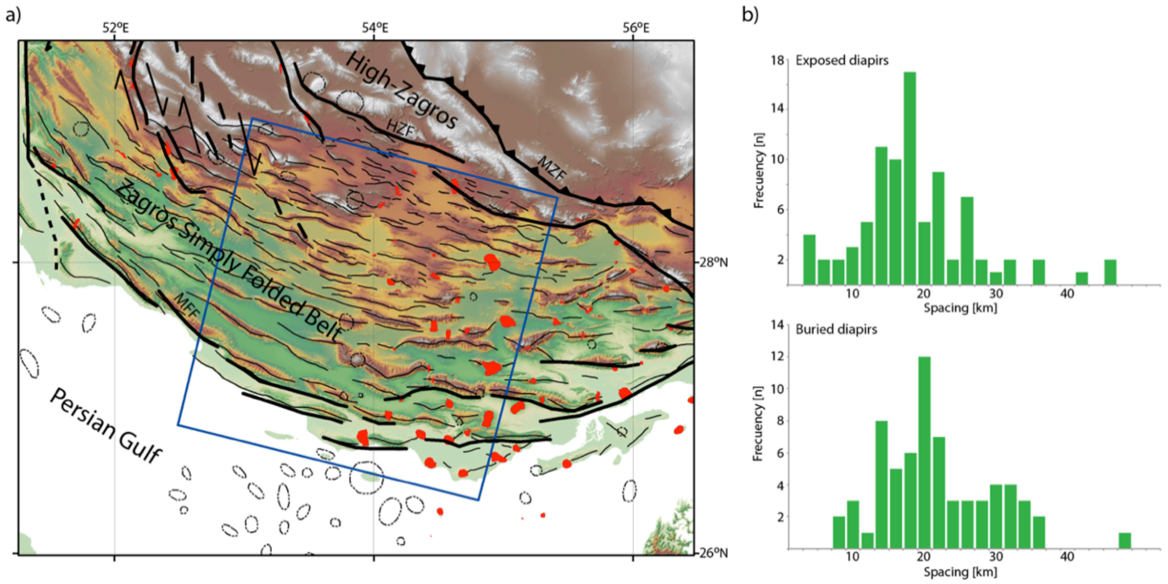

Figure 3.1. a) Digital elevation model of the south-eastern Zagros showing the axial traces of the anticlines (thin black lines) and the exposed (in red) and buried diapirs (dashed lines), from different sources (Geological maps of Iran, scale 1:250,000, Jahani et al., 2007; Jahani et al., 2009). Thick black lines indicate inferred basement faults (compiled from Berberian, 1995 and Talebian and Jackson, 2004) with the following abbreviations: Mountain Front Fault (MFF), High-Zagros Fault (HZF) and Main Zagros Thrust (MZT). b) Histogram plot of exposed and buried spacing of the salt diapirs shown in the map of a).

3.4 Experiment description

We have performed several high-resolution 3D runs using different model domains. We employed a folding multilayer setup under the influence of gravity, in which a sedimentary cover composed of seven layers overlies a lower detachment level (see Figure 3.2).

The relationship between the physical parameters that control the folding wavelength and growth rate is known from the thick-plate analysis. We can therefore use the thick-plate analysis solution to tune the rheological parameters such that they result in folding with the appropriate wavelength for our study (Table 3.1). The chosen thicknesses for the overburden layers and the basal detachment salt layer are different than in the Zagros, and have a ratio of the thickness of overburden to salt close to one. This was done to allow folding to develop after a reasonable amount of timesteps. Using linear rheologies and a geometrical setup similar to the Zagros would result in very low growth rates as discussed in Yamato et al. (2011).

Table 3.1. Parameters of the three different setups used in this work

	Units	Setup1	Setup2
L_{salt}	[m]	3000	3000
L_1	[m]	500	500
L_2	[m]	500	500
L_3	[m]	500	500
L_4	[m]	500	500
L_5	[m]	500	500
L_6	[m]	500	500
L_7	[m]	500	500
$L_{sticky\ air}$	[m]	3500	3500
η_s	[Pa s]	10^{19}	10^{19}
η_c	[Pa s]	10^{23}	$3.5\text{x}10^{22}$
η_w	[Pa s]	10^{19}	10^{19}
$\eta_{sticky\ air}$	[Pa s]	10^{17}	10^{17}
$\dot{\varepsilon}_{bg}$	[s^{-1}]	10^{-14}	10^{-15}
g	[m/s^2]	10	10
ρ_s	[kg/m^3]	2200	2200
ρ_o	[kg/m^3]	2700	2700
$\rho_{sticky\ air}$	[kg/m^3]	0.00	0.00
λ_{dom}	[km]	16.58	14.62
q_{dom}	[]	156.00	134.00

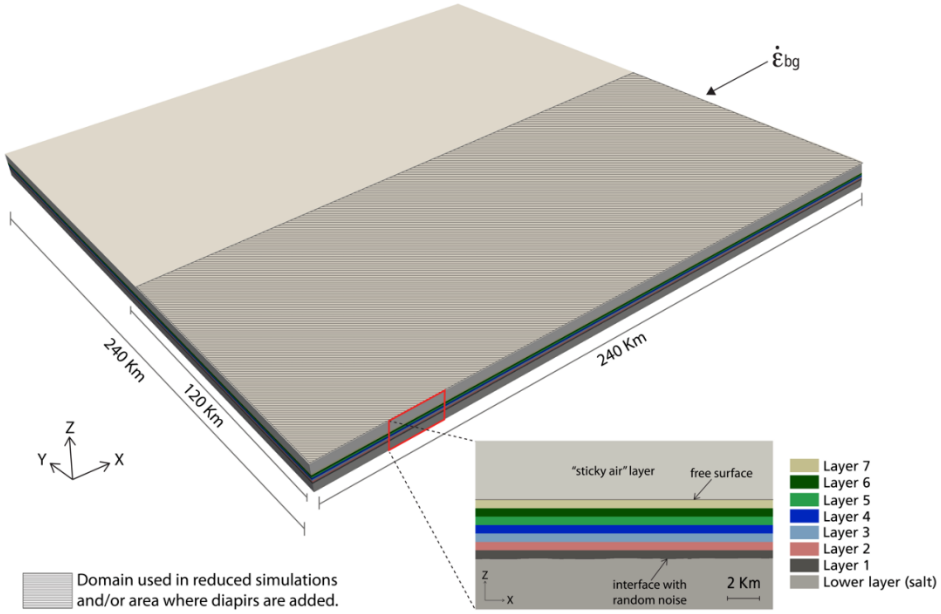

Figure 3.2. Setup used in the simulations described here. Most simulations only used the dark grey coloured region, whereas in some cases also the light-grey area is included, which is always free of pre-existing diapirs. The basal salt layer has a thickness of 3000 m, the overburden has a thickness of 3500 m, and the sticky air layer, which simulates a free surface, has a thickness of 3500 km.

3.4.1 Setups

Rheological parameters of the different layers (Table 3.1) were chosen such that the dominant wavelength of the model is close to the 14-15 km observed in the south-eastern Zagros (e.g. Talbot and Alavi, 1996; Yamato et al., 2011). However, for setup 1, the predicted wavelength is slightly higher than the observed one, see Table 3.1. The predicted wavelength for the used background strain results in considerable folding amplitudes after less than hundred time steps (around 0.45 Myrs), and around 120 timesteps for setup 2 (6 Myrs).

The wavelength versus growthrate diagrams of setup 1 and 2 (Figure 3.3) have a maximum growthrate at wavelengths 16.58 km (setup 1) and 14.62 km (setup 2). In addition, the growthrate diagrams show that wavelengths with positive growthrate reach up to ~40 km (setup 1) and ~20 km (setup 2).

It is known from previous work that the initial random noise controls the final 3D folding patterns (e.g. Fernandez and Kaus, in press; Schmid et al., 2008). We therefore used the same initial random noise in all simulations (with and without salt diapirs).

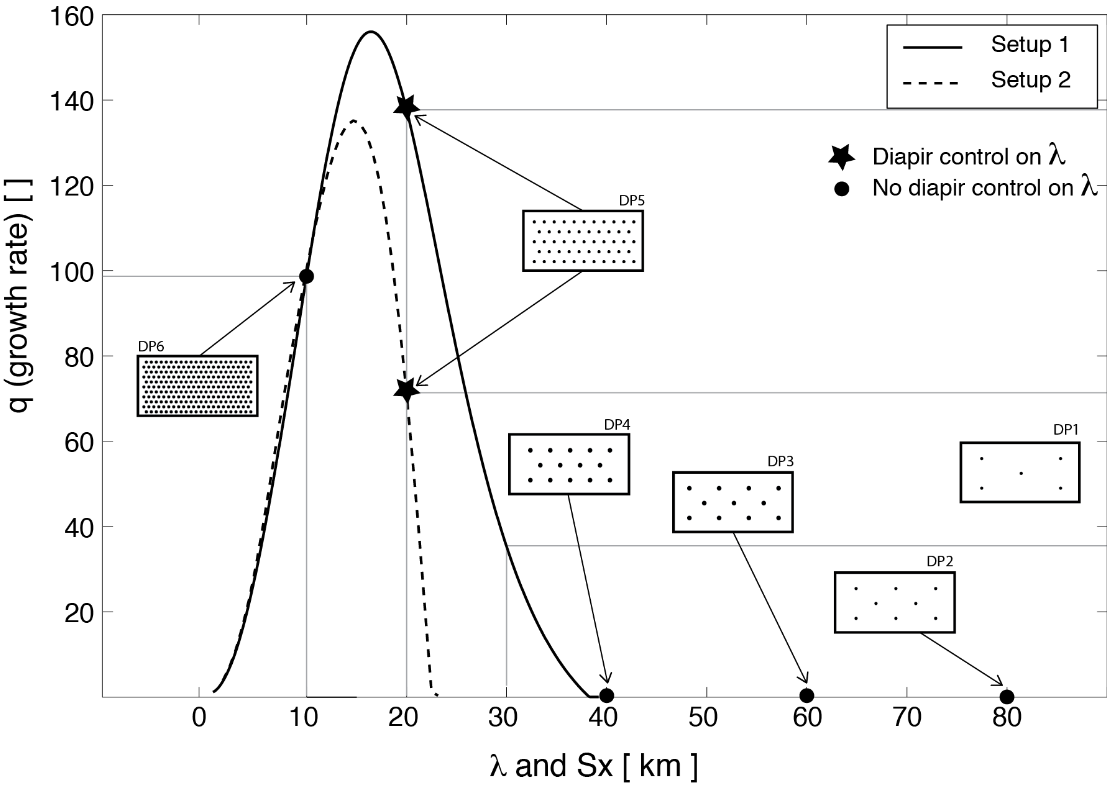

Figure 3.3. Folding growth rate (normalized over background strain rate) versus wavelength calculated with a semi-analytical solution for the multilayer setup 1 and 2 (see parameters in Table 3.1). Setup 1 has a dominant wavelength of 16.58 km and setup 2 a wavelength of 14.62 km and a slightly smaller growthrate (see Table 3.2). The dominant wavelength amplifies faster than all other wavelengths and is therefore expected to develop in nature. Diapir distribution (see Figure 3.4) positions in the growth rate graph are indicated according to their spacing in x directions. Pre-existing diapirs control fold spacing only in cases in which the diapir spacing is slightly larger than the dominant folding growthrate.

Random noise was added by perturbing the position of the particles close to the salt-overburden interface, resulting in a random perturbation of the interface with maximum amplitude of 100 meters.

Two different resolutions have been used in this work: 256x256x200 cells for a domain of size 240x240x10 km and 256x128x200 cells for a reduced domain of 240x120x10 km correspondingly. These resolutions and domain sizes result in grid size of 1 km x 1 km in the horizontal directions. Reduced domain simulations correspond only to setup 1, where all the diapir distributions have been tested. The full domain, which required the use of more computational resources, was used for certain diapir distributions only. The high resolution in vertical direction is required to properly track the random noise from which the fold instabilities develop. For each the model domains sizes and rheological setups, we have performed a pure folding simulation as comparison for the runs with pre-existing salt plugs.

The number of iterative Krylov solver iterations varies from 100-200 per time step for the folding-only simulations, to 200-400 iterations per time step for setups in which salt plugs are present. The increase in number of iterations is due to the high viscosity contrast in lateral directions.

Pre-existing salt diapirs are modelled as circular plugs that are added to the setup of Figure 3.2. These salt plugs are of cylindrical shape and rise from the basalt salt layer to a given height, and they have the same material properties as the basal salt layer. In the reduced domain, diapirs were widely distributed across the modelled domain, whereas in the case of the full domain, the diapirs were only added in half of the domain (see Figure 3.2), to check how folds propagate into the other half of the domain.

We varied the height and diameter of diapirs as well as their distribution.

3.4.2 Diapir height

The diapirs in south-eastern Zagros are exposed at different stratigraphic levels (Callot et al., 2012). In some of our simulations we keep the diapirs always buried, whereas in other simulations some of them are exposed at the surface. For the buried diapirs we have chosen their height such that they are always just below one of the competent layers in the overburden (Figure 3.2). As a result, the used initial height of the diapirs is 3500, 4000, 4500, 5000, 5500 and 6000 meters, implying that they are at least 500 meters above the initial salt surface.

3.4.3 Diameter of the diapirs

As discussed, the diameter of diapirs in the south-eastern Zagros varies widely. In our numerical models we need to employ a minimum diapir diameter to ensure that they are numerically well resolved. We therefore varied the diapir diameter between 4, 6 and 8 km. An initial simulation was done accounting for all the combinations of diameters and height of diapirs using the above-mentioned values. For most of the other simulations with regular diapir spacing, we employed a diameter of 4 km.

3.4.4 Spacing of the diapirs

We tested the effect of diapir spacing by using a fixed spacing in x- (referred as Sx) and y-direction (referred as Sy) which results in the regular patterns of Figure 3.4. In order to test a tighter spacing in the x-direction (parallel to compression), each second row of diapirs was offset in relation to the previous one. The offset (referred as Sxo) causes the spacing in y-direction to be half of the defined one. The regular patterns used in the simulations (Figure 3.4) will be referred to as diapir distribution 1 (DP1) to diapir distribution 6 (DP6). DP1 denotes the distribution with the highest spacing in the x directions, and DP6 the one with the smallest spacing in x direction (Figure 3.4). In simulations with diapir distributions DP1 to DP6, both height and diameter of diapirs are kept constant with a height of 5 km and a diameter of 4 km. In simulations with diapir distribution DP4b, both diapir diameter and height were varied.

3.4.5 Zagros like spacing

The diapir distributions DP1 to DP6 have regular spacing of the diapirs in x and y directions. However, in south-eastern Zagros, although there is an overall spacing close to 20 km or smaller (12 km in the area delimited by the rectangle in Figure 3.1) this spacing is not constant over the area. Therefore, we also test a more realistic diapir distribution and for that purpose we reproduced the distribution of the exposed salt outcrops of Figure 3.1. This Zagros-like diapir distribution is named DPZagros and can be seen in Figure 3.4. In DPZagros, not only the position of the diapirs is changed but also the size of the diapirs within the study area. However, for simplification we have assumed that all diapirs are circular in shape. Diapirs with a radius below < 2 km have been assigned a 2 km radius which ensures that we can numerically resolve them. In diapir distribution DPZagros all diapirs are buried and have a height of 5 km (as in diapir distributions from DP1 to DP6). An additional simulation where the diapirs were either exposed or buried according to the recent work of Jahani et al. (2007) has also been performed and is referred to as DPZagrosExp (Figure 3.4).

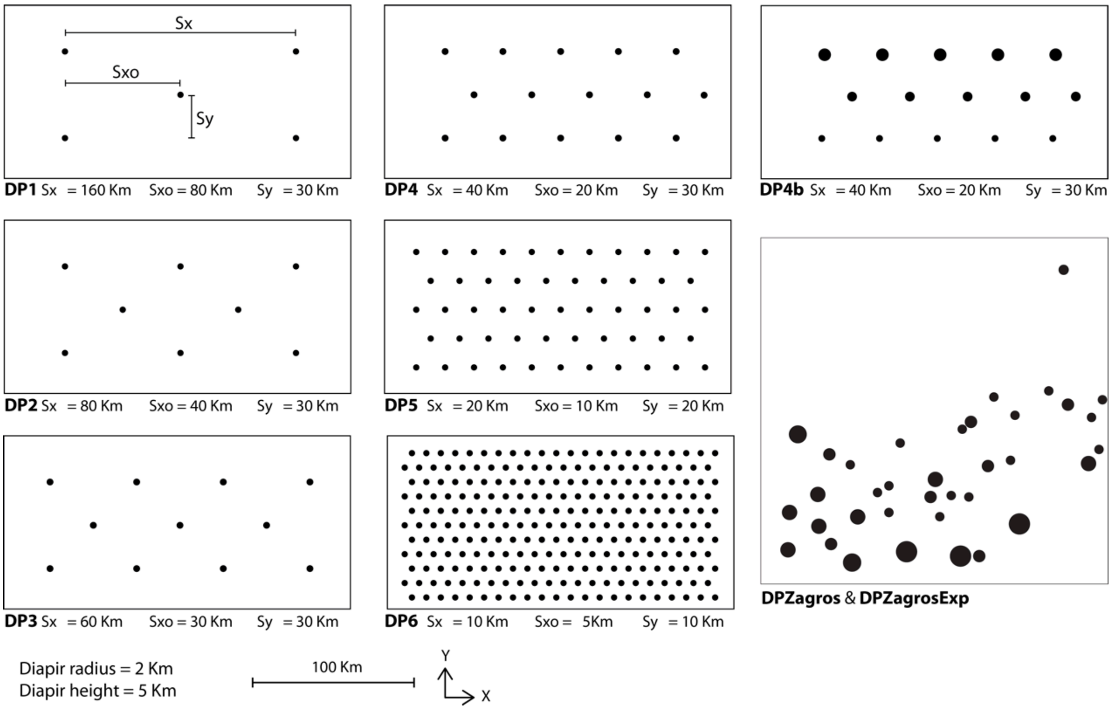

Figure 3.4. Diapir distribution patterns (referred as DP in this work) that are added to the multilayer setups 1 and 2 in the different numerical simulations. The corresponding spacing in X (Sx and Sxo) and Y (Sy) directions is indicated. DPZagros and DPZagrosExp represent the present day diapir distribution in the area of the rectangle in Figure 3.1.

3.5 Results

3.5.1 Folding only

Reference setup 1 (see Table 3.1) was performed in both the reduced and full domain. Results of the full domain simulations are shown in Figure 3.5a. This setup did not contain salt plugs/diapirs and was run for around 90 time steps, which represents ~0.4 Myrs. The folds start to amplify at approximately the same time across the domain (Figure 3.5a). After 0.4 Myrs and a shortening of around 12%, the approximate wavelength of 15 km is clearly visible, with fold amplitude of 1200 meters. Initially, a few folds start to amplify, usually in a group of one anticline with a syncline to each of the sides. Amplified fold segments have a length varying from 10 to 20 kilometres, resulting in an initial aspect ratio of the folds that ranges between 0.5 and 1.5. However, with ongoing deformation, those fold segments link with other segments which, depending on their position with respect to each other, results in long straight folds (due to linear linkage) or sinuous folds (due to oblique linkage). At the end of the simulation, the fold pattern looks quite complex even if the dominant wavelength of folds is in most cases close to the expected one (Figure 3.5a).

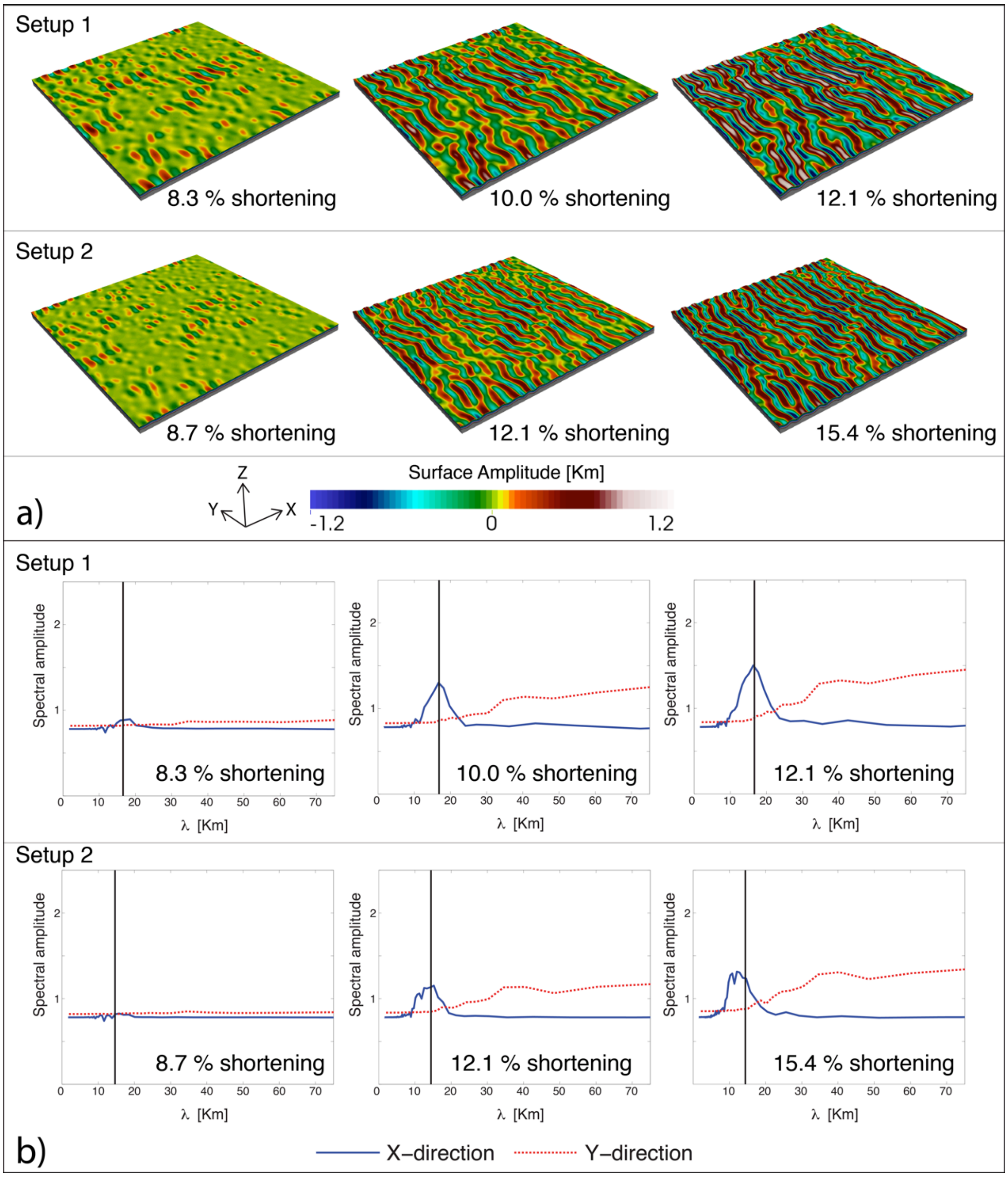

Figure 3.5. a) Snapshots of the reference folding simulations of setup 1 and 2 without pre-existing diapirs at different shortening stages. b) Measured spectral amplitude of the topography for setup 1 and 2 (folding reference simulations) at different shortening stages. Vertical black line indicates the dominant wavelength. In all cases, the spacing of folds in the x-direction is close to that of the dominant wavelength.

A similar simulation, with no initial diapirs, was performed for setup 2 (see Table 3.1), which uses slightly different material parameters. In this case, the simulation was run for about 120 timesteps, which represents around 5 Myrs or a shortening of around 15 %. The amplification of folds occurred slightly later and the amplitude is overall smaller than in setup 1 (see Figure 5a), even though still considerable amplitudes of around 1000 m are reached after 15 % shortening.

The wavelength of the folding simulations of setup 1 and setup 2 is controlled by the parameters shown in Table 3.1, and was measured with a spectral analysis of the topography (see Figure 3.5b). Before the folds start to amplify dynamically there is some pure shear shortening (more pronounced in setup 2, which has a lower growth rate). It is not until a shortening of around 10% that the selected wavelength is the prevalent signal in the x-direction in the spectral graphs (Figure 3.5b). The spectral analysis in Y direction (orthogonal to compression) shows no clear peak in the graph (Figure 3.5b), implying that there is not a clear aspect ratio of folds present in the topography. The lack of a unique folding aspect ratio is also evident by visual inspection of the topography of simulations in Figure 3.5a.

3.5.2 Diapir distribution and folding patterns

The wavelength predicted for the given parameters of setup 1 and 2 is 16.58 and 14.62 km respectively. The diapir-absent folding simulations indeed develop the predicted wavelength as shown by the spectral analysis of the topography (Figure 3.5b). Next, we study how the final wavelength compares to the spacing of the diapirs when diapirs are present. For this purpose, the areas with pre-existing diapirs were compared to the ones without diapirs.

The following observations are valid for all simulations with pre-existing diapirs. The deformation starts to localize where the salt plugs are, by initially doming the area above the diapirs. With ongoing shortening, these initial folds grow rapidly in the lateral direction (y direction) developing into elongated folds. The next folds that form in the direction orthogonal to compression are the ones adjacent to the ones above the diapirs. In diapir-absent areas, folds develop last.

The specific folding patterns that form in the simulations as the diapir spacing is decreased from DP1 to DP6 are explained next.

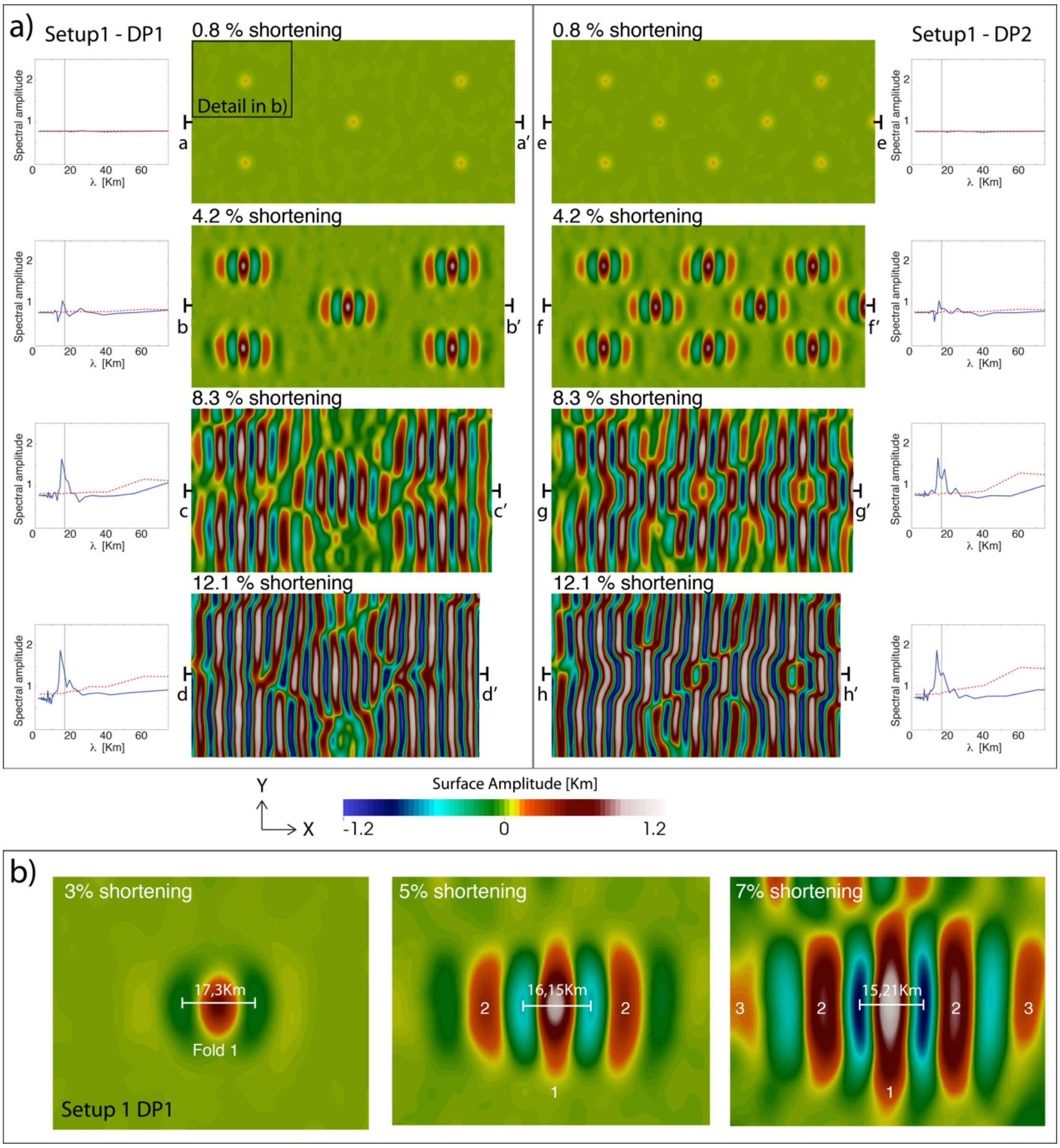

Figure 3.6. a) Map view and spectral analysis of the topography of simulation in the reduced initial domain (240x120x10 km) of Setup 1 with diapir distributions DP1 and DP2. Letters a-h indicate the traces of cross sections shown in Figure 3.7. b) Zoom-in on one fold that localizes above a diapir in Setup 1, DP1. Note the decrease of wavelength with increasing shortening.

Diapir distribution DP1, and DP2, have only been used in setup 1 simulations using a reduced domain. The reason is that the minimum spacing between the diapirs (160 km and 80 km for Sx) is already much larger than dominant wavelength of setup 1 (see Figure 3.3) and unlikely to be of controlling importance for the folding instability. Results show that compared to simulations without diapirs, amplification localizes above the diapirs and is larger during earlier shortening stages (see map views in Figure 3.6a and cross-sections in Figure 3.7). The insets with the spectral amplitude

(Figure 3.6a) show that after 4% of shortening the initial peak of the graph is only slightly smaller than the dominant wavelength. With ongoing shortening, the peak in the spectral signal becomes more prominent and clearly smaller than the dominant wavelength, which is likely caused by the higher amplification velocity than in the folding-only simulation. We try to illustrate this effect in Figure 3.6b, where a detail of setup 1 with DP1 is shown. Deformation localizes above the diapirs, where the initial fold nucleates (number 1 in Figure 3.6b) and it forms two adjacent synclines after a shortening of 3%. The measured wavelength at this stage is close to the predicted one. After 5% shortening, two new anticlines (number 2 in Figure 3.6b) on both sides of the fold above the diapir are clearly visible, and the measured wavelength is already decreasing due to the shortening. The initial fold has also grown laterally and is therefore more elongated. After 7%, new anticlines (number 3) have formed adjacent to the last ones (number 2). The previously formed anticlines are more elongated due to the lateral growth as well. The higher amplification velocity causes folds to form earlier and therefore their wavelength can be kinematically decreased earlier as well, as it can be seen in Figure 3.6b. This process illustrates how the bulk fold structure grows in the compression direction by sequential formation of new folds and not only by the amplification of the initial fold above the diapir. The effect of sequential folding on the overall bulk shortening has been recently described and quantified by (Frehner, submitted).

Cross sections that correspond to setup 1 simulation with DP1 and DP2 (Figure 3.7) show that the pre-existing diapirs have accommodated the fold in their position, however, due to the significant spacing between the diapirs, many folds can form in between diapirs.

DP3 is also only tested in setup 1 (Figure 3.8), as the diapir spacing (Sx = 60 km, Figure 3.4) is well outside the folding growthrate diagrams of both setups 1 and 2. However, Sxo is 30 km, and lies within the growthrate diagram of setup 1. As in the previous runs, the initial folds are localized above the diapirs. However, the diapir spacing of 60 kilometres, allows for two additional folds to develop between two diapirs that will have a wide syncline in between them. Due to the offset and position of the diapirs, it is the folds adjacent to the diapirs in X direction the ones that link together in an oblique manner (Figure 3.8). The initial folds formed above the diapirs are locked in their lateral propagation (Figure 3.8).

DP4 diapir distribution has Sx of 40 km with an offset or Sxo of 20 km (Figure 3.4). While the spacing of 40 km lies outside growthrate graphs of setup 1 and 2 (Figure 3.3), the spacing of 20 km lies above both graphs and therefore it has been tested in both setups. The growthrate diagrams of setup 1 and 2 show significantly different growthrates for wavelengths longer than 10 kilometres. A wavelength of 20 km would be close to the dominant growthrate in setup 1 (see Figure 3.3) and there is space for one sequential fold to form between the diapirs separated by 40 km. The sequential fold is aligned with other folds above diapirs and therefore they will link linearly (see Figure 3.8). The result is that diapir spacing of 20 km (Sxo) is slightly controlling the fold wavelength. This can also be observed in the spectral graph of the topography (see Figure 3.8) that shows an initial peak at spacing of 20 km after 4.2% of shortening.

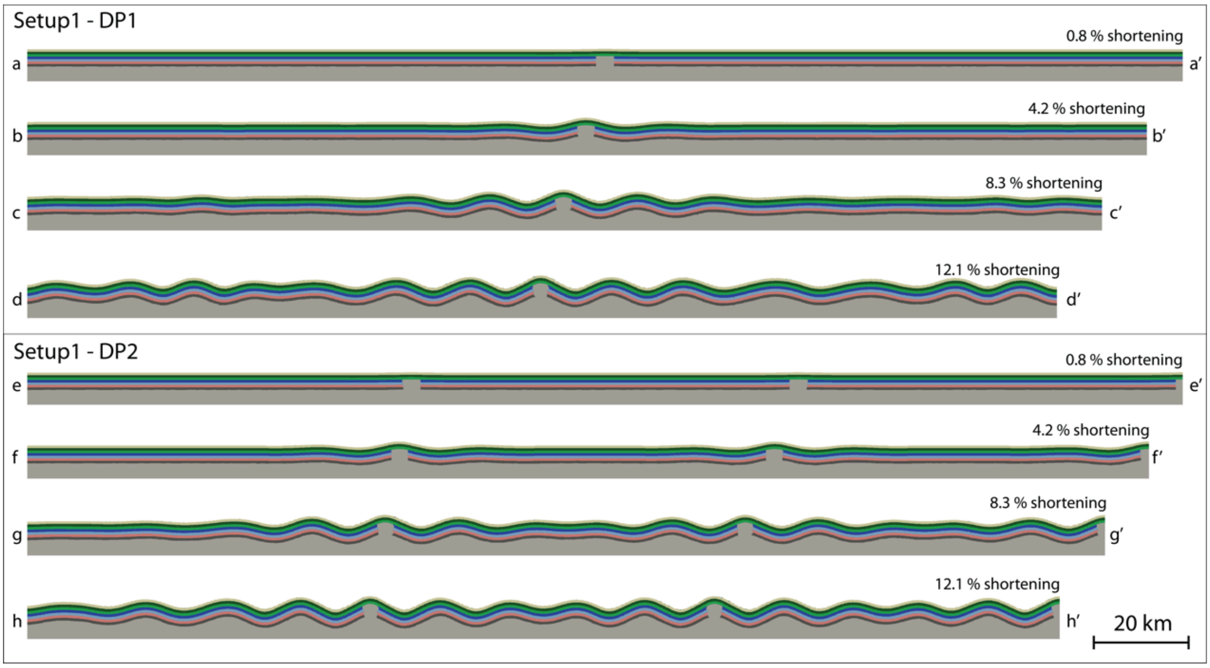

Figure 3.7. Cross sections along the X axis of setup 1 with diapir distributions DP1 and DP2 (initial length is 240 km). Location of the cross sections is indicated in Figure 3.6 with letters a to h. We see that after 4% of shortening, the initial folds has already localized above the diapirs, and two adjacent anticlines to each side of the initial fold are starting to develop.

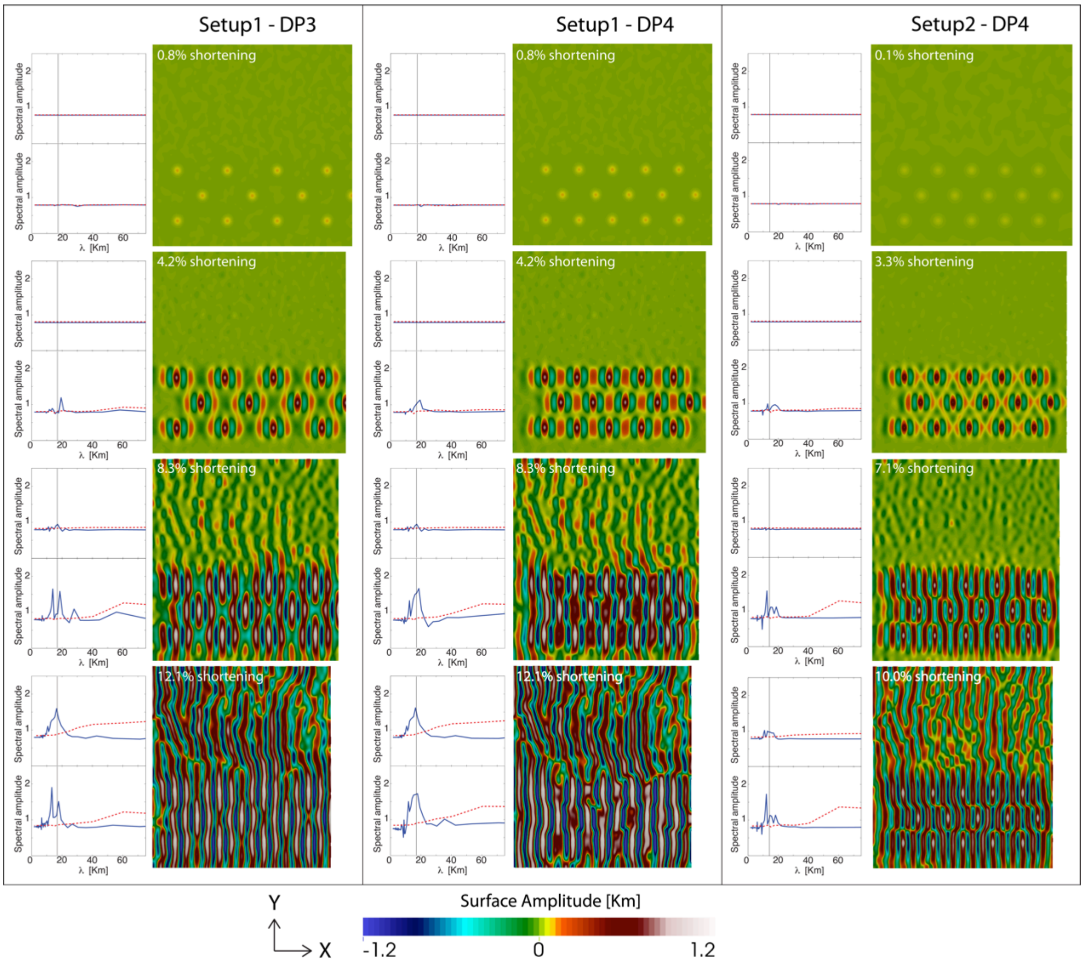

Figure 3.8. Map view and spectral analysis of the topography of simulations in full domain (240x240x10km) of Setup 1 and Setup 2 with diapir distributions DP3, and DP4 in the lower part of the domain. Folds initiate in the area where pre-existing diapirs are present and later propagate into the diapir-absent area. The spectral analysis is shown for both the diapir-absent (top) and diapir-present areas, and shows that folds have a wavelength that is closer to the dominant folding wavelength if diapirs are absent (continuous blue line).

Diapir distribution DP4 in setup 2 results in a completely different fold pattern than in setup 1 (Figure 3.8) although the predicted fold wavelength differs by no more than two kilometres (Figure 3.3). At the beginning of the simulation of setup 2, only one fold forms between the diapirs and it has a wavelength equivalent to Sxo (20km) as in setup 1. At 3.3 % of shortening, the fold between the diapirs splits into two folds of smaller wavelength and higher growthrate and closer to the dominant one (Figure 3.8). The effect of fold splitting can also be observed in the spectral analysis of the topography: at 3.3% shortening there is a strong peak at 20 km wavelength, which is later overtaken by a peak at a smaller wavelength (Figure 3.8).

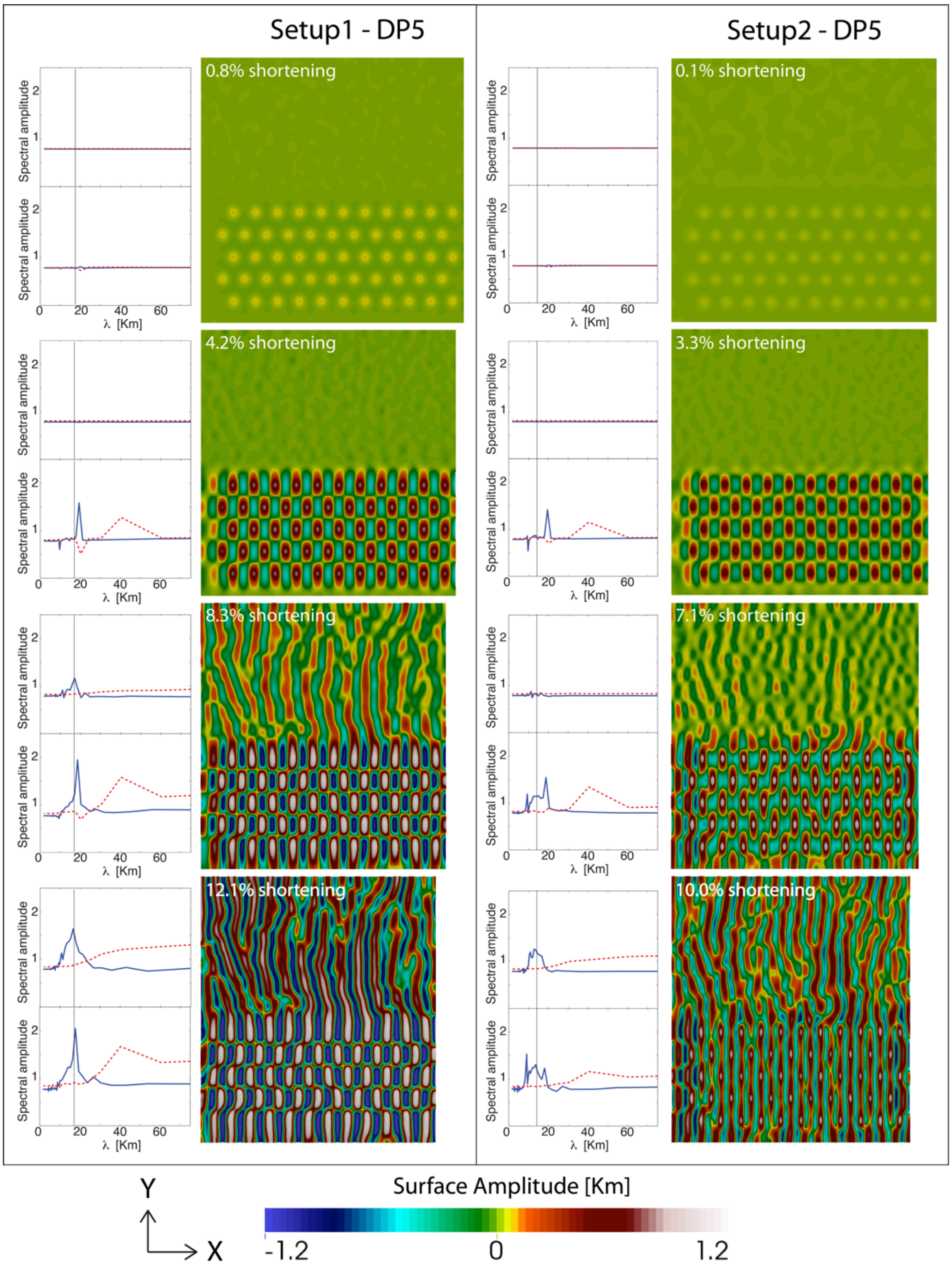

Figure 3.9. Map view and spectral analysis of the topography of simulations in full domain (240x240x10km) of Setup 1 and Setup 2 with diapir distributions DP5 in the lower part of the domain. Folds initiate in the area where pre-existing diapirs are present and later propagate into the diapir-absent area. The spectral analysis is shown for both the diapir-absent (top) and diapir-present areas, and shows that folds have a wavelength that is closer to the dominant folding wavelength if diapirs are absent (continuous blue line). Note that the spectral analysis in y-direction (dashed red line) shows also a peak at 40 km in both Setup 1 and 2 that corresponds to the length of the folds which is also controlled by the diapir spacing.

DP5 is a distribution with a diapir spacing Sx of 20 km and an offset spacing Sxo 10 km. For setup 1, 20 kilometres spacing has a higher folding growth rate than 10 kilometres spacing (Figure 3.3). Interestingly, in DP5 simulation, folds start to localize above the diapirs giving rise to a clear wavelength of 20 km in accordance with the diapir spacing (Figure 3.9). The position of the fold segments in relation with the diapir offset prevents the folds from propagating linearly, and a constant length of folds of around 40 km develops (see also spectral analysis in Y direction in Figure 3.9).

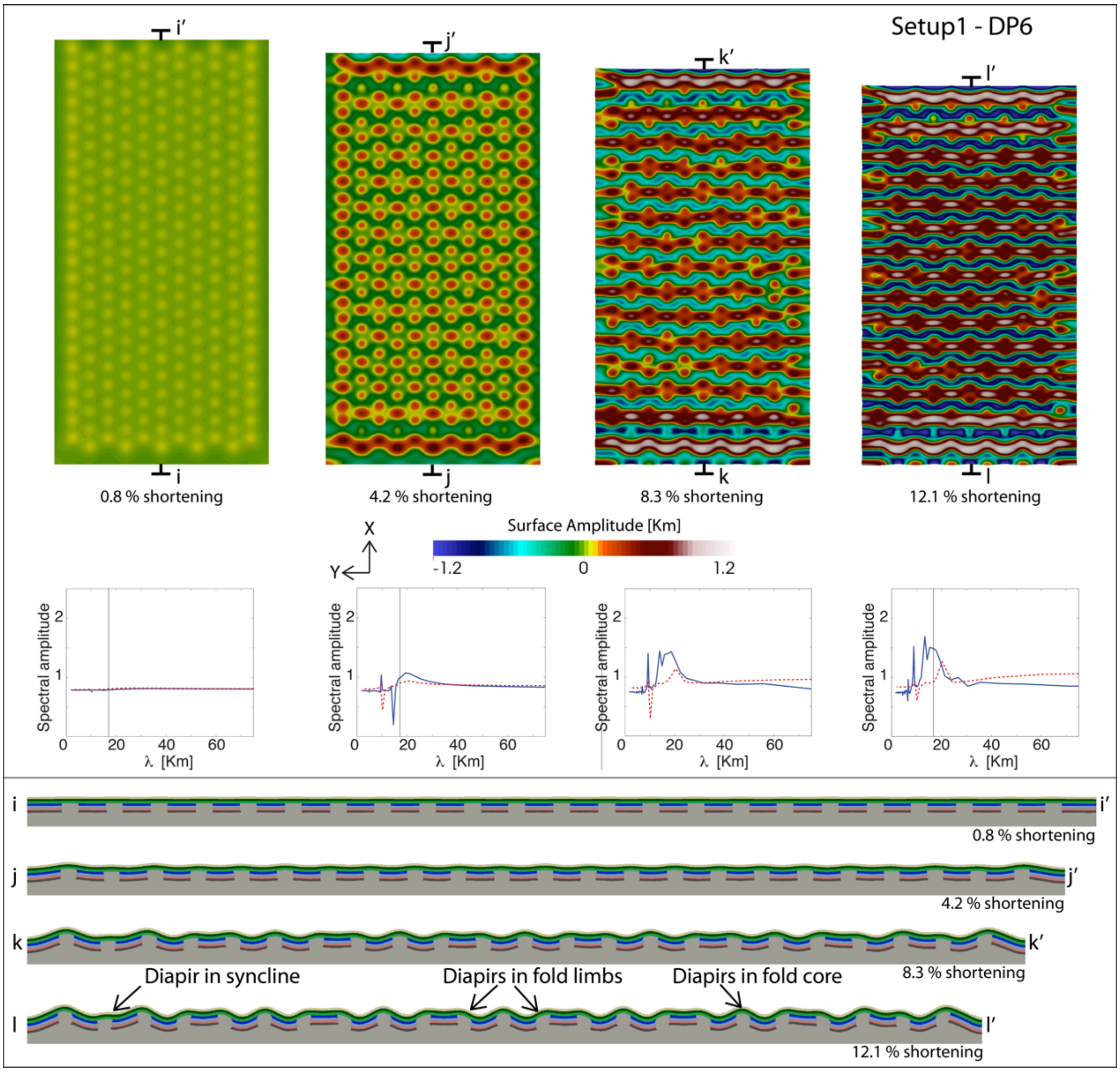

Figure 3.10. Map view and spectral analysis of the topography of simulation in reduced domain (240x120x10km) of Setup 1 with diapir distributions DP6. Spectral analysis shows a strong signal at the predicted wavelength, and peaks at smaller wavelength corresponding to diapir spacing. Cross sections at the indicated traces in the map views and named with letters i to l are shown in the lower panel. Note the position of diapirs in fold cores, synclines and fold limbs.

DP6 is the diapir distribution with the smallest spacing in both X and Y direction (10 kilometres) and with an offset of 5 kilometres in X. Neither 5 nor 10 kilometres are wavelengths close to the dominant wavelength (Figure 3.3). As in all the simulations, however, deformation starts to localize above the diapirs (Figure 3.10). Since the folds cannot be accommodated in between the tightly spaced diapirs, folds form by amplification of pairs of diapir rows together, forming straight topographic highs, which have irregular shapes due to the diapirs (Figure 3.10). The folds that form have a wavelength that is close to the dominant folding wavelength. Yet, the diapir spacing is also noticeable in the spectral graph that shows a peak at 10 km (Figure 3.10).

One general observation that is valid for all simulations with pre-existing diapirs is that folds start to develop earlier in the area where the diapirs are present. This results in a clear differentiable characteristic between the areas with and without diapirs. The areas where the pre-existing diapirs are present have folds with higher amplitudes and in general a higher average elevation if we consider the topography (see Figure 3.8 and Figure 3.9). Another observation is that folds are more straight (less sinuous) in an area where diapirs are present (south/lower part of simulation domain) than in the area without diapirs (see Figure 3.8 and Figure 3.9).

The simulations with regularly spaced diapir distributions show that whether the folding wavelength will be controlled by diapir spacing or not, depends on how the Sx spacing compares with the (dominant) growth rate of the folding instability. We can summarize this control in the following three cases: 1) If the diapir spacing is larger than but close to the dominant wavelength, the folding wavelength is controlled by the diapir spacing. 2) If the diapir spacing is smaller than the predicted wavelength, even if it is close to it, the wavelength that develops will be the dominant folding wavelength. 3) When the spacing between the diapirs Sx is sufficiently large such that several folds of dominant wavelength can be accommodated in-between diapirs, the resulting folding wavelength is indirectly controlled by the diapirs and can be calculated as:

$$\lambda = \frac{S_x}{N_{folds}}$$

where N_{folds} is the number the of folds that can be accommodated between two diapirs which can be calculated as:

$$N_{folds} \approx \frac{S_x}{\lambda_{dom}}$$

However, the number of folds that forms between two diapirs depends also on the growthrate of the wavelength. The wavelength that can be accommodated between two diapirs can in certain cases change with strain. Table 3.2 shows the calculated wavelength (maximum and minimum) that can be accommodated between the diapirs. With diapir distribution DP3 the number of folds that can form between two diapirs is either 3 or 4 with wavelengths of 20 and 15 km respectively (see Table 3.2). The growthrate of the 15 km wavelength is larger than the one of 20 km in setup 1 (see Figure 3.3) and therefore this is the wavelength that is predicted to develop. The numerical simulation of setup 1 with DP3 shows that initially only 3 folds are accommodated between diapirs, by forming 2 anticlines that are separated by a wide syncline (Figure 3.8). As shortening continues, the folds above the diapirs grow laterally into the synclines, such that at the end the wavelength of 15 km prevails in the domain. The same phenomena can be observed for DP5 in setup 2. In this case, even though the 20 km diapir spacing initially controls the wavelength, the wavelength with the highest growthrate is 10 km and it is the one that prevails (Figure 3.9).

Table 3.2. Predicted folding wavelength for the different diapir distributions.

		SETUP 1						SETUP 2					
			Maximum number of folds		Minimum number of folds				Maximum Number of folds		Minimum number of folds		
	S_X	S_x/λ_{dom}	N_{folds}	λ	N_{folds}	λ	λ with max q	S_x/λ_{dom}	N_{folds}	λ	N_{folds}	λ	λ with max q
	[km]	[]	[]	[km]	[]	[km]	[km]	[]	[]	[km]	[]	[km]	[km]
DP1	160	9.65	10	16	9	17.78	16	10.94	11	14.55	10	16	14.55
DP2	80	4.83	5	16	4	20	16	5.47	6	13.33	5	16	13.33
DP3	60	3.62	4	15	3	20	15	4.1	5	12	4	15	15
DP4	40	2.41	3	13.33	2	20	SAME	2.74	3	13.33	2	20	13.33
DP5	20	1.21	2	10	1	20	20	1.37	2	10	1	20	10
DP6	10	0.6	1	10	0	5	10	0.68	1	10	0	5	10

Fold patterns, however, do not only depend on the diapir spacing in x direction Sx, but also on Sy and Sxo, as these two parameters control the interactions between different fold segments. It is known from analogue modelling that fold propagation is locked when the offset in the compression direction is half the wavelength of the folds (Dubey and Cobbold, 1977). In that case, folds do not link with other fold segments but rather develop rapidly plunging terminations. When the offset distance is smaller than half the wavelength, the fold segments will link together in an oblique manner. This locking of lateral growth can be seen in our simulations. One example is found in Setup 1 with diapir distribution DP5 (in Figure 3.8), where fold wavelength is controlled by Sx and fold aspect ratio by Sy and Sxo. Another example of lateral growth locking is observed in Setup 2 with diapir distribution DP4 (Figure 3.8), where the folds that form above the diapirs in the middle row (in Y direction), are locked and do not grow laterally. As can be observed in most of the simulations, it is mainly the second generation of folds, adjacent to diapirs, that interact with other fold segments initially (see for example DP3 and DP4 simulations in Figure 3.8). On the contrary, the initial folds that develop above the diapirs do not initially link with other segments. However, after a certain amount of shortening, the first generation of folds will also interact with other segments (see DP4 in Figure 3.8 after 7% of shortening).

3.5.3 Diapir height and diameter

So far, all diapir distributions that have been tested (DP1 to DP6) had varying Sx, Sxo and Sy spacing but the same height and diameter in all diapirs. Next, we test the effect of varying diapir diameter and height on the vertical velocity above diapirs or at the topographic surface and evaluate their influence on the folding pattern. For this purpose, we used one new diapir distribution (DP4b) in setup 1, where spacing is equal to DP4 but the diameter and height of the diapirs are varied (Figure 3.4). The surface velocity and wavelength of the folding above the diapirs was measured after one time step corresponding to a shortening of 0.8%. Results are shown in Figure 3.11.

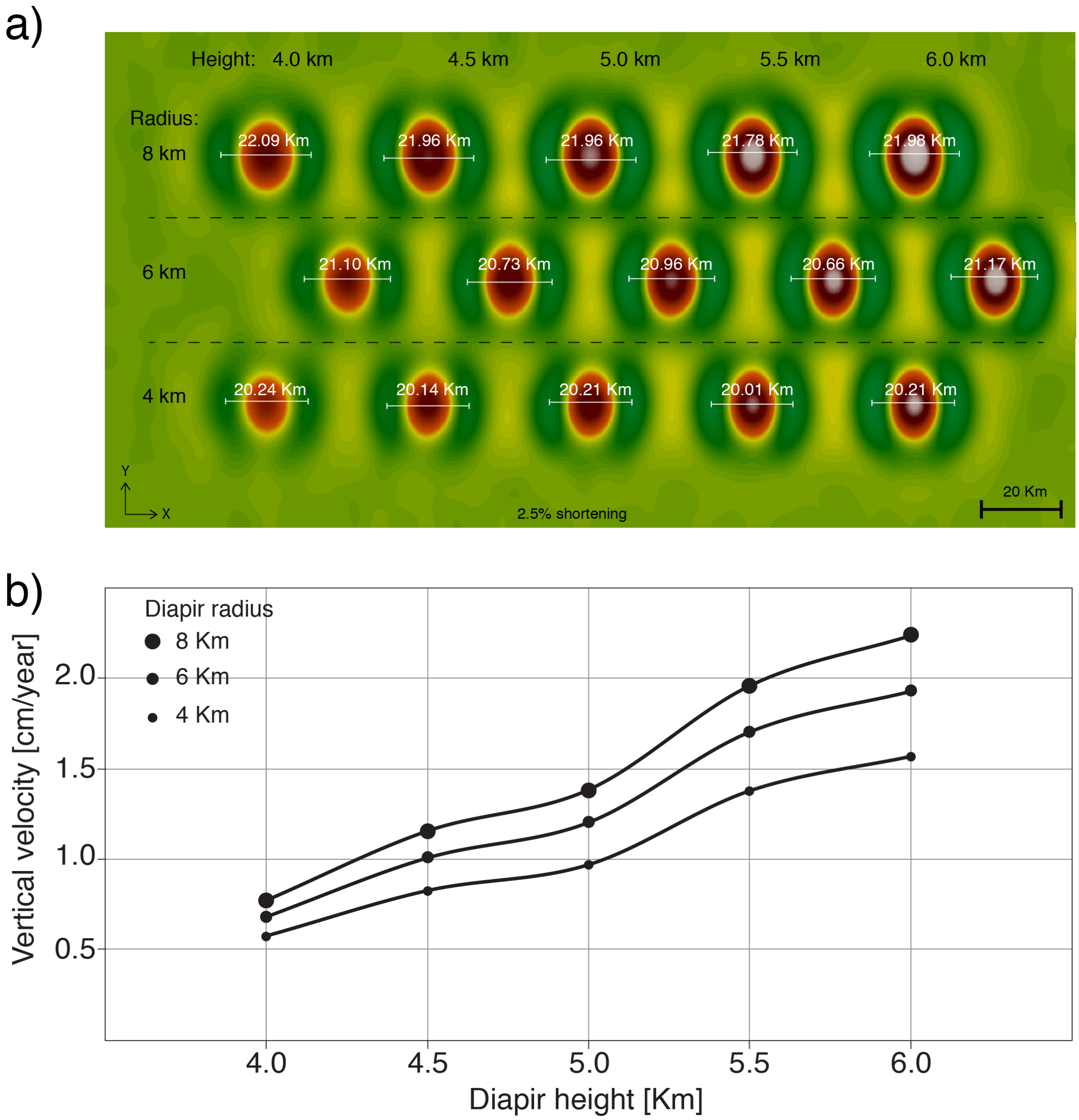

Figure 3.11. a) Wavelength of folds above diapirs after 2.5% shortening in setup 1 simulation with DP4bis diapir distribution. The uppermost row of diapirs has a larger radius and results in folds with a larger wavelength. b) Effect of diapir height and diameter on vertical velocity at the surface above the diapirs after one time step of setup 1, DP4bis.

The closer the diapirs are to the surface, the higher the initial vertical surface velocity is (Figure 3.11). In addition, it matters whether the diapirs are directly below a strong or a weak layer (Figure 3.11b). Diapirs that end beneath a strong layer have a linearly increasing velocity above the diapir. Diapirs that end below weak layers do not have such linear tendency, as the weak layers take up part of the deformation. The wider the diapir diameter is, the larger the vertical surface velocities.

After 2.5% shortening, the adjacent synclines that form close to the folds localized above the diapir are clearly visible (Figure 3.11a). We have measured the wavelength of each of the initial folds as the distance between the surrounding synclines (Figure 3.11a). While the height of the diapir does not have an effect in the wavelength of the folds at the surface, the diameter of the diapir itself does have an effect: the wider it is, the wider the wavelength of the fold that develops at the surface. This is important, because as we can see from Figure 3.1, the diapirs that outcrop in the Zagros show a wide range of diameters. The difference in fold wavelength above the diapirs could therefore potentially result in different fold patterns as the offset between folds in X direction can either promote linkage of laterally growing fold segments or can block them from growing.

3.5.4 Zagros like diapir distribution

So far we have tested regularly spaced diapir distributions with synthetic setups. Yet, even though the present day distribution of diapirs in the south-eastern Zagros shows a prevalent distance between the diapirs of about 18 to 20 km, there is no regular spacing in the compression or orthogonal direction. It is thus interesting to perform simulations with a diapir distribution that is close to the one of the present day south-eastern Zagros. As mentioned, the diapirs in the area might have been close to or exposed at the surface at the onset of folding (Jahani et al., 2007). Yet, for simplicity reasons we kept the diapir height constant at 5 km. We did vary the diapir diameter by scaling it with the outcropping area of the exposed diapir in the Zagros.

Results show that the fold-patterns in the two simulations corresponding to Setup 1 and 2 show a very similar folding pattern in locations where diapirs are present (Figure 3.12), even though the fold amplitude is different. There are, however, some changes with respect to which fold segments link to form long folds. In setup 2, these folds are more sinuous and slightly shorter. When the diapirs are wide and after a certain amount of shortening, the fold growthrate decreases, and there are cases where the roof above the diapir sinks in setup 2 (see Figure 3.12).

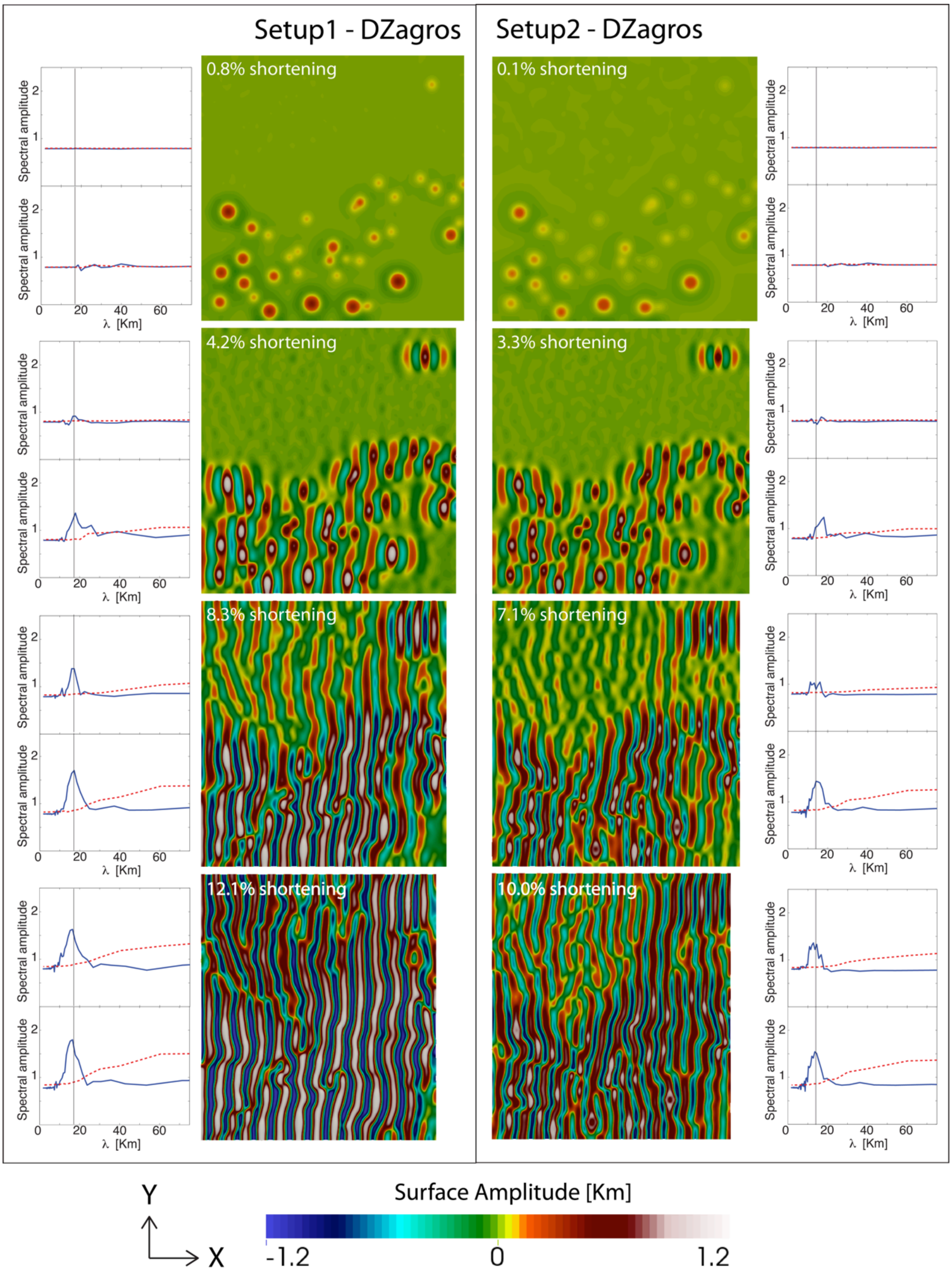

Figure 3.12. Map view and spectral analysis of the topography of simulations in full domain (240x240x10km) of Setup 1 and 2 with a Zagros-like diapir distribution. As with the synthetic setups, folds initially form in regions with pre-existing diapirs after which they propagate to other domains. The spectral analysis in X direction (continuous blue line) shows that the areas with diapirs and the area without diapirs show a wavelength very close to the predicted fold wavelength.

Next, we have focused on setup 2 and tested one simulation with exposed diapirs. The diapirs that are exposed in the simulation correspond to the diapirs that are indicated as having had their activity before the onset of Zagros folding by Jahani et al. (2009). It must be considered that other diapirs could have also been exposed at the surface or very close to it. Exposed diapirs in the simulation also localize the initial deformation, but in addition part of the salt is extruded above the topographic surface (Figure 3.13). Because salt is extruded above the folded surface, it can also flow laterally (Figure 3.13), which is more noticeable in the flanks of the folds (cross-sections *I-I'* and *III-III'* in Figure 3.13).

As in the simulations with a regular diapir distribution, the setup with Zagros-like diapir spacing has a higher mean elevation in areas with pre-existing salt diapirs.

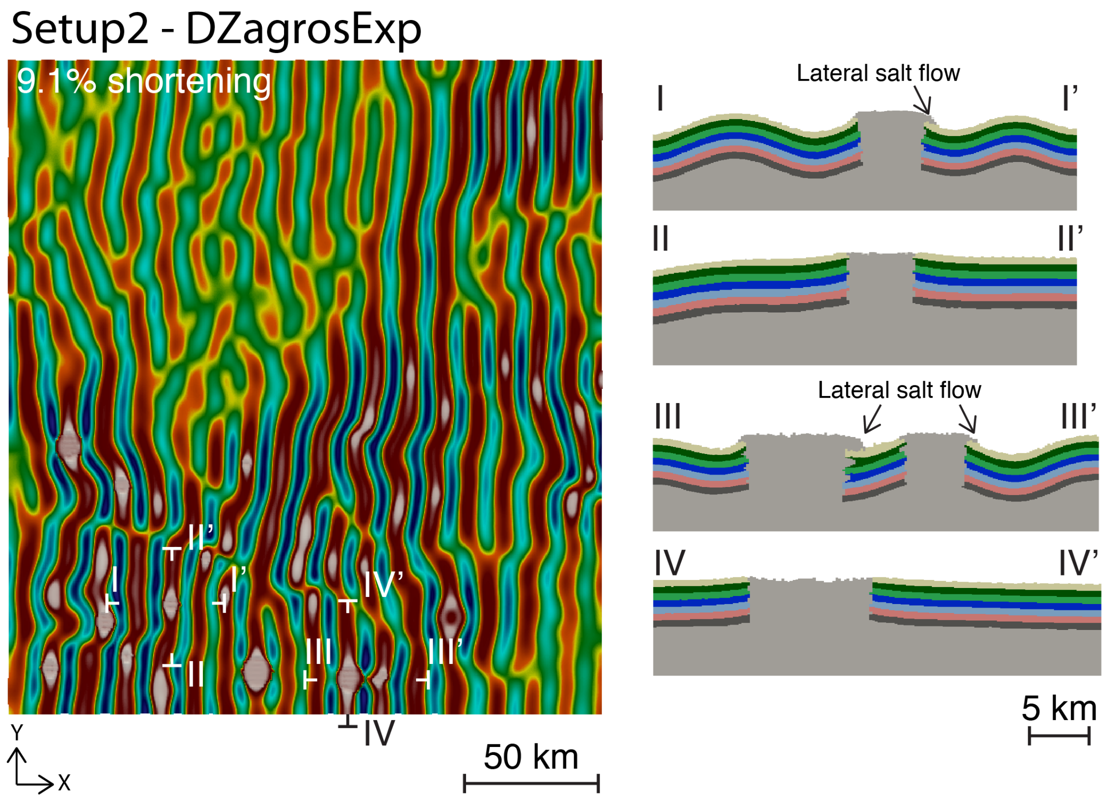

Figure 3.13. Map view of the topography of simulation in full domain (240x240x10km) of Setup 2 with Zagros like diapir distribution, including initially exposed diapirs, after 9.1% of shortening. Cross sections at the indicated positions (I to IV) show the lateral flow of salt along the lateral fold flanks.

3.6 Discussion

The fold trains in the south-eastern Zagros Simply Folded Belt (Figure 3.1) are aligned with the outcropping salt diapirs that appear in most cases in the core of folds or at the periclinal ending of them. This can be explained by the fact that diapir spacing in the area was quite close to the fold wavelength that corresponds to the mechanical stratigraphy in the area. For this reason, there is not a marked change in the wavelength between the area with diapirs and the area without diapirs. In the south-eastern Zagros, there are only few exceptions (< 2%) to the diapirs being located either at the core of folds or at the periclinal closure. One explanation for those exceptions could be that the diapirs were too close together to accommodate a syncline in between. Another example where the diapir position can be explained with the difference between spacing and fold wavelength has been proposed in La Popa basin in Mexico, where one of the diapirs appears in the fold flank at a distance of 7 km from the diapir at the core of the anticline. It was suggested that the reason for this was that the fold wavelength of the sedimentary cover was larger than the separation between diapirs (Rowan et al., 2003).

Previous analogue modelling by Callot et al. (2012) already suggested that the difference between diapir spacing and fold wavelength could explain why some of the diapirs occur in syncline positions. This effect has been systematically studied in our work, by using synthetic distributions of diapirs with fixed spacing that can be compared to the predicted fold wavelength. Our results confirm that when diapir spacing is too small, predicted folding wavelength cannot be accommodated and diapirs will be located in the synclines or fold flanks.

The areas of the simulations that are diapir-absent are areas where the folding instability is driven only by the presence of random noise between the salt and overburden interface. In the absence of diapirs, folding patterns show the usual complexity described in previous 3D folding runs (e.g. Fernandez and Kaus, in press; Schmid et al., 2008). In the area with pre-existing diapirs, however, the fold patterns that develop can be better understood if we compare the results with previous works with initial non-random perturbations (Frehner, in press; Grasemann and Schmalholz, 2012). The pre-existing diapirs play the same role as those perturbations by localizing the initial deformation, and further shortening is accommodated through the development of sequential folds in the compression direction (Frehner, in press). This work illustrates that the number of sequential folds that can be accommodated between diapirs depends on the distance between the diapirs and the folding wavelength. Our results thus confirm that sequential fold growth (Frehner, in press) plays an important role in the linkage of isolated fold structures.

One characteristic feature of the relationship between folds and diapirs in the south-eastern Zagros is that most salt diapirs occur at the periclinal closure of folds, rather than in the core of the folds. In our simulations of non-exposed and exposed diapirs, folds start to localize since the very initial stages above the diapirs. The initial folds are active during the full duration of the simulation, and therefore the diapirs are mainly located in the core of the anticlines and not at their endings. An exception is found in the simulation of Setup1, DP6 (Figure 3.10). In this simulation, some of the diapirs are located at the flanks of long straight folds that show higher culminations above the diapirs along the axial trace of the fold. In their work, Callot et al. (2012) propose that some of the folds related to diapirs might stop amplifying or growing laterally if the diapir walls are welded. In that case folds that are laterally growing close to diapirs stop growing at the location of the welded diapir, which explains why diapirs are located at periclinal closures. In our simulations, we do not observe such welding of the diapirs itself, due to the thickness of the diapirs relative to the thin overburden, but we reckon that this can be a potentially effective process to stop folding amplification. For example when diapirs are exposed at the surface, part of the shortening of the cover is accommodated by salt extrusion both on the surface (Figure 3.13), and into weaker inter-bedded layers at depth (Figure 3.13). This can also potentially delay the onset of folding compared to a setup with non-exposed diapirs.

Our simulations show that diapirs can occur in different structural positions (for example in synclines or fold flanks) when the diapir spacing is much smaller than the dominant fold wavelength. Another mechanism that might contribute to the occurrence of diapirs in synclinal positions of folds are pre-existing thickened stratigraphic sequences around diapirs. In our simulations, we used a simplified setup in which the basal salt layer had a constant thickness. In reality, this layer is likely to have had a more variable thickness and potentially included welded areas caused by lateral withdrawal of salt. In addition, the sedimentary cover can be pushed downwards into the salt layer, if salt intrudes into the weaker layers during ongoing compression. These effects may prevent ongoing folding above diapirs (Callot et al., 2012).

One of the simplifications assumed in our model setup is that the initial salt thickness, regardless on the existence of salt diapirs in the setup, is constant at 3000 m. Of course, this can be argued to be unrealistic, as it would be expected that initial salt would be irregular after the start of halokinetic phase. This implies that there could even be areas with complete salt extrusion and subsequent welding between sedimentary cover and basement that could prevent folds from developing altogether. Potentially we could use a more complex setup, by adding the top of the salt surface obtained from one simulation of salt tectonics. In such simulations, the diapir pattern would be controlled by both the rheological parameters and the sedimentation rate. Analogue modelling of contracted diapirs in which the diapirs are formed previous to contraction as a result of Rayleigh-Taylor overturns, extension, down-building (Koyi, 1988; Roca et al., 2006) results in a more realistic salt topography previous to compression. However, we have chosen the same approach as in Callot et al. (2007) and Dooley et al. (2009), where the salt topography is more or less regular, except for the diapirs. A constant salt layer thickness with pre-existing diapirs as used in our simulation allows for comparison between simulations and fold and growthrate diagrams calculated from thick-plate analysis.

3.7 Conclusions

We have performed several high-resolution numerical simulations to study the influence of pre-existing salt diapirs of varying height, diameter and spacing, on the folding patterns that develop from a compressed multilayer sequence.

Adding pre-existing salt diapirs to simulations of multilayer detachment folding drastically changes the initial fold patterns, as the pre-existing salt diapirs localize the deformation and control where the initial folds will form.

In these cases, the folding wavelength is adapted to fit in between two existing diapirs in the main compression direction. The final folding pattern depends on both the X and Y diapir spacing (Sx and Sy) as well as on the offset between regularly spaced diapir rows (Sxo). When the diapir spacing in the compression direction is close to the dominant folding wavelength, diapir spacing controls the final fold wavelength. In that case, the diapirs are always located in the core of the anticlines (along the compression direction) and below the culminations of the folds, along the strike. Yet, when diapir spacing is too small to accommodate folds in between diapirs, the folding wavelength that develops corresponds to the dominant wavelength and diapir spacing does not control the wavelength. In this case, diapirs can appear at different structural positions with respect to the folds (e.g. synclines and fold flanks). In all the cases, the areas with pre-existing diapirs show at the end an overall higher average elevation than areas without diapirs. This is caused by the fact that folds in areas with pre-existing diapirs form earlier and attain higher amplitudes than folds in diapir-absent areas.

Our results thus show that one can estimate the effect of pre-existing heterogeneities on folding patterns in a straightforward manner, by computing a folding growthrate curve and by comparing the growthrate of heterogeneities with that of the dominant folding growthrate.

Different than in the south-eastern Zagros, our simulations do not result in diapirs that are located at the periclinal or lateral ends of folds (or in saddle areas of long anticlines). This might be because the fold growth rates in our simulations do not allow for sufficient salt to be extruded or because we did not consider surface processes.

3.8 Acknowledgements

Funding was provided by the European Research Council under the European Community’s Seventh Framework program (FP7/2007-2013) ERC Grant agreement #258830. 3D simulations were performed on the IBM Blue Gene/Q JUQUEEN supercomputer of the Forschungszentrum Jülich, Germany and MOGON supercomputer of Johannes Gutenberg University Mainz, Germany.

3.9 References

Ala, M.A., 1974, Salt Diapirism in Southern Iran: AAPG Bulletin, v. 58, p. 1758-1770.

Bahroudi, A., and Koyi, H., 2003, Effect of spatial distribution of Hormuz salt on deformation style in the Zagros fold and thrust belt: an analogue modelling approach: Journal of the Geological Society, v. 160, p. 719-733.

Berberian, M., 1995, Master “blind” thrust faults hidden under the Zagros folds: active basement tectonics and surface morphotectonics: Tectonophysics, v. 241, p. 193-224.

Callot, J.-P., Trocmé, V., Letouzey, J., Albouy, E., Jahani, S., and Sherkati, S., 2012, Pre-existing salt structures and the folding of the Zagros Mountains: Geological Society, London, Special Publications, v. 363, p. 545-561.

Callot, J.P., Jahani, S., and Letouzey, J., 2007, The Role of Pre-Existing Diapirs in Fold and Thrust Belt Development, *in* Lacombe, O., Roure, F., Lavé, J., and Vergés, J., eds., Thrust Belts and Foreland Basins: Frontiers in Earth Sciences, Springer Berlin Heidelberg, p. 309-325.

Colman-Sadd, S.P., 1978, Fold development in Zagros simply folded belt, Southwest Iran: AAPG Bulletin, v. 62, p. 984-1003.

Costa, E., and Vendeville, B.C., 2002, Experimental insights on the geometry and kinematics of fold-and-thrust belts above weak, viscous evaporitic décollement: Journal of Structural Geology, v. 24, p. 1729-1739.

Crameri, F., Schmeling, H., Golabek, G.J., Duretz, T., Orendt, R., Buiter, S.J.H., May, D.A., Kaus, B.J.P., Gerya, T.V., and Tackley, P.J., 2012, A comparison of numerical surface topography calculations in geodynamic modelling: an evaluation of the ‘sticky air’ method: Geophysical Journal International, v. 189, p. 38-54.

Davis, D.M., and Engelder, T., 1985, The role of salt in fold-and-thrust belts: Tectonophysics, v. 119, p. 67-88.

Dooley, T.P., Jackson, M.P.A., and Hudec, M.R., 2009, Inflation and deflation of deeply buried salt stocks during lateral shortening: Journal of Structural Geology, v. 31, p. 582-600.

Dubey, A.K., and Cobbold, P.R., 1977, Noncylindrical flexural slip folds in nature and experiment: Tectonophysics, v. 38, p. 223-239.

Fernandez, N., and Kaus, B.J.P., in press, Fold interaction and wavelength selection in 3D models of multilayer detachment folding: Tectonophysics.

Frehner, M., in press, 3D fold growth rates: Terranova.

Grasemann, B., and Schmalholz, S.M., 2012, Lateral fold growth and fold linkage: Geology, v. 40, p. 1039-1042.

Hudec, M.R., and Jackson, M.P.A., 2007, Terra infirma: Understanding salt tectonics: Earth-Science Reviews, v. 82, p. 1-28.

Jahani, S., Callot, J.-P., Lamotte, D., Letouzey, J., and Leturmy, P., 2007, The Salt Diapirs of the Eastern Fars Province (Zagros, Iran): A Brief Outline of their Past and Present, *in* Lacombe, O., Roure, F., Lavé, J., and Vergés, J., eds., Thrust Belts and Foreland Basins: Frontiers in Earth Sciences, Springer Berlin Heidelberg, p. 289-308.

Jahani, S., Callot, J.-P., Letouzey, J., and Frizon de Lamotte, D., 2009, The eastern termination of the Zagros Fold-and-Thrust Belt, Iran: Structures, evolution, and relationships between salt plugs, folding, and faulting: Tectonics, v. 28, p. TC6004.

Kaus, B.J.P., 2005, Modelling approaches to geodynamic processes, PhD Thesis, ETH-Zurich.

Kaus, B.J.P., and Becker, T.W., 2007, Effects of elasticity on the Rayleigh–Taylor instability: implications for large-scale geodynamics: Geophysical Journal International, v. 168, p. 843-862.

Kaus, B.J.P., and Podladchikov, Y.Y., 2001, Forward and reverse modeling of the three-dimensional viscous Rayleigh-Taylor instability: Geophysical Research Letters, v. 28, p. 1095-1098.

Kent, P.E., 1958, Recent studies of south Persian salt plugs: AAPG Bulletin, v. 42, p. 2951-2972.

Kent, P.E., 1979, The emergent Hormuz salt plugs of southern Iran: Journal of Petroleum Geology, v. 2, p. 117-144.

Koyi, H., 1988, Experimental modeling of role of gravity and lateral shortening in Zagros mountain belt: AAPG Bulletin, v. 72, p. 1381-1394.

Letouzey, J., Colleta, B., Vially, R., and Chermette, J.C., 1995, Evolution of salt-related structures in compressional settings: Journal Name: AAPG Memoir; Journal Issue: 65; Other Information: PBD: 1995, p. Medium: X; Size: pp. 41-60.

Letouzey, J., and Sherkati, S., 2004, Salt Movement, Tectonic Events, and Structural Style in the Central Zagros Fold and Thrust Belt (Iran), Salt Sediment Interactions and Hydrocarbon Prospectivity: Concepts, Applications, and Case Studies for the 21st Century: 24th Annual, Volume 24, SOCIETY OF ECONOMIC PALEONTOLOGISTS AND MINERALOGISTS, p. 753-778.

May, D.A., 2012, Volume reconstruction of point cloud data sets derived from computational geodynamic simulations: Geochemistry, Geophysics, Geosystems, v. 13, p. Q05019.

Roca, E., Sans, M., and Koyi, H.A., 2006, Polyphase deformation of diapiric areas in models and in the eastern Prebetics (Spain): AAPG Bulletin, v. 90, p. 115-136.

Rowan, M.G., Lawton, T.F., Giles, K.A., and Ratliff, R.A., 2003, Near-salt deformation in La Popa basin, Mexico, and the northern Gulf of Mexico: A general model for passive diapirism: AAPG Bulletin, v. 87, p. 733-756.

Rowan, M.G., and Vendeville, B.C., 2006, Foldbelts with early salt withdrawal and diapirism: Physical model and examples from the northern Gulf of Mexico and the Flinders Ranges, Australia: Marine and Petroleum Geology, v. 23, p. 871-891.

Ruh, J.B., Kaus, B.J.P., and Burg, J.-P., 2012, Numerical investigation of deformation mechanics in fold-and-thrust belts: Influence of rheology of single and multiple décollements: Tectonics, v. 31, p. TC3005.

Schmid, D.W., Dabrowski, M., and Krotkiewski, M., 2008, Evolution of large amplitude 3D fold patterns: A FEM study: Physics of the Earth and Planetary Interiors, v. 171, p. 400-408.

Talbot, C.J., and Alavi, M., 1996, The past of a future syntaxis across the Zagros: Geological Society, London, Special Publications, v. 100, p. 89-109.

Talbot, C.J., Rönnlund, P., Schmeling, H., Koyi, H., and Jackson, M.P.A., 1991, Diapiric spoke patterns: Tectonophysics, v. 188, p. 187-201.

Talebian, M., and Jackson, J., 2004, A reappraisal of earthquake focal mechanisms and active shortening in the Zagros mountains of Iran: Geophysical Journal International, v. 156, p. 506-526.

Vendeville, B.C., and Nilsen, K.T., 1995, Episodic growth of salt diapirs driven by horisontal shortening, *in* Travis, C.J.H., H., Hudec, M.R., Vendeville, B.C., Peel, F.J. Perkins, B.F., ed., SEPM Gult Coast Section 16th Annual Research Fundation Conference, Volume Salt, Sediment, and Hydrocarbons.

Yamato, P., Kaus, B.J.P., Mouthereau, F., and Castelltort, S., 2011, Dynamic constraints on the crustal-scale rheology of the Zagros fold belt, Iran: Geology, v. 39, p. 815-818.

Chapter 4

Pattern formation in 3D numerical models of down-built diapirs

Abstract

Many salt diapirs are thought to have formed as a result of down-building, which implies that the top of the diapir remained close to the surface during sediment deposition. This process is largely three-dimensional and in order to better understand what controls the patterns that form as a result of this down-building process, we here perform three-dimensional numerical models. In our models, we vary several parameters such as initial salt thickness, sedimentation rate, salt viscosity, salt-sediment viscosity contrast as well as the density of sediments.

Down-building of three-dimensional diapirs is limited to a combination of the various parameters and is favoured by lower viscosity contrasts and sedimentation rates in agreement with previous findings from 2D models. However, the models show that the sedimentation rate has an additional effect on the formation and evolution of three-dimensional diapir patterns. The preservation of salt ridges related to the initial Rayleigh-Taylor instability phase is favoured for lower sedimentation rates. The formation of finger-like diapirs at the junction of salt ridges is favoured for higher sedimentation rates, which results in different salt exposure patterns at the surface. Once the initial pattern of diapirs is formed, higher sedimentation rate can also result in covered diapirs if the diapir extrusion velocity is not high enough.

We quantify the effect of sedimentation rate on the number of diapirs exposed at the surface as well as on their spacing. In some cases, this final pattern is distinctly different from the initial polygonal pattern. We also study the extrusion of salt through time in the simulations, and show that it can be related to the geometries of the sedimentary layers surrounding the diapirs.

Keywords: down-building, salt tectonics, passive diapirs, numerical modelling

4.1 Introduction

Two end member processes are described to explain how salt diapirs form: (1) buoyancy instability (i.e. Rayleigh-Taylor instability) in which the density difference between salt and overburden induces upward motion of salt and (2) a down-building or syn-depositional process in which salt structures grow while sediments are being deposited (Figure 4.1a).

Purely buoyancy driven salt diapirism was introduced in early experiments of the Rayleigh-Taylor instability by Nettleton (1934). The dynamics of up-building diapirs as a result of the buoyancy instability have been extensively studied with different methods such as linear stability (Biot and Odé, 1965; Ramberg, 1968a, b), analogue modelling (e.g. Dixon, 1975; Ramberg, 1967; Talbot et al., 1991) and numerical modelling (e.g. Schmeling, 1987; Woidt, 1978). Such studies have provided information about the shapes and geometries related to up-built diapirs in 2D and 3D. However, it was argued that it would be difficult for salt to pierce through piles of sediments that commonly reach thicknesses of several thousand meters if they were assumed to have deposited prior to salt movement.

Therefore, in recent years, syn-depositional movement of salt is considered a key mechanism to allow upward movement of salt through the overburden. Initial works on syn-depositional diapirism mechanism were introduced by Biot and Odé (1965). In the work by Biot and Odé (1965), based on linear stability analysis, the time-dependency of the characteristic Rayleigh-Taylor was related to sedimentation and compaction. Numerical modelling investigating the effect of the sedimentation during diapir growth confirmed that wavelength of diapirs are shorter than the wavelength of a purely Rayleigh-Taylor instability (van Keken et al., 1993). Analogue modelling has also provided an account on how diapirs relate to the loading of the overburden and other tectonic forces (e.g. Jackson et al., 1988; Talbot, 1992; Vendeville and Jackson, 1992a, b).

Diapir shapes and geometries in numerical models that account for sedimentation and erosion (redistribution of sediments at the surface) are various (Chemia et al., 2008; Fuchs et al., 2011; Ismail-Zadeh et al., 2001; Kaus, 2005; Poliakov et al., 1993). In such cases, diapir shapes depend not only on the viscosity or density contrast, but also on the sedimentation rate. Furthermore, it was illustrated that down-building of diapirs occur at regimes of low viscosity contrasts or low sedimentations rate, as opposed to regimes of high viscosity contrast and sedimentation rate were diapirs are buried and their growth disrupted (Chemia et al., 2008; Fuchs et al., 2011).

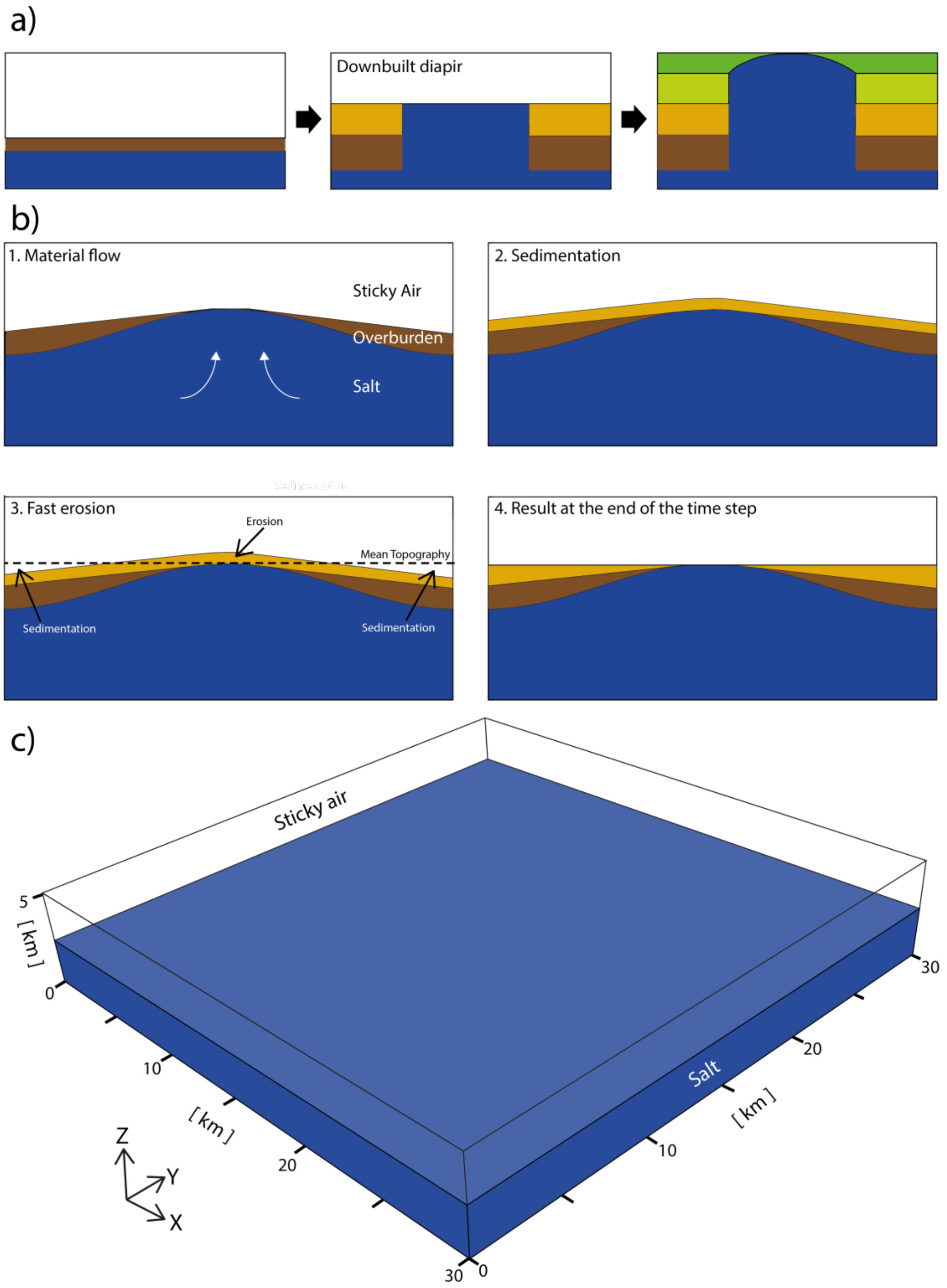

Figure 4.1. a) Schematic cartoon of the formation of a diapir by down-building or passive diapirism. A down-built diapir is formed by the deposition of new sediments around it and subsequent salt withdraw from below the surrounding sediments. b) Conceptual scheme of our numerical implementation of the down-building process. For each time step particles are advected with the velocity that is obtained by solving the 3D equations (1), new material is sedimented (2) according to a specified sedimentation rate and fast erosion is applied (3). The result is a flat internal surface (4) at the end of the time step. c) 3D initial setup used in the simulations of this study.

Numerical studies that include sedimentation and erosion (redistribution of surficial sediments) have been limited to 2D (Chemia et al., 2008; Fuchs et al., 2011; Poliakov et al., 1993), where the characteristic spacing is translated to a characteristic wavelength that can be estimated from the physical parameters (Biot and Odé, 1965). However, salt diapirs are intrinsically 3D structures as seismic studies have beautifully illustrated in areas of active hydrocarbon exploration (e.g. Guerra and Underhill, 2012). Biot (1966) derived the three-dimensional solutions from their previous 2D works (Biot and Odé, 1965) and described the periodic patters that result from extending the development of the 2D characteristic wavelength into 3D. The polygonal 3D pattern predicted by the works of Biot (1966) was reproduced in analogue modelling by Talbot et al. (1991), where neither sedimentation nor erosion was considered.

Although many numerical models of the 3D Rayleigh-Taylor instability exist, there are only few that focus on the particular study of salt diapirs (Ismail-Zadeh et al., 2004; Kaus, 2005; Kaus and Podladchikov, 2001). The patterns resulting from numerical models can be complex, and most studies highlighted the difficulty of developing wall-like structures unless strong 2D perturbations (such as basement faults) are present.

It is widely accepted that sedimentation and erosion influence the diapir evolution. Yet, it remains unclear how such processes affect the 3D diapir patterns and/or the individual 3D shapes of diapirs. Here, we focus on how different sedimentation rates as well as other varying parameters (viscosity contrast between salt and sediments, salt layer thickness) affect the 3D dynamics of diapir formation and the final shapes of the diapirs and the sediments surrounding them. For simplicity, our study focuses on the case in which both the overburden and the salt are Newtonian viscous materials, which allows a straightforward comparison with previous studies. Future work should address the effect of a brittle overburden rheology and regional tectonics.

4.2 Method

We use a continuum mechanics approximation where the equations used to describe geological processes consists of a set of balance equations for mass and momentum together with their constitutive relationships.

Conservation of mass and momentum for slowly moving incompressible fluids are given by:

$$\frac{\partial v_i}{\partial x_i} = 0 \qquad [4.1]$$

$$-\frac{\partial P}{\partial x_i} + \frac{\partial \tau_{ij}}{\partial x_j} = -\rho g_i \qquad [4.2]$$

where *i,j* represent spatial directions and repeated indices are summed, v_i are the velocities, x_i are the coordinates, $P = -\sigma_{ii}/3$ is pressure, σ_{ij} are the components of the total stress tensor, τ the deviatoric stress tensor, ρ the density and g, the gravitational acceleration.

We employ a linear viscous (Newtonian) constitutive relationship given by

$$\tau_{ij} = 2\eta\, \dot{\varepsilon}_{ij}$$

where η is the Newtonian viscosity which is constant for each of the material phases, and $\dot{\varepsilon}_{ij}$, the deviatoric strain rate tensor is given by

$$\dot{\varepsilon}_{ij} = \frac{1}{2}\left(\frac{\partial v_i}{\partial x_j} + \frac{\partial v_j}{\partial x_i}\right) \qquad [4.3]$$

Equations [4.1] to [4.3] are discretized with a staggered grid finite differences scheme as implemented in the parallel code LaMEM (Lithosphere and Mantle Evolution Model). Material properties are tracked using markers, here referred simply as particles. These particles are advected in a Lagrangian manner with the velocities obtained from solving the equations [4.1] and [4.2].

LaMEM uses PETSc Libraries and solvers that allow running massively parallel forward simulations. The internal free surface that allows topography to form is approximated in LaMEM by the “sticky air” approach, in which a low viscosity layer overlies the free internal surface. Recent benchmark studies have shown that the sticky air is a good approximation of the free surface in the finite differences method as long as the viscosity is sufficiently low and the layer is sufficiently thick (Crameri et al., 2012). An implementation of the Voronoi cells for phases visualization as described in May (2012) is implemented in LaMEM in order to visualize the runs.

4.3 Setup

The process of down-building diapirism (Figure 4.1a) is implemented in the code by using a fast erosion boundary condition at the internal free surface and a sedimentation rate. Above the salt layer, sediments are deposited according to a sedimentation rate, which is constant throughout the simulation. The fast erosion sedimentation-erosion or sediment redistribution approach has been used in previous works (Burg et al., 2004; Poliakov et al., 1993) and it is basically a redistribution of the mass as illustrated in Figure 4.1. Within each time step, the following steps are implemented that mimic the down-building processes: 1) particles and internal free surface are advected according to the velocities obtained from the mechanical solvers of the code. 2) Above the deformed internal surface a layer of sediments is deposited, by calculating the corresponding deposit thickness according to the time internal and the prescribed sedimentation rate. Sedimentation is achieved by converting particles of air phase to the sediment phase. 3) Then, the average of the new topography is calculated and the free surface is flattened to that height. The sediments above that surface are “eroded” by converting the sediment phase particles to air, whereas new sediments are “deposited” below the surface, by converting the air particles to sediment phase. 4) At the end of the time step and after applying all those processes the resulting internal surface is flat. This process is summarized in Figure 4.1b.

One of the assumptions of this work, which is the same as in previous studies by Chemia et al. (2008) and Fuchs et al. (2011), is that the initial density of the sediments is already higher than that of the salt. This is done in order to accelerate the down-building process in the simulations. The implementation of a depth dependency of sediment density has been used in 2D simulations by Poliakov et al. (1993) and resulted in an initial phase of active diapirism at the beginning.

The setup consists of a 30x30x10 km box domain that is discretized with 128x128x32 cells. The boundaries of the box are set to be free-slip (Figure 4.1c). An initial pre-halokinetic sequence is omitted on purpose, to understand the influence of down-building of sediments on the initial patterns that develop. The pre-halokinetic sequence has also been omitted in previous 2D studies of down-built diapirs by Chemia et al. (2008) and Fuchs et al. (2011). For this reason, in time step zero, only a layer of salt is present, separated from the “sticky air layer” by the internal free surface (see Figure 4.1c).

The different sediment layers have the same physical properties but are given different colors every 0.5 Myrs for visualization purposes. Initially phase number 1 is deposited. Once the defined time for the phase change is reached, phase number 2 will start to deposit and so on, until number of phases is reached, in which case phase 1 will start being deposited again.

Each of the simulations was run on 64 cores, and we used a fully coupled stokes solver, with fieldsplit and algebraic multigrid (ML) as velocity solvers. The iterations required for each time step and therefore the time of the simulations varied from run to run, ranging between several tens iterations for low viscosity contrast to several hundred for the higher viscosity contrasts.

In order to make all the simulations comparable, we have used the same random noise in the initial particle distribution of all simulations shown here. The random noise is created using a built-in function within PETSc and its maximum amplitude is 100 meters.

The parameters we have changed in this work are: the initial thickness of the salt layer, the viscosity of the salt layer, the viscosity of the sediment layers above and the sedimentation rate. The varied parameters and ranges are specified in Table 4.1.

Table 4.1. Parameters used in the simulations and corresponding minimum and maximum values of each of the parameters that were varied for this study.

	Units	Minimum	Maximum
η_{salt}	[Pa s]	10^{17}	10^{19}
$\eta_{sediment}$	[Pa s]	10^{20}	10^{23}
η_{sticky_air}	[Pa s]	10^{16}	10^{16}
$\eta_{sediment}/\eta_{salt}$	[ ]	10	1000000
ρ_{salt}	[Kg/m^3]	2200	2200
$\rho_{sediment}$	[Kg/m^3]	2400	2900
ρ_{sticky_air}	[Kg/m^3]	0	0
Sedimentation rate	[cm/year]	0.01	0.1
Thickness of salt	[m]	500	1500

Table 4.2. List of all simulations performed in this work with corresponding parameters. The number of output time steps and the time reached at the indicated time step are also indicated. A small description of the observed salt structures has been added. When no diapirism is observed, this is also indicated.

Num.	**Name**	**Sed. rate**	**Salt thicknes**	**Salt viscosity**	**Seds. viscosity**	**Viscosity ratio**	**Seds. density**	**Time step**	**Final time**	**Diapir shape**
[]	**[]**	**[cm/year]**	**[m]**	**[Pa s]**	**[Pa s]**	**[]**	**[Kg/m^3]**	**[]**	**[Myrs]**	**[]**
1	DB_01	0.1	1000	1.00E+18	1.00E+21	1.00E+03	2700	780	3.86	finger
2	DB_001	0.01	1000	1.00E+18	1.00E+21	1.00E+03	2700	500	5.00	finger
3	DB_005	0.05	1000	1.00E+18	1.00E+21	1.00E+03	2700	500	4.67	finger
4	DB_b_01	0.1	1000	1.00E+18	1.00E+20	1.00E+02	2700	500	4.57	finger
5	DB_b_001	0.01	1000	1.00E+18	1.00E+20	1.00E+02	2700	500	5.00	linear
6	DB_b_005	0.05	1000	1.00E+18	1.00E+20	1.00E+02	2700	500	4.92	elongated/finger
7	DB_c_01	0.1	1000	1.00E+18	1.00E+22	1.00E+04	2700	500	5.00	NO
8	DB_c_001	0.01	1000	1.00E+18	1.00E+22	1.00E+04	2700	500	4.98	linear/dome
9	DB_c_005	0.05	1000	1.00E+18	1.00E+22	1.00E+04	2700	800	4.54	dome
10	DB_d_01	0.1	1000	1.00E+18	1.00E+23	1.00E+05	2700	500	5.00	NO
11	DB_d_001	0.01	1000	1.00E+18	1.00E+23	1.00E+05	2700	200	2.04	ridges/domes
12	DB_d_005	0.05	1000	1.00E+18	1.00E+23	1.00E+05	2700	280	2.81	NO
13	DB_01_S19	0.1	1000	1.00E+18	1.00E+19	1.00E+01	2700	500	4.41	plumes
14	DB_001_S19	0.01	1000	1.00E+18	1.00E+19	1.00E+01	2700	500	4.80	plumes
15	DB_005_S19	0.05	1000	1.00E+18	1.00E+19	1.00E+01	2700	500	4.74	plumes
16	DB_T1500_01	0.1	1500	1.00E+18	1.00E+21	1.00E+03	2700	500	2.00	finger/dome
17	DB_T1500_001	0.01	1500	1.00E+18	1.00E+21	1.00E+03	2700	500	4.76	finger/dome
18	DB_T1500_005	0.05	1500	1.00E+18	1.00E+21	1.00E+03	2700	500	3.82	finger
19	DB_T1500_b_01	0.1	1500	1.00E+18	1.00E+20	1.00E+02	2700	500	3.80	finger
20	DB_T1500_b_001	0.01	1500	1.00E+18	1.00E+20	1.00E+02	2700	500	4.73	linear pattern
21	DB_T1500_b_005	0.05	1500	1.00E+18	1.00E+20	1.00E+02	2700	500	4.49	linear pattern
22	DB_T1500_c_01	0.1	1500	1.00E+18	1.00E+22	1.00E+04	2700	800	1.80	ridges/domes
23	DB_T1500_c_001	0.01	1500	1.00E+18	1.00E+22	1.00E+04	2700	500	4.51	ridges/domes
24	DB_T1500_c_005	0.05	1500	1.00E+18	1.00E+22	1.00E+04	2700	500	2.64	ridges/domes
25	DB_T1500_d_01	0.1	1500	1.00E+18	1.00E+23	1.00E+05	2700	500	5.00	NO
26	DB_T1500_d_001	0.01	1500	1.00E+18	1.00E+23	1.00E+05	2700	120	0.87	ridges/domes
27	DB_T1500_d_005	0.05	1500	1.00E+18	1.00E+23	1.00E+05	2700	105	0.67	ridges/domes
28	DB_T0500_01	0.1	500	1.00E+18	1.00E+21	1.00E+03	2700	500	5.00	NO
29	DB_T0500_001	0.01	500	1.00E+18	1.00E+21	1.00E+03	2700	500	5.00	dome
30	DB_T0500_005	0.05	500	1.00E+18	1.00E+21	1.00E+03	2700	500	5.00	NO
31	DB_T0500_b_01	0.1	500	1.00E+18	1.00E+20	1.00E+02	2700	500	5.00	pillow/NO
32	DB_T0500_b_001	0.01	500	1.00E+18	1.00E+20	1.00E+02	2700	500	5.00	elongated/dome
33	DB_T0500_b_005	0.05	500	1.00E+18	1.00E+20	1.00E+02	2700	500	3.71	mushroom
34	DB_T0500_c_01	0.1	500	1.00E+18	1.00E+22	1.00E+04	2700	500	5.00	NO
35	DB_T0500_c_001	0.01	500	1.00E+18	1.00E+22	1.00E+04	2700	500	5.00	domes
36	DB_T0500_c_005	0.05	500	1.00E+18	1.00E+22	1.00E+04	2700	500	5.00	NO
37	DB_S17_01	0.1	1000	1.00E+17	1.00E+21	1.00E+04	2700	795	3.21	fingers
38	DB_S17_001	0.01	1000	1.00E+17	1.00E+21	1.00E+04	2700	860	6.98	fingers
39	DB_S17_005	0.05	1000	1.00E+17	1.00E+21	1.00E+04	2700	815	3.57	fingers
40	DB_S17_b_01	0.1	1000	1.00E+17	1.00E+20	1.00E+03	2700	500	2.34	narrow fingers
41	DB_S17_b_001	0.01	1000	1.00E+17	1.00E+20	1.00E+03	2700	500	3.66	linear
42	DB_S17_b_005	0.05	1000	1.00E+17	1.00E+20	1.00E+03	2700	500	3.18	fingers/linear
43	DB_S17_c_01	0.1	1000	1.00E+17	1.00E+22	1.00E+05	2700	165	0.28	domes
44	DB_S17_c_001	0.01	1000	1.00E+17	1.00E+22	1.00E+05	2700	230	0.90	domes
45	DB_S17_c_005	0.05	1000	1.00E+17	1.00E+22	1.00E+05	2700	165	0.37	domes
46	DB_S17_S19_01	0.1	1000	1.00E+17	1.00E+19	1.00E+02	2700	500	3.67	plumes
47	DB_S17_S19_001	0.01	1000	1.00E+17	1.00E+19	1.00E+02	2700	500	3.84	plumes
48	DB_S17_S19_005	0.05	1000	1.00E+17	1.00E+19	1.00E+02	2700	500	3.86	plumes
49	DB_S19_01	0.1	1000	1.00E+19	1.00E+21	1.00E+02	2700	500	5.00	NO
50	DB_S19_001	0.01	1000	1.00E+19	1.00E+21	1.00E+02	2700	500	5.00	elongated/dome
51	DB_S19_005	0.05	1000	1.00E+19	1.00E+21	1.00E+02	2700	500	5.00	NO
52	DB_S19_b_01	0.1	1000	1.00E+19	1.00E+20	1.00E+01	2700	500	5.00	domes/RT
53	DB_S19_b_001	0.01	1000	1.00E+19	1.00E+20	1.00E+01	2700	500	5.00	elongated/linear
54	DB_S19_b_005	0.05	1000	1.00E+19	1.00E+20	1.00E+01	2700	500	5.00	mushroom
55	DB_S19_c_01	0.1	1000	1.00E+19	1.00E+22	1.00E+03	2700	500	5.00	NO
56	DB_S19_c_001	0.01	1000	1.00E+19	1.00E+22	1.00E+03	2700	500	5.00	domes
57	DB_S19_c_005	0.05	1000	1.00E+19	1.00E+22	1.00E+03	2700	500	5.00	NO
58	DB_S19_d_01	0.1	1000	1.00E+19	1.00E+23	1.00E+04	2700	500	5.00	NO
59	DB_S19_d_001	0.01	1000	1.00E+19	1.00E+23	1.00E+04	2700	500	5.00	NO
60	DB_S19_d_005	0.05	1000	1.00E+19	1.00E+23	1.00E+04	2700	500	5.00	NO
61	DB_D2400_01	0.1	1000	1.00E+18	1.00E+21	1.00E+03	2400	500	5.00	NO
62	DB_D2400_001	0.01	1000	1.00E+18	1.00E+21	1.00E+03	2400	500	5.00	domes
63	DB_D2400_005	0.05	1000	1.00E+18	1.00E+21	1.00E+03	2400	800	4.68	domes
64	DB_D2900_01	0.1	1000	1.00E+18	1.00E+21	1.00E+03	2900	500	2.74	fingers
65	DB_D2900_001	0.01	1000	1.00E+18	1.00E+21	1.00E+03	2900	500	4.95	ridges/domes
66	DB_D2900_005	0.05	1000	1.00E+18	1.00E+21	1.00E+03	2900	465	4.29	fingers

4.4 Results

We have performed a total of 66 simulations. The specific parameters used in each of them and whether they resulted in diapirism or not are listed in Table 4.2. As in the previous 2D study by Fuchs et al. (2011), we have also delimited the parameter ranges under which the transition from diapirism to no-diapirism occurs. Some of the overall characteristics of the simulations can be observed in Figure 4.2 and Figure 4.3. As soon as sediments start to deposit above the salt, the salt starts flowing. The salt can be exposed at the surface after piercing through small thicknesses of sediments or it can be exposed at the surface from the beginning of the simulation. The salt will form a characteristic pattern of ridges delimiting the polygonal shaped area where sediments start to deposit and form minibasins. Upward salt flow concentrates at the junctions of several ridges. Some of these ridges might be covered, allowing mainly horizontal flow to occur through them, whereas in other cases the salt ridge remains exposed and forms a salt wall. In the examples of Figure 4.2, it can be observed that simulations with lower sedimentation rates result in more elongated salt exposures. Simulations with higher sedimentation rates, on the other hand, result in more finger-like salt diapirs. The thickness of sediments and the height to which the internal free surface can reach depends on the sedimentation rate: in simulations with the same parameters, at any given time, a higher sedimentation rate will result in a higher internal free surface and thicker sediment sequences. The polygonal pattern that develops during the initial stages depends largely on the physical parameters of the simulation (density difference, and viscosity contrast). However, the ultimate pattern and geometry of the 3D diapir structures are also highly dependent on the sedimentation rate. Once the depocenter of the minibasin has reached the bottom of the box they tend to flatten on the bottom, which helps to further extrude salt out the diapirs.

Figure 4.3 shows the effect of different initial salt layer thickness. The salt flows earlier for larger salt thicknesses and therefore it can reach the surface during earlier stages (Figure 4.3, 0.35 Myrs). At the initial stages of diapirism, the heights in the salt topography that can potentially localize the diapirs, have a higher spacing with higher salt thickness as well (Figure 4.3, 1.20 Myrs). The effects of the different parameters in various aspects of 3D down-built diapir development are commented in more detail in the following sections.

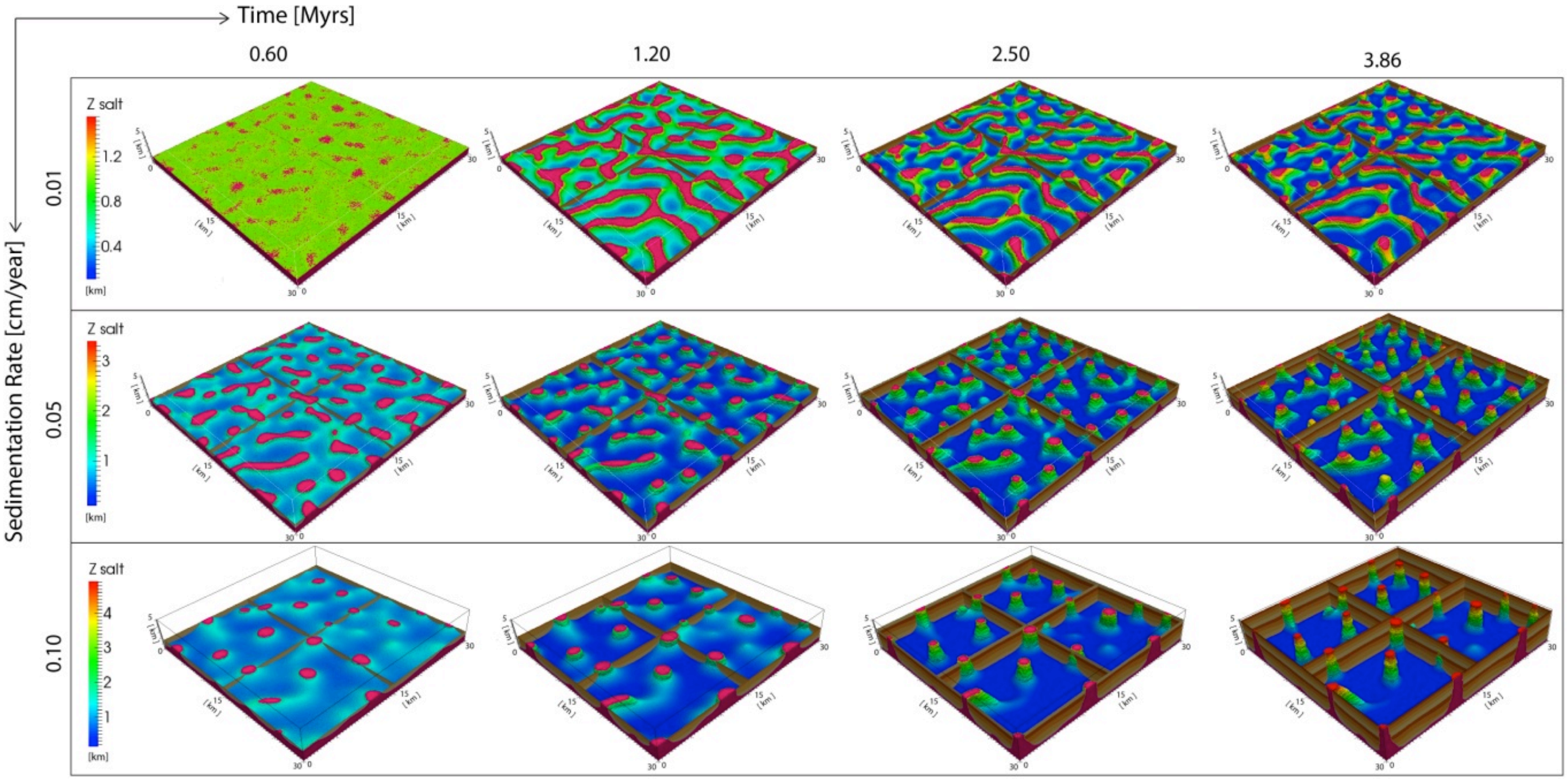

Figure 4.2. 3D perspective views of time evolution of three simulations with same parameters but different sedimentation rates (Simulations number 1 to 3 of Table 4.2). The higher the sedimentation rates the fewer diapirs that will be exposed at the surface at the final stages. Diapir spacing depends on the sedimentation rate, and the resulting structures are more finger-like for higher sedimentation rates.

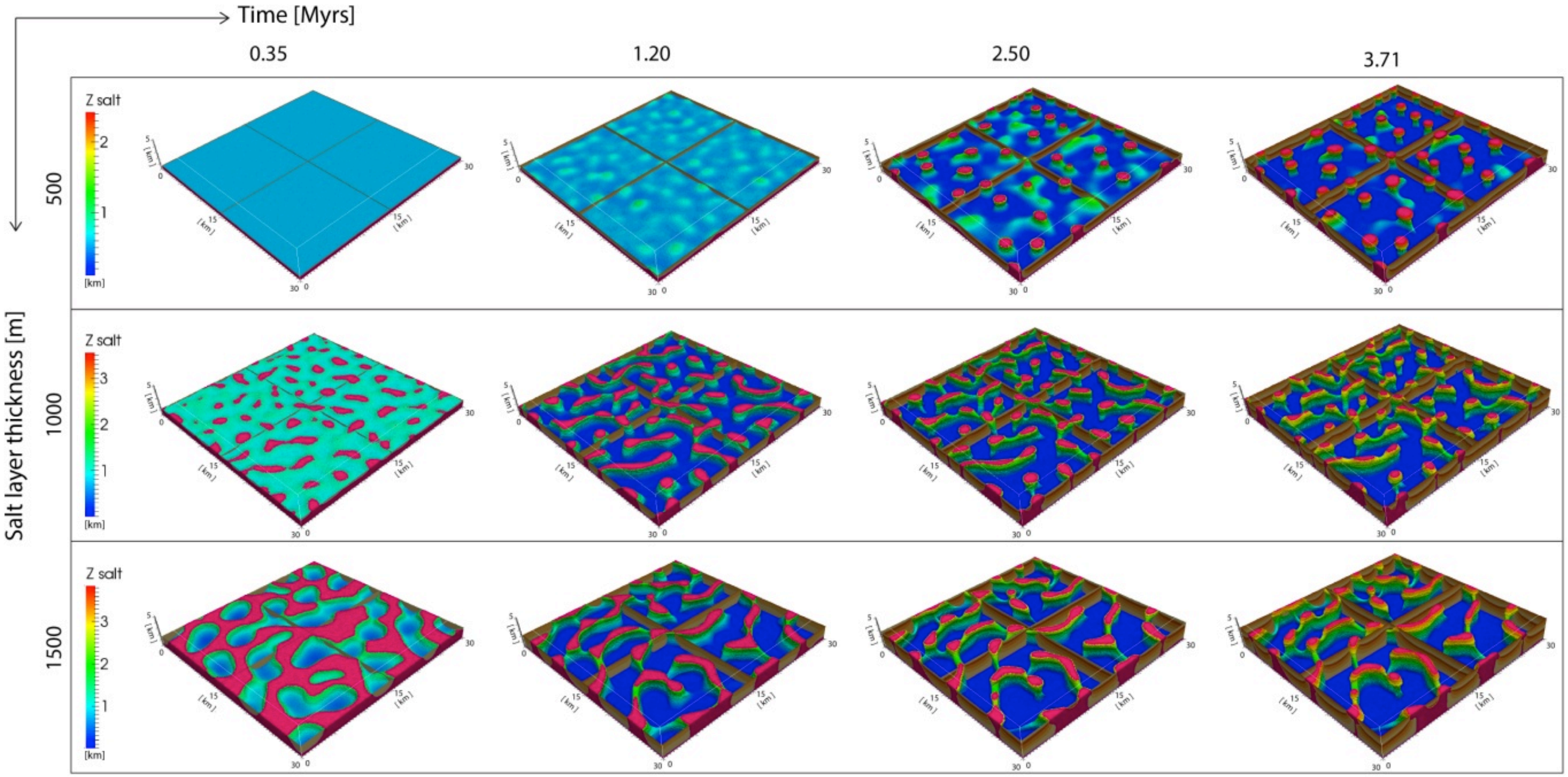

Figure 4.3. 3D perspective views of time evolution of three simulations with the same parameters but different initial salt layer thickness (Simulations number 6, 21 and 33 of Table 4.2). The higher the salt thickness, the earlier salt start to flow (0.35 Myrs) and the larger the spacing is between the initial highs at the salt topography (1.20 Myrs).

4.4.1 Regimes of down-built diapirism and no-diapirism

The effect of the sedimentation rate was previously studied in 2D numerical simulations by Chemia et al. (2008) and Fuchs et al. (2011). Fuchs et al. (2011) performed systematic simulations of a synthetic setup with an initial wavelength perturbation in order to test the effect of sedimentation in diapir down-building. They showed that sedimentation rate is a key parameter to distinguish between successful diapirism regimes in different parameter spaces. Critical sedimentation rates required for diapirs to develop based on a channel flow approximation proved a valid parameter in 2D (Fuchs et al., 2011).

Among the several simulations that were performed for this study, in some of them no diapirism occurred (see Table 4.2). We have tried to delimit parameter ranges for which the transition from diapirism to no-diapirism occurs. Simulations with no diapirism are the ones at which the interface between the salt and the overburden remains flat after a considerable thickness of sediments have been deposited and the model box is filled. In this study we do not consider active diapirism that may occur after longer time periods in these simulations once the model box is filled.

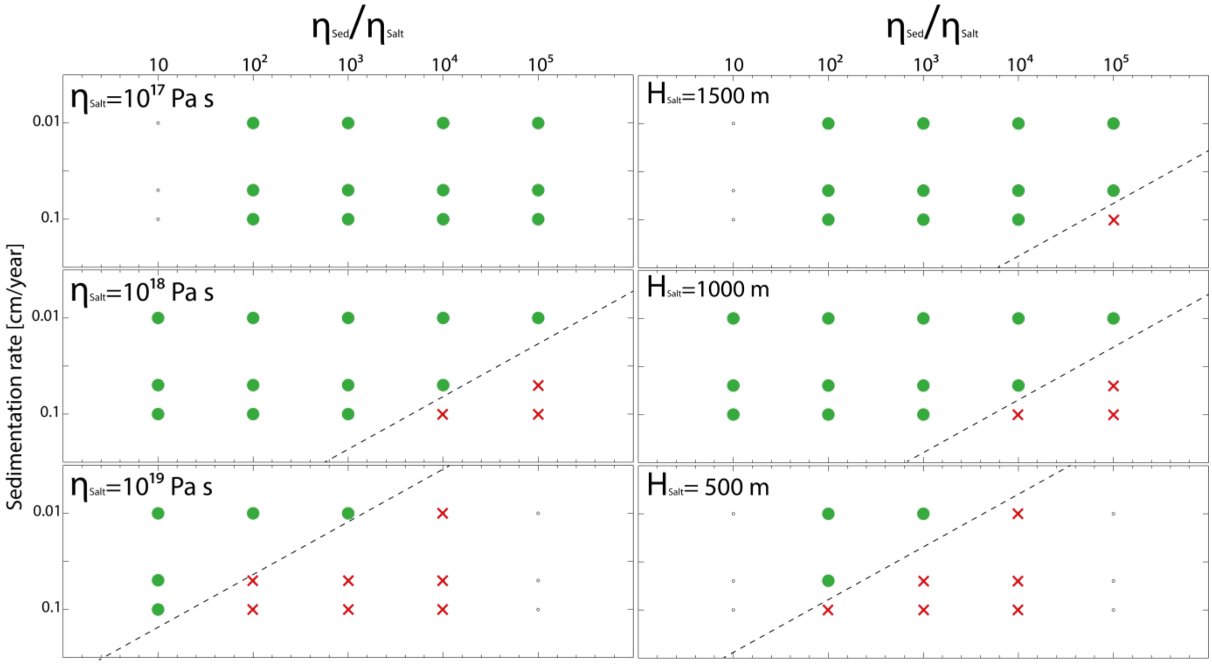

Figure 4.4. Graphs in the sedimentation rate – viscosity contrast parameter space that illustrate whether the simulations resulted in down-built diapirs (green circles) or in no diapirs (red crosses). Dashed line is the suggested transition between the two domains.

The results of systematic simulations show that down-built diapirs occur for lower sedimentation rates and viscosity contrasts (Figure 4.4). The transition between diapirs and no diapirs also depends on salt viscosity and salt thickness as it can also be observed. The higher the salt viscosity and the thinner the initial salt layer, the more difficult it gets to develop diapirs.

4.4.2 Effect of salt viscosity and thickness on initial polygonal patterns

One of the initial works studying the polygonal patterns that arise from the gravity instability was Biot (1966), who extended the 2D linear stability results to 3D. He showed that the linear stability analysis predicted several patterns of diapir formation, depending on the used geometrical approach, and which ranged from triangular to polygonal patterns (see Figure 4.5a and b). Some of the well-known salt provinces fit to these regular patterns reasonably well, e.g. Santos Basin of Brazil (Guerra and Underhill, 2012), the Gulf of Mexico (Rowan and Vendeville, 2006) or the Zagros Folded Belt (Kent, 1979). Some of them are already interpreted in the framework of salt withdrawal minibasins (Rowan and Vendeville, 2006).

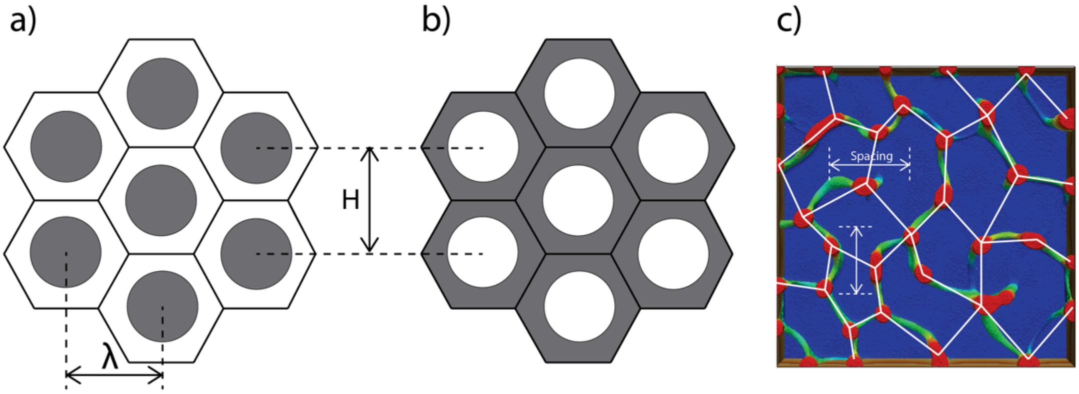

Figure 4.5. a) and b) represent hexagonal patterns derived from a linear stability analysis by Biot (1966). Salt is represented by a dark grey colour. In a) the diapirs would form in the middle of the cells, whereas in b) the salt forms a system of ridges where the diapirs would form at the intersection between the ridges. The situation described in b) is the one that best applies to the simulations of this study, which is illustrated in c). In our simulations, the salt forms ridges (green colours) delimiting a polygonal pattern (not uniquely hexagons), and diapirs (red coloured) form at the intersections of ridges.

Biot (1966) mentioned that hexagonal patterns can develop in two ways. In one case, the highs are developed in the centre of the polygon (Figure 4.5a) and a network of valleys would form the skeleton of the polygon pattern. On the opposite case, a network of elevated ridges would form the pattern itself, while the centre of the polygons would be where the lower topographic areas are located (Figure 4.5b). This latter case is the one that applies to our simulations, which in most of the cases exhibits a polygonal pattern defined by interconnected salt ridges (Figure 4.5c). When such a pattern develops, the diapirs are located in the connections between the ridges. The relation between the wavelength of the instability predicted by the 2D stability analysis and the height or spacing between the polygons is also shown in Figure 4.5. The characteristic distance between the polygon centres is equal to 1.155λ and therefore quite similar to the wavelength predicted by linear theory.

The wavelength predicted by the 2D solution of the gravity instability, depends of course on the physical parameters involved in the setup. Biot and Odé (1965) grouped these parameters in three non-dimensional parameters relating the thickness, viscosity and density ratios between the dense and less dense material.

Regarding the viscosity contrast, wavelengths are larger when there is a higher viscosity contrast between the two materials. However, at the same time the amplification rate (characteristic time of the instability) is smaller.

The thickness ratio between the two materials influences the wavelength in such a manner, that when a thinner overburden is present the dominant wavelength is smaller. Depending on salt layer thickness and viscosity contrast, different diapirism modes occur. For a certain range of parameters and very thick salt layer compared to the thickness of the overburden, scaling laws predict a matrix diapirism mode, where there is no dependency on the overburden thickness (Kaus, 2005). In our setup, we start with no initial overburden above the salt layer and the thickness of the overburden increases according to the sedimentation rate. Due to this time dependency, it can happen that if the time needed for the instability is too long, there will be a thicker overburden deposited before the instability kicks off. Depending on the initial thickness of salt layer and viscosities, the accumulated sediments above might cause a change in the wavelength. This effect would be stronger the thinner the initial salt layer is.

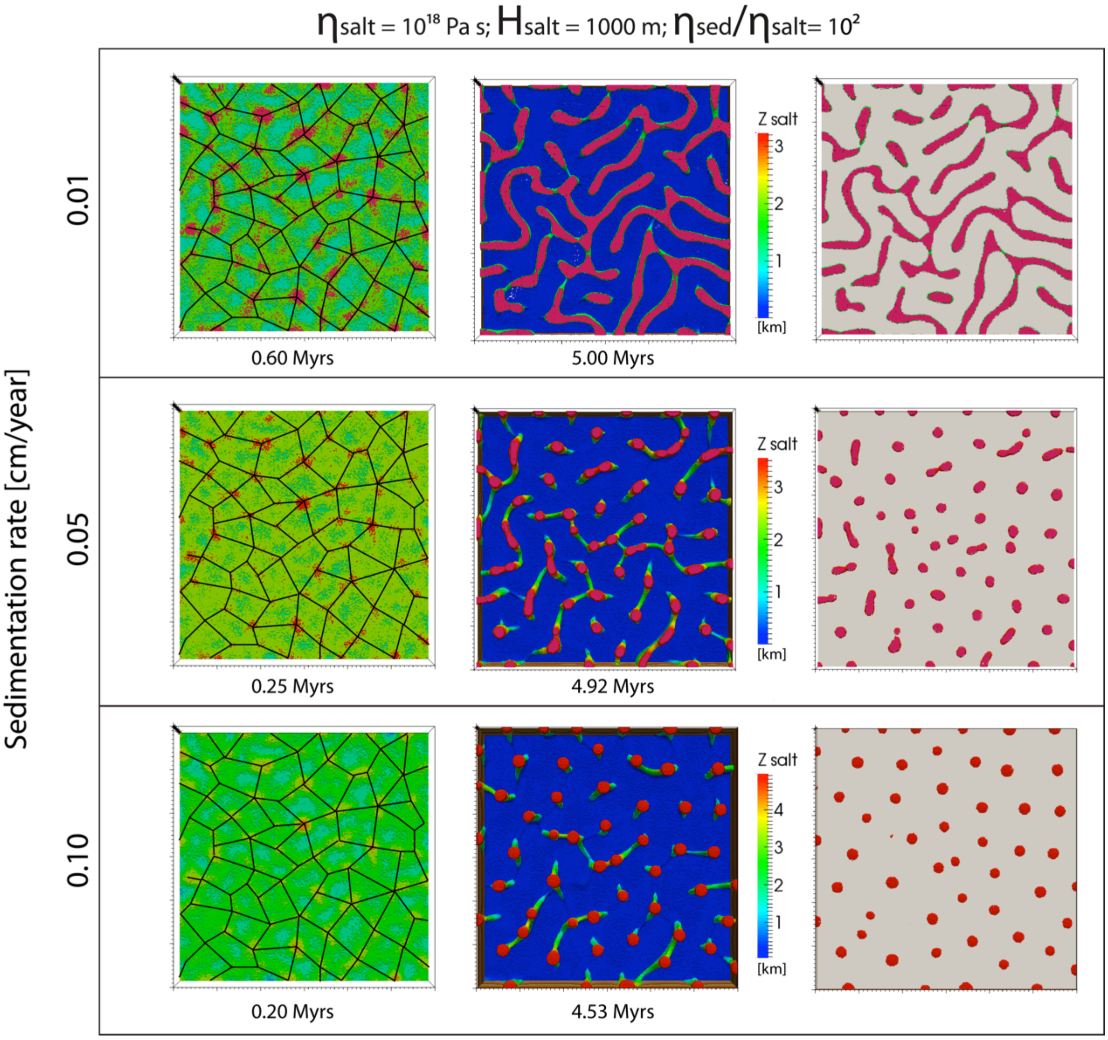

Figure 4.6. Map view of three different simulations with H_{salt}*= 1000 m and different sedimentation rate. Left and middle panels show the topography of the salt, where higher elevation is indicated by yellow-red colours and low elevation by blue colours. Right panel shows the salt diapirs (pink colour) exposed at the surface. During initial stages (left panel) the polygonal pattern is similar in all simulations. However, as sediments are added the development of the salt ridges and diapirs is different. In the example with small sedimentation rate, parts of the initial salt ridges are preserved which ultimately results in linear and elongated diapirs at the final model stages. With higher sedimentation rates, salt is preferably extruded through diapirs instead of ridges and more circular diapiric patterns develop.*

The 2D wavelength that is predicted by the analytical theory is translated into 3D, by developing characteristic regular patterns as mentioned earlier. Therefore, it is expected that the initial salt thickness and viscosities of sediments and salt will result in different spacing of the regular polygonal patterns that develop in the simulations. The parameters varied in this work are: viscosity of salt and overburden, density of sediments and thickness of salt. We want to investigate, whether the viscosity contrast between salt and overburden is the only important ratio or if keeping same viscosity contrast, the absolute viscosity of salt is important. Scaling laws derived for salt diapirs with fast erosion boundary show that growth rate is inverse proportional to absolute salt viscosity Kaus (2005), so therefore, an effect of absolute viscosity of salt can be expected.

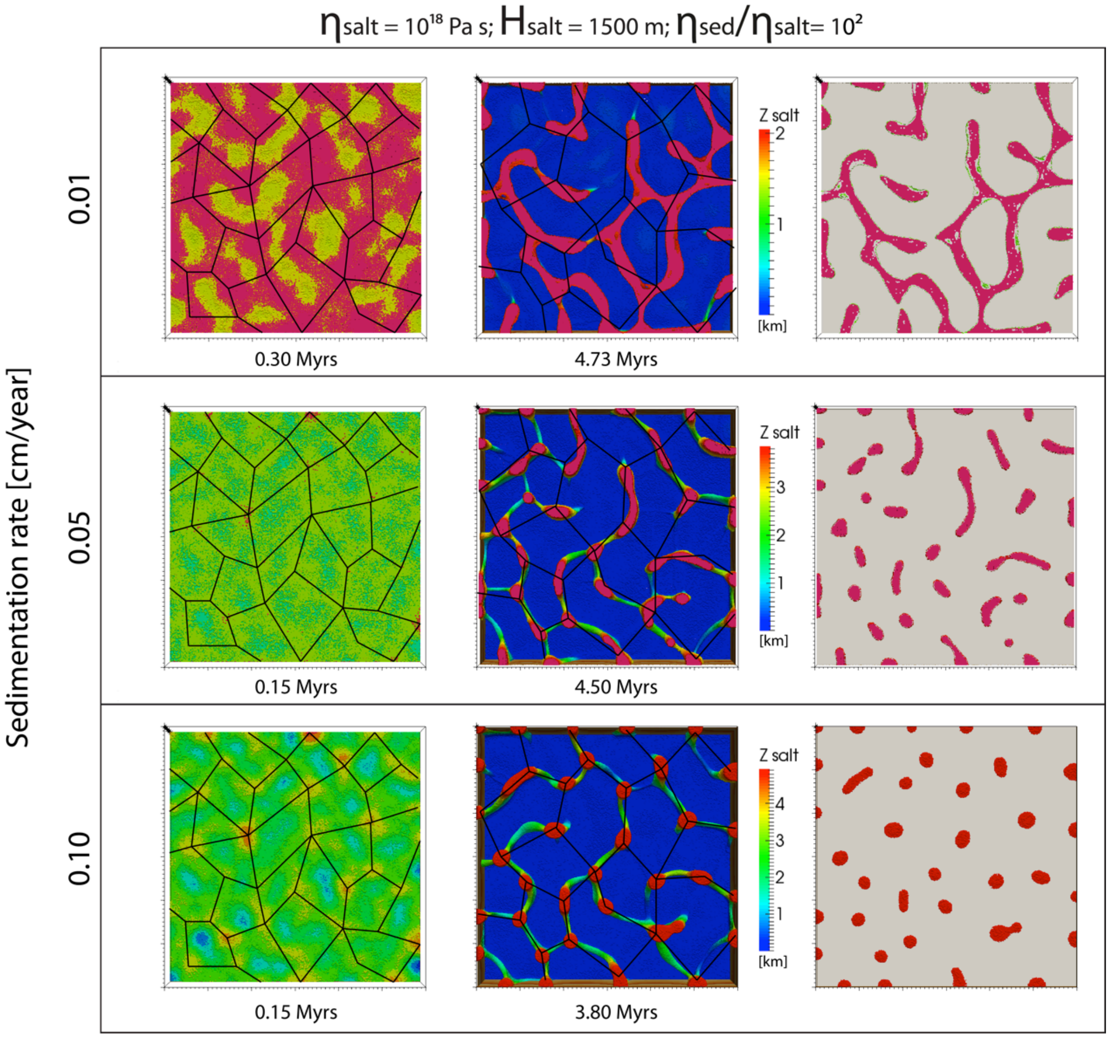

Figure 4.7. Map view of three different simulations with H_{salt}= 1500 m and three different sedimentation rates. Left and middle panels show the topography of the salt, whereas the right panel shows the salt diapirs (pink colour) exposed at the surface. During the initial stages (left panel) the polygonal pattern is similar in two of the simulations but cannot be recognized in the simulation with the smallest sedimentation rate. The spacing between polygons is larger than in the example of Figure 4.6.

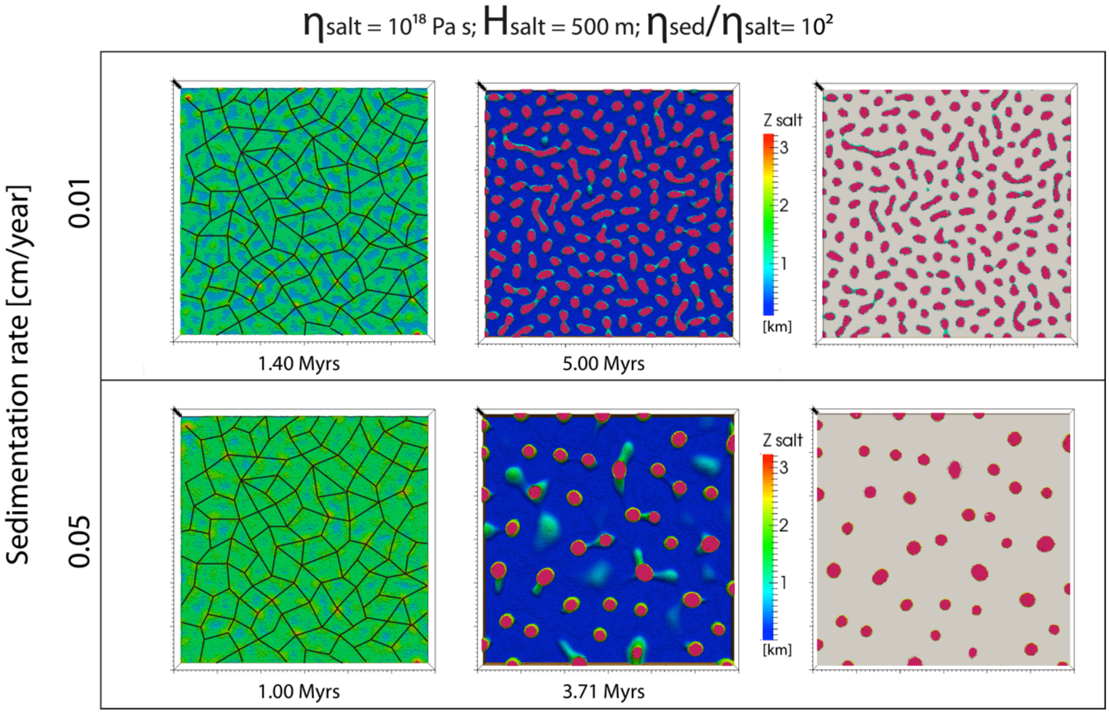

Figure 4.8. Simulations with H_{salt}= 500 m and with two different sedimentation rate. During initial stages (left panel) the polygonal pattern is similar in the simulations but cannot be recognized at evolved stages with higher sedimentation rate where the number of diapirs is much smaller. In this case sedimentation rate thus clearly affects diapir spacing.

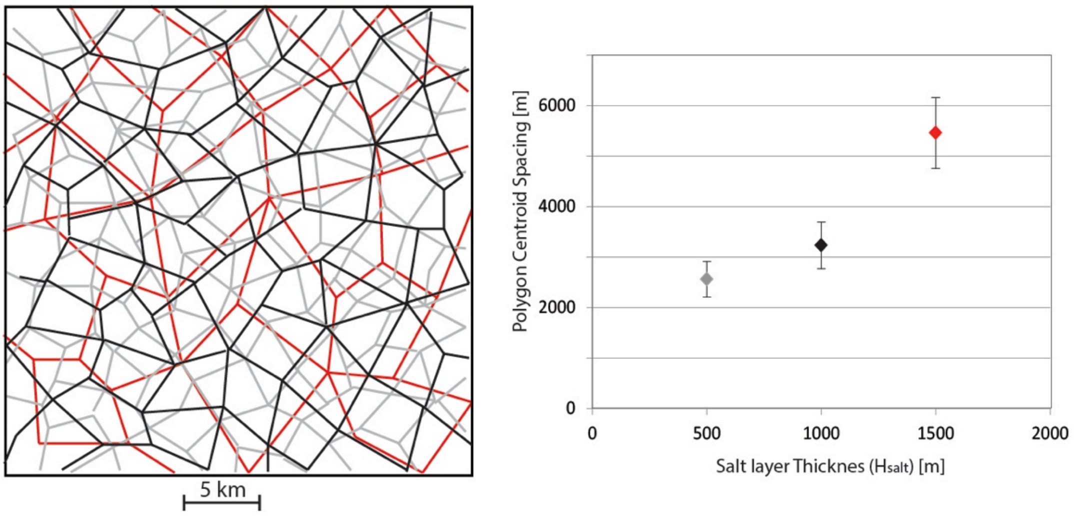

Figure 4.9. Comparison of the polygonal patterns for three different salt thicknesses (left panel): 500 meters (grey lines), 1000 meters (black lines) and 1500 meters (red lines). Graph on the right panel shows the mean polygon centroid spacing versus salt thickness. The same colour key for the salt thickness is used on the markers. Error bars indicate the standard deviation.

The results of the simulations show that the most important parameter in the initial polygonal patterns of the simulations is the thickness of the salt. In Figure 4.6, Figure 4.7 and Figure 4.8, simulations with the same parameters but different salt thicknesses are shown. For each salt thickness, simulations with different sedimentation rate are also shown. During the initial stages where the deposited sediment thickness is small, the salt has already started to flow and different areas start to accumulate more sediments than the surroundings. Initial patterns with higher salt topography below the sediments or with exposed salt show some patterns that exhibit a polygonal pattern (Figure 4.6, Figure 4.7 and Figure 4.8). Although the proposed polygonal patters in the figures are probably not the unique solution, it can be clearly observed that initial spacing, between polygons is smaller in simulations with a smaller salt thickness and vice versa (Figure 4.9). Spacing of the polygonal pattern has been calculated by measuring the distances between the centroids inside of the polygons and the average of the spacing and standard deviation is shown in the graph of Figure 4.9b.

The initial polygonal patterns do not change in terms of spacing between the polygons when different viscosities for the salt or the overburden are used (compare Figure 4.6 and Figure 4.10). The initial polygonal pattern is quite similar for all simulations with a salt thickness of 1000 meters (Figure 4.6, Figure 4.10 and Figure 4.11). The fact that not only the spacing is similar in these simulations with same salt thickness, but also that the same polygonal pattern can be fitted, is due to the use of the same random noise in all the simulations. The lack of effect of the viscosities in the initial patterns is related to the fact that the instability develops for an overburden thickness that is much smaller than the salt layer and the impact of viscosity is overcome by the impact of the salt thickness itself.

4.4.3 Effect of sedimentation on down-building process

In our study we focus on 3D diapirs that develop from random noise where all the wavelengths are initially present. As we will show, the different sedimentation rates do not change the initial polygonal patterns when the same parameters are used; however whether these initial polygonal patterns survive during later stages in the simulation depends also on the sedimentation rate. The evolution of the initial salt ridges and the geometries of the minibasins depend on the feedback between the salt flow and sedimentation rate. In this work, we keep the sedimentation rate constant throughout the simulations. However, due to the way we implement the surface redistribution, the more salt is withdrawn from the minibasin the more this subsides and the more sediments can be deposited above.

The effect of the sedimentation rate that is observed in our simulations is two-fold. The first effect occurs during the very early stages when the instability is developing and the polygonal patterns form. When the initial sedimentation rate is low, the ridges of the polygonal pattern will be the prevalent structures. Higher sedimentation rates favor the localization of the salt flow towards ridge junctions, and therefore diapirs will be more prevalent than ridges.

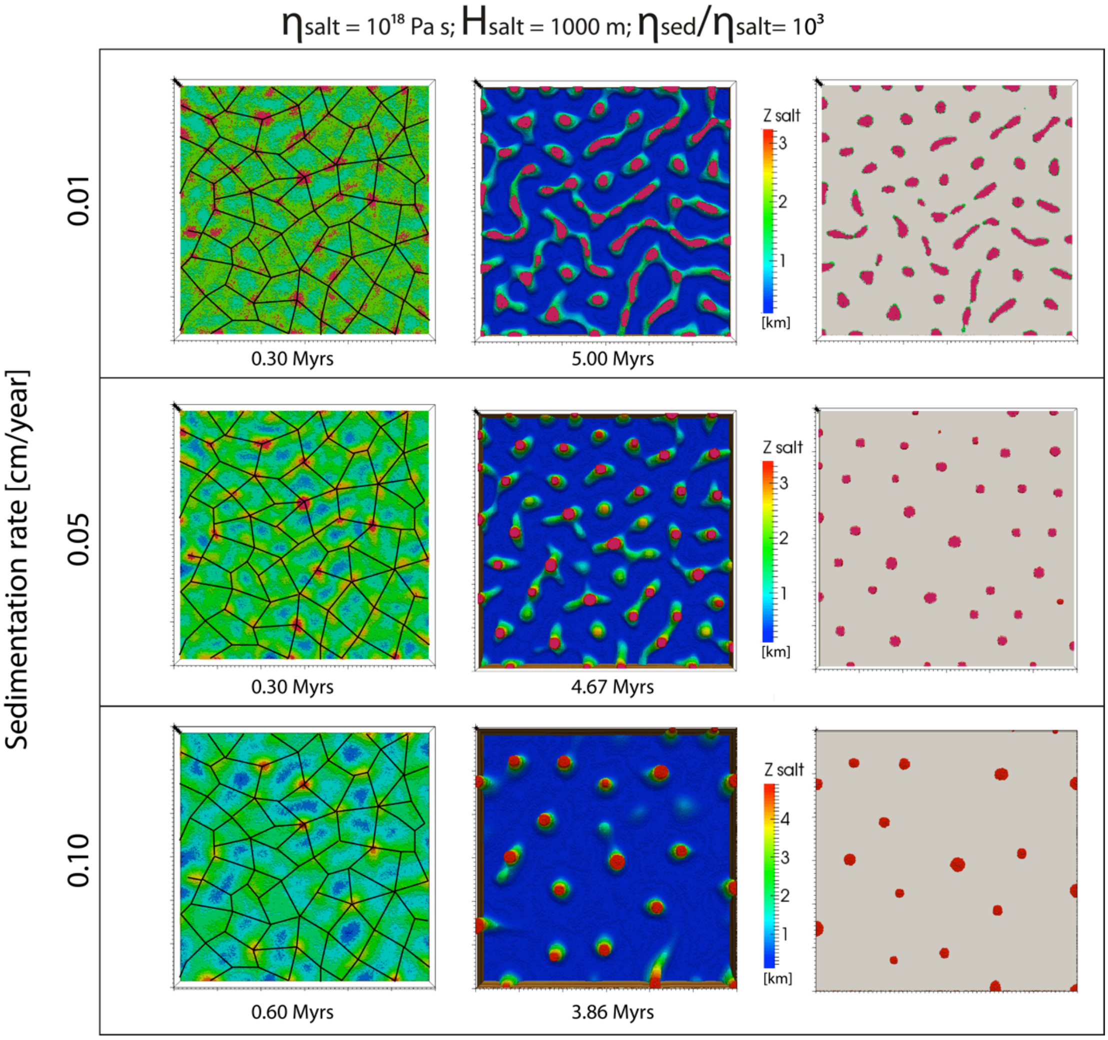

Figure 4.10. Map view simulations with different sedimentation rate. Compared to the example of Figure 4.6, the viscosity contrast between sediments and salt is higher. At higher sedimentation rates an increased number of diapirs is covered with sediments and does not extrude at the surface.

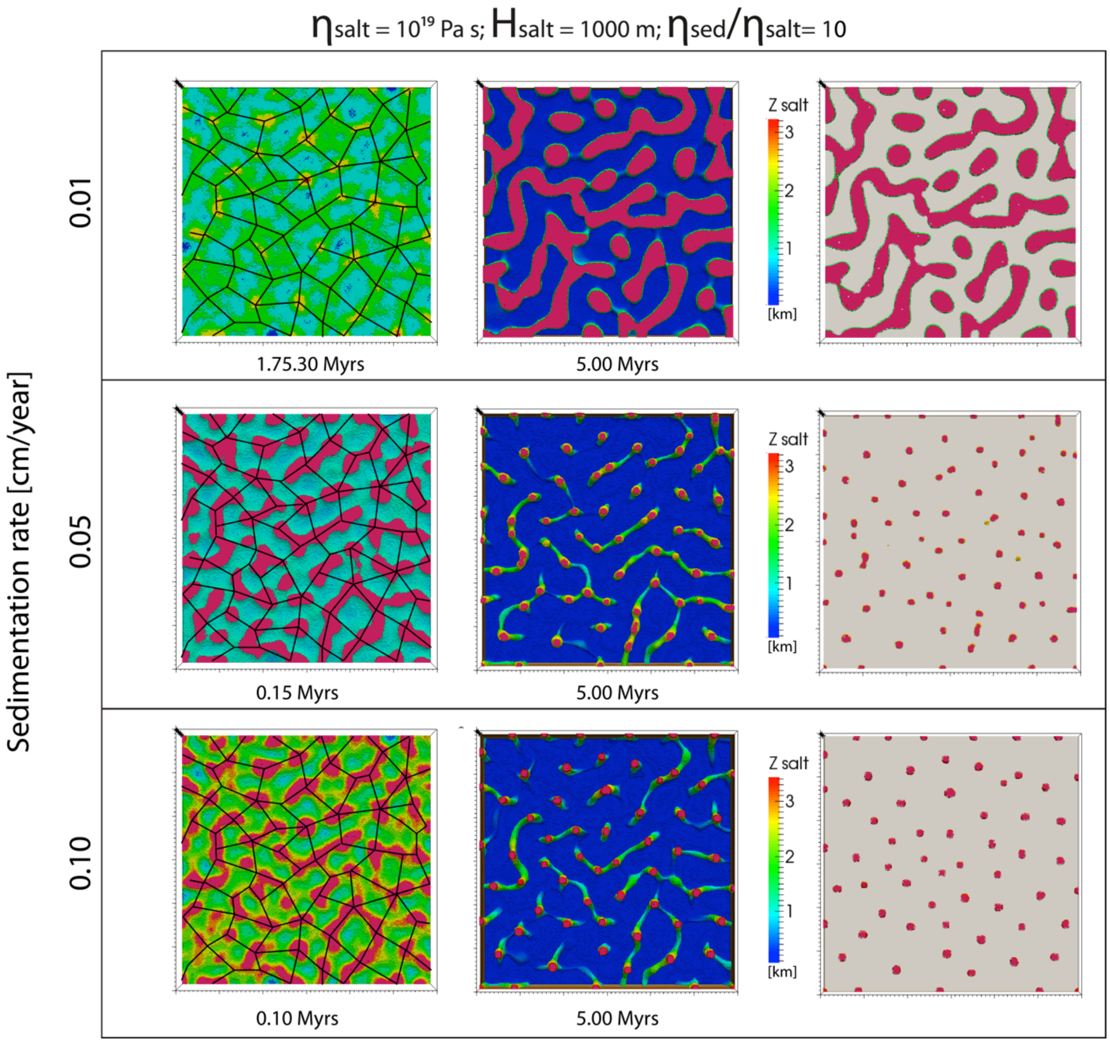

Figure 4.11. Map view of simulations with different sedimentation rate but with a salt viscosity of 10^{19} Pa s. During the initial stages the polygonal pattern is similar for all simulations (left panel) and can be recognized as well during more evolved stages in simulations with higher sedimentation rate.

This effect of sedimentation rate can be observed in the examples of Figure 4.6, Figure 4.7, Figure 4.10 and Figure 4.11. In the right panel of the figures, a map view of the salt exposed at the surface (at the internal free surface of the simulations) in pink/red color is shown. In the mentioned examples, simulations with the lowest sedimentation rate of 0.01 cm/years salt are not well covered by sediments and therefore the salt ridge systems are prevalent initially. The result is that during the more advanced stages, the diapirs that will be exposed at the surface (right panels in Figure 4.6, Figure 4.7, Figure 4.10 and Figure 4.11) are more elongated or linear (e.g. Figure 4.10 with sedimentation rate 0.01 cm/year). On the contrary, at higher sedimentation rates, the salt exposures at the surface are circular in shape, indicating finger like diapirs below. These finger-like diapirs might be either completely isolated from the ridge (e.g. Figure 4.10 with sedimentation rate 0.1 cm/year) or connected and rising from the salt ridge underneath (Figure 4.10 with sedimentation rate 0.05 cm/year).

The second effect of sedimentation occurs during more advanced stages. When finger-like or dome-like diapirs develop in the simulations, a high sedimentation rate can in some cases cover them and keep them buried (e.g. Figure 4.10 with sedimentation rate 0.05 cm/year). This burying of diapirs happens mainly when the salt has been withdrawn from below the minibasins, and as a result less salt can flow into the diapir. When this happens, the salt rising velocity (salt extrusion velocities) can be lower than that of the sedimentation rate. For higher sedimentation rates, the covering of diapirs with sediment happens during earlier stages and they will look like buried salt domes (e.g. Figure 4.10 with sedimentation rate 0.1 cm/year).

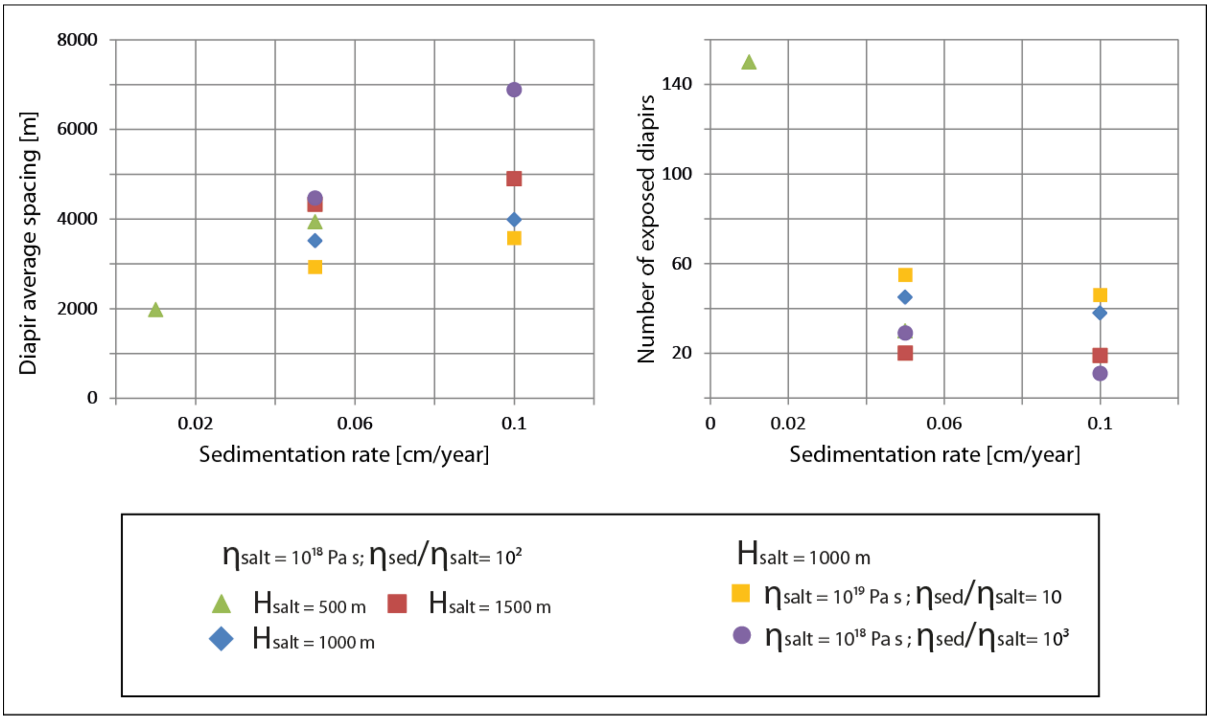

Figure 4.12. Effect of different sedimentation rates in five different simulations (see symbols). The measurements were performed with the salt exposure at the final stages of the simulations but are limited to the simulations were exposures were isolated patches (higher sedimentation rates). Left plot shows the change in average exposed diapir spacing with varying sedimentation rate. The overall trend is that higher sedimentation rate results in higher average spacing because less diapirs are exposed at the surface. The number of diapirs exposed at the surface is shown in the right plot.

The fact that diapirs can be covered by sediments and buried during early stages of their development implies that from the same initial polygonal pattern, different number of diapirs will be exposed at the surface. If we only consider the more developed diapirs that remain exposed at the surface and compare them to the initial polygonal patterns, we can see the important effect of sedimentation rate. The number of exposed diapirs at the final stage and their average spacing was calculated for different sedimentation rate of the examples shown in Figure 4.6, Figure 4.7, Figure 4.8, Figure 4.10 and Figure 4.11. With the lowest sedimentation rates, some simulations show a continuous pattern of linear salt structures exposed at the surface (e.g. Figure 4.6 and Figure 4.7 with sedimentation rate 0.01 cm/year) instead of isolated features and could not be used to calculate spacing. The number of diapirs and their average spacing in simulations with salt exposures formed by isolated diapirs is plotted in Figure 4.12. Clearly, there is an overall tendency for higher sedimentation rate to result in less exposed diapirs and therefore a higher average spacing between them (Figure 4.12).

4.4.4 Salt extrusion velocities and sediment geometries

Salt withdrawal sedimentary basins or minibasins are syn-sedimentary basins that subside into salt (Jackson and Talbot, 1991). The removal of salt underlying the basin creates the space for the basin to subside and accommodate new sediments. They are common features in many salt tectonic provinces such as the Gulf of Mexico and offshore Brazil among others. Minibasins attain an important economic interest since they are host to important hydrocarbon reservoirs in salt tectonic provinces. The mechanism by which the minibasin starts to subside into the salt cannot be due to buoyancy of salt alone (Hudec et al., 2009), as non-compacted siliciclastic sediments have a density that is lower than that of the salt. The average density required for the minibasins to subside into the salt is only attained after several hundreds of meters thickness is reached (Hudec et al., 2009). With this in mind, it is important to realize that the salt extrusion velocities measured in our simulations result from a purely buoyancy driven subsidence into the salt and are therefore an overestimation. Yet, it is nevertheless interesting to establish a relationship between the minibasin subsidence velocity and the sediment geometry at the contact to the salt diapirs, also because density-driven subsidence of minibasins is of major importance in formation of diapirs despite its limitations to initiate those (Hudec et al., 2009).

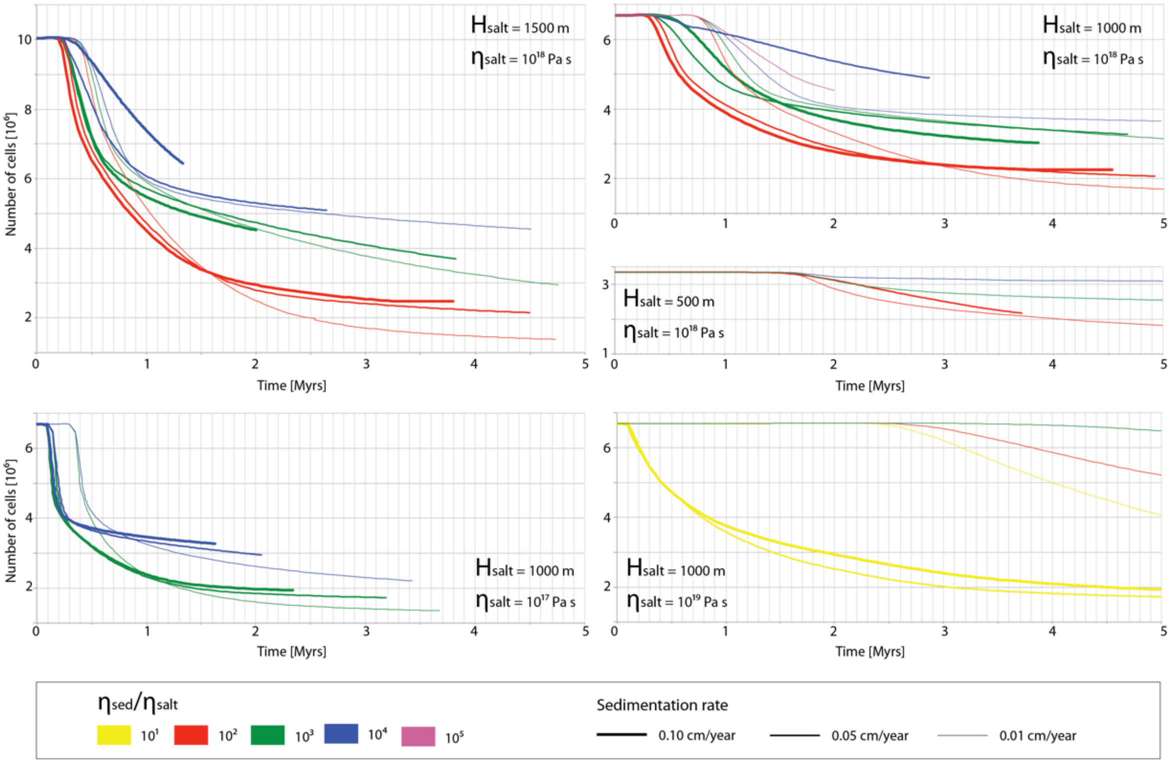

Figure 4.13. Graphs showing the evolution of the number of salt phase cells in the numerical simulation for different salt viscosities and different salt thicknesses. The graphs clearly show the varying time of onset of salt extrusion at the surface (which is the point when salt cells start to decrease). Slopes of the extrusion velocity change for the different parameters of the simulations, but in most of the cases three stages can be distinguished: a flat initial stage before the salt is exposed at the surface, followed by a very steep slope when the minibasins are subsiding into the salt and cause salt extrusion, and the final stage after all salt is withdrawn from beneath a minibasins (less steep slope).

Due to the implementation of the fast erosion boundary condition, a volume of salt will be extruded and eroded according to the implemented boundary condition each time step. The amount of salt that is extruded depends on the overall salt movement due to the sinking of the minibasins around the diapir itself once the diapirs have reached the surface. We measured the evolution of the volume of salt through time in the simulations. For this purpose, we have plotted the number of salt phase cells in each of the numerical outputs through time in Figure 4.13. The colours of the lines indicate different viscosity contrast between sediment and salt, whereas the width of the line depends on the sedimentation rate. The curve of the measured volume shows three different slopes that can be related to the dynamics of the system itself. Initially, the graph has a flat part (no salt volume change), which can be related to the time that the salt needs to move through the sediment and reach the surface. Once the salt is at the surface it starts to be extruded and this is observed in the graphs as a steep slope that is related to the sinking of the minibasins. This steep slope is disrupted once all the salt is drained from beneath the minibasin. From this moment on, the extrusion of salt occurs due to the squeezing of the ridges and diapirs of salt and therefore the slope is less steep than before.

Overall, the time required for the salt volume to decrease significantly is longer for smaller sedimentation rates of 0.01 cm/year in the simulations with the same parameters. For similar parameters, simulations with smaller initial salt thickness (500 meters) also require longer times (e.g. 1.4-1.8 Myrs) for the salt volume to start decreasing, instead of the shorter times (< 0.5 Myrs) for the thicker initial salt thickness (1500 meters).

Two examples in which there is an initial long stage before the diapirs reach the surface correspond to the simulations with salt viscosity of 10^{19} Pa s and sedimentation rates of 0.01 cm/year (Figure 4.13, right bottom graph), and to simulations with a salt viscosity of 10^{18} Pa s and a salt thickness of 500 meters (Figure 4.13, right mid graph). In the case of the simulations with salt viscosity of 10^{19} Pa s, between 2.5 and 3 Myrs are needed before there is a significant extrusion of salt (Figure 4.13, right bottom graph). On the simulations with a salt viscosity of 10^{18} Pa s and a salt thickness of 1000 meters, around 1.4 Myrs is needed before most of the diapirs are exposed at the surface (Figure 4.13, right mid graph). In both cases, there is a significant amount of sediments deposited around the diapirs at the moment the diapir makes it through the sediments onto the surface. To better illustrate this process, we show cross-sections of the model for different time steps (Figure 4.14). Before the diapir reaches the surface the sediment layers that are being deposited on the minibasins are being eroded above the diapir (Figure 4.14, 1.50 Myrs). This, results in clear unconformities around the diapir that record the moment at which they reached the surface. Below the unconformity the deformation of the layer is mainly related to a phase of active diapirism (Figure 4.14).

The higher the viscosity contrast between sediment and salt, the shorter time is required to start salt extrusion, and the steeper the extrusion curve will be initially (e.g. Figure 4.13, left top panel).

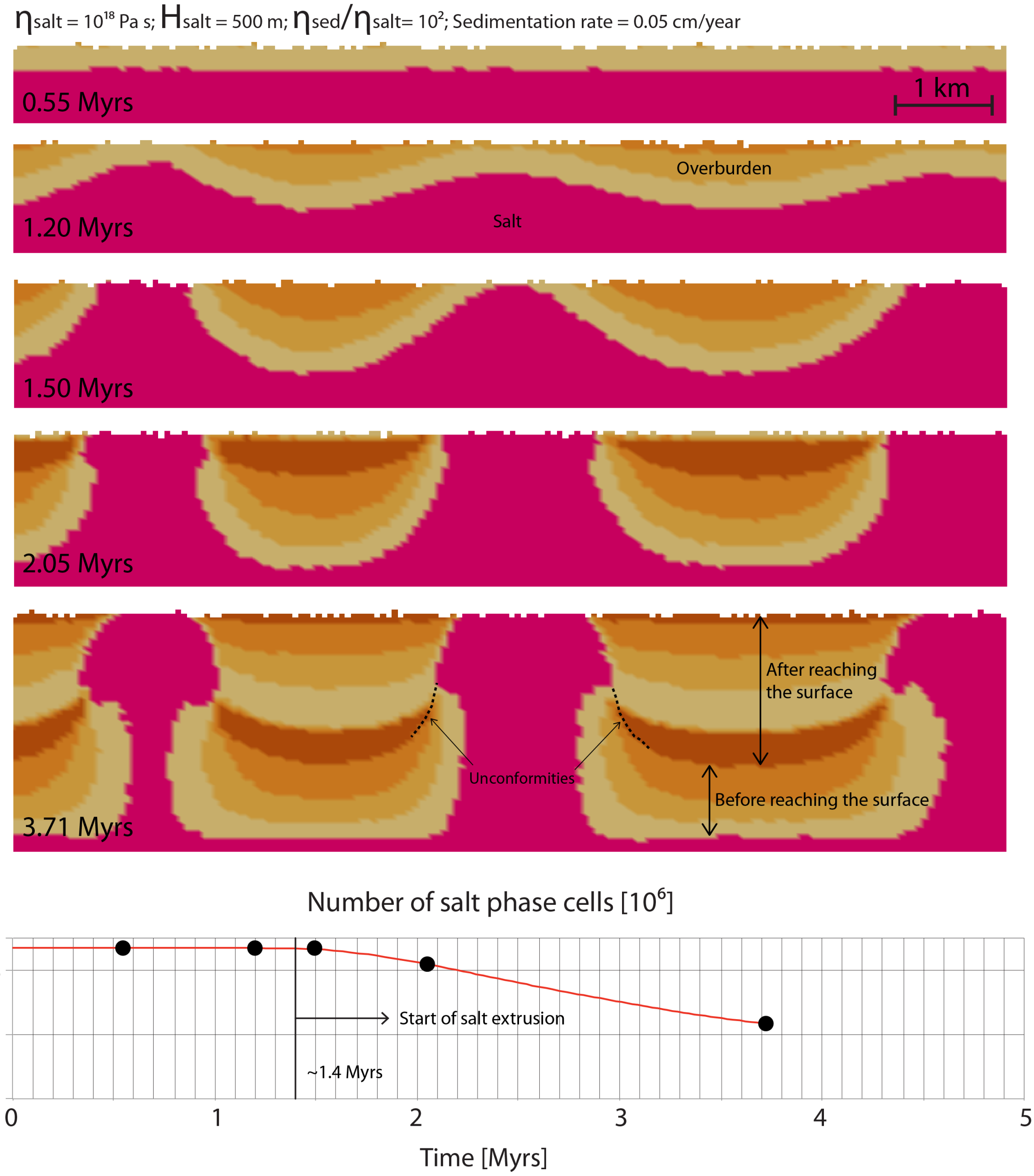

Figure 4.14. Cross section view illustrating the development of diapirs with an initial active phase followed by a later downbuilding phase. Each sedimentary layer in the overburden is formed in a time-span of 0.5 Myrs.The graph shows the evolution of the salt phase cells for the time steps (black dot) that correspond to the cross sections. The diapirs need around 1.4 Myrs before reaching into the surface. From that time onwards, the diapirs are kept at the surface allowing salt extrusion. The transition between those two stages of diapir history is marked by the development of unconformities close to the diapirs (marked in the central diapir with dashed lines).

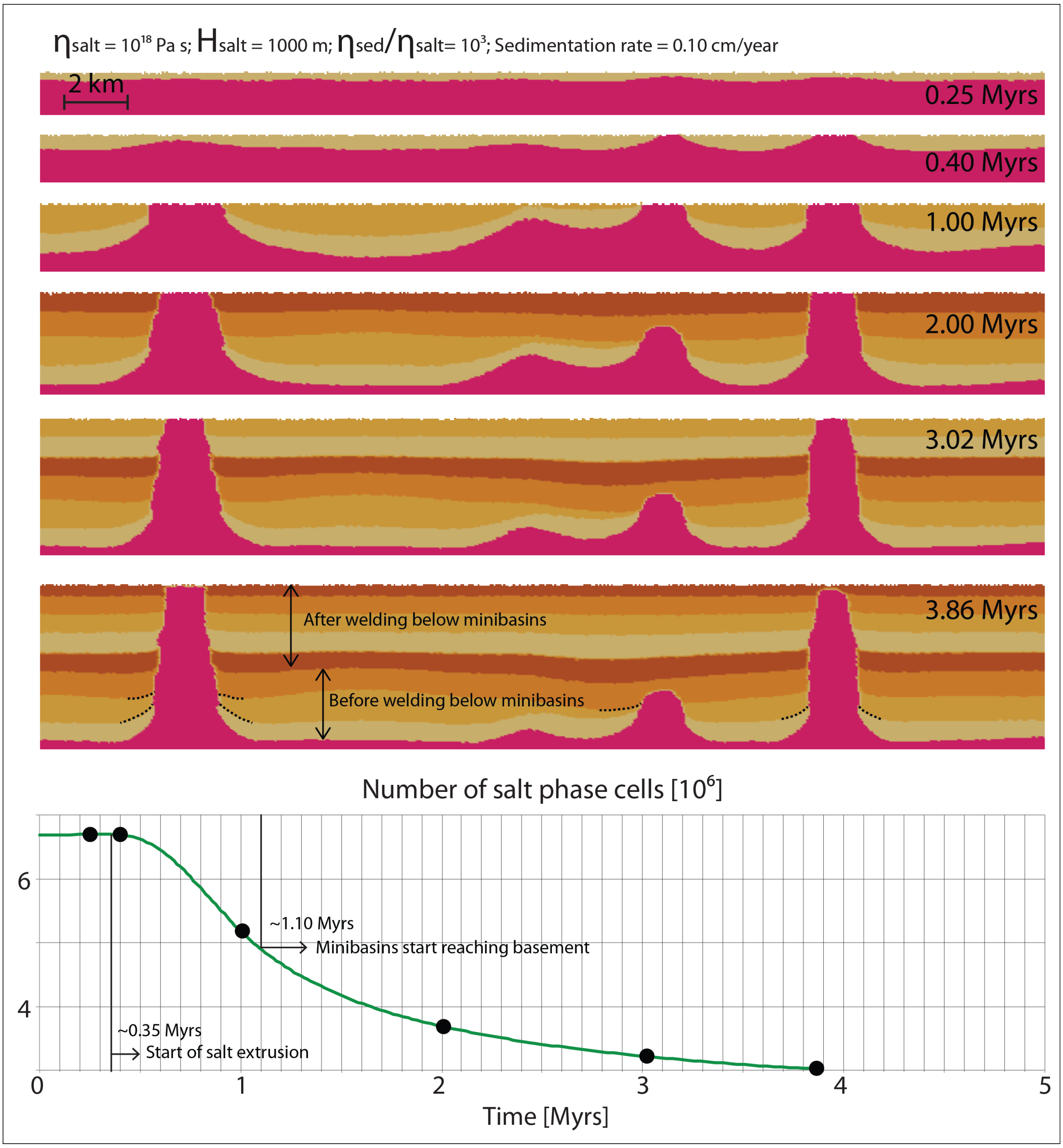

Figure 4.15. Cross sections illustrating the evolution of diapirs with an initial short active phase and a subsequent down-building phase. The transition between the two stages is marked with the dashed lines that indicate unconformities. The graph shows the evolution of the salt phase cells for the time steps (black dot) that correspond to the cross sections. The sediment layers above the unconformities are almost horizontal and truncated against the salt without deformation, as a result of a downbuilding phase.

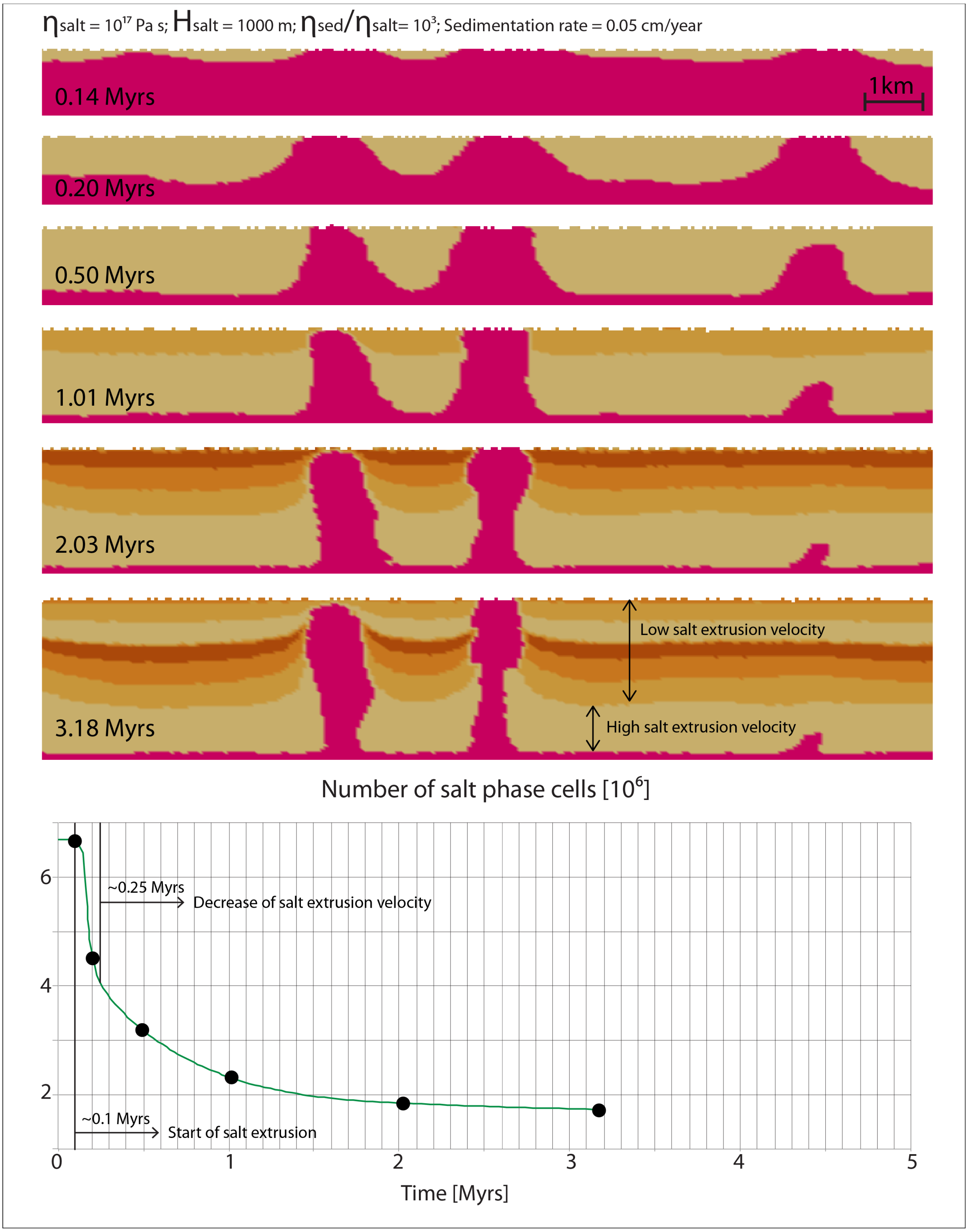

Figure 4.16. Cross sections illustrating the evolution of diapirs with a very short time lapse before salt starts to be extruded. The graph shows the evolution of the salt phase cells for the time steps (black dot) that correspond to the cross sections. As soon as salt starts to extrude, the velocity is very high for a short period until around 0.25 Myrs. At that time salt extrusion velocity decreases, which can be clearly observed by the different thickness of the deposited sediment layers (each sedimentary layer is deposited in 0.5 Myrs).

In most of the curves of Figure 4.13, the slope changes quite gradually from the initial extrusion velocity to the final extrusion velocity (e.g. Figure 4.13, right top panel). However, salt viscosity of 10^{17} Pa s (Figure 4.13, left bottom panel) show an abrupt change in the slope. Because the sediment phase change has been fixed to a time of 0.5 Myrs, the relative thickness of the different layers within the models also offers some insights into the salt extrusion history during the simulations. Cross-section views of a simulation with a gradually changing extrusion slope are shown on Figure 4.15 (corresponding to a sedimentation rate of 0.1 cm/year). The cross sections show when the initial unconformities related to the salt reaching the surface form (Figure 4.15, 0.4 Myrs). After the diapirs reach the surface, they are kept at the surface through their evolution, growing by purely passive diapirism. The result is that the stratigraphic contacts are completely horizontal and end abruptly against the diapir. The fact that the slope of extrusion changes gradually results in a gradual, almost no noticeable, change in the thickness of the sediment layers.

Figure 4.16 shows a simulation in which the salt extrusion velocity is very fast for a short period once salt is extruded to the surface (between 0.10 – 0.25 Myrs). At 0.25 Myrs the extrusion velocity is considerably decreased. Although the slope change is not as abrupt as in simulations with the same parameters but lower sedimentation rates (see other curves of Figure 4.13, left bottom panel), the velocity change is more marked than in previous examples. In the sediment layers this change in velocity can be identified as a change from the thick layers (before the minibasins reach the bottom of the model domain) to the thinner sediment layers after (Figure 4.16).

4.5 Discussion

Although gravity loading has been proposed as the mechanism that can maintain the diapirs growing once they have been initiated, it has been discarded as the mechanism that can alone initiate the process. The reason for that is that when sediments are deposited above the salt their density is lower than that of the salt, and it is only during further deposition and compaction of sediments that a density inversion can occur. Depending on empirical compaction curves, the estimated thickness of sediments to attain an average higher density than that of the salt ranges between 600 (Nettleton, 1934) and 1500 m (Hudec et al., 2009). This basically implies that the minibasins would not subside in the salt unless that thickness is reached. Therefore a different mechanism is needed to explain how diapirs start. Numerical models by Poliakov et al. (1993) have considered the effect of compacting sediments by implementing empirical depth dependent density curves from Nettleton (1934). Taking into account depth-density curves shows that there is indeed a minimum sediment thickness that must be acquired before density driven flow starts and diapirs form by an initial pure Rayleigh-Taylor instability (Poliakov et al., 1993). Once the diapirs have reached the surface, their shape is strongly influenced by the sedimentation rate (Poliakov et al., 1993). Chemia et al. (2008) and Fuchs et al. (2011) considered a density of the sediments initially higher than the one of the salt and therefore triggered the diapirs by differential loading.

The patterns that are discussed in this work are the result of Rayleigh-Taylor instability during the initial stage of simulations, when denser sediments start to deposit above the salt. Therefore, they are probably not exactly the same as if a different mechanism for the initiation of the diapirism is considered. However, the influence of the different investigated parameters will probably hold. Although the subsidence velocities of the minibasins during the simulations would also be different, the fact that the subsiding velocity is maximum at the beginning of the diapirism can still apply. Also, the relation of the velocity history of the minibasins with the geometries developed around the diapirs is applicable to diapirs initiated by different mechanism but maintained by differential loading.

Initiation of diapirs and minibasin subsidence remains a matter of debate. The fact that initially non-compacted sediments have densities that are lower than that of the salt, poses a problem for diapir initiation by differential loading only. Many mechanisms have been proposed to explain how diapirs are initiated. It has, for example, been recognized that salt upwelling is related to regional extension in some cases and extension is thus considered a possible trigger of diapirism (Jackson and Vendeville, 1994). Regional shortening can also potentially initiate diapirism as it was shown in analogue models by Bonini (2003) and Roca et al. (2006). More recently, the effect of compression has been quantified (Ings and Beaumont, 2010). In any case, once diapirs are initiated the importance of the process of differential loading and down-building cannot be ignored.

4.6 Conclusions

We have presented several 3D simulations of down-built diapirs to illustrate the key parameters that influence diapir pattern formation as well as the shape of individual diapirs. Results highlight the importance of the sedimentation rate.

Initial sedimentation causes a flow that initiates the development of a salt ridge system where the ridges delimit polygonal shaped basins (minibasins). The salt diapirs start to form at the junctions of the salt ridges by being feed by the salt flow along the ridges. The 3D patterns are related to the physical parameters of the simulations in a similar way as they are related to the characteristic wavelength in 2D works.

In accordance with previous 2D work (Fuchs et al., 2011) the down-building regime is favoured by low sedimentation rates and low viscosity contrasts. At relative high viscosity contrast and sedimentation rates, diapirs are never initiated or are stopped at their early stages (only salt ridges or salt pillows are formed). However, the effect of the sedimentation rate has been further studied in our work, and has two other effects. Firstly, lower sedimentation rates favour the preservation of salt ridges and result in more elongated exposed diapirs, whereas higher sedimentation rates favour the formation of dome or finger-like diapirs that initiate at the junctions of the salt ridges. Secondly, sediments can cover diapirs at more advanced model stages when the salt extrusion velocities are lower than the sedimentation rate. As a result, not all of the initially formed diapirs will be exposed at the surface and therefore a higher sedimentation rate will result in a larger spacing between the exposed diapirs.

We quantified the velocity of salt extrusion through time. The resulting curves have different slopes through time depending on the physical parameters of the simulations. We have shown that the shape of the extrusion curves can be related to the geometries of the sediments around diapirs.

4.7 Acknowledgements

Funding was provided by the European Research Council under the European Community's Seventh Framework program (FP7/2007-2013) ERC Grant agreement #258830. 3D simulations were performed on MOGON supercomputer of Johannes Gutenberg University Mainz, Germany.

4.8 References

Biot, M., and Odé, H., 1965, Theory of gravity instability with variable overburden and compaction: Geophysics, v. 30, p. 213-227.

Biot, M.A., 1966, Three-dimensional gravity instability derived from two-dimensional solutions: GEOPHYSICS, v. 31, p. 153-166.

Bonini, M., 2003, Detachment folding, fold amplification, and diapirism in thrust wedge experiments: Tectonics, v. 22, p. 1065.

Burg, J.-P., Kaus, B.J.P., and Podladchikov, Y.Y., 2004, Dome structures in collision orogens: Mechanical investigation of the gravity/compression interplay: Geological Society of America Special Papers, v. 380, p. 47-66.

Chemia, Z., Koyi, H., and Schmeling, H., 2008, Numerical modelling of rise and fall of a dense layer in salt diapirs: Geophysical Journal International, v. 172, p. 798-816.

Crameri, F., Schmeling, H., Golabek, G.J., Duretz, T., Orendt, R., Buiter, S.J.H., May, D.A., Kaus, B.J.P., Gerya, T.V., and Tackley, P.J., 2012, A comparison of numerical surface topography calculations in geodynamic modelling: an evaluation of the 'sticky air' method: Geophysical Journal International, v. 189, p. 38-54.

Dixon, J.M., 1975, Finite strain and progressive deformation in models of diapiric structures: Tectonophysics, v. 28, p. 89-124.

Fuchs, L., Schmeling, H., and Koyi, H., 2011, Numerical models of salt diapir formation by down-building: the role of sedimentation rate, viscosity contrast, initial amplitude and wavelength: Geophysical Journal International, v. 186, p. 390-400.

Guerra, M.C.M., and Underhill, J.R., 2012, Role of halokinesis in controlling structural styles and sediment dispersal in the Santos Basin, offshore Brazil: Geological Society, London, Special Publications, v. 363, p. 175-206.

Hudec, M.R., Jackson, M.P.A., and Schultz-Ela, D.D., 2009, The paradox of minibasin subsidence into salt: Clues to the evolution of crustal basins: Geological Society of America Bulletin, v. 121, p. 201-221.

Ings, S.J., and Beaumont, C., 2010, Shortening viscous pressure ridges, a solution to the enigma of initiating salt 'withdrawal' minibasins: Geology, v. 38, p. 339-342.

Ismail-Zadeh, A., Tsepelev, I., Talbot, C., and Korotkii, A., 2004, Three-dimensional forward and backward modelling of diapirism: numerical approach and its applicability to the evolution of salt structures in the Pricaspian basin: Tectonophysics, v. 387, p. 81-103.

Ismail-Zadeh, A.T., Talbot, C.J., and Volozh, Y.A., 2001, Dynamic restoration of profiles across diapiric salt structures: numerical approach and its applications: Tectonophysics, v. 337, p. 23-38.

Jackson, M.P.A., Talbot, C.J., and Cornelius, R.R., 1988, Centrifuge Modeling of the Effects of Aggradation and Progradation on Syndepositional Salt Structures (Report of Investigations, No 173).

Jackson, M.P.A., and Vendeville, B.C., 1994, Regional extension as a geologic trigger for diapirism: Geological Society of America Bulletin, v. 106, p. 57-73.

Jackson, P.A., and Talbot, C.J., 1991, A Glossary of Salt Tectonics, Bureau of Economic Geology, University of Texas at Austin.

Kaus, B.J.P., 2005, Modelling approaches to geodynamic processes, PhD Thesis, ETH-Zurich.

Kaus, B.J.P., and Podladchikov, Y.Y., 2001, Forward and reverse modeling of the three-dimensional viscous Rayleigh-Taylor instability: Geophysical Research Letters, v. 28, p. 1095-1098.

Kent, P.E., 1979, The emergent Hormuz salt plugs of southern Iran: Journal of Petroleum Geology, v. 2, p. 117-144.

May, D.A., 2012, Volume reconstruction of point cloud data sets derived from computational geodynamic simulations: Geochemistry, Geophysics, Geosystems, v. 13, p. Q05019.

Nettleton, L.L., 1934, Fluid mechanics of salt domes: AAPG Bulletin, v. 18, p. 1175-1204.

Poliakov, A.N.B., van Balen, R., Podladchikov, Y., Daudre, B., Cloetingh, S., and Talbot, C., 1993, Numerical analysis of how sedimentation and redistribution of surficial sediments affects salt diapirism: Tectonophysics, v. 226, p. 199-216.

Ramberg, H., 1967, Gravity, deformation and the earth's crust, Academic P.

Ramberg, H., 1968a, Instability of layered systems in the field of gravity. I: Physics of the Earth and Planetary Interiors, v. 1, p. 427-447.

Ramberg, H., 1968b, Instability of layered systems in the field of gravity. II: Physics of the Earth and Planetary Interiors, v. 1, p. 448-474.

Roca, E., Sans, M., and Koyi, H.A., 2006, Polyphase deformation of diapiric areas in models and in the eastern Prebetics (Spain): AAPG Bulletin, v. 90, p. 115-136.

Rowan, M.G., and Vendeville, B.C., 2006, Foldbelts with early salt withdrawal and diapirism: Physical model and examples from the northern Gulf of Mexico and the Flinders Ranges, Australia: Marine and Petroleum Geology, v. 23, p. 871-891.

Schmeling, H., 1987, On the relation between initial conditions and late stages of Rayleigh-Taylor instabilities: Tectonophysics, v. 133, p. 65-80.

Talbot, C.J., 1992, Centrifuged models of Gulf of Mexico profiles: Marine and Petroleum Geology, v. 9, p. 412-432.

Talbot, C.J., Rönnlund, P., Schmeling, H., Koyi, H., and Jackson, M.P.A., 1991, Diapiric spoke patterns: Tectonophysics, v. 188, p. 187-201.

van Keken, P.E., Spiers, C.J., van den Berg, A.P., and Muyzert, E.J., 1993, The effective viscosity of rocksalt: implementation of steady-state creep laws in numerical models of salt diapirism: Tectonophysics, v. 225, p. 457-476.

Vendeville, B.C., and Jackson, M.P.A., 1992a, The fall of diapirs during thin-skinned extension: Marine and Petroleum Geology, v. 9, p. 354-371.

Vendeville, B.C., and Jackson, M.P.A., 1992b, The rise of diapirs during thin-skinned extension: Marine and Petroleum Geology, v. 9, p. 331-354.

Woidt, W.D., 1978, Finite element calculations applied to salt dome analysis: Tectonophysics, v. 50, p. 369-386.

Chapter 5

Reverse modelling of 2D and 3D salt structures

Abstract

Forward modelling of salt diapirs formed by either buoyancy (up-building or active diapirism) or as a result of differential loading is well established. Such models typically start with an initial horizontal salt layer and model their evolution forward in time. Previous work demonstrated that it is possible to perform reverse modelling of active diapirism, which starts with the present-day observed geometry and models it backwards in time. Both two and three-dimensional models using simple rheologies for the salt and overburden (Kaus and Podladchikov, 2001) showed that such dynamic retro-deformation is possible as long as the correct material parameters are employed for the reverse simulation. If incorrect parameters are employed, it is often not possible to make the initial salt layer horizontal which makes reverse modelling a technique that also constrains the material parameters. However, retro-deformation of down-building diapirs (which is syn-depositional process in which salt structures grow while sediments are being deposited) using mechanical codes has only been done in two dimensions (Ismail-Zadeh et al., 2001) for simple rheologies. Here, we have used a two-dimensional visco-elasto-plastic finite element code and a three-dimensional parallel finite differences code to perform both forward and reverse simulations and to check the validity of a reversed time step method (Ismail-Zadeh et al., 2004; Ismail-Zadeh et al., 2001; Kaus and Podladchikov, 2001). Our focus is on retrodeformation of Rayleigh-Taylor instabilities with non-linear viscous rheologies and on down-built diapirs in 3D. Results show that modelled two and three dimensional salt structures formed by pure down-building can be retro-deformed to the geometry close to the initial one, if the correct rheological parameters and sedimentation rate history is employed. In that case, the retro-deformation thus provides insights into the deformation history of the studied salt structures.

Keywords: down-building, salt tectonics, passive diapirs, numerical modelling, reverse modelling, dynamic retrodeformation

5.1 Introduction

Retrodeformation or restoration of a geological cross section is the process by which the present day deformation state is reverted to a previous undeformed state. Although the concept of kinematically balanced and restorable section was established long time ago (Dahlstrom, 1969), the idea of conservation of area and length of strata was already introduced by Chamberlin (1910) in his depth-to-detachment calculation. Retrodeformation is a widely used technique in industry and academia because it allows to test and validate structural interpretations and to ensure the coherency of a model or interpretation (Gibbs, 1983).

Kinematic restoration was initially conceived as a 2D technique to be used to restore cross sections based on geometric rules such as conservation of lines length and of area. However the technique has also been extended to 2D map views (Cobbold, 1979; Rouby et al., 1993) and to 3D (Griffiths et al., 2002; Rouby et al., 2000). Some of the assumptions on which kinematic methods are based are that deformation can be modelled as plane strain and that length of stratigraphic contacts (and surface between those contacts) does not change during deformation. In order to comply with the mentioned assumptions, different kinematic deformation mechanisms were proposed such as flexural slip, vertical and inclined shear and tri-shear among others.

Due to the high mobility of salt and the intrinsic three-dimensional nature of its flow, the presence of salt poses an additional challenge to traditional kinematic restoration methods. Retrodeformation of cross sections in which salt is involved is of significant economic interest as many of world’s hydrocarbon provinces are located in sedimentary basins that are salt related (Archer et al., 2012). Therefore several works have been focused on retrodeformation in areas affected by salt tectonics (see Rowan and Ratliff (2012) for a recent review). Kinematic retrodeformation of salt structures have been performed for example in cross-section (Rowan, 1993; Rowan et al., 2003) and maps (Rouby et al., 1993; Yin and Groshong Jr, 2006). However, it is not always the case that the various problems that arise from retrodeformation of cross sections with salt are considered or mentioned (Rowan and Ratliff, 2012). Furthermore, specific geometric rules for section balancing of salt structures have been proposed (Hossack, 1995; Rowan, 1993) and best practices and potential pitfalls mentioned (Rowan and

Ratliff, 2012). Complexities that have been previously considered in the kinematic cross sections restoration of areas of salt tectonics include the compaction of sediments (Rowan 1993) and halokinetic sequences (Rowan et al., 2003) as defined in Giles and Lawton (2002).

Mechanical retrodeformation techniques on the other hand are of more recent application to geological problems. They are typically based on a continuum mechanics approach, where the medium deforms according to linear elastic constitutive laws (e.g. Guzofski et al., 2009; Maerten et al., 2006; Moretti et al., 2006). As opposed to kinematic methods, where the deformation mechanism is imposed (e.g. flexural slip, vertical shear etc.), in mechanical restoration techniques the kinematic mechanisms are not imposed and are an outcome of assigning physical properties and the application of the boundary conditions. Although they are an improvement over purely kinematic restoration methods because they are not based on the plain strain assumption of kinematic methods, they also have some pitfalls (Lovely et al., 2012). One of the main disadvantages is the fact that the imposed boundary conditions are different from the forces driving the forward geologic deformation and might therefore be unphysical (Lovely et al., 2012). For example, in traditional mechanical retrodeformation techniques, the boundary conditions are imposed such that one or more stratigraphic horizons are flattened. Because predefined faults are allowed to slip in order to reduce shear tractions the deformation propagates according to linear elastic constitutive laws. Due to the unphysical boundary conditions it has been argued that they are not equivalent to forward deformation models (Lovely et al., 2012).

Mechanical retrodeformation techniques are nowadays incorporated in many of the industry standard software packages. They provide an important tool to validate interpretations of large datasets and models that can also be developed within the same software package. They have thus become widely used both in academia and industry. However, besides the mentioned pitfalls, they still lack the ability to properly capture salt mobility and flow that completely depends on rheological parameters such as viscosity. In fact, one of the still debated properties of salt is its rheological behaviour at long term with published viscosity values of Newtonian rheologies between 10^{17}-10^{20} Pa s (Mukherjee et al., 2010), and exponential coefficients of up to 5 for non-linear viscous rheology, representing the dislocation creep mechanism of coarse grained salt (Urai et al., 2008).

A more recent retrodeformation approach, usually referred as dynamic retrodeformation (after Lechmann et al., 2010) is also based on the continuum mechanics approach. It consists in taking the present-day geometry of the geological structures and use it as an initial condition for a reverse model. One of the main differences with respect to the mechanical retrodeformation discussed in the previous paragraph is the application of boundary conditions that are equivalent to reversing the forces that drove the deformation forward. Dynamic retrodeformation has been successfully tested for fold structures using either power law viscous materials (Frehner et al., 2012; Lechmann et al., 2010) or linear viscous materials in 3D (Schmalholz, 2008). In the case of dynamic unfolding, the forward modelling is done by applying extension (instead of compression) that effectively corresponds to a reverse timing modelling approach. The reverse time modelling approach has also been previously used to retrodeform salt structures (Ismail-Zadeh et al., 2004; Ismail-Zadeh et al., 2001; Kaus and Podladchikov, 2001). The works by Ismail-Zadeh et al. (2004) and Kaus and Podladchikov (2001), showed that a diapir formed by purely density driven buoyancy can be successfully retrodeformed using the reverse time approach as long as there are no strong overhangs present in the initial geometries. On the other hand, Ismail-Zadeh et al. (2001), had applied the same approach to restore 2D cross sections of a salt diapirs formed by down-building, where redistribution of material occurs at the topography.

Here, we show some new examples on how the dynamic retrodeformation technique (reverse time modelling) can successfully retrodeform salt diapirs formed by two different end-member processes (Figure 5.1): (1) buoyancy instability (i.e. Rayleigh-Taylor instability) or up-building in which the density difference between salt and overburden induces upward motion of salt and (2) a down-building or syn-depositional process in which salt structures grow while sediments are being deposited. Both processes have been extensively studied using forward numerical models, but few studies focus on the mechanical retrodeformation (reverse modelling) of salt diapirs, regardless their origin.

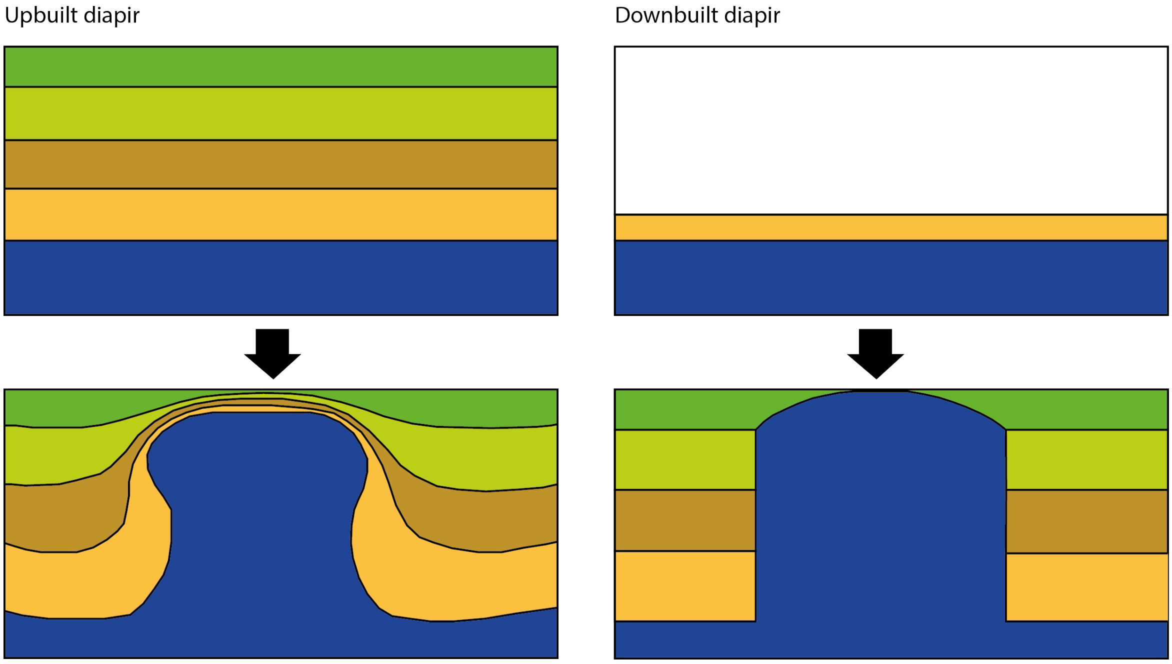

Figure 5.1. Cartoons of two different processes to form salt diapirs. Up-built (active) diapirs are formed by salt movement through the pre-halokinetic overburden. Down-built (passive) diapirs are formed by the upward movement of salt that is being pushed by the loading of new sediments that are deposited. Modified after (Hudec and Jackson, 2007).

To illustrate the validity of the method we show examples of dynamic retrodeformation (reverse modelling) of salt diapirs formed by up-building with a non-linear viscous rheology in 2D and salt diapirs formed by down-building in 3D using simple rheologies. Although some numerical issues are still to be solved related to the specific implementation of the algorithm that mimics the down-building processes, our results show that dynamic retrodeformation of salt structures could potentially be used to validate cross sections, and at the same time to constrain rheological parameters of the crust.

5.2 Method

In this study we perform forward and reverse simulations using numerical codes that assume continuum mechanics approximation where the equations used to describe geological processes consists of a set of balance equations for mass and momentum together with their constitutive relationships. Conservation of mass and momentum for slowly moving incompressible fluids are given by the following equations:

$$\frac{\partial v_i}{\partial x_i} = 0 \qquad [5.1]$$

$$-\frac{\partial P}{\partial x_i} + \frac{\partial \tau_{ij}}{\partial x_j} = -\rho g_i \qquad [5.2]$$

where i,j represent spatial directions and repeated indices are summed, v_i are the velocities, x_i are the coordinates, P = -$\sigma_{ii}/3$ is pressure, σ_{ij} are the components of the total stress tensor, τ the deviatoric stress tensor, ρ the density (no temperature dependent) and g, the gravitational acceleration.

A viscous constitutive law is used

$$\tau_{ij} = 2\eta_{eff}\, \dot{\varepsilon}_{ij} \qquad [5.4]$$

where $\dot{\varepsilon}_{ij}$ is the deviatoric strain rate tensor

$$\dot{\varepsilon}_{ij} = \frac{1}{2}\left(\frac{\partial v_i}{\partial x_j} + \frac{\partial v_j}{\partial x_i}\right) \qquad [5.5]$$

and η_{eff} is the effective viscosity given by

$$\eta_{eff} = 2\eta_0 \left(\frac{\dot{\varepsilon}_{II}}{\dot{\varepsilon}_0}\right)^{\frac{1}{n}-1} \qquad [5.6]$$

where η_0 is the viscosity at the reference strain rate $\dot{\varepsilon}_0$, which is is set to 10^{-15}s^{-1}, $\dot{\varepsilon}_{II}$ is the second invariant of the strain rate and n, the power law coefficient.

Two different numerical codes have been used in this study, a 2D sequential finite element code and a 3D parallel finite difference code. In each of the codes the equations [5.1] to [5.6] are discretized using different methods that will be briefly described next.

MILAMEN_VEP (Kaus, 2010) is a two dimensional finite element, visco-elasto-plastic code based on Matlab solvers (Dabrowski et al., 2008). MILAMIN_VEP has a Maxwell visco-elasto-plastic rheology (Kaus, 2010). In this work, however, we have focused in power-law viscous rheologies. In order to limit ourselves to non-linear viscous rheologies we have deactivated the effects of elasticity and brittle rheology in the code. The lower and upper viscosity cut-offs are 10^{16}Pa s and 10^{24} Pa s, allowing up to 8 orders of magnitude differences in the viscosity.

LaMEM (Lithosphere and Mantle Evolution Model) is a three-dimensional parallel code in which the equations [5.1] to [5.5] are discretized using a staggered grid finite differences scheme. Material properties are tracked using markers, here referred simply as particles. These particles are advected in a Lagrangian manner with the velocities obtained from solving the equations [5.1] and [5.2].

We employ linear viscous (Newtonian) rheology where the viscosity is constant for the defined material phases.

LaMEM uses PETSc Libraries and solvers that allow running massively parallel forward simulations. The internal free surface that allows topography to form is approximated in LaMEM by the “sticky air” approach, in which a low viscosity layer overlies the free internal surface. Recent bench mark studies have shown that the sticky air is a good approximation of the free surface in the finite differences method (Crameri et al., 2012). An implementation of the Voronoi cells for phases visualization as described in (May, 2012) is implemented in LaMEM, which optimized the visualization of the runs.

In LaMEM, diapir down-building processes are mimicked by using a fast erosion boundary condition on the internal free surface. The fast erosion sedimentation-erosion or sediment redistribution approach has been used in previous works (e.g. Kaus and Podladchikov, 2001; Poliakov et al., 1993) and it is basically a redistribution of the mass as follows: particles and internal free surface are advected according to the velocities obtained from the mechanical solvers of the code. Next, on top of the deformed internal surface a new layer of sediments is deposited, by calculating the corresponding thickness according to the time interval and the prescribed sedimentation rate. Particles of air phase are converted to the sediment phase. After that, the mean of the new topography is calculated and the free surface flattened to that height. The sediments above that surface are “eroded” by converting the sediment phase particles to air, whereas material is “deposited” below the surface, by converting the air particles to sediment phase. This process is summarized in Figure 5.2 (subfigures 1 to 4).

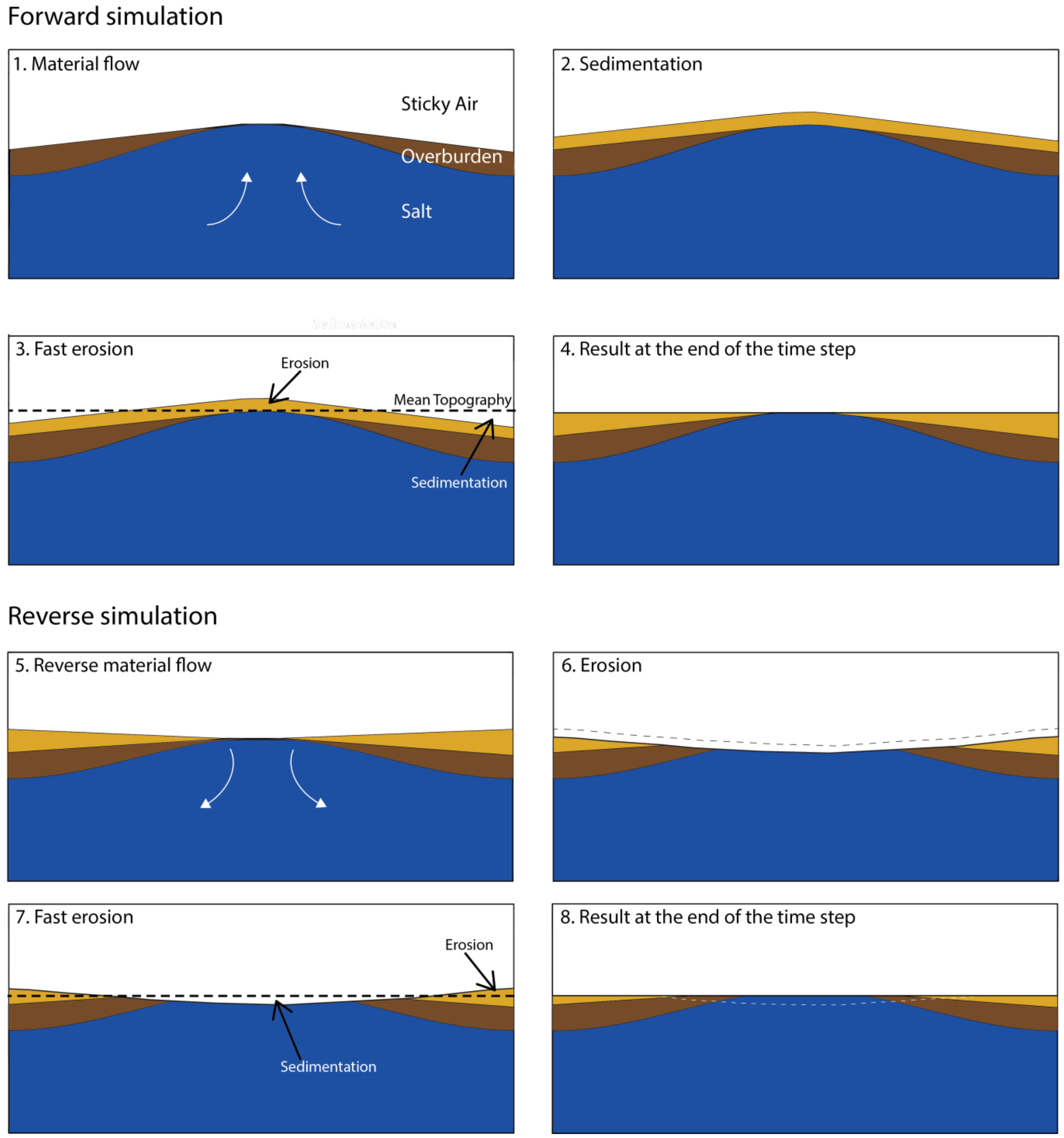

Figure 5.2. Schematic representation on how the down-building process of diapirs is implemented in our numerical code. Within each mechanical solver time step the following actions are performed: 1) Particles are advected according to the velocities calculated from the Stokes equations. 2) The amount of sediments depends on the time step interval and on the sedimentation rate. The new sediments are deposited above the topography. 3) The average topography that corresponds to the new topography is calculated. 4) The topography is flattened to the calculated mean (mimicking a fast erosion process), by converting sediment particles above to air (erosion) and air particles below to sediments (sedimentation). Steps are reversed in the case of reverse simulation as indicated by the schematic subfigures 5 to 8.

5.2.1 Reserve time step approach

Time dependency in the codes is introduced with the advection equation, which is given by

$$\frac{\partial \varphi_k}{\partial t} + v_i \frac{\partial \varphi_k}{\partial x_i} = 0 \qquad [5.7]$$

Markers (φ_k) coordinates evolve as:

$$\frac{\partial x_i}{\partial t} = v_i \qquad [5.8]$$

In the reverse time step approach, an intermediate (or final stage) from a forward simulation is used as a starting point and the simulation is performed using a negative time step. This is possible thanks to the characteristics of the advection equation, which has the same form for the forward and reverse velocity field (Ismail-Zadeh et al., 2001). The reverse time step approach has been successfully used in previous works (Ismail-Zadeh et al., 2004; Kaus and Podladchikov, 2001).

Besides the advection of the particles, time is also involved in the implementation of down-built diapirs within the 3D code (Figure 5.2). The specified sedimentation rate is used to add a sediment layer whose thickness depend on time. Therefore the topographic surface height at every new time step is given by

$$\mathit{Height}_{time+dt} = \mathit{Heigth}_{time} + dt \times \mathit{Sedimentation\ Rate} \qquad [5.9]$$

where dt is the time interval of the time step.

The physical meaning of the equation [5.9] changes whether we consider the forward or the reverse modelling. Within the forward simulations, the surface topography of the internal free surface increases by addition sediments (sedimentation). When a reverse time step approach is used, the negative time step will cause the surface topography to decrease by subtracting sediments (erosion). In the reverse time approach, after the particles have been advected according to the obtained velocities, the salt and sediments that were eroded in the forward simulations will need to be injected. The reversed process of the algorithm that is implemented in the code to mimic down-building processes is summarized in Figure 5.2 (subfigures 5 to 8).

5.3 Setup

We have performed 2D forward and reverse modelling simulations of active diapirism with power-law viscous rheologies. For the 2D simulations only one geometric setup was used. The 3D forward and reverse modelling of salt structures were aimed at diapirs formed by the two processes of active and passive diapirism (Figure 5.1). Therefore, we use two different geometric setups (Figure 5.3) one for each of the diapirism process. The setups are described in more detail next.

5.3.1 2D simulations

2D simulations have a resolution of 500x150 elements for a domain size of 25 x 2 km that results in a cell size of 50x14 meters (Figure 5.3). The 2D setup is a simple two-layer setup, with the interface between the two layers at a height of 1 km. All boundary conditions are free slip and the model is purely driven by density difference between the two layers. We have tested different viscosities of the two layers as well as different *n* exponents as listed in Table 5.1 (2D_RT_1 and 2D_RT_2).

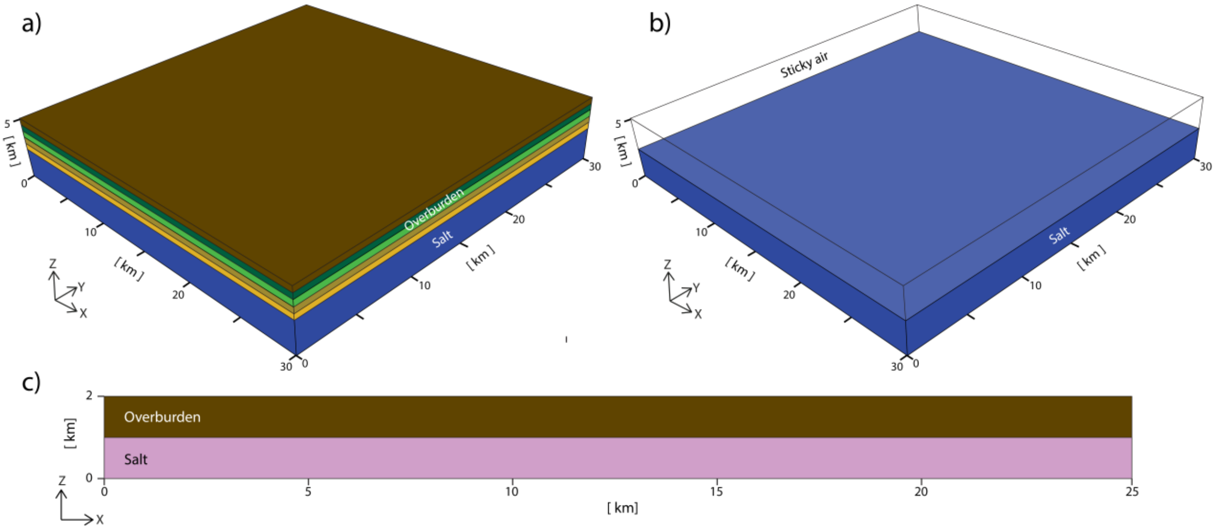

Figure 5.3. Initial setups used in the 3D forward simulations corresponding to the up-built/active diapirism (a) and to the down-built/passive diapirs case (b). Initial setup for the 2D simulations of Rayleigh-Taylor instability with non-linear rheologies is shown in c).

5.3.2 3D simulations

Two different 3D setups have been used in our work that correspond to the up-built and down-built diapirs simulations. In the case of the simulation of the up-built diapir, the setup has 128x128x32 cells for a domain of 30x30x5 km. The initial setup consists of a salt layer which is 2500 meters thick overlain by an overburden of 2500 meters composed of 5 different layers of 500 meters. Two different viscosities are used in the overburden to represent a multilayer sequence with three competent layers inter-bedded with weak layers (see Table 5.1, 3D_RT). Boundary conditions of the box are all free slip as in the case of the 2D simulations.

The setup of the down-built diapir consists of a 30x30x5 km domain, with 96x96x24 cells. We have omitted a pre-halokinetic sequence, in order to study the influence of down-building of sediments on the diapiric pattern formation. Therefore, the setup initially consists of only a layer of salt, which is separated from the “sticky air layer” by the internal free surface. The remaining boundaries are free slip. Different layers of sediments are defined for visualization purposes, even though they all have the same physical properties. Also, the time lapse at which the sedimentation phase is changed is fixed during the simulations to 0.5 Myrs. Initially, sediments with phase number 1 are sedimented. Once the defined time for the phase change is reached, phase number 2 will start to deposit and so on, until a maximum number of phases is reached in which case phase 1 will start being deposited again. Two different sets of viscosities and sedimentation rates have been used in the forward models (see Table 5.1, DB_005 and DB_b).

Table 5.1. Parameters used in the 2D and 3D simulations of the up-built and down-built diapirs. Asterisks symbol indicates that the same parameters have been used for the corresponding reverse simulation.

	[cm/year]	H_{salt} [m]	H_{over} [m]	η_{salt} [Pa s]	η_{over1} [Pa s]	η_{over2} [Pa s]	η_{sticky_air} [Pa s]	n_{salt} [ ]	n_{over} [ ]	ρ_{salt} [Kg/m^3]	ρ_{over} [Kg/m^3]
2D_RT_1*	-	1000	1000	10^{18}	10^{19}	10^{19}	-	5	1	2200	2700
2D_RT_2*	-	1000	1000	10^{18}	10^{19}	10^{19}	-	1	5	2200	2700
3D_RT*	-	2500	2500	10^{18}	10^{19}	10^{18}	-	1	1	2200	2700
3D_RT_wrong1	-	2500	2500	10^{18}	10^{20}	10^{19}	-	1	1	2200	2700
3D_RT_wrong2	-	2500	2500	10^{18}	10^{19}	10^{18}	-	1	1	2200	2300
DB_005*	0.05	1000	-	10^{18}	10^{21}	10^{21}	10^{16}	1	1	2200	2700
DB_b*	0.1	1000	-	10^{18}	10^{20}	10^{20}	10^{16}	1	1	2200	2700
DB_b_wrong	0.1	1000	-	10^{18}	10^{21}	10^{21}	10^{16}	1	1	2200	2700

Each of the 3D simulations was run on 64 cores (one full node) of the MOGON supercomputer of the University of Mainz. We used a fully coupled stokes solver, with fieldsplit and algebraic multigrid (ML) as velocity solvers. The iterations required for each time step and therefore the time of the simulations varied from run to run, ranging between several tens of iterations for low viscosity contrast to several hundred iterations for higher viscosity contrasts.

5.4 Results

5.4.1 2D forward and reverse simulations of Rayleigh-Taylor instability with power law viscous rheologies

Both power law viscous rheologies of the salt and of the overburden have been tested. Previous works showed that dynamic retrodeformation of folded cross sections can be performed for non-linear rheologies as well (Frehner et al., 2012; Lechmann et al., 2010). The power law coefficient (n) used in these previous studies was 3, however it has been argued that the salt can follow creep laws with power law coefficient of 5 (Urai et al., 2008). We therefore employed for both the salt and the overburden a power law coefficient of 5 (See Table 5.1 for the used parameters). A large power law exponent in the overburden is a parameterized manner of representing a layer anisotropic media with layers of lower power law exponent.

The forward simulations with a power law viscous salt result in diapirs distributed along the modelling domain. Several diapirs form along the width of the modelled domain (Figure 5.4). The forward simulation is stopped at 1.407 Myrs when at one location the salt has been completely drained. The reverse modelling of the simulation with non-linear rheology of the salt successfully retrieves the initial flat geometry of the salt overburden interface (Figure 5.4).

On the other hand, when an overburden with power law viscous rheology is considered, the behaviour is quite different. It takes longer for the salt to start flowing upwards, but once salt upwelling is localized into a single area in the overburden, it rises rapidly and reaches the top boundary of the modelled domain after 0.689 Myrs (Figure 5.5). The forward simulation is stopped at this stage. Reverse modelling of the setup with power law viscous overburden successfully retrieves the initial flat geometries (Figure 5.5).

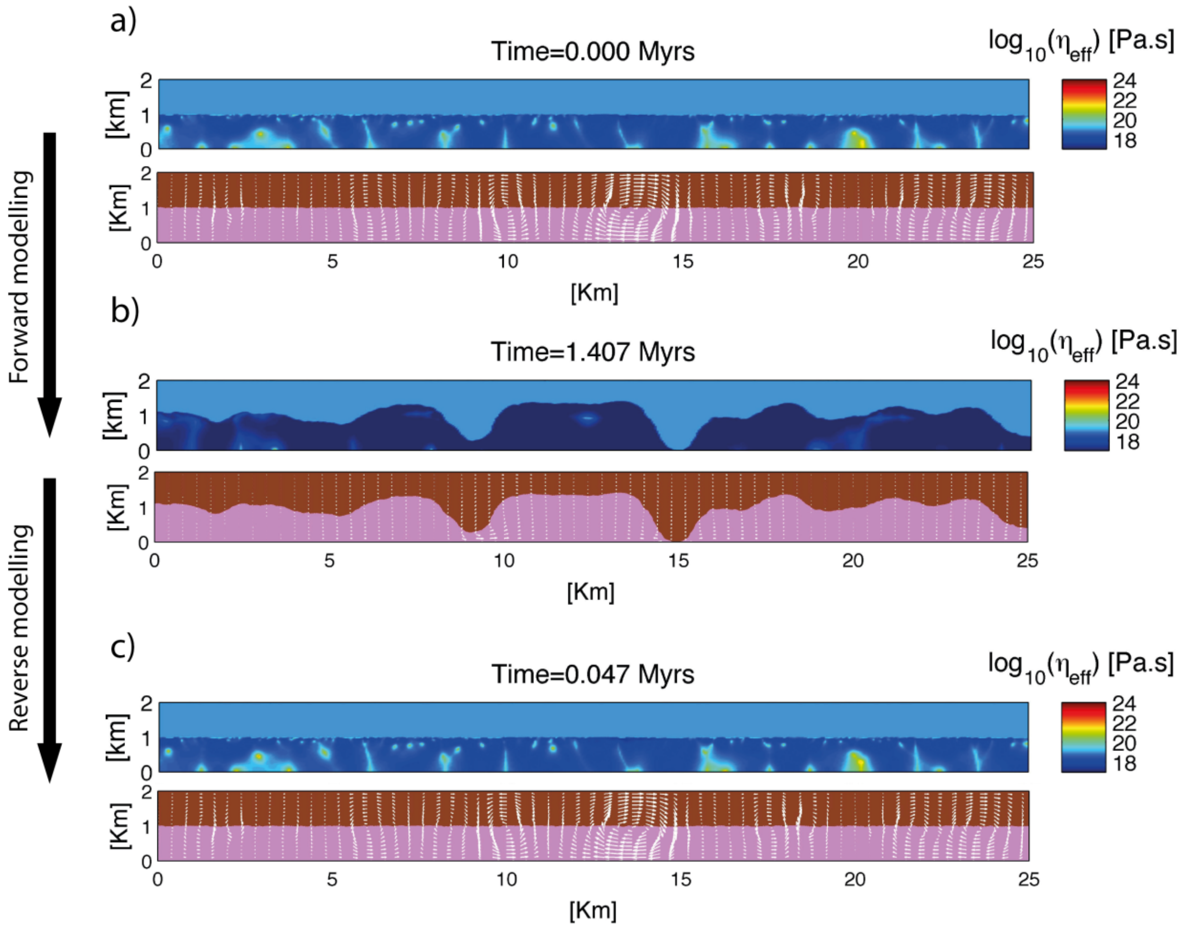

Figure 5.4. 2D simulations of up-built diapirs with power law viscous salt with a power law coefficient of 5 (Table 5.1, 2D_RT_1). a) Initial setup used for the forward simulation. b) Result of the forward simulation after time of 1.407 million years. This stage is used as an initial stage in the reverse modelling. c) Result of the reverse modelling initiated from the stage shown in b). The reverse modelling recovers the initial geometries and velocity fields.

In both reverse simulations with non-linear viscous salt and overburden, not only the initial flat geometry is retrieved. The plot of the effective viscosity shows that the values and distribution of effective viscosity is quite similar between the initial forward simulation and the result of the reverse simulation (Figure 5.4 and Figure 5.5).

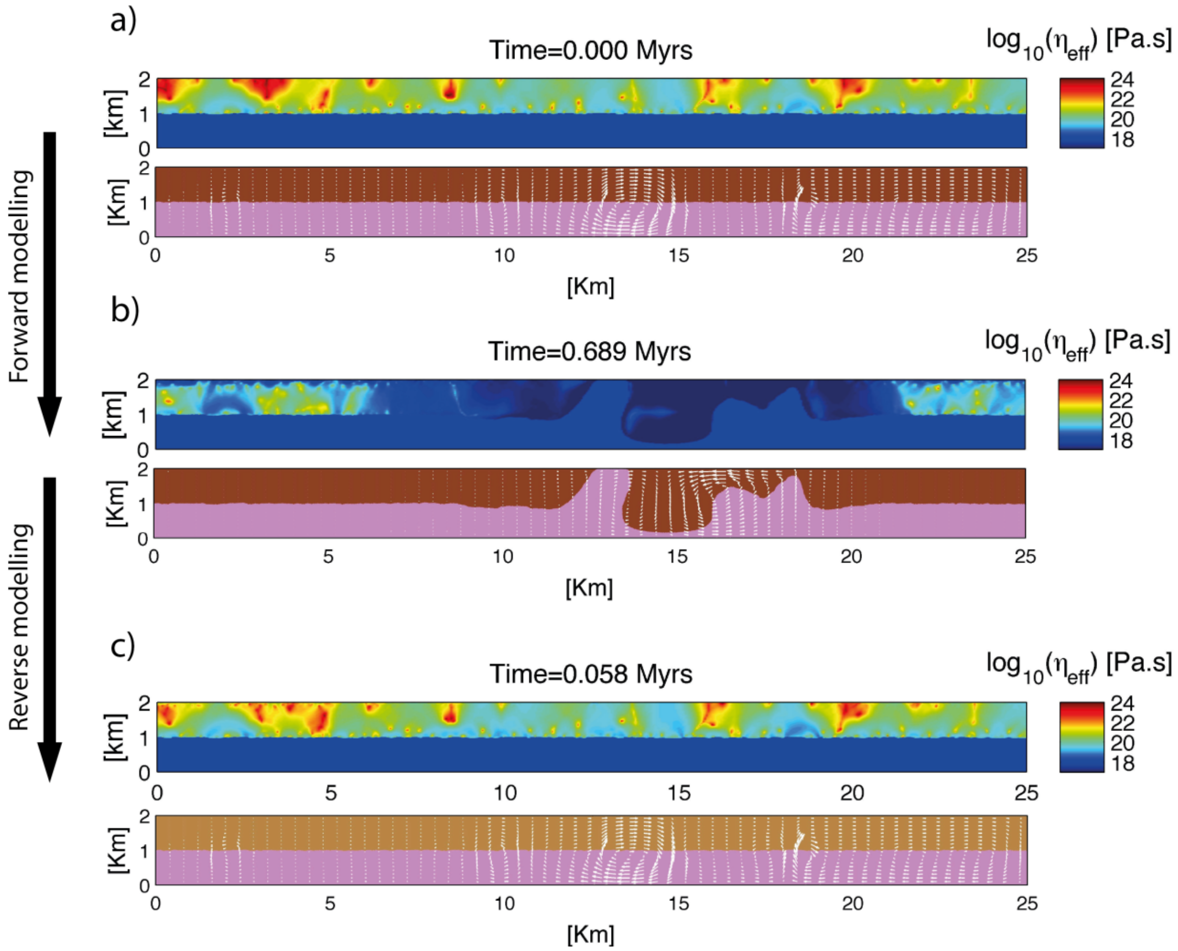

Figure 5.5. 2D simulations of up-built diapirs with power law viscous overburden with a power law coefficient of 5 (Table 5.1, 2D_RT_2). a) Initial setup used for the forward simulation. b) Result of the forward simulation after time of 0.689 million years. It shows that salt upwelling has been localized and only two diapirs are formed. This stage is used as an initial stage for the reverse modelling. c) Result of reverse modelling initiated from the stage shown in b). The reverse modelling recovers the initial geometries and velocity fields.

5.4.2 3D forward and reverse simulations of diapirs formed by up-building

3D simulations of up-building (active) diapirism have been performed to compare the reverse time step approach with previous works by Ismail-Zadeh et al. (2004) and Kaus and Podladchikov (2001). A forward simulation of an up-built diapir is shown in Figure 5.6 (see Table 5.1 for parameters), where after 0.8 Myrs the salt-overburden interface shows several topographic highs and depressions due to the purely buoyancy driven instability. The overburden is composed of a multilayer system composed of three competent layers and two inter-bedded weak layers (see Figure 5.3 and Table 5.1). The forward simulation was stopped after the overburden reached the bottom boundary and significant deformation of the layers occurred (Figure 5.6). Reverse modelling of this example was able to successfully retrieve the initial flat geometry of the salt overburden interface (Figure 5.6), confirming earlier findings of Ismail-Zadeh et al. (2004) and Kaus and Podladchikov (2001) with a single overburden layer.

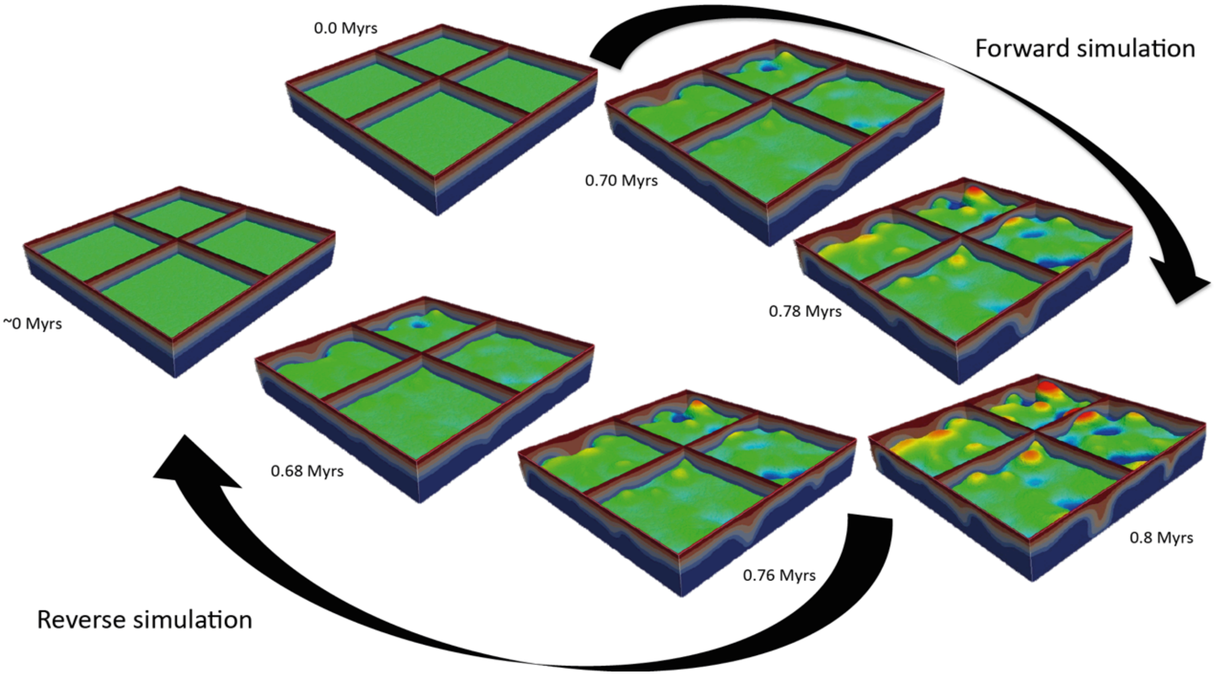

Figure 5.6. Forward and reverse modelling of salt diapirs formed by Rayleigh-Taylor instabilities (Table 5.1, 3D_RT). Several salt domes and diapirs are formed after 0.8 Myrs. The final stage is used as an initial stage for the reverse modelling. It can be seen that the intermediate geometries are well retrieved and that the initial flat geometries are successfully recovered.

We have also used the forward simulation of up-building diapirism of Figure 5.6 to test the effect of using incorrect material parameters during reverse modelling (see Table 5.1 for used parameters). First, we employed an overburden viscosity that is 1 order of magnitude higher for both the weak and competent layers compared to the ones employed in the forward simulations. Clearly, the salt-overburden interface cannot be flattened to the original initial geometry (Figure 5.7). Next, we tested the effect of employing an incorrect overburden density. In this case, reverse modelling is not able to recover the initial flat interface in the same period of time. Yet, ultimately, it would be recovered. This can be understood as for the case of the Rayleigh-Taylor instability, the density difference affects the timescale of instabilities but not shape of growthrate curves.

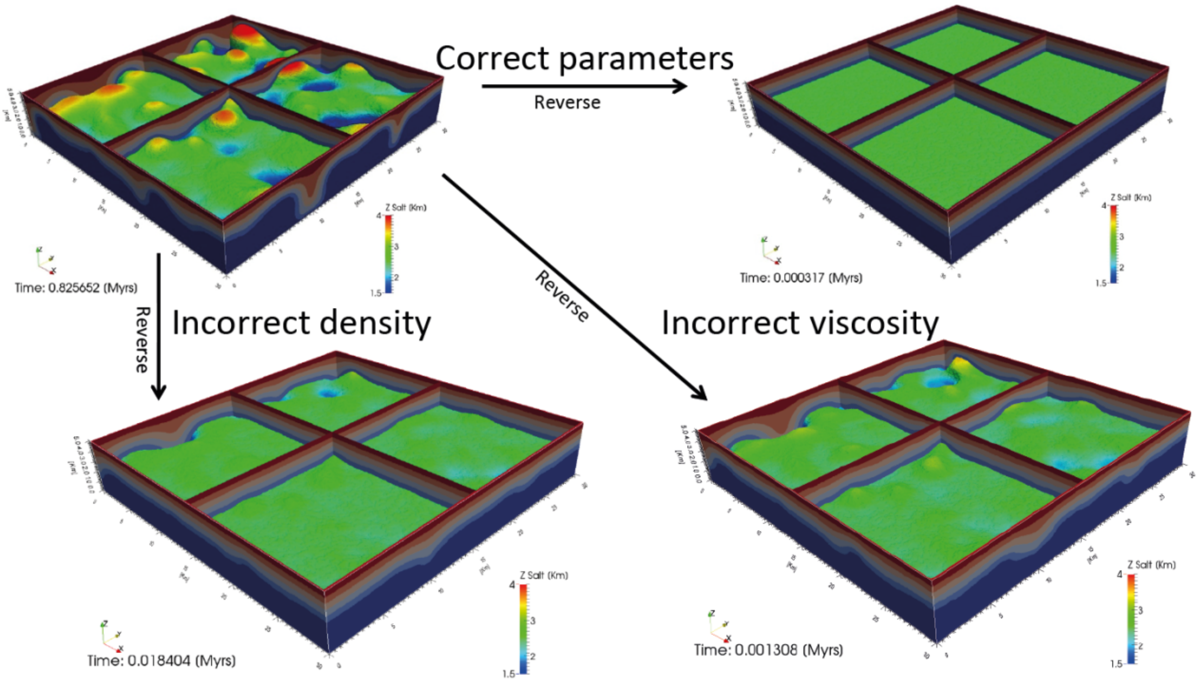

Figure 5.7. Comparison of three different reverse models at times close to the initial time (Table 5.1, 3D_RT, 3D_RT_Wrong1 and 3D_RT_Wrong2). In one of the reverse modelling simulations, the correct parameters were employed while in the other two cases incorrect density respectively viscosities were used. The initial flat geometries can only be recovered when the correct parameters are used.

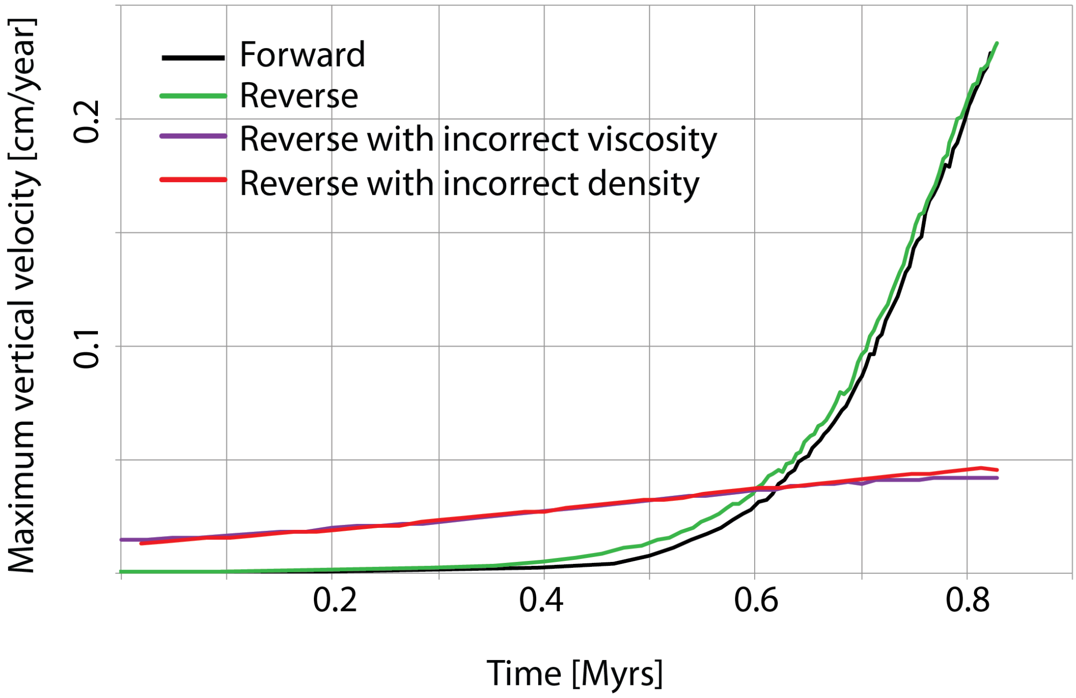

Figure 5.8. Graph showing the temporal evolution of maximum vertical velocity in the 3D up-built diapirism simulations. The reverse modelling simulation (green line) reproduces the forward model (black line) quite well, if the correct parameters are employed, but are far off if incorrect parameters are used.

The maximum vertical velocity during the forward simulation (Figure 5.8, black line) increases continuously until the end of the simulation at 0.8 Myrs. The maximum vertical velocity during the reverse simulation reproduces this curve closely (Figure 5.8, green line). However there are small misfits during part of the simulation that do not result in considerable differences between the forward and the reverse simulations. On the other hand, the maximum velocity during reverse simulations with incorrect parameters is clearly different and therefore results in an unsuccessful restoration.

5.4.3 3D forward and reverse simulations of diapirs formed by down-building

Surface redistribution of sediments as well as the sedimentation rate influences both the shape and the evolution of the diapirs that develop by differential loading (Chemia et al., 2008; Fuchs et al., 2011; Poliakov et al., 1993). We illustrate these effects with two forward simulations that employ a different sedimentation rate and different viscosity of the overburden (Figure 5.9 and Figure 5.10). The fast erosion upper boundary condition causes the diapirs to be exposed at the surface after a certain amount of time. The time it takes for the diapirs to reach the surface (or if they will be never be covered with sediments) depends both on the rheological parameters as on the sedimentation rate. Once the diapirs are exposed at the surface, they will be fed with salt that is displaced from below the surrounding areas where sediments are being deposited (salt withdrawal areas). Yet, in the simulations where sedimentation rate is higher than the velocity of salt extrusion, they can be covered with sediments and stop growing (Figure 5.9 and Figure 5.10).

Reverse modelling of down-built diapirs requires not only a reverse time approach, but also an inverse approximation to the sedimentation-erosion processes. In a forward model approach the sedimentation rate is used to calculate the thickness of the new sediment layer that will be deposited. When a fast erosion boundary condition is applied, the particles are changed from sediment or salt to air (erosion) and from air to sediments (sedimentation). During a reverse modelling simulation, these steps need to be reversed as sketched in Figure 5.2.

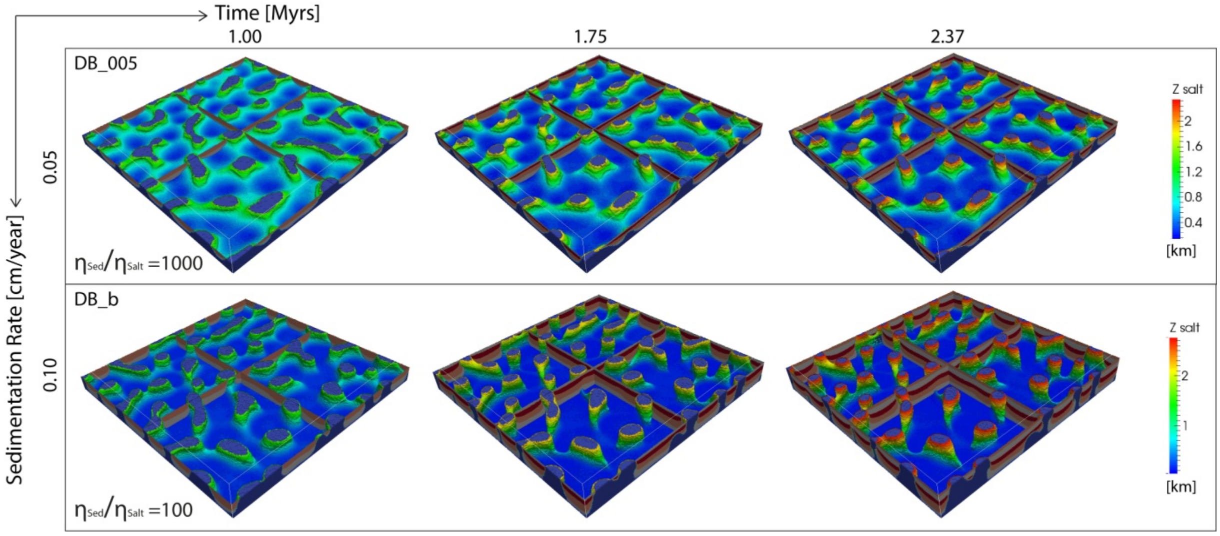

Figure 5.9. Results of two 3D forward simulations of diapirs formed by down-building. The two simulations differ in the overburden viscosity and in sedimentation rate they employ (see parameters in Table 5.1, DB_005 and DB_b). Many of the salt diapirs are exposed at the surface from the beginning of the simulation onwards. In the example with higher sedimentation rate, several covered diapirs occur.

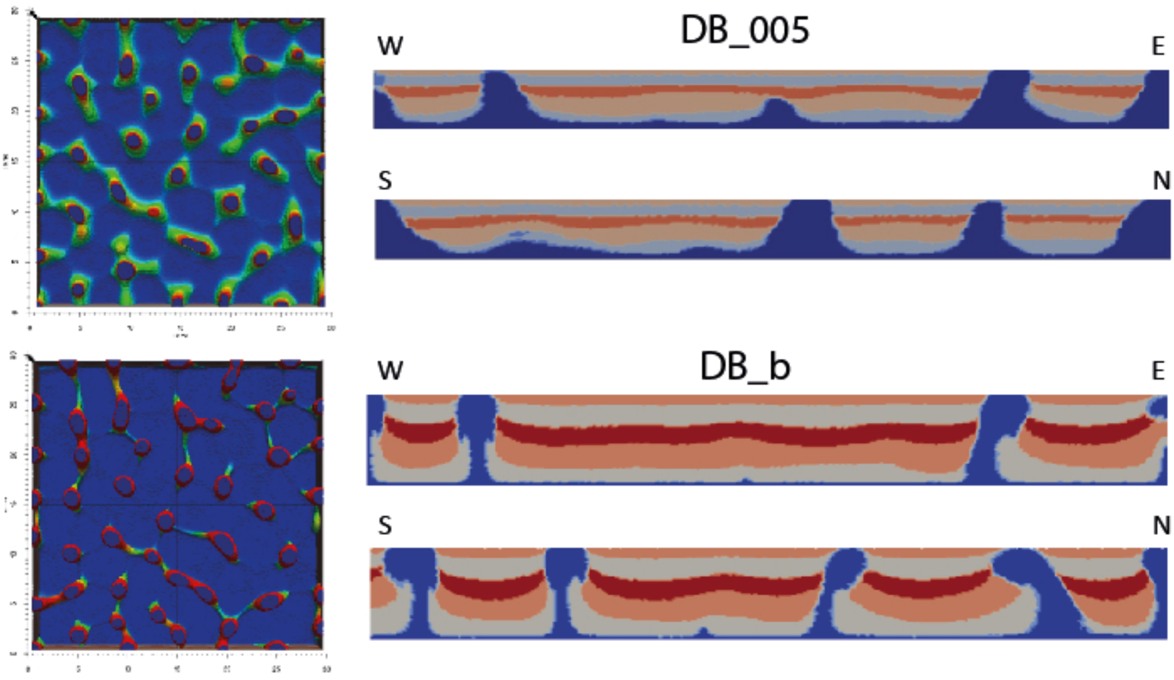

Figure 5.10. Map view and cross sections of two different simulations of down-built diapirs with different initial parameters (see Figure 5.9). Although patterns of diapirs are quite similar, in the simulation with the highest sedimentation rate, some of the diapirs are covered by sediments and not exposed at the surface any more.

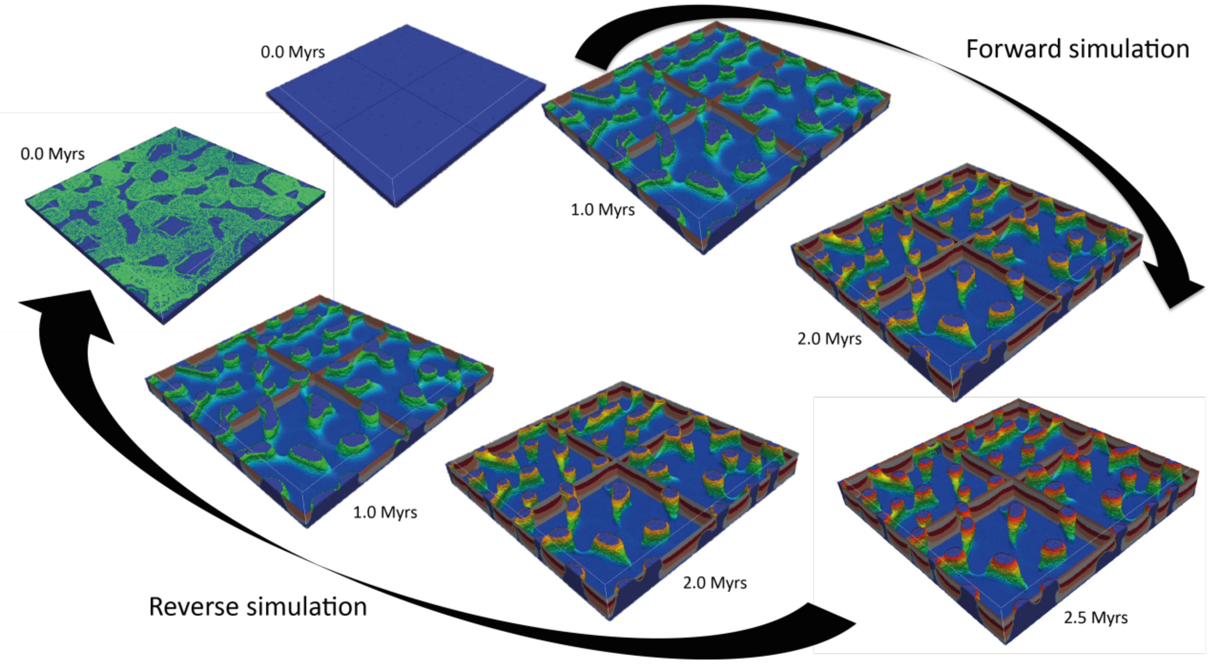

Figure 5.11. 3D snapshots of forward and reverse simulations of diapirs formed by down-building (Table 5.1, DB_b). The simulation was stopped at 2.5 Myrs, which was used as initial condition for the reverse modelling. It can be seen that the intermediate geometries of the simulation are well recovered, even when down-building processes are included in the simulations. However, the initial stages are not well reproduced.

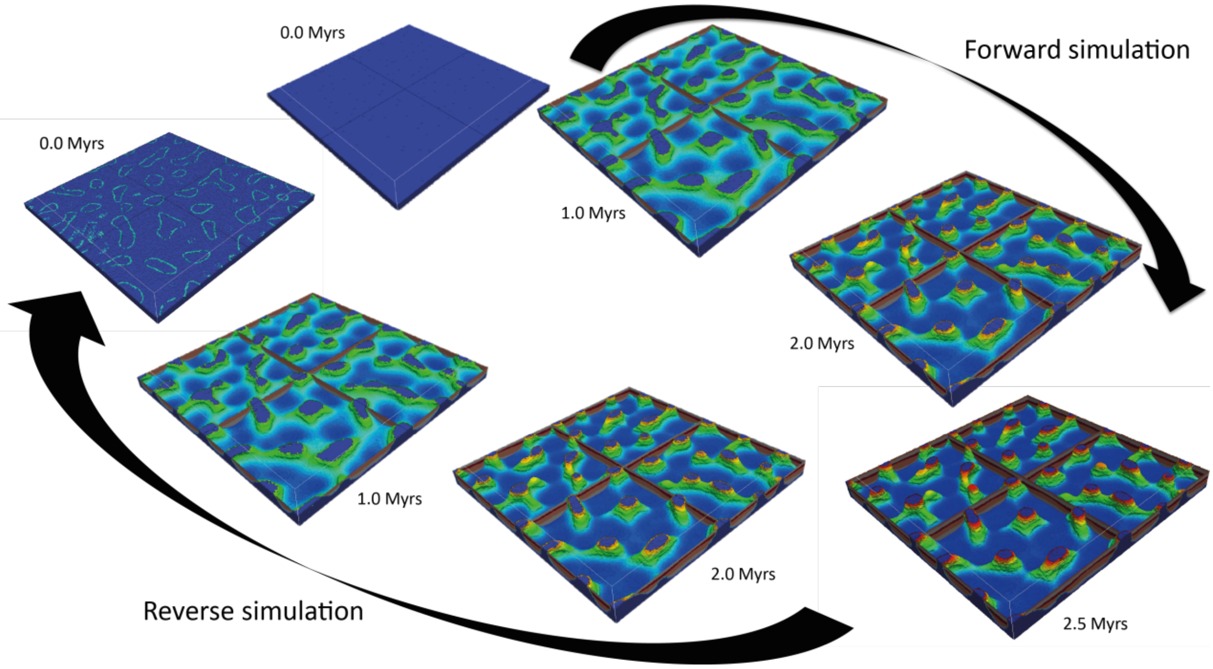

Figure 5.12. Snapshots of the forward and reverse simulations of diapirs formed by down-building that with different sedimentation rate and overburden viscosity (Table 5.1, DB_005). It can be seen that the intermediate geometries of the simulation are well recovered, even when down-building processes are included in the simulations. The initial stages are less well recovered.

Reverse modelling of salt diapirs formed by down-building can successfully retrieve the intermediate geometries (Figure 5.11 and Figure 5.12). However, after a certain time, the reverse modelling simulation starts to differ from that of the original forward model even if the correct parameters are employed. The differences are particularly pronounced when the salt layer is nearly horizontal. The results show that during reverse modelling and at stages close to the initial ones, the salt diapirs are kept exposed at the surface (Figure 5.11 and Figure 5.12) and are not covered as they initially were during the forward simulations.

Even though the initial flat geometries can thus not be completely retrieved by reverse modelling, the method works reasonably well for intermediate stages. Therefore as in the case of the up-built diapirism, we have also performed reverse modelling simulations with down-building diapirs, but using incorrect parameters. An example of using an overburden viscosity that is one order of magnitude larger is shown in Figure 5.13. In this case, as in the case of up-built diapirs, the intermediate geometries are also incorrect as it can be seen in Figure 5.13.

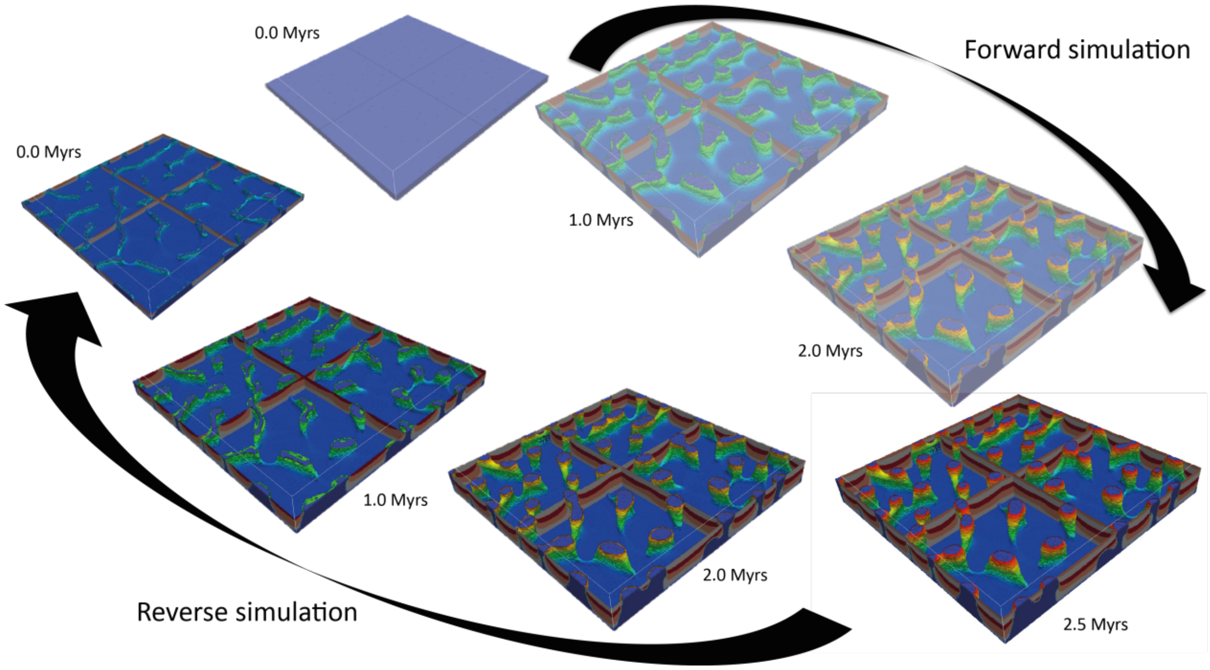

Figure 5.13. Example of a reverse simulation of down-building diapirs that employed an incorrect overburden viscosity (Table 5.1, DB_b_Wrong). Even though the differences are not that big during the initial stage of the reverse model, they become more pronounced after a certain amount of time. At intermediate stages the simulations start to differ.

In order to identify when the forward and reverse simulations start to differ, we compare the evolution of the maximum vertical velocities in the simulations as well as the number of salt cells in the modelled domain (Figure 5.14). Comparing the velocities shows that there is a peak after which the vertical velocity decreases in the forward modelling (Figure 5.14). During the reverse simulation, the velocity starts to deviate from the forward modelling velocities when approaching the peak of the velocity curve. As the simulations approach the zero time, the maximum velocities of the reverse simulation are higher than the ones of the forward models.

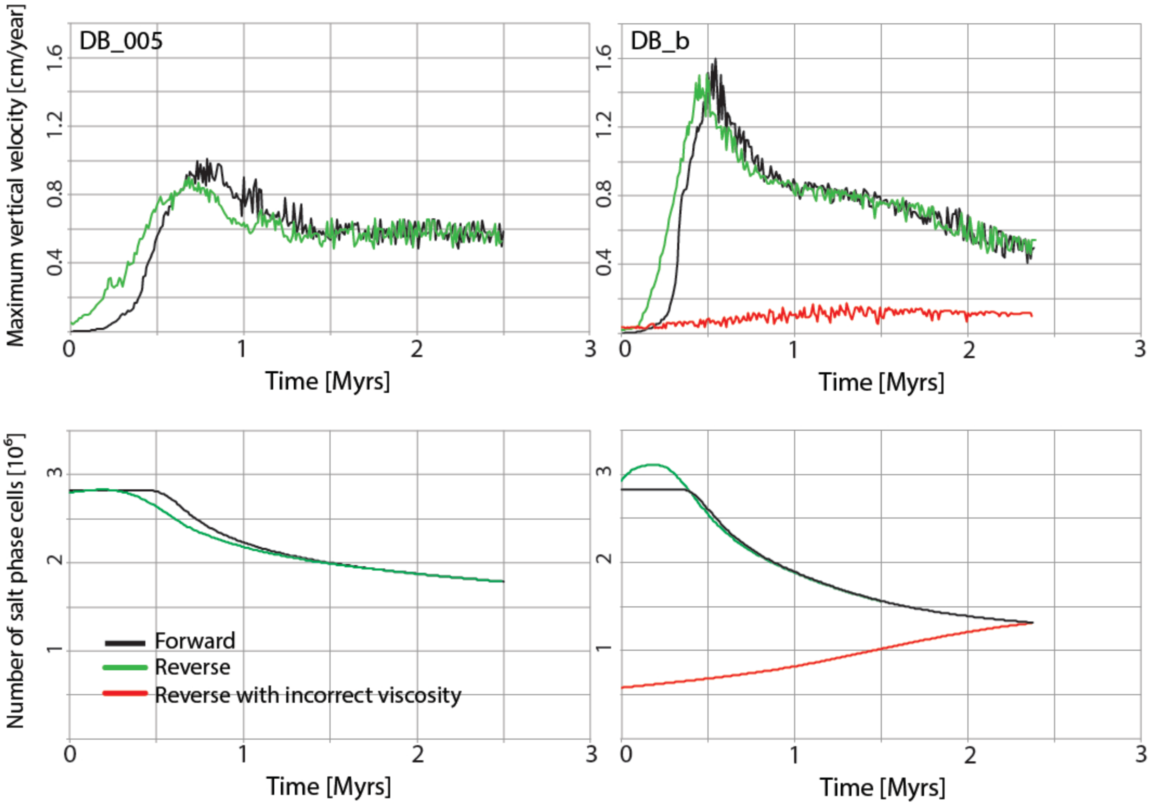

Figure 5.14. Temporal evolution of the maximum vertical velocity in the 3D down-built diapirism simulations (top graphs) and the evolution of the number of salt phase cells (lower graphs). In both examples there is a peak in vertical velocity after which the velocity decreases. The velocity of the reverse modelling simulations deviates from the forward modelling velocities. The number of salt phase cells in the reverse model also deviates from the forward modelling curves.

During a forward simulation, the number of salt phase cells initially stays constant as no salt escapes the model domain (Figure 5.14). After the first diapirs reach the surface, salt is extruded and eroded in our models and as a result the number of salt phase cells decreases considerably (Figure 5.14) until the slope becomes less steep. During reverse simulations the curves of the number of cell also deviate from the forward modeling curves. This deviation is particularly pronounced in one of the simulations whereas in the other one, significant deviations only occur close to time zero.

These reverse modelling artefacts are most likely caused by the fact that our 'inverse erosion' algorithm is imperfect. During the initial stages of forward simulations sediments where eroded above the salt, which is difficult to reconstruct during a reverse modelling stage.

5.5 Discussion

Here, we have focused in linear viscous and power law viscous materials to test whether reverse modelling of up-build and down-built diapirs can be performed using a reverse time step approach.

Dynamic retrodeformation has already been applied to unfold sedimentary sequences in previous studies (Frehner et al., 2012; Lechmann et al., 2010). The method has further been compared with traditional kinematic restorations, and it was shown that the latter ones underestimate shortening in cross section by ignoring the pure shear shortening that is associated with folds (Chapple, 1968). Dynamic retrodeformation has also been applied to retrodeform diapirs resulting from the Rayleigh-Taylor instability in 2D and 3D, and from down-building processes in 2D. Our work has extended these previous findings and included power law viscous rheologies for the Rayleigh-Taylor instability.

It had been argued that any nonlinear properties in the mechanics of the modelled system introduce a path dependency of deformation and that for that reason the forward and reverse modelling outcomes should differ (Lovely et al., 2012). Yet, for even highly non-linear power law materials, which results in a strong localization of deformation, reverse modelling is still capable of recovering the initial geometry, which is in agreement with previous work (Frehner et al., 2012; Lechmann et al., 2010). The feasibility of reverse modelling in the presence of (plastic) rheologies that exhibits shear localization remains a subject of future study (Frehner et al., 2012).

We have illustrated the feasibility of 3D reverse modelling in the presence of down-building. Despite the initial geometries of the simulations could not be completely retrieved during the reverse simulation, the intermediate stages of the forward modelling are correctly reproduced during the reverse modelling. However, reversing the fast erosion algorithm causes some deviation in the volumes of materials that enter the system, which causes some differences from the forward models. Therefore, a different approach might be needed to reverse the down-building processes when close to the initial stages. In any case, we argue that the reverse time step approach has an important potential for the application to down-built diapirs as well.

One of the potential powerful applications of a reverse modelling method is that it generally only works when the correct material parameters are used. In this study, we have performed both the forward and reverse modelling of the illustrated setups, and therefore we know the correct parameters for the reverse modelling. However, the inverse approach could be used with cross-sections of 3D reconstructions, where the parameters are not known. Testing for which parameters one can reach an initially flat geometry thus gives us a method to constrain the material properties of the crust. Depending on the number of free parameters, this potentially requires scanning a large parameter space. For such case, the reverse modelling approach can be combined with a Markov Chain Monte-Carlo based parameter search strategy which can scan the correct parameters in a nonlinear parameter space in a reasonably efficient manner (Baumann et al., in press).

It has been widely discussed that the initiation of diapirs cannot be due to differential loading alone, because the un-compacted sediments have densities that are lower than that of the salt. It is well-established from empirical depth-density curves, that the average density needed for salt to flow due to differential loading is achieved when 600 to 1500 meters of sediments are deposited (Hudec et al., 2009). Several mechanisms have been suggested to initiate diapirism, most of them related to regional extension. Initiating diapirism by extension would require the use of a brittle overburden in our simulations. Here, we focused on forward and reverse modelling of salt structures without considering the specific mechanism by which diapirism is started. In any case, cross-sections in which the driving forces are extension and compression can also potentially be dynamically retrodeformed by using an opposite sign of the velocities of background strain rates imposed as boundary conditions.

5.6 Conclusions

We have tested the reverse modelling approach to retrodeform diapirs formed by up-building with power law viscous rheologies and by down-building in 3D. Modelled up-built diapirs using power law viscous rheologies with a power law coefficient of up to 5 can be successfully retrodeformed.

Modelled three dimensional salt structures formed by up-building diapirism with a multi-layered overburden can be retrodeformed to their initial flat stages. Modelled three-dimensional down-built diapirs can be retro-deformed to the intermediate stages if the correct rheological parameters and sedimentation rate history is known. Reversing the sedimentation erosion processes that mimic the down-building processes however causes some deviation in the volumes of materials that enter the system. As a result, the initial geometries cannot be perfectly retrieved.

In all cases, we have tested that the intermediate and final geometries can only be retrieved if the correct parameters are assigned to the material phases.

Dynamic retrodeformation thus provides insights in the deformation history of the studied salt structures, which has a number of potential applications. For example, our approach could be applied to natural examples where the rheological parameters are unknown, in order to better constrain the rheology of the salt and the involved cover and at the same time to validate available geometric interpretations.

5.7 Acknowledgements

Funding was provided by the European Research Council under the European Community’s Seventh Framework program (FP7/2007-2013) ERC Grant agreement #258830. 3D simulations were performed on MOGON supercomputer of Johannes Gutenberg University Mainz, Germany.

5.8 References

Archer, S.G., Alsop, G.I., Hartley, A.J., Grant, N.T., and Hodgkinson, R., 2012, Salt tectonics, sediments and prospectivity: an introduction: Geological Society, London, Special Publications, v. 363, p. 1-6.

Baumann, T.S., Kaus, B.J.P., and Popov, A.A., in press, Constraining effective rheology through parallel joint geodynamic inversion: Tectonophysics.

Chamberlin, R.T., 1910, The Appalachian Folds of Central Pennsylvania: The Journal of Geology, v. 18, p. 228-251.

Chapple, W.M., 1968, A Mathematical Theory of Finite–Amplitude Rock–Folding: Geological Society of America Bulletin, v. 79, p. 47-68.

Chemia, Z., Koyi, H., and Schmeling, H., 2008, Numerical modelling of rise and fall of a dense layer in salt diapirs: Geophysical Journal International, v. 172, p. 798-816.

Cobbold, P.R., 1979, Removal of finite deformation using strain trajectories: Journal of Structural Geology, v. 1, p. 67-72.

Crameri, F., Schmeling, H., Golabek, G.J., Duretz, T., Orendt, R., Buiter, S.J.H., May, D.A., Kaus, B.J.P., Gerya, T.V., and Tackley, P.J., 2012, A comparison of numerical surface topography calculations in geodynamic modelling: an evaluation of the 'sticky air' method: Geophysical Journal International, v. 189, p. 38-54.

Dabrowski, M., Krotkiewski, M., and Schmid, D.W., 2008, MILAMIN: MATLAB-based finite element method solver for large problems: Geochemistry, Geophysics, Geosystems, v. 9, p. Q04030.

Dahlstrom, C.D.A., 1969, Balanced cross sections: Canadian Journal of Earth Sciences, v. 6, p. 743-757.

Frehner, M., Reif, D., and Grasemann, B., 2012, Mechanical versus kinematical shortening reconstructions of the Zagros High Folded Zone (Kurdistan region of Iraq): Tectonics, v. 31, p. TC3002.

Fuchs, L., Schmeling, H., and Koyi, H., 2011, Numerical models of salt diapir formation by down-building: the role of sedimentation rate, viscosity contrast, initial amplitude and wavelength: Geophysical Journal International, v. 186, p. 390-400.

Gibbs, A.D., 1983, Balanced cross-section construction from seismic sections in areas of extensional tectonics: Journal of Structural Geology, v. 5, p. 153-160.

Giles, K.A., and Lawton, T.F., 2002, Halokinetic Sequence Stratigraphy Adjacent to the El Papalote Diapir, Northeastern Mexico: AAPG Bulletin, v. 86, p. 823-840.

Griffiths, P., Jones, S., Salter, N., Schaefer, F., Osfield, R., and Reiser, H., 2002, A new technique for 3-D flexural-slip restoration: Journal of Structural Geology, v. 24, p. 773-782.

Guzofski, C.A., Mueller, J.P., Shaw, J.H., Muron, P., Medwedeff, D.A., Bilotti, F., and Rivero, C., 2009, Insights into the mechanisms of fault-related folding provided by volumetric structural restorations using spatially varying mechanical constraints: AAPG Bulletin, v. 93, p. 479-502.

Hossack, J., 1995, Geometric rules of section balancing for salt structures, *in* Jackson, M.P.A., Roberts, D.G., and Snelson, S., eds., AAPG Special Volumes, Volume Salt Tectonics: A Global Perspective AAPG.

Hudec, M.R., and Jackson, M.P.A., 2007, Terra infirma: Understanding salt tectonics: Earth-Science Reviews, v. 82, p. 1-28.

Hudec, M.R., Jackson, M.P.A., and Schultz-Ela, D.D., 2009, The paradox of minibasin subsidence into salt: Clues to the evolution of crustal basins: Geological Society of America Bulletin, v. 121, p. 201-221.

Ismail-Zadeh, A., Tsepelev, I., Talbot, C., and Korotkii, A., 2004, Three-dimensional forward and backward modelling of diapirism: numerical approach and its applicability to the evolution of salt structures in the Pricaspian basin: Tectonophysics, v. 387, p. 81-103.

Ismail-Zadeh, A.T., Talbot, C.J., and Volozh, Y.A., 2001, Dynamic restoration of profiles across diapiric salt structures: numerical approach and its applications: Tectonophysics, v. 337, p. 23-38.

Kaus, B.J.P., 2010, Factors that control the angle of shear bands in geodynamic numerical models of brittle deformation: Tectonophysics, v. 484, p. 36-47.

Kaus, B.J.P., and Podladchikov, Y.Y., 2001, Forward and reverse modeling of the three-dimensional viscous Rayleigh-Taylor instability: Geophysical Research Letters, v. 28, p. 1095-1098.

Lechmann, S.M., Schmalholz, S.M., Burg, J.P., and Marques, F.O., 2010, Dynamic unfolding of multilayers: 2D numerical approach and application to turbidites in SW Portugal: Tectonophysics, v. 494, p. 64-74.

Lovely, P., Flodin, E., Guzofski, C., Maerten, F., and Pollard, D.D., 2012, Pitfalls among the promises of mechanics-based restoration: Addressing implications of unphysical boundary conditions: Journal of Structural Geology, v. 41, p. 47-63.

Maerten, L., Gillespie, P., and Daniel, J.-M., 2006, Three-dimensional geomechanical modeling for constraint of subseismic fault simulation: AAPG Bulletin, v. 90, p. 1337-1358.

May, D.A., 2012, Volume reconstruction of point cloud data sets derived from computational geodynamic simulations: Geochemistry, Geophysics, Geosystems, v. 13, p. Q05019.

Moretti, I., Lepage, F., and Guiton, M., 2006, Une nouvelle méthode de restauration 3D basée sur une approche couplée géométrie-mécanique: Oil & Gas Science and Technology - Rev. IFP, v. 61, p. 277-289.

Mukherjee, S., Talbot, C.J., and Koyi, H.A., 2010, Viscosity estimates of salt in the Hormuz and Namakdan salt diapirs, Persian Gulf: Geological Magazine, v. 147, p. 497-507.

Poliakov, A.N.B., van Balen, R., Podladchikov, Y., Daudre, B., Cloetingh, S., and Talbot, C., 1993, Numerical analysis of how sedimentation and redistribution of surficial sediments affects salt diapirism: Tectonophysics, v. 226, p. 199-216.

Rouby, D., Cobbold, P.R., Szatmari, P., Demercian, S., Coelho, D., and Rici, J.A., 1993, Least-squares palinspastic restoration of regions of normal faulting—application to the Campos basin (Brazil): Tectonophysics, v. 221, p. 439-452.

Rouby, D., Xiao, H., and Suppe, J., 2000, 3-D Restoration of Complexly Folded and Faulted Surfaces Using Multiple Unfolding Mechanisms: AAPG Bulletin, v. 84, p. 805-829.

Rowan, M.G., 1993, A systematic technique for the sequential restoration of salt structures: Tectonophysics, v. 228, p. 331-348.

Rowan, M.G., Lawton, T.F., Giles, K.A., and Ratliff, R.A., 2003, Near-salt deformation in La Popa basin, Mexico, and the northern Gulf of Mexico: A general model for passive diapirism: AAPG Bulletin, v. 87, p. 733-756.

Rowan, M.G., and Ratliff, R.A., 2012, Cross-section restoration of salt-related deformation: Best practices and potential pitfalls: Journal of Structural Geology, v. 41, p. 24-37.

Schmalholz, S.M., 2008, 3D numerical modeling of forward folding and reverse unfolding of a viscous single-layer: Implications for the formation of folds and fold patterns: Tectonophysics, v. 446, p. 31-41.

Urai, J.L., Schléder, C.J., Spiers, C.J., and Kukla, P., 2008, Flow and transport properties of salt rocks, *in* R., L., ed., Dynamics of Complex Intracontinental Basins: The Central European Basin System: Berlin, Springer, p. 277-290.

Yin, H., and Groshong Jr, R.H., 2006, Balancing and restoration of piercement structures: geologic insights from 3D kinematic models: Journal of Structural Geology, v. 28, p. 99-114.

Chapter 6

Dynamics of thin-skinned fold and thrust belts with a tilted detachment

Abstract

Many existing fold and thrust belts have a basement that increasingly deepens below the foredeep. One example is the Jura fold and thrust belt, which formed during the Alpine orogeny. However, it is still a matter of debate why the Jura was formed tens of kilometres away from the active deformation front while the Molasse basin that lies in between the Jura and the Alps remained mostly undeformed. Progressive thickening of the Molasse basin due to its infill with sediments, and the existence of a tilted potential detachment level at the Triassic evaporitic units have been proposed as the main causes recently (e.g. Willett and Schlunegger, 2010). In order to better understand the dynamics of a thin-skinned fold and thrust belt with a tilted detachment we have performed systematic forward 2D numerical simulations to study the following factors: 1) the applied boundary conditions 2) the angle of a tilted detachment 3) the mechanical stratigraphy and 4) the geometry of a curved detachment using the critical wedge and flexural foreland basin profile equations.

Results show that the two tested boundary conditions reproduce the overall dynamics of the simulations. The effect of the basal angle on the simulations is in agreement with the critical wedge theory. Due to the low taper angles of viscous detachment wedges, a small initial basal angle switches the wedge from subcritical to critical state transferring the deformation to the front. Introducing a change on the slope of the detachment further changes the deformation sequence. Mechanical stratigraphy is also an important factor, as it completely changes the deformation mode from symmetric to asymmetric thrusting, and to folding dominated.

Keywords: thin-skinned deformation, tilted detachment, critical wedge theory, numerical modelling, flexural foreland basin

6.1 Introduction

The Jura is an arcuate fold-and-thrust belt located on the front of the western Alpine arc (Figure 6.1). It is the latest and most external fold-and-thrust belt of the Alps and developed after Middle Miocene on the external side of the Molasse foredeep (Burkhard and Sommaruga, 1998; Laubscher, 1992). The formation of the Jura and Molasse basin are closely linked (e.g. Burkhard, 1990; Laubscher, 1992), yet why the Jura formed so far away from the Alps, while the Molasse basin in between remained mostly undeformed remains matter of debate. The two main views on the formation of Jura suggest that it was either formed by thick-skinned deformation that involved the basement below (e.g. Pavoni, 1961) or that it was formed due to thin-skinned deformation of the sedimentary cover above a weak detachment level, the so called “Fernschub” theory (e.g. Laubscher, 1961). It is the latter theory that is currently more widely accepted.

The Jura indeed displays some of the main characteristics attributed to thin-skinned fold and thrust belts that formed over a weak detachment (Sommaruga, 1999). Its arcuate outward convex shape in map view clearly coincides with the shape of the thickest part of the Triassic evaporitic levels at depth (e.g. Philippe, 1994). There are however, other characteristics that differentiate thin-skinned deformation over frictional or viscous detachments. Thrust belts forming above weak viscous detachments (such as evaporites) have lower taper angles (Davis and Engelder, 1985), rapid propagation of deformation, a tendency to develop more symmetric structures (non-foreland verging) and also, non-forelandward migration of the deformation (e.g. Costa and Vendeville, 2002; Cotton and Koyi, 2000).

The wedge shape of the Molasse and the existence of a weak detachment level are usually considered key ingredients that explain the jump in deformation from the Alpine front to the Jura Mountains. More recently, the slope change or curvature of the detachment as a result of plate flexure due to the Alpine wedge load have been invoked to explain how part of the Molasse basin could become a stable wedge and transfer the deformation to its front (Willett and Schlunegger, 2010).

The dynamics and mechanics of thin-skinned fold and thrust belts have been addressed by analogue modelling (e.g. Bonini, 2007; Costa and Vendeville, 2002; Cotton and Koyi, 2000) and numerical modelling (e.g. Ruh et al., 2012; Simpson, 2009; Stockmal et al., 2007; Wissing et al., 2003). Furthermore, there have been benchmark studies comparing numerical codes and analogue models of thrust wedges (Buiter et al., 2006). In most cases, the numerical simulations employ a setup that consist of initially sub-critical wedges (with constant thickness) that during deformation, evolve to critical wedges due to their growth or critical wedges with a basal angle of zero (flat bottom) (e.g. Ruh et al., 2012; Simpson, 2011; Simpson, 2009; Wissing et al., 2003). More sophisticated setups take lithospheric flexure into account under the load of an evolving wedge (Fillon et al., 2013a; Fillon et al., 2013b; Simpson, 2010a; Simpson, 2010b; Stockmal et al., 2007).

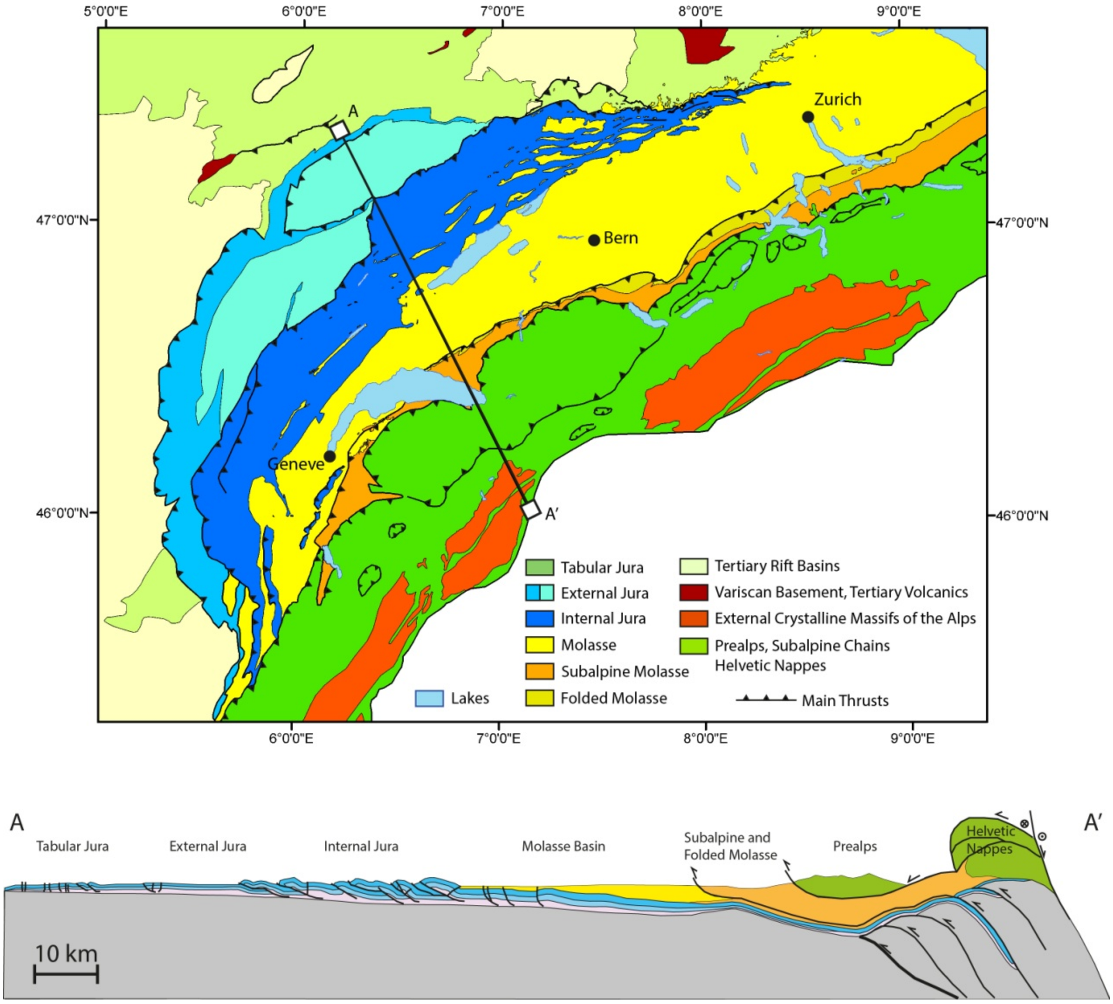

Figure 6.1. Simplified geological map of the Jura-Molasse system (compiled from Ibele (2011), Sommaruga (1999) and the Swiss Geological and Tectonic Map at 1:500,000 scale). Cross section along the indicated trace in the map (A-A') is modified from Sommaruga (1999).

The basement of the Jura-Molasse system is tilted towards the foredeep with about 1-3 degrees (see Figure 6.1 and Sommaruga, 1999), therefore the case of a fold and thrust belt with a tilted detachment must be considered. Here, we performed 2D numerical simulations to study the effects of several factors in the dynamics of such a fold and thrust belt evolution. We compare two different boundary conditions in the numerical simulations and take weaker shales and evaporite levels within the sedimentary cover into account. These weak layers within the sedimentary cover could have acted as intermediate detachments during deformation (Sommaruga, 1999). Also, the effect of employing either a uniform or discontinuously tilted detachment on the simulations has been studied.

Finally, we have also investigated the impact of the shape of the flexed plate and basal angle on the configuration of the surface slope, by using the analytical solutions of critical wedge theory and flexure foreland basin (Willett and Schlunegger, 2010) but considering a pure viscous detachment rather than a brittle detachment. A viscous detachment is a better representation of the ductile rheology of salt.

6.2 Method

We use a continuum mechanics approximation where the equations used to describe geological processes consists of a set of balance equations for mass and momentum together with their constitutive relationships. Equations are solved with the 2D Lagrangian finite element code MILAMIN_VEP (Kaus, 2010) that solves the equations of conservation of momentum and of mass for incompressible materials with visco-elasto-plastic rheologies. MILAMIN_VEP employs the MATLAB based solvers MILAMIN (Dabrowski et al., 2008) for efficiency.

Conservation of mass and momentum for slowly moving incompressible fluids are given by

$$\frac{\partial v_i}{\partial x_i} = 0 \qquad [6.1]$$

$$-\frac{\partial P}{\partial x_i} + \frac{\partial \tau_{ij}}{\partial x_j} = -\rho g_i \qquad [6.2]$$

where i,j represent spatial directions and repeated indices are summed, v_i are the velocities, x_i the coordinates, P = -$\sigma_{ii}/3$ the pressure, σ_{ij} the components of the total stress tensor, τ the deviatoric stress tensor ($\tau_{ij} = \sigma_{ij} + P$), ρ the density and g, the gravitational acceleration.

We use a Maxwell visco-elasto-plastic rheology given by

$$\dot{\varepsilon}_{ij} = \dot{\varepsilon}_{ij}{}^{viscous} + \dot{\varepsilon}_{ij}{}^{elastic} + \dot{\varepsilon}_{ij}{}^{plastic} = \frac{1}{2\eta}\tau_{ij} + \frac{1}{2G}\frac{D\tau_{ij}}{Dt} + \dot{\lambda}\frac{\partial Q}{\partial \sigma_{ij}} \qquad [6.3]$$

where η is the effective viscosity, G the elastic shear modulus, t time, $\dot{\lambda}$ the plastic multiplier and Q the plastic flow potential.

If differential stresses exceed the yield stress, rocks fail plastically according to the Mohr-Coulomb failure criterion. In 2D, the yield function is defined as

$$F = \tau^* - \sigma^* \sin\varphi - \mathrm{C}\cos\varphi \qquad [6.4]$$

and the plastic flow Q as

$$Q = \tau^* - \sigma^* \sin\psi \qquad [6.5]$$

where $\tau^* = \sqrt{\left(\frac{\sigma_{xx}-\sigma_{zz}}{2}\right)^2 + \sigma_{xz}^2}$ and $\sigma^* = (\sigma_{xx} + \sigma_{zz})$ and C is the cohesion, φ the friction angle and ψ the dilation angle, which is zero for incompressible systems.

6.3 Setup

The modelled setup consists of a tilted detachment overlaid by a sedimentary cover of constant thickness and a wedge shaped basin infill such that the initial surface slope of the system is zero. The sedimentary cover is a simplified stratigraphic profile from Sommaruga, (1997), which has been separated into five different units and the tertiary Molasse sediments above (Figure 6.2). The properties of the different layers in the sedimentary cover are chosen such that they represent either a homogeneous cover or a cover with some intermediate weak layers (Figure 6.2).

Two different boundary conditions are tested (A and B) in models with length of 75 km (see Figure 6.3). In model A, boundary conditions are no slip on the right side, free slip with constant velocity on the bottom and on the left and free surface at the top. Velocity is constant and defined in *x* direction and split into x and y components such that it is parallel to the detachment. Boundary conditions of B are no slip at the bottom and at the left, free slip with constant velocity at the right and free surface at the bottom. Model B has a no slip condition at the bottom, which is employed for longer models (150 Km), with or without basal slope change (Figure 6.3).

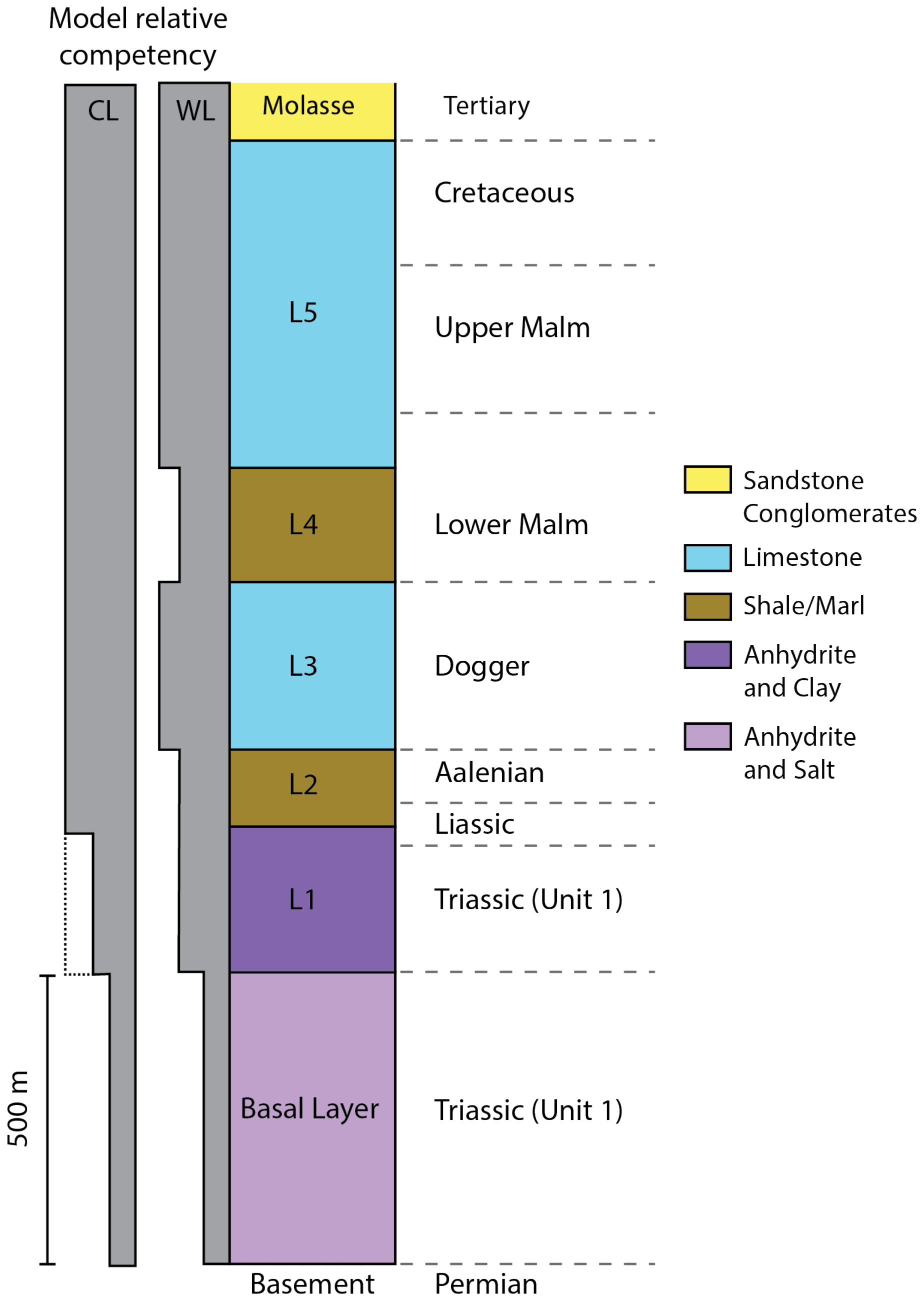

Figure 6.2. Simplified stratigraphic log (after (Sommaruga, 1996)) used in the simulations. Thickness of the tertiary Molasse sediments (in yellow) is not indicated as it has been implemented as a wedge shaped and depends on the detachment angle itself. The left profile indicates the relative competence of the layers and the values of the parameters can be seen in Table 6.1 and Table 6.2.

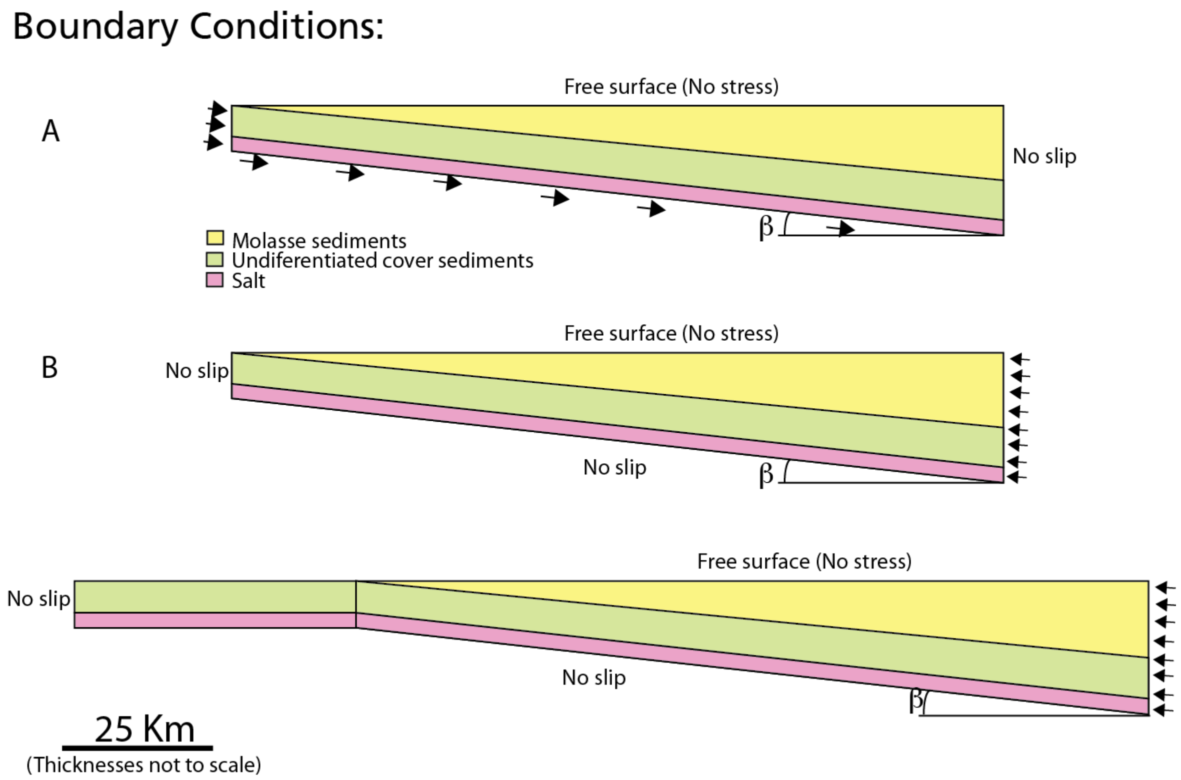

Figure 6.3. Schematic representation of the setups used in our simulations. Two different boundary conditions are employed referred to as A and B. A boundary conditions are free slip with constant velocity on the left and bottom, no slip on the right and a free surface on top. B boundary conditions are no slip on the left and bottom, free slip with constant velocity of the right and a free surface on top. Boundary conditions of B are also used in a longer setup with a break of slope (lower panel).

We use two sets rheological parameters in the experiments, which differ in terms of the viscosity structure of the sedimentary cover, such that they correspond to an overall weak (Table 6.1) or a strong cover (Table 6.2). Within each set of parameters of Table 6.1 and Table 6.2, we distinguish between one in which we used intermediate weak layers (WL) or one in which we employed a homogeneous competent sedimentary sequence (CL). In all cases the basal evaporite layer was purely viscous with a viscosity of 10^{18} Pa s (except when indicated otherwise). All simulations employed the same horizontal velocity applied on one side of 1 cm/year.

Table 6.1. Mechanical properties of the different layers used for simulations with a weak cover.

	Cover with weak layers (WL)			Cover without weak layer (CL)		
	η	C	φ	η	C	φ
	[Pa s]	[MPa]	[°]	[Pa s]	[MPa]	[°]
L1	10^{20}	20	10	10^{22}	20	30
L2,L4	10^{20}	20	10	10^{22}	20	30
L3,L5	10^{22}	20	30	10^{22}	20	30
Molasse	10^{22}	20	30	10^{22}	20	30
Basal Layer	10^{18}	500	0	10^{18}	500	0

Table 6.2. Mechanical properties of the different layers used for simulations with a strong cover.

	Cover with weak layers (WL)			Cover without weak layer (CL)		
	η	C	φ	η	C	φ
	[Pa s]	[MPa]	[°]	[Pa s]	[MPa]	[°]
L1,L2,L4	10^{20}	20	10	10^{25}	20	30
L3,L5	10^{25}	20	30	10^{25}	20	30
Molasse	10^{25}	20	30	10^{25}	20	30
Basal Layer	10^{18}	500	0	10^{18}	500	0

6.4 Results

6.4.1 Influence of boundary conditions

We have tested two different boundary conditions that have a different geological meaning (Figure 6.3). Boundary condition A represents a subducting plate that is moving and transporting the upper levels of the crust against a backstop. In boundary condition B, on the other hand, the overriding plate is the one pushing the backstop that will scrape the sediments off the subducting plate. Four representative simulations of using the parameters of Table 6.1 are shown in Figure 6.4, for a basal angle of 0.1 and 1.0 degree. Although there are some minor differences between the two boundary conditions (see simulation with basal angle of 0.1 degrees and mechanical stratigraphy CL, Figure 6.3), the general behaviour is reproduced with both boundary conditions. With lower basal angles, deformation (either thrusts or folds) is more widely distributed along the model domain, whereas it concentrates on the left side of the models for higher basal angles. The effect of the mechanical stratigraphy is the same for both boundary conditions and results in folding if weaker layers are present in the overburden whereas it results in outwards verging thrusts for a homogeneous overburden. The results related to the mechanical stratigraphy and the basal angle will be commented in more detail in the following sections.

Because both boundary conditions give similar results regarding the overall dynamics of the simulations, we use model setup with boundary conditions B for the remaining part of this work, which simplifies the implementation of irregular basement topography.

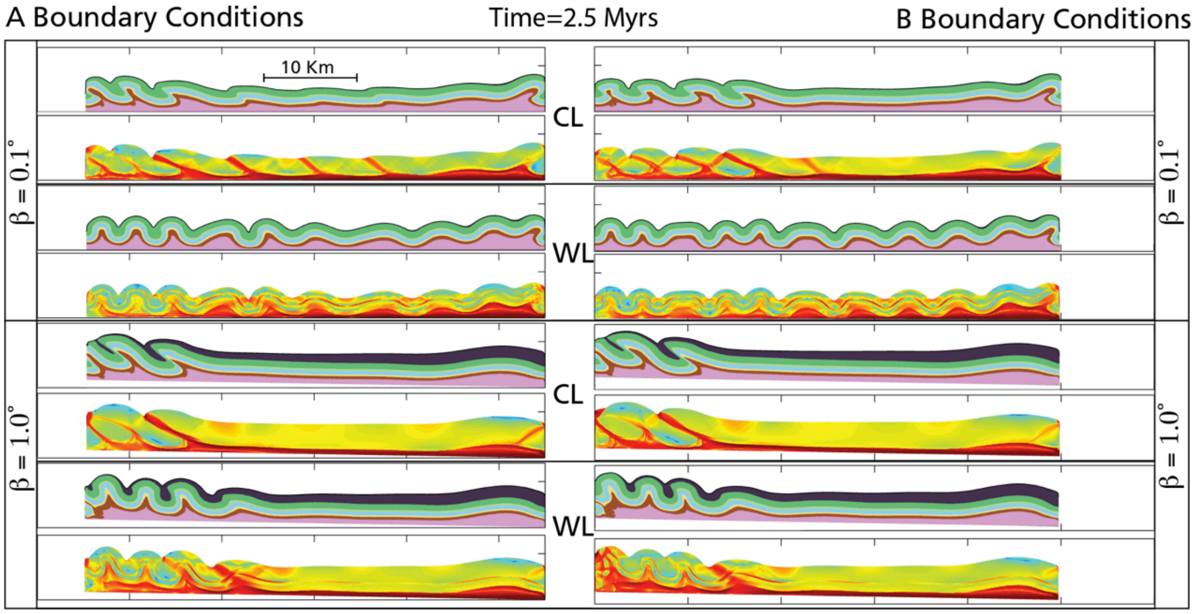

Figure 6.4. Comparison of simulations with two different boundary conditions and using a weak cover (Table 6.1): competent layers (CL) implies that the cover has homogeneous material properties, while weak layer (WL) implies there are two weak layers within the sedimentary cover (see Figure 6.2).

6.4.2 Critical wedge theory and the influence of the basement angle

As already noted by Davis and Engelder (1985) the experiments of Carter and Hansen (1983) demonstrated that the salt rock has a rheology that cannot be modelled with a frictional Coulomb failure criteria.

Here, we use a purely linear viscous material as a detachment layer to model salt. The resistance to shearing of such a purely viscous material is given by

$$\tau = \eta \frac{\Delta u}{H_s} \qquad [6.6]$$

where η is the viscosity of the viscous fluid, H_S the thickness of the viscous material and Δu the horizontal velocity gradient over the viscous material.

The critical taper (Davis and Engelder, 1985) is given by

$$\alpha + \beta = \frac{\beta + \left(\frac{\tau_b}{\rho g H}\right)}{1 + (1-\lambda)\left(\frac{2}{\csc \varphi - 1}\right)} \qquad [6.7]$$

where ρ is rock density, g the acceleration of gravity, H the depth to the basal detachment, λ the pore fluid pressure ratio, τ_b is the shear stress on the basal layer, φ is the friction angle of the wedge materials, and α and β the surface and basal angles.

If we introduce a decreased friction angle that accounts for the effects of the fluid pore pressure named φ_b and considering that $\csc \varphi = \frac{1}{\sin \varphi}$ then equation [6.7] becomes

$$\alpha + \beta = \frac{\beta + \left(\frac{\tau_b}{\rho g H_{sed}}\right)}{1 + \left(\frac{2 \sin \varphi_b}{1 - \sin \varphi_b}\right)} \qquad [6.8]$$

which can be rearranged for H_{sed} as

$$H_{sed} = \frac{\tau_b}{\rho g \left[\left(1 + \left(\frac{2 \sin \varphi_b}{1 - \sin \varphi_b}\right)\right)(\alpha + \beta) - \beta\right]} \qquad [6.9]$$

In viscous detachments, shear resistance is not pressure dependent; but depends on the viscosity and thickness of the detachment layer. A purely viscous material with low viscosity is easily sheared and therefore it flows. In comparison to frictional detachment levels, the strength of the detachment layer is pressure independent and as a consequence, the thickness of the overburden influences the shape of the wedge.

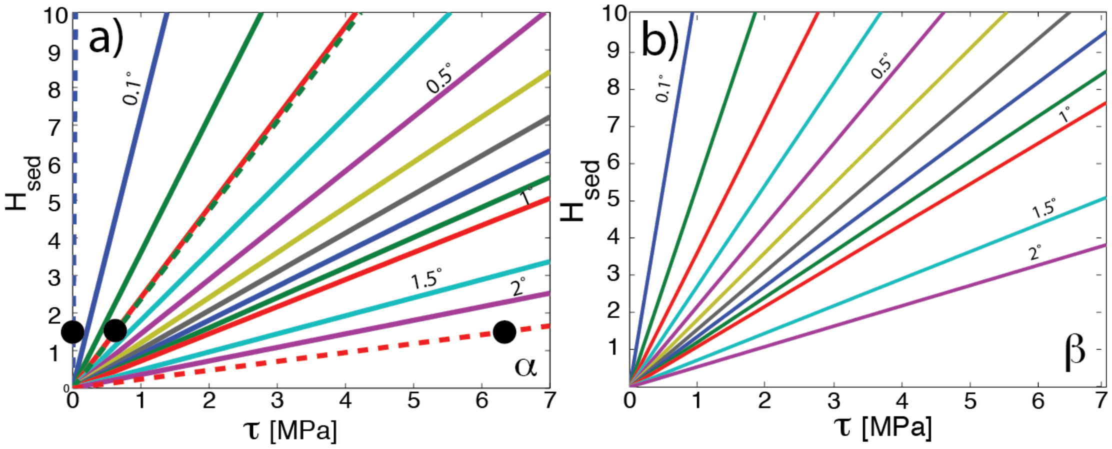

Figure 6.5. Plot of H_{sed} versus τ for different α and β computed using critical wedge theory. The values that correspond to η=10^{16}, 10^{18}, and 10^{19} Pa s (from left to right respectively) for a thickness that corresponds to the a simulation with no basal tilting is indicated by the black dots.

This dependency on the cover sequence is illustrated in Figure 6.5, which was obtained by setting either α or β to zero in Equation [6.9]. Wedges forming over a viscous detachment level (e.g. salt) have lower taper angles and faster propagation of deformation than over a frictional detachment (Davis and Engelder, 1985). Analogue models have reported the simultaneous growth of structures that are more symmetrical when a viscous detachment is involved (Bonini, 2007; Costa and Vendeville, 2002; Cotton and Koyi, 2000).

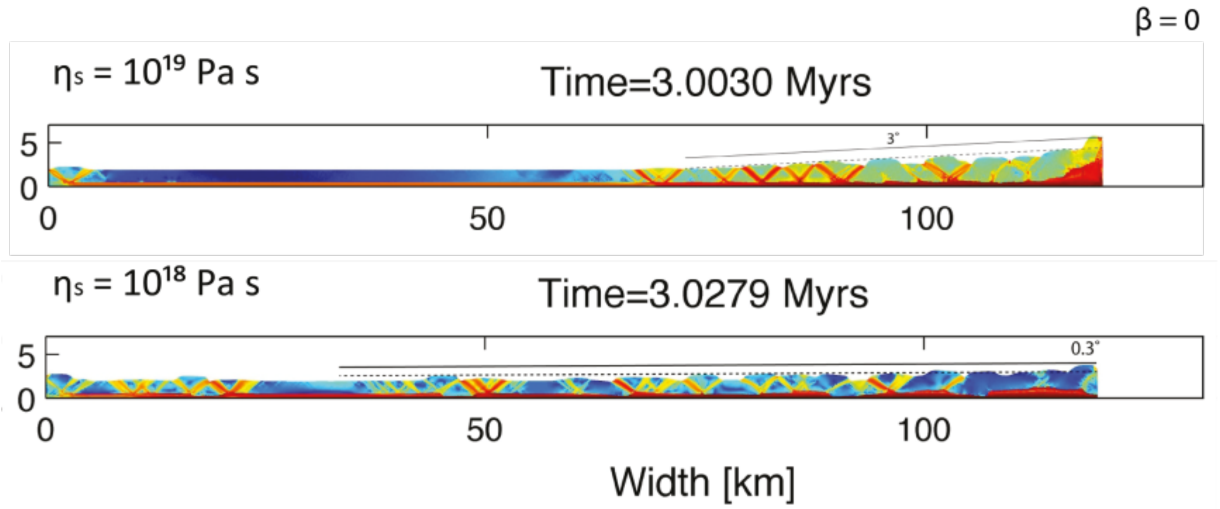

Figure 6.6. Results of simulations with a basal angle of zero and initial surface slope of zero after around 3 Myrs. The surface slope angle that develops is different for different viscosity of the detachment layer.

The taper angle also depends on the detachment viscosity (Figure 6.5), which is confirmed in numerical simulation with a horizontal detachment and varying viscosity (Figure 6.6). The taper angle develops as a result of applied compression, and is steeper in simulations with a higher viscosity (varying from 0.003 degrees when $\eta=10^{16}$ Pa s to 3 degrees for $\eta=10^{19}$ Pa s as shown in Figure 6.5). It is obvious that when taper angles are as small as 0.03 degrees, any initial deformation in the form of an anticline or thrust close to the backstop will already behave as a stable wedge.

Figure 6.7 shows a plot where both α and β are shown. The figure allows distinguishing where stable and instable wedges are separated (solid lines) when both angles (basal and surface) are considered. The dependency of η and Φ is illustrated as well. The advantage of this graph is that both angles can be non-zero to illustrate how the use of an initial detachment angle changes the initial conditions between stable and unstable wedges. Dashed lines of Figure 6.7 show, the β and α relation considering our case of initial tilted detachment (β>0) and corresponding maximum sediment cover thickness (depending on β and L).

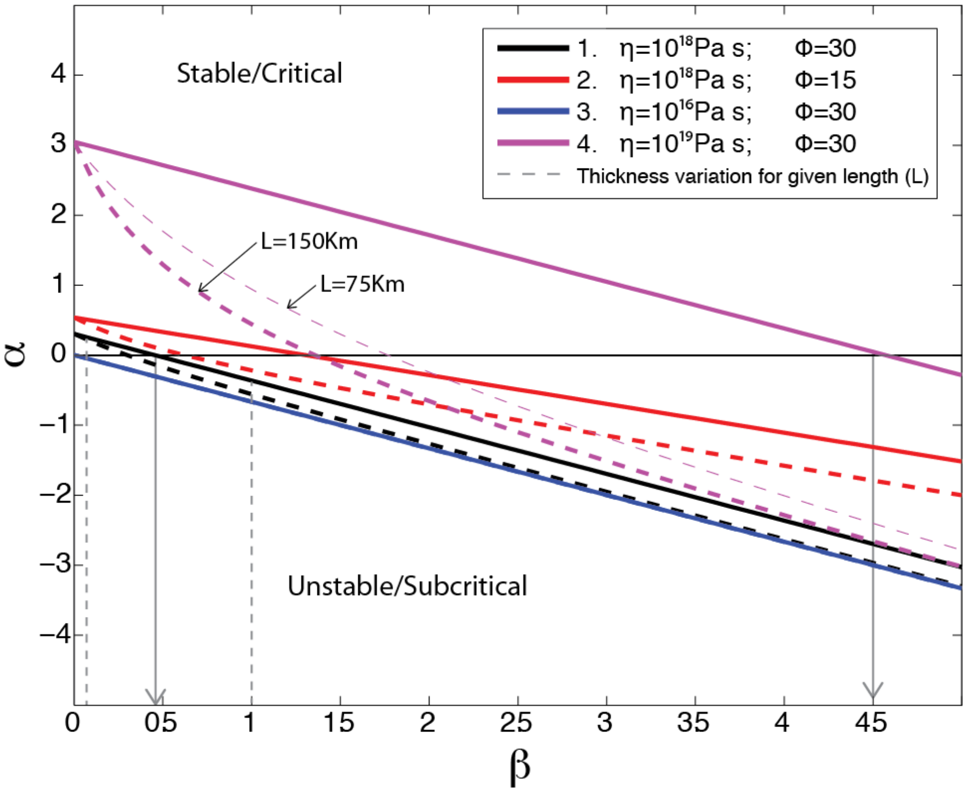

Figure 6.7. Plot of α versus β for different viscosities and friction angle. The different lines indicate the transition from a stable or critical wedge to an unstable or subcritical wedge for different material properties..

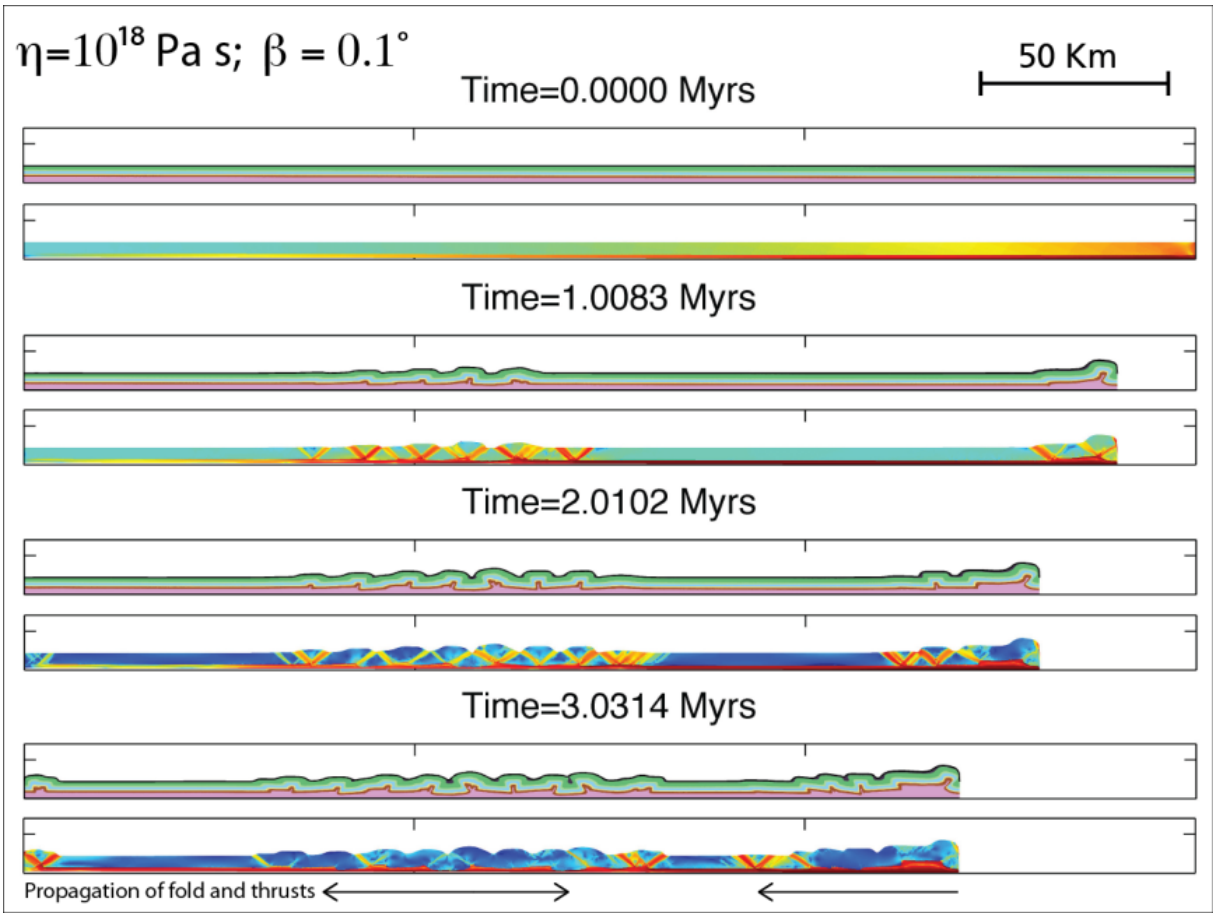

Figure 6.8. Evolution of a simulation with a strong cover, no weak layers (Table 6.2, CL) and an initial detachment angle of 0.1 degrees. Initial deformation localizes on the right side by forming folds and thrust. Because the taper angle required for the wedge to be stable is less than 0.03 degrees, the deformation is rapidly transferred to another area of the domain.

For $\eta = 10^{18}$Pa s, with a tilting angle of β and initial α=0, the transition from an unstable to stable wedge occurs at 0.45°. For $\eta = 10^{19}$Pa s, with a tilting angle of β and initial α=0, the transition from unstable to stable occurs at 4.5° as shown in the graph. When α=0 and the detachment basal angle is bigger than the transition angle from unstable to stable , all deformation is transferred to the model end and the thickest wedge shaped Molasse sediments remain essentially undeformed. For smaller angles, deformation starts at the inner part but is rapidly transferred to other areas.

Figure 6.8 and Figure 6.9 show the evolution of two different simulations using the same parameters corresponding to homogeneous competent layers (CL) of Table 6.2 but for two different basal angles: 0.1 and 1.0 degrees. In Figure 6.8, with a basal angle of 0.1 degrees, the initial deformation is localized close to the backstop (right side of the domain), where an initial structure is formed. However, as soon as this initial fold has reached certain amplitude, the deformation is transferred to the inner part of the model (Figure 6.8, 1 Myrs). The thrust and folds that develop next, form to both sides of the initial structure in the central part, and therefore the deformation propagates in two directions. Once the structures in the central part of the domain reach certain amplitude, deformation is transferred to the left side of the model, far from the backstop (Figure 6.8, 3 Myrs). These jumps in deformation occur due to the low taper angle (0.45 degrees) that is needed to make the wedge stable, and as can be observed in Figure 6.8, this effect is not limited to the wedge that forms close to the backstop, but also to the structure forming in the middle of the domain.

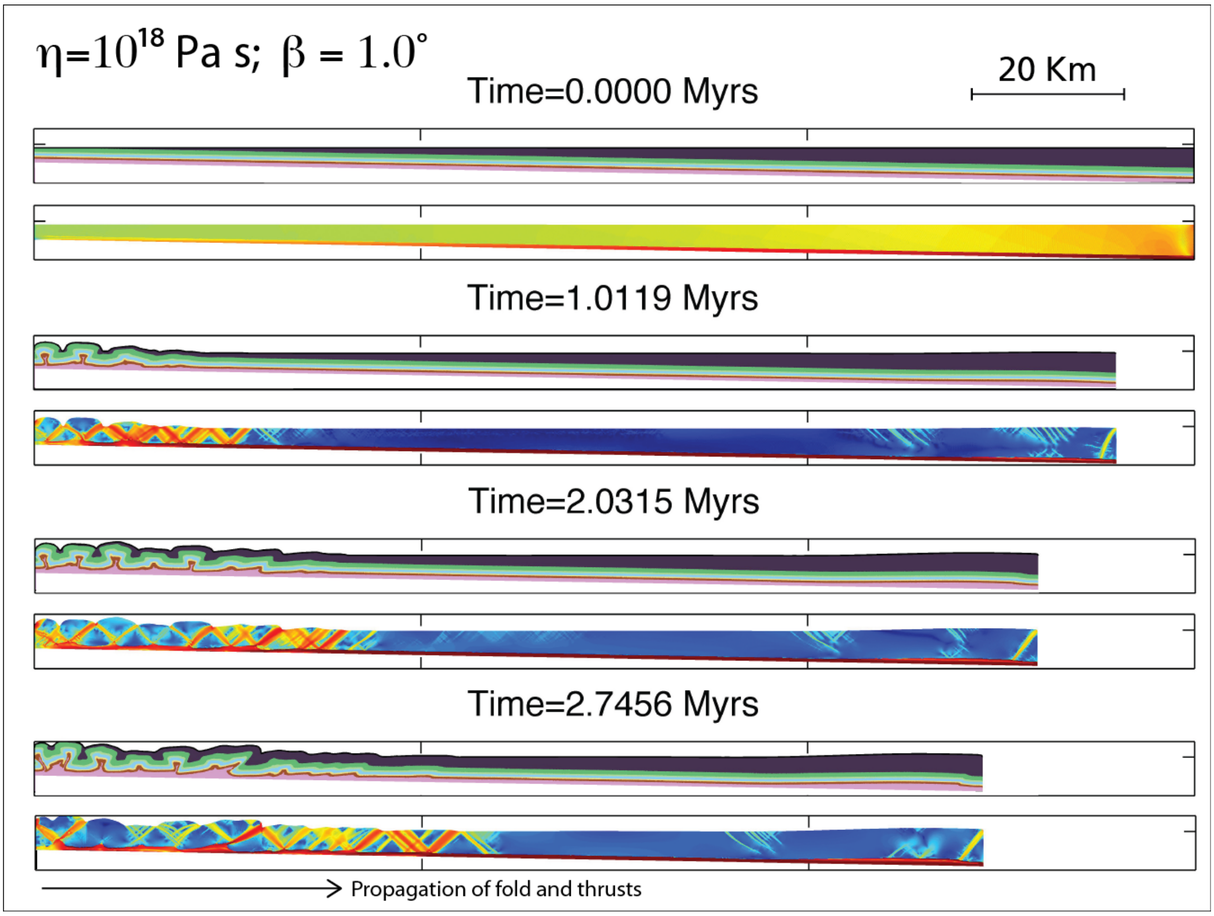

Figure 6.9. Evolution of a simulation with a strong cover, no weak layers (Table 6.2, CL) and an initial detachment angle of 1 degree. With that inclination and an initial surface slope of zero, the wedge is already stable and therefore the deformation is already transmitted to the left side of the domain at the beginning of the simulation.

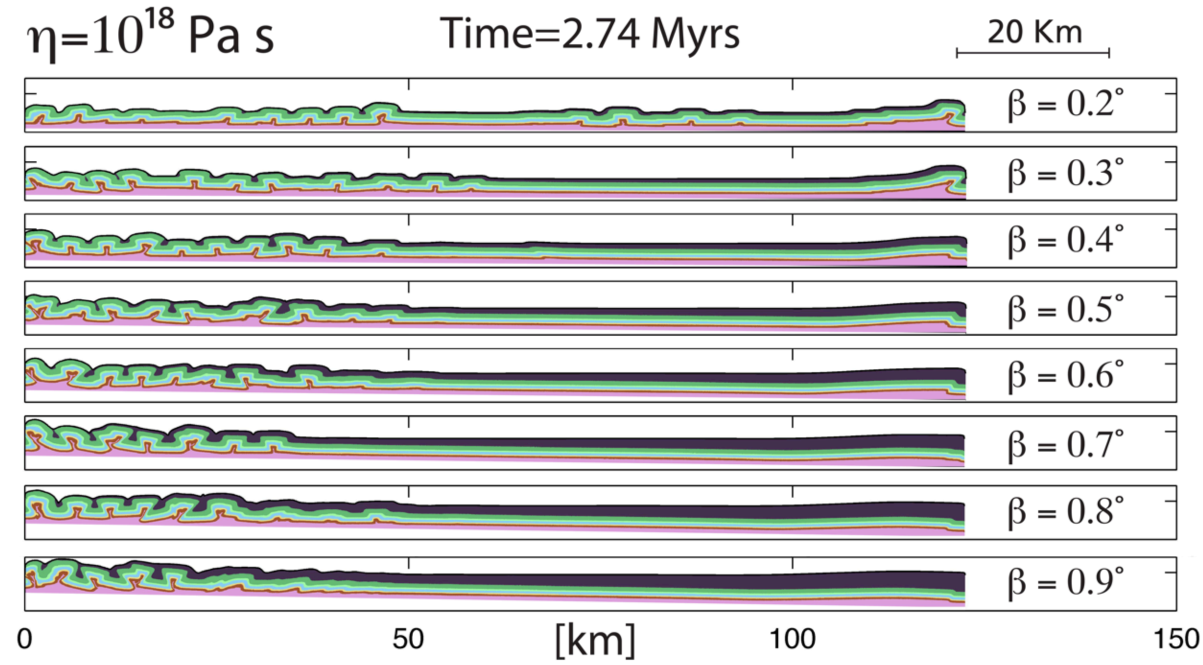

Figure 6.10. Simulations with a strong cover, no weak layers (Table 6.2, CL) and different basal angles after 2.74 Myrs of shortening. The lower the detachment angles are, the more deformation is accommodated on the right side of the domain, although it is soon transferred to the left side. The simulations with higher detachment angle have initial deformation starting on the left side of the domain.

A simulation with a larger taper angle of 1.0 degree, exhibits a complete different behaviour because the basal angle is already higher than the one predicted for the wedge to be stable (Figure 6.9). As a result of the wedge being already stable, the deformation is transferred far away from the backstop to the left side of the model domain. The initial structures form at the left side and propagate in an out of sequence manner towards the backstop.

The final stage of simulations for strong homogeneous cover (Table 6.2, CL), and initial basal angles between 0.2 and 0.9 are shown in Figure 6.10. The transition between stable and instable wedges for the viscous detachment with viscosity of 10^{18}Pa s is predicted to happen with basal angle of 0.45. The results of Figure 6.10 show that the simulation with the lowest basal angle of 0.2 degrees exhibits a widely distributed deformation along the modelled domain. A basal angle of 0.3, also localized initial deformation by forming a structure at the backstop, but deformation is afterwards transferred away from the backstop. Basal angles between 0.4 and 0.6 localize much less deformation close to the backstop before transferring the deformation to the other end of the model. Because, once a little deformation occurs in the backstop the taper angle is already above the stable taper angle, the deformation is transferred to the other end. From the left side of the domain, the deformation is propagating towards the backstop. Therefore, in simulations between 0.4 and 0.9 degrees of basal angle, the fact that the deformation is transferred earlier for simulations with lower angles, causes the deformation to propagate further within the domain. For the highest initial basal angles of 0.7-0.9 degrees there is almost no deformation at the backstop.

6.4.3 Influence of a slope break or change in detachment angle

Simulations with a constant slope of the basement are in good agreement with critical wedge theory and show that when the basal angle is higher than the critical taper angle, the deformation is transferred from the backstop to the opposite end of the model domain. However, in the case of the Jura, it has been proposed that the initial deformation of the Jura started at its southern end and deformation subsequently propagated northwards (Philippe et al., 1995; Sommaruga, 1999). In our simulations, deformation is transferred to the model domain, with continued propagation towards the hinterland, opposite as it is thought to be the case in the Jura. One of the characteristics of the basement topography in the Jura-Molasse system is that its dip is not constant, but has a changing angle with a steeper slope below the Molasse. Therefore, we also tested the influence of a basal change in slope within the model domain, changing from a flat detachment (basal angle of zero), to a detachment of at least 0.1 degrees towards the backstop. The schematic representation of a setup with a slope change in the basement is shown in Figure 6.3. The results of simulations with a slope change from zero degrees to a basal angle of 0.1, 0.5 and 1.0 degree are shown in Figure 6.11. Those simulations have been tested with different mechanical stratigraphy, whose effects will be commented later.

In simulation with a slope change and a basal angle of 0.1 degree, the deformation initially localizes close to the backstop and propagates outwards. As soon as the taper angle is reached, however, there is a jump in the deformation front that is transferred to the other end of the model domain. From this side, deformation propagates towards the backstop. Different dynamics can be seen when the basal angle of the tilted segment is 0.5 degrees. In this case, we can distinguish between the dynamics when deformation is folding dominated and when it is thrusting dominated. In the case of folding, one single structure develops close to the backstop, which is sufficient for the deformation to be transferred. However, instead of the deformation being transferred to the other end of the domain, it is transferred to the central part of the model domain in the flat basement area. From this position, deformation starts propagating outwards. Doing the same simulation but with a different mechanical stratigraphy, which results in thrusting, deformation is transferred from the beginning of the simulation to the middle of the model domain. From this point onwards it propagates in both directions, while at the same time a back thrust starts to develop close to the backstop. When the initial basal angle of the tilted segment of the detachment is higher (1.0 degree), deformation with both mechanical stratigraphies is transferred to the flat area of the domain with no structures developing at the backstop.

The simulations with the slope change in the basement completely change the sequence at which the deformation evolves, which is more consistent with what is proposed for the Jura deformation.

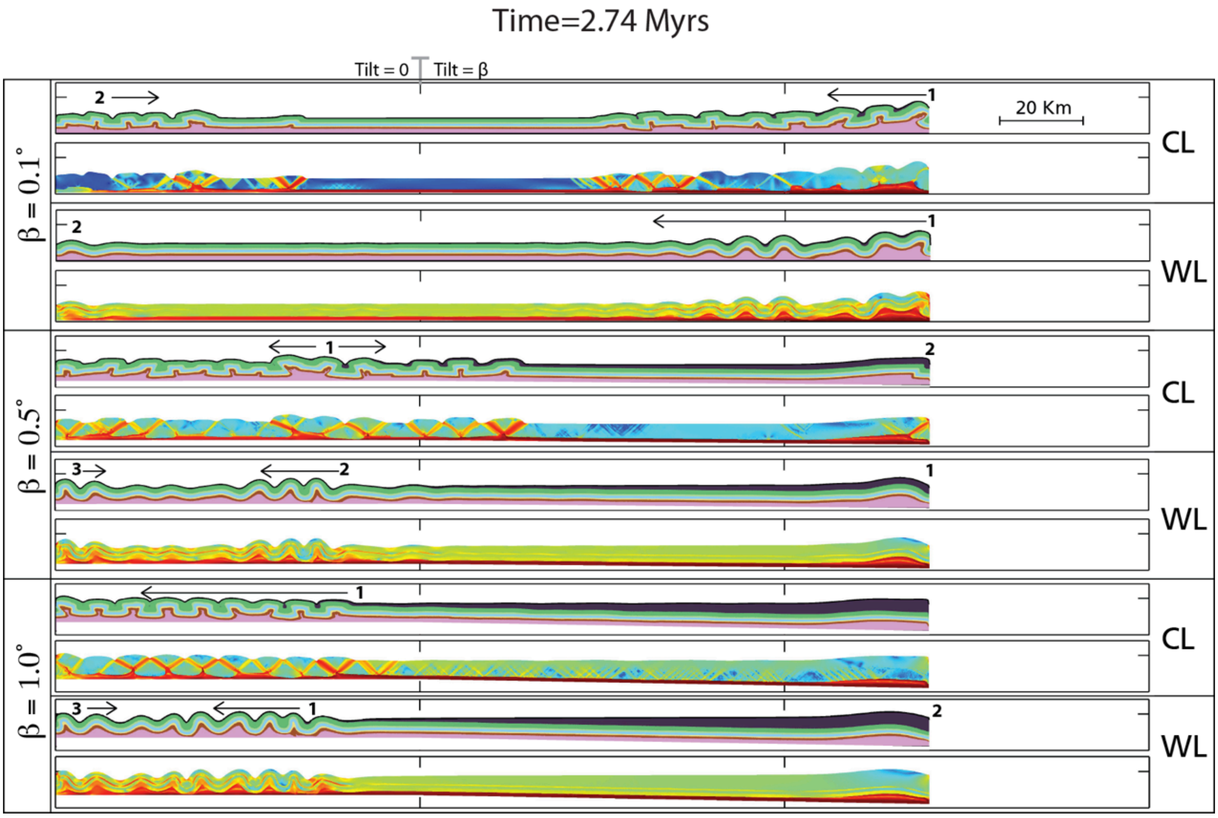

Figure 6.11. Comparison of simulations with a strong cover (Table 6.2, CL and WL) and a change in angle of the basal slope: on the left side, the detachment is flat and on the right side, the detachment has an angle ranging from 0.1 to 1 degree. Numbers indicate sequence of deformation of the structures.

6.4.4 Influence of mechanical stratigraphy

Overall, two different sets of parameters have been used in our models (see Table 6.1 and Table 6.2). In the case of Table 6.2, the viscosities of the competent layers are up to seven orders of magnitude different than that of the viscous detachment, which ensures that the layers essentially behave as elasto-plastic materials. On the other hand, the parameters of Table 6.1, have viscosity of the competent layers of four orders of magnitude difference. When comparing the simulations that use the homogeneous competent layers of Figure 6.4 and Figure 6.11, the impact of using different viscosity values for the cover sequence can be seen. With lower viscosities, thrusts develop lower angles and with a dominant vergence outwards from the backstop. Besides, the thrust sheets that develop in the simulation with lower viscosity of the cover are longer. With higher viscosities, thrusting is almost symmetric with the development of conjugate thrusts that form at higher angles.

When the parameters that correspond to a cover with weak layers (WL) are used, the deformation is clearly dominated by folding in the case of both parameter sets of Table 6.1 and Table 6.2. When deformation is mostly accommodated by folding, the simulations with the higher basal angle show that deformation can be more readily accommodated close to the backstop by the development of a wide low amplitude fold. On the other hand, when a homogeneous cover is used favouring thrusting, the deformation at the backstop is in most cases accommodated by a back thrust. Whether a fold or a back thrust develops in the vicinity of the backstop can also change how the deformation sequence develops within the model. One example can be seen in the case of a simulation with a slope change and a basal angle of 0.5 degrees (Figure 6.11). Here, when weak layers are present, a fold develops initially and only afterwards the deformation is transferred to the central part of the domain. When a homogeneous cover is considered on the other hand, deformation is transferred since the beginning to the central part of the domain, and only after a certain amount of time a thrust starts to develop close to the backstop.

6.4.5 Curved basement

In this study, we have performed simulations with a tilted detachment with constant slope and with a change in the slope. Within the simulations, the topography of the detachment does not change during the simulations. However, the tilting of the basement in the Jura-Molasse system is likely the result of flexural bending due to the load of the Alpine wedge. The evolution of such a system has been studied widely in terms of loading (Burkhard and Sommaruga, 1998; Homewood et al., 1986; Kempf and Adrian Pfiffner, 2004; Pfiffner et al., 2002). In this case, plate flexure profile would have varied as a result of the advancement of the Alpine wedge from a more distant position to its current position. Recent models have integrated the evolution of such a plate as an elastic beam due to the increasing load during the evolution of the wedge (Fillon et al., 2013a). Here, we do not consider such a setup with an evolving basement, but we have performed some analytical investigation of the effect of the flexural shape of the basement on the surface slope of the fold and thrust belt.

The deflection of a flexural foreland basin can be modelled as a broken elastic plate under a line load. In that case, the vertical displacement of the plate (ω) at a given distance (x) is given by

$$\omega = \omega_0 \exp(-\lambda x) \cos(\lambda x) \qquad [6.10]$$

where ω_0 is the initial end displacement and λ is the end load defined as,

$$\lambda = \left[\frac{4D}{(\rho_m - \rho_s)g}\right]^{-\frac{1}{4}} \qquad [6.11]$$

where ρ_m and ρ_s are the densities of mantle and sediments, g is the acceleration of gravity and D is the flexural rigidity that depends on lithospheric plate thickness (h) and on the elastic Young's modulus (E) and on the Poisson ratio (ν) as follows

$$D = \frac{Eh^3}{12(1-\nu)^2} \qquad [6.12]$$

The flexural profile equation [6.10] and the critical wedge theory [6.8] can be combined to account for the shape of the orogen overriding the flexed detachment (e.g. Wang, 2001; Willett and Schlunegger, 2010). Willett and Schlunegger (2010) derived their solution under the assumption that both surface and basal angles change slowly and that therefore the critical wedge theory can be applied in a point wise manner in x direction. They showed that the surface slope in such an orogen does not have a constant angle and that it will instead have a convex upwards shape (with a negative angle), as illustrated in Figure 6.12. The area where the surface slope has a negative angle (shaded area in the graph) will dip towards the orogen. Because this is the surface slope of the critical wedge, any deposition that occurs above this area will keep the wedge stable.

Willett and Schlunegger (2010) calculated the solution for the shape of an orogen above a flexed frictional detachment. However, the Jura is known to have formed above a detachment that consists of several salt layers and other Triassic evaporites (Sommaruga, 1999). We have applied the same approach as in Willett and Schlunegger (2010) but considering a viscous instead of frictional detachment.

The history of foreland basin evolution can be reconstructed by the analysis of lithostratigraphic units and their correlation (Burkhard and Sommaruga, 1998) and the total subsidence can be derived from this data (Burkhard and Sommaruga, 1998). Figure 6.13 shows the total subsidence points and subsidence curves from two sites compiled by Burkhard and Sommaruga (1998). These points do not take into account compaction or isostasy. However, the lines have been used to calculate a total subsidence rate in the area and to calculate the depth at which the area was at the times shown in Figure 6.13.

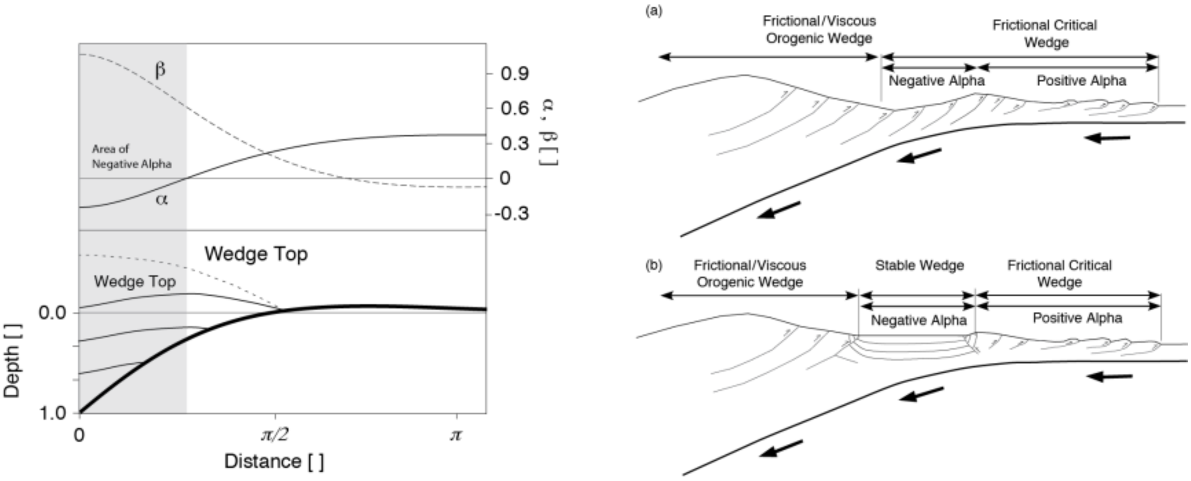

Figure 6.12. Result of combining the critical wedge theory and the flexure solution. The topography of the basal detachment is plotted in the lower graph (thick-black line). The basal slope angle (β) reflects the curvature variation of the flexed detachment, whereas the surface slope (α) is obtained from the surface slope and wedge and detachment strength. Sketches on the right show the formation mechanism of the Negative Alpha basin, and how it could be maintained in a stable manner with deposition. Figures are modified from (Willett and Schlunegger, 2010).

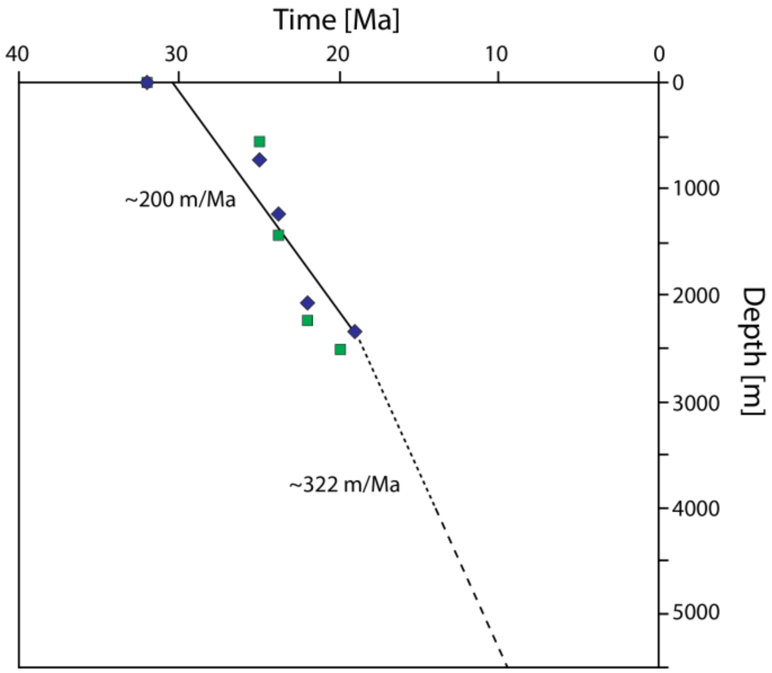

Time [Ma]	ω_0 [m]
30	1524
28	1724
26	1924
24	2124
22	2524
20	2924
18	3568
16	4212
14	4856
12	5500

Figure 6.13. Total subsidence points compiled by (Burkhard and Sommaruga, 1998). The graphs have been used to obtain a raw subsidence rate that does not consider isostasy or compaction, and to obtain a depth at different times. The points of two sites are plotted: Lausanne (Savigny drill hole) and Mt. Pelerin. For more details see Burkhard and Sommaruga (1998).

Several values for the elastic flexural fit of the present day basal shape in the Jura-Molasse system can be found in the literature (e.g. Burkhard and Sommaruga, 1998; Willett and Schlunegger, 2010). The current shape of the basal detachment is quite well constrained and dips towards the foredeep (e.g. Pfiffner et al., 2002). The values that correspond to the elastic plate that can reproduce the current plate curvature are chosen such that they fit this shape. We have used the parameters by Burkhard and Sommaruga (1998): ρ_m=3250 kg/m^3, ρ_s =2500 kg/m^3, h=25 km, E = 70 GPa and ν=0.3. We calculated the profile for two different depths (end displacement), assuming that the load causing the deflection did not change position, but that it grew and caused further deflection at the end. This simple assumption is consistent with the idea that between Oligocene and Miocene the evolution of the Alps changed and switched from a frontal accretion phase, to an internal thickening phase (Pfiffner et al., 2002). Our aim is to perform a simple analysis to understand how the negative alpha basin position might have changed for different flexure profiles and parameters of the cover and viscous detachment. The results for values of the deflection of 1500 meters and 5500 meters are shown in Figure 6.14. Different viscosity values of the detachment layer or different friction angle of the sedimentary sequence do not change the basal angle that only depends on the elastic properties of the basement. However, the friction angle of the sediments and the viscosity of the viscous detachment influence the surface slope as seen in Figure 6.14. Changing the viscosity displaces the surface slope curve parallel either upwards (higher viscosity) or downwards (lower viscosity), whereas changing the friction angle changes the angle distribution of surface slope and decreases the angles in the case of lower friction angle.

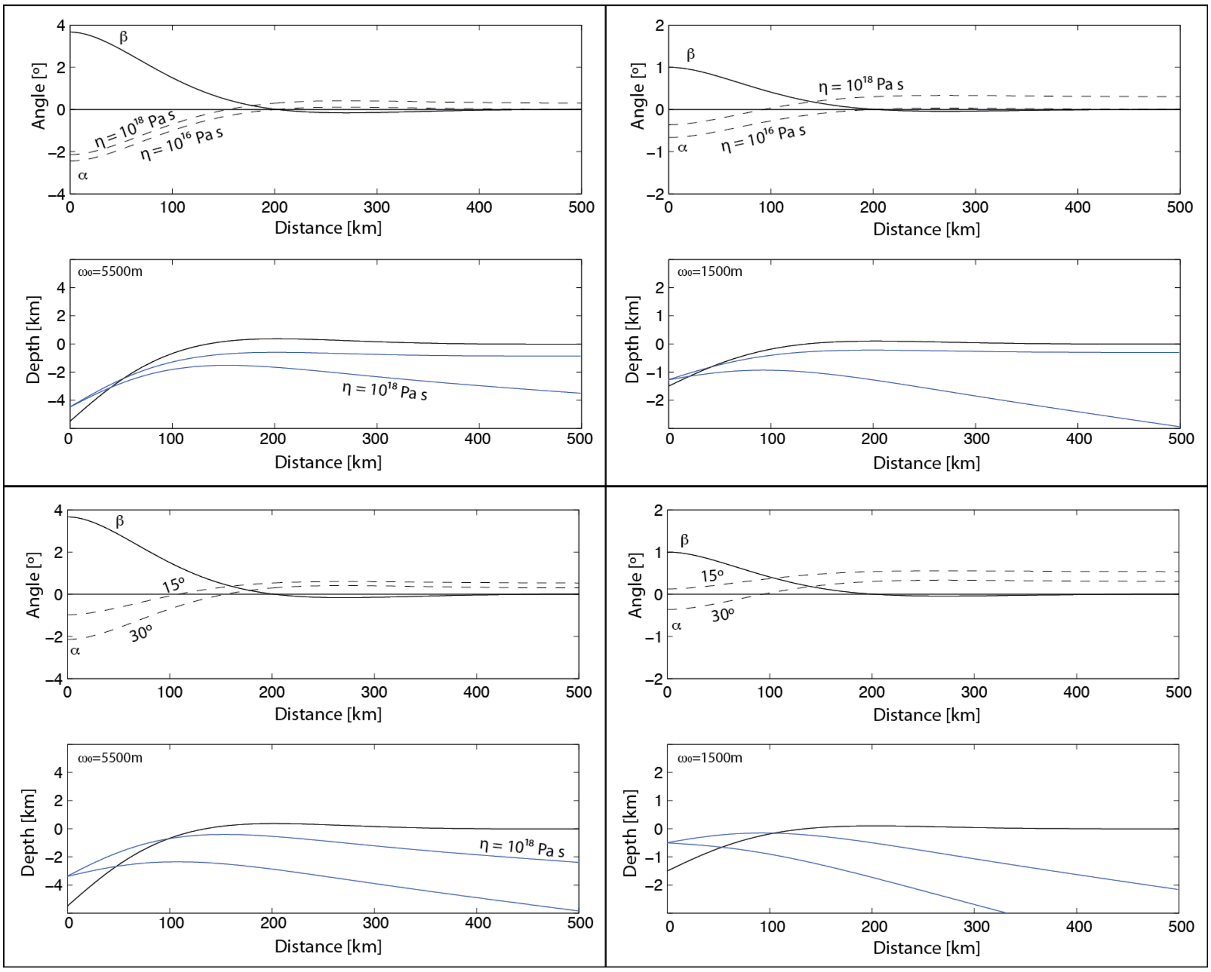

Figure 6.14. Surface and basal slopes for two different flexed plate profiles. The effect of the sedimentary cover friction angle and of the viscous detachment viscosity is visible in the surface angle and in the wedge top topography profile (blue lines). The wedge top profiles are drawn at an arbitrary height, and they would be parallel for different chosen heights.

The results of Figure 6.14 show that for a flexural profile of the basal slope with an end displacement of 5500 meters (similar to what it is currently observed), the surface slope (alpha slope) has a negative segment for both viscosity values of the detachment (10^{16} Pa s, and 10^{18} Pa s). The same applies for both friction angle values of the sedimentary cover, although in the case of 15 degrees, the initial negative angle of the surface slope changes from -2 degrees to less than -1 degree. However, if the alpha negative basin theory is to be invoked to explain the change of the Molasse basin from subcritical to critical wedge, this must have occurred at a time when the end displacement was less. To evaluate what is the impact of the end displacement of the flexed plate on the surface slope, we have plotted the result for a much smaller end displacement of 1500 meters. This value was calculated by using the curves of Figure 6.13. The result (shown in the right panels of Figure 6.14), illustrates, that even for such a configuration, the surface slope tends to have a negative segment. The exception is in the case of a sedimentary cover with friction angle of 15 degrees. Therefore, we argue that the surface slope calculated with jointly critical wedge and flexural foreland are not only very sensitive to the basal shape of the flexed plate, but also to the parameters of the materials being deformed above the detachment level and the nature of the detachment level itself. Because we considered the case of a purely viscous detachment, the viscosity is an important parameter as well.

6.5 Discussion

The critical taper theory can explain why a wedge shaped Molasse basin might have reached a critical taper angle that allowed the Molasse to transfer all the deformation to the frontal part. This dynamics can be reproduced with simple models using a constant basement slope in the basement, a sedimentary cover composed of different layers and a homogenous tertiary filled wedge shaped basin representing the Molasse basin. The deformation sequence in such a simple system with a basal angle higher than the taper angle would still allow for certain deformation in the Molasse basin itself. This deformation is more pronounced when folding rather than thrusting is the deformation mechanism. However, a basement with a constant slope does not explain the position at which the Jura deformation started. The current shape of the basement is best reproduced by a basement with a slope change, which we have simplified in our simulations as having a constant angle close to the foredeep and flat on the opposite side. This change in the slope causes deformation to jump from the backstop area to an area close to where the slope change happens. We propose that such a setup is more applicable to the Jura-Molasse system.

However, if the tilting of the basement is interpreted as a result of the flexure due to the load of the Alpine wedge, the approximation by a two-slope basement is overly simplistic. In that case, a curved profile of the detachment should be considered instead.

It has been proposed that with a surface slope of zero, the weakness of detachment and dipping angle must be considered to allow a jump in deformation (Willett and Schlunegger, 2010). For the surface to be flat, the same authors propose that sedimentation at the wedgetop area should have been continuous during formation of the Jura, which would be possible if accommodation space was created by the flexural loading of the Alpine wedge. The surface slope above flexed plate shows a convex upward shape for the critical wedge above, with a negative alpha angle area dipping towards the foredeep. This area of negative slope creates space for new sediments to deposit, which would at the same time make the wedge critical, and able to transfer deformation. If this is the case for the Jura-Molasse system, there must have been a change in the wedge shape from a positive alpha to a negative alpha basin at some stage during the formation of the Molasse basin.

In our simulations, we have not considered the effect of syn-tectonic erosion, which could be an important parameter during the formation and evolution of thrust wedges and accretionary prisms (Fillon et al., 2013a; Simpson, 2010a). Syn-tectonic sedimentation could have caused a change of a sub-critical Molasse basin to a stable basin that is able to transfer the deformation (Willett and Schlunegger, 2010). Our simplified setups assume that accommodating space has been created during the tilting of the basement and that therefore the basin can be filled with sediments such that the surface slope is flat. Although this would have needed further explanation of how the accommodation space is created, we have focused on a simple setup to study the relation between the basal angle and the taper angle and how they fit to the critical wedge theory.

The thickness distribution of the Triassic evaporitic layers could also be considered if the different deformation domains within the Jura-Molasse system should be explained. The salt thickness distribution coincides overall with the arcuate shape of the Jura fold and trust belts towards the NW, but it extents below the Molasse basin. Although the current evaporite distribution in the area is the result of compressional tectonics that the area have underwent, the overall thickness tendency observed might have been close to the distribution before the formation of the Jura fold-and-thrust belt. The effect of the thickness of the detachment layer with respect to its overlaying sedimentary cover is known to have an effect on the structures developing on the cover sequence (e.g. Bonini, 2003; Ruh et al., 2012). The thickness ratio between the detachment layer and overlying sequence switches the deformation mode between thrusting and folding (Simpson, 2009) and might need to be considered in future studies aimed at explaining the different tectonic zones within the Jura fold and thrust belt.

6.6 Conclusions

Two different boundary conditions have been tested and no major differences in the overall dynamics of the system have been observed between them. The choice of using one of the boundary conditions with respect to the other one is mainly due to the possibility of implementing easily more complex geometries of the basement such as a discontinuous slope or curved basement.

The influence of the tilting angle is discussed in terms of critical wedge theory with a viscous detachment. Tilting with a certain angle can cause the wedge to be stable from initial stages therefore causing the deformation to be transferred to the frontal area. However, the position to which the deformation jumps in the setups with constant angle of the basement is basically the result of the model length. The new deformation front is, however, jumping to a different position when a slope change is considered in the setups. In this case, the wedge transfers the deformation close to the area where the slope change occurs. In such systems with a change of slope, the new deformation propagation can further be transferred to opposite end of the domain (outwards from the foredeep), if the critical taper is reached by the new developing wedge.

A more complex curved geometry of the basement is also tested and discussed with an analytical approximation that integrates the critical taper theory with the flexural bending of an elastic plate. We have investigated the changes in the surface slope shape above the bended plate for different end displacement that are assumed to potentially represent different time stages during the evolution of the Jura-Molasse system.

The influence of the mechanical stratigraphy on the dynamics and sequence of deformation has also been studied with different physical configurations of the sedimentary cover. Inclusion of a weak layer in the cover changes the deformation style from either symmetric or asymmetric thrust systems to symmetric fold trains. This change of deformation mode is shown to have an effect on the sequence of deformation.

6.7 Acknowledgements

Funding was provided by the European Research Council under the European Community's Seventh Framework program (FP7/2007-2013) ERC Grant agreement #258830.

6.8 References

Bonini, M., 2003, Detachment folding, fold amplification, and diapirism in thrust wedge experiments: Tectonics, v. 22, p. 1065.

Bonini, M., 2007, Deformation patterns and structural vergence in brittle–ductile thrust wedges: An additional analogue modelling perspective: Journal of Structural Geology, v. 29, p. 141-158.

Buiter, S.J.H., Babeyko, A.Y., Ellis, S., Gerya, T.V., Kaus, B.J.P., Kellner, A., Schreurs, G., and Yamada, Y., 2006, The numerical sandbox: comparison of model results for a shortening and an extension experiment: Geological Society, London, Special Publications, v. 253, p. 29-64.

Burkhard, M., 1990, Aspects of the large-scale Miocene deformation in the most external part of the Swiss Alps (Subalpine Molasse to Jura fold belt): Eclogae Geologicae Helvetiae, v. 83, p. 559-583.

Burkhard, M., and Sommaruga, A., 1998, Evolution of the western Swiss Molasse basin: structural relations with the Alps and the Jura belt: Geological Society, London, Special Publications, v. 134, p. 279-298.

Carter, N.L., and Hansen, F.D., 1983, Creep of rocksalt: Tectonophysics, v. 92, p. 275-333.

Costa, E., and Vendeville, B.C., 2002, Experimental insights on the geometry and kinematics of fold-and-thrust belts above weak, viscous evaporitic décollement: Journal of Structural Geology, v. 24, p. 1729-1739.

Cotton, J.T., and Koyi, H.A., 2000, Modeling of thrust fronts above ductile and frictional detachments: Application to structures in the Salt Range and Potwar Plateau, Pakistan: Geological Society of America Bulletin, v. 112, p. 351-363.

Dabrowski, M., Krotkiewski, M., and Schmid, D.W., 2008, MILAMIN: MATLAB-based finite element method solver for large problems: Geochemistry, Geophysics, Geosystems, v. 9, p. Q04030.

Davis, D.M., and Engelder, T., 1985, The role of salt in fold-and-thrust belts: Tectonophysics, v. 119, p. 67-88.

Fillon, C., Huismans, R.S., and van der Beek, P., 2013a, Syntectonic sedimentation effects on the growth of fold-and-thrust belts: Geology, v. 41, p. 83-86.

Fillon, C., Huismans, R.S., van der Beek, P., and Muñoz, J.A., 2013b, Syntectonic sedimentation controls on the evolution of the southern Pyrenean fold-and-thrust belt: Inferences from coupled tectonic-surface processes models: Journal of Geophysical Research: Solid Earth, v. 118, p. 5665-5680.

Homewood, P., Allen, P., and Williams, G., 1986, Dynamics of the Molasse Basin of western Switzerland: Foreland basins, v. 8, p. 199-217.

Ibele, T., 2011, Tectonics of the Western Swiss molasse basin during Cenozoic times, PhD Thesis, Université de Fribourg.

Kaus, B.J.P., 2010, Factors that control the angle of shear bands in geodynamic numerical models of brittle deformation: Tectonophysics, v. 484, p. 36-47.

Kempf, O., and Adrian Pfiffner, O., 2004, Early Tertiary evolution of the North Alpine Foreland Basin of the Swiss Alps and adjoining areas: Basin Research, v. 16, p. 549-567.

Laubscher, H.P., 1961, Die Fernschubhypothese der Jurafaltung: Eclogae Geologicae Helvetiae, v. 54, p. 221-280.

Laubscher, H.P., 1992, Jura kinematics and the Molasse basin: Eclogae Geologicae Helvetiae v. 85, p. 653-676.

Pavoni, N., 1961, Faltung durch Horizontalverschiebung: Eclogae Geologicae Helvetiae, v. 54, p. 515-534.

Pfiffner, O.A., Schlunegger, F., and Buiter, S.J.H., 2002, The Swiss Alps and their peripheral foreland basin: Stratigraphic response to deep crustal processes: Tectonics, v. 21, p. 3-1-3-16.

Philippe, Y., 1994, Transfer Zone in the Southern Jura Thrust Belt (Eastern France): Geometry, Development, and Comparison with Analogue Modeling Experiments, *in* Mascle, A., ed., Hydrocarbon and Petroleum Geology of France, Volume 4: Special Publication of the European Association of Petroleum Geoscientists, Springer Berlin Heidelberg, p. 327-346.

Philippe, Y., géologie-géochimie, I.f.d.p.D., and géodynamique, U.d.S.L.d., 1995, Rampes latérales et zones de transfert dans les chaînes plissées: géométrie, condition de formation et pièges structuraux associés, Technip.

Ruh, J.B., Kaus, B.J.P., and Burg, J.-P., 2012, Numerical investigation of deformation mechanics in fold-and-thrust belts: Influence of rheology of single and multiple décollements: Tectonics, v. 31, p. TC3005.

Simpson, G., 2011, Mechanics of non-critical fold–thrust belts based on finite element models: Tectonophysics, v. 499, p. 142-155.

Simpson, G.D.H., 2009, Mechanical modelling of folding versus faulting in brittle–ductile wedges: Journal of Structural Geology, v. 31, p. 369-381.

Simpson, G.D.H., 2010a, Formation of accretionary prisms influenced by sediment subduction and supplied by sediments from adjacent continents: Geology, v. 38, p. 131-134.

Simpson, G.D.H., 2010b, Influence of the mechanical behaviour of brittle–ductile fold–thrust belts on the development of foreland basins: Basin Research, v. 22, p. 139-156.

Sommaruga, A., 1997, Geology of the Central Jura and the Molasse Basin: New Insight Into an Evaporite-based Foreland Fold and Thrust Belt, Société neuchâteloise des sciences naturelles.

Sommaruga, A., 1999, Décollement tectonics in the Jura forelandfold-and-thrust belt: Marine and Petroleum Geology, v. 16, p. 111-134.

Stockmal, G.S., Beaumont, C., Nguyen, M., and Lee, B., 2007, Mechanics of thin-skinned fold-and-thrust belts: Insights from numerical models: Geological Society of America Special Papers, v. 433, p. 63-98.

Wang, W.-H., 2001, Lithospheric flexure under a critically tapered mountain belt: a new technique to study the evolution of the Tertiary Taiwan orogeny: Earth and Planetary Science Letters, v. 192, p. 571-581.

Willett, S.D., and Schlunegger, F., 2010, The last phase of deposition in the Swiss Molasse Basin: from foredeep to negative-alpha basin: Basin Research, v. 22, p. 623-639.

Wissing, S.B., Ellis, S., and Pfiffner, O.A., 2003, Numerical models of Alpine-type cover nappes: Tectonophysics, v. 367, p. 145-172.

Chapter 7

Conclusions

During the work presented in this thesis, numerical modelling methods were used to address the questions that were posed in the introduction. Numerical modelling allows studying long term deformation processes (folding and thrusting) involved in areas affected by compressive salt tectonics such as the Zagros and the Jura Mountains. It has been recently argued that folding and thrusting dominated deformations are two end-member modes of deformation (Ruh et al., 2012; Simpson, 2009; Yamato et al., 2011). While the Zagros Simply Folded belt is an example of a folding dominated fold-and-thrust belt, the Jura is interpreted to be an intermediate case, being both folding and thrusting dominated. Also, salt tectonics purely driven by gravity (halokinesis) has been addressed in this thesis focusing on down-built salt diapirs and retrodeformation of salt diapirs formed by different processes.

Next, the main conclusions from all of the previous chapters are briefly summarized and potential future work outlined in three different blocks.

7.1 Multilayer detachment folding

Two different approaches were used to study the multilayer detachment folding instability: a semi analytical 2D approach based on a thick plate analysis and 3D numerical simulations. The 2D analytical approach was used to derive phase diagrams that predict several folding modes. The scaling laws and boundary equations derived from the folding phase diagrams can be used to predict the folding modes for observable parameters of normalized wavelength of fold and salt layer thickness. The results are applicable to crustal scale folding.

Numerical simulations in 2D and 3D have shown that the analytically predicted wavelength is preserved for finite amplitude folding of multilayer detachment models. Yet, compared to 2D cases a somewhat wider spread in folding wavelengths occurs around a dominant value. 3D high-resolution numerical models were used to study fold interactions between the growing fold segments. The complex folding patterns that develop within our simulations is the result of the different interactions between the folding segments. The wide variety of folds shapes that can be observed in south-eastern Zagros (short folds, long straight folds or sinuous folds) are thus reproduced by the simulations. A comparison of observations of the Fars region in the Zagros show a number of similarities, reinforcing the idea large parts of the Zagros could have formed as a result of a crustal-scale folding instability, despite other deformation mechanisms cannot be ignored.

Adding pre-existing salt diapirs to simulations of multilayer detachment folding drastically changes the initial fold patterns, as the pre-existing salt diapirs localize the deformation and control where the initial folds will form. Our results show that the effect of pre-existing heterogeneities on folding patterns can be estimated, by computing a folding growthrate curve and by comparing the growthrate of heterogeneities (spacing of diapirs) with that of the dominant folding growthrate.

When the diapir spacing in the compression direction is close to the dominant folding wavelength, diapir spacing controls the final fold wavelength. In that case, the diapirs are always located in the core of the anticlines (along the compression direction) and below the culminations of the folds, along the strike. Yet, when diapir spacing is too small to accommodate folds in between diapirs, the folding wavelength that develops corresponds to the dominant wavelength and diapir spacing does not control the wavelength. In this case, diapirs can appear at different structural positions with respect to the folds (e.g. synclines and fold flanks). In all the cases, the areas with pre-existing diapirs show at the end an overall higher average elevation than areas without diapirs. This is caused by the fact that folds in areas with pre-existing diapirs form earlier and attain higher amplitudes than folds in diapir-absent areas.

Different than in the south-eastern Zagros, our simulations do not result in diapirs that are located at the periclinal or lateral ends of folds (or in saddle areas of long anticlines). This might be because the fold growth rates in our simulations do not allow for sufficient salt to be extruded or because we did not consider surface processes.

It has been argued that even when more complex visco-elasto-plastic rheologies are used in 2D, the presence of intermediate weak layers causes the deformation to be folding dominated in the Zagros (Yamato et al., 2011). Thus, the results of our study are applicable to such folding dominated areas. However, we have been limited to linear viscous rheologies and therefore, in order to have a folding dominant wavelength similar to the one observed in the Zagros, a simplified setup has been used. The thicknesses of the different layers in the cover of our setup are equal so that there is not disharmonic folding in the simulations. However, spatial variations in the thickness or in the rheological properties of the different layers of the cover cause more complex spatial patterns of folding, including different wavelengths and locally disharmonic folding such as described for Lurestan province in the Zagros (Casciello et al., 2009). These spatial variations should be considered in future work. Besides, the overburden to salt thickness ratio of the Zagros would result in very low fold growth rate if linear viscous rheologies were to be used. A power law viscous rheology would be more appropriate if the interest was to exactly reproduce the Zagros fold belt by using a geometric setup similar to Yamato et al. (2011) .

7.2 Forward and reverse modelling of salt diapirs

We have presented several 3D simulations of down-built diapirs to illustrate the key parameters that influence diapir pattern formation as well as the shape of individual diapirs. Results highlight the importance of the sedimentation rate. In accordance with previous 2D work (Fuchs et al., 2011) the down-building regime is favoured by low sedimentation rates and low viscosity contrasts. However, the sedimentation rate has other further effects. Firstly, lower sedimentation rates favour the preservation of salt ridges and result in more elongated exposed diapirs, whereas higher sedimentation rates favour the formation of dome or finger-like diapirs that initiate at the junctions of the salt ridges. Secondly, sediments can cover diapirs at more advanced model stages when the salt extrusion velocities are lower than the sedimentation rate. As a result, not all of the initially formed diapirs will be exposed at the surface and therefore a higher sedimentation rate will result in a larger spacing between the exposed diapirs.

The numerical models allow quantifying the volume of salt in the numerical domain through time, which gives a proxy of the salt that is being extruded during the simulation. The salt extrusion curves are different for the different properties used in the simulations but in all the cases, extrusion velocity changes can be related to the geometries of the sediments around diapirs.

Although our study uses linear viscous rheology and assumes that sediments have a higher density than the salt, the effects of the sedimentation rates and the relation between the salt extrusion velocities and sediment geometries would still be applicable for more complex rheologies. Diapirism initiation cannot be explained uniquely by differential loading, as various hundreds of overburden need to be deposited before there is density inversion (Hudec and Jackson, 2007). In that case, other tectonics forces need to be considered such as extension or compression. Future work should investigate how the polygonal patterns that are observed in several salt basins can be developed when compression and extension are included.

The same numerical codes that are used for forward modelling have been tested to retrodeform salt diapirs formed by up-building with power law viscous rheologies and by down-building in 3D with linear rheology. Modelled up-built diapirs using power law viscous rheologies with a power law coefficient of up to 5 can be successfully retrodeformed. Also, three dimensional salt structures formed by up-building diapirism with a multi-layered overburden can be retrodeformed to their initial flat stages. However, modelled three-dimensional down-built diapirs can only be retro-deformed to the intermediate stages if the correct rheological parameters and sedimentation rate history is known. Reversing the sedimentation erosion processes that mimic the down-building processes causes some deviation in the volume of materials that enter the system. As a result, the initial geometries cannot be perfectly retrieved. The implementation of the reverse modelling of down-building processes requires further work that might need considering new approaches when injecting material phases that were eroded during the forward simulations. In any case, dynamic retrodeformation or reverse modelling is a potential tool that can provide insights into the deformation history of the studied salt structures. For example, our approach could be applied to natural examples where the rheological parameters are unknown, in order to better constrain the rheology of the salt and the involved cover and at the same time to validate available geometric interpretations.

7.3 Fold-and-thrust belts with tilted detachment

We performed systematic 2D simulations to study fold and thrust belts with tilted detachment. Two different boundary conditions were tested that are applicable to convergent regions and that for the studied setup showed no major differences in the overall dynamics of the system. The influence of the tilting angle in the simulations is in agreement with the behaviour predicted by the critical wedge theory with a viscous detachment. Due to the low taper angles of wedges above a viscous detachment, a small basal angle can cause the wedge to be stable from initial stages. Therefore, the basal angle controls the deformation sequence in the simulations. A basement with a slope change is needed in order to reproduce more complex deformation sequences. More complex curved geometry of the basement is also tested and discussed with an analytical approximation that integrates the critical taper theory with the flexural bending of an elastic plate. The predicted surface slope is sensitive to the parameters of the elastic plate but also to the properties of the viscous detachment. Future work in this sense, should contemplate simulations that include the flexed shape of the basement. This would provide insights into the mechanics of the analytical solutions that was used in this work.

The influence of the mechanical stratigraphy on the dynamics and sequence of deformation has also been studied with different physical configurations of the sedimentary cover. Using a strong or weak cover changes the deformation style from either symmetric with no dominant vergence to asymmetric thrust systems with a dominant forelandward vergence and longer thrust sheets. Considering weak layers within the sedimentary cover, further switches the deformation mode to symmetric fold trains which is in agreement with previous works (Yamato et al., 2011).

7.4 References

Casciello, E., Vergés, J., Saura, E., Casini, G., Fernández, N., Blanc, E., Homke, S., and Hunt, D.W., 2009, Fold patterns and multilayer rheology of the Lurestan Province, Zagros Simply Folded Belt (Iran): Journal of the Geological Society, v. 166, p. 947-959.

Fuchs, L., Schmeling, H., and Koyi, H., 2011, Numerical models of salt diapir formation by down-building: the role of sedimentation rate, viscosity contrast, initial amplitude and wavelength: Geophysical Journal International, v. 186, p. 390-400.

Hudec, M.R., and Jackson, M.P.A., 2007, Terra infirma: Understanding salt tectonics: Earth-Science Reviews, v. 82, p. 1-28.

Ruh, J.B., Kaus, B.J.P., and Burg, J.-P., 2012, Numerical investigation of deformation mechanics in fold-and-thrust belts: Influence of rheology of single and multiple décollements: Tectonics, v. 31, p. TC3005.

Simpson, G.D.H., 2009, Mechanical modelling of folding versus faulting in brittle–ductile wedges: Journal of Structural Geology, v. 31, p. 369-381.

Yamato, P., Kaus, B.J.P., Mouthereau, F., and Castelltort, S., 2011, Dynamic constraints on the crustal-scale rheology of the Zagros fold belt, Iran: Geology, v. 39, p. 815-818.

Acknowledgements

Curriculum Vitae